

**Twisted Bilayers
of
Folded Graphene:
Morphology and Electronic Transport**

Von der QUEST-Leibniz-Forschungsschule
der Gottfried Wilhelm Leibniz Universität Hannover
zur Erlangung des Grades
Doktor der Naturwissenschaften
Dr. rer. nat.
genehmigte Dissertation

von
MSc Johannes Rode

2017

Referent: Prof. Dr. Rolf J. Haug
Leibniz Universität Hannover

Korreferent: Prof. Dr. Patrik Recher
Technische Universität Braunschweig

Korreferent: Prof. Dr. Peter Behrens
Leibniz Universität Hannover

Tag der Promotion: 21.12.2016

Abstract

The present dissertation investigates twisted bilayer graphene (TBG), created by folding of a monolayer. Monolayer graphene is prepared via mechanical exfoliation from graphite, in some cases yielding flipped-over flakes of general rotational mismatch between folded top and bottom layer, which thus constitute a convenient source of TBG.

In this work, folding is induced on purpose via nanomachining with the help of an Atomic Force Microscope (AFM). The latter is further employed to investigate primary TBG parameters like degree of rotational mismatch, interlayer distance and shape of the folded edge. Correlations between these are demonstrated to hold information about more implicit properties like interlayer interaction energy, furthermore allowing for inference about TBG creation via a thermally activated growth process following the initiation via AFM.

A number of samples are furthermore probed in magnetotransport measurements, finding two general phenomena:

Firstly, energetic crossover between layer-decoupled and -coupled behavior is observed in a TBG sample of 2.5° interlayer twist angle, together with a transition in Berry phase from π to 2π . The findings are put into theoretical context; additional features are discussed with respect to gated layer asymmetries.

Secondly, satellite Landau fans in magnetoresistance indicate secondary Dirac singularities in the spectra of several TBG with twist angles at and below 1.5° . The findings are ascribed to separate electronic scenarios, i.e. a reflection of graphene's pseudospin structure in TBG interlayer coupling, and backfolding into the mini-Brillouin zone of the TBG superlattice respectively.

Keywords:

twisted bilayer graphene, nanomachining, magnetotransport

Kurzzusammenfassung

Die vorliegende Dissertation befasst sich mit gegeneinander verdrehten Bilagen aus gefaltetem Graphen. Letzteres wird über mechanische Exfoliation aus Graphit gewonnen; mitunter werden hierbei Graphenflocken -in willkürlicher Orientierung- aufeinander gefaltet, wodurch turbostratisches Bilagen-Graphen (tBG) entsteht.

Im Rahmen dieser Arbeit wird Graphen gezielt durch mechanisches Nanostrukturieren per Rasterkraftmikroskop (RKM) gefaltet. Letzteres kommt im Anschluss auch zur Vermessung primärer tBG-Parameter wie Rotationswinkel und Abstand zwischen den Lagen, sowie Form der Faltkante zum Einsatz. Verschiedene Zusammenhänge in den untersuchten Größen erlauben Rückschluss auf schwerer zugängliche Daten wie interplanare Bindungsenergie; ferner kann der tBG-Entstehungsmechanismus auf thermisch aktivierten Wachstum -initiiert per RKM- zurückgeführt werden.

Magnetotransport-Messungen offenbaren zwei grundlegende elektronische tBG-Signaturen:

Der energetische Übergang zwischen ent- und gekoppelten Lagen, sowie ein Wechsel in der Berry-Phase zwischen π und 2π konnten in einer Bilage mit $2,5^\circ$ Rotationswinkel beobachtet werden. Die asymmetrische Induktion von Ladungsträgern führt hierbei zu interessanten Modifikationen der theoretischen Erwartung.

In weiteren Proben mit kleinen Rotationswinkeln unter $1,5^\circ$ weisen zusätzliche Landau-Fächer im Magnetowiderstand auf sekundäre Dirac-Singularitäten unterschiedlichen Ursprungs hin: Dies ist zum Einen das Zurückfalten der Bandstruktur in die Mini-Brillouinzone des tBG-Übergitters; eine weitere Messung zeugt von der Manifestation des Pseudospins in der Kopplung zweier Graphen-Dispersionen.

Schlagwörter:

turbostratisches Bilagen-Graphen, Magnetotransport, mechanisches Nanostrukturieren

Contents

1	Introduction	17
2	Graphene and its Twisted Bilayer: Theoretical Background	23
2.1	Lattice Structure	24
2.1.1	Monolayers and <i>AB</i> -stacking	25
2.1.2	Moiré Superstructures	28
2.1.3	Commensurate Superlattices	33
2.1.4	Lattice Distortion and Relaxation	48
2.2	Electronic Dispersion	56
2.2.1	Monolayer and <i>AB</i> -bilayer	57
2.2.2	Twisted Bilayer: Low-Energy Dispersion	65
2.2.3	The Superlattice mini-Brillouin zone	72
2.3	Magnetotransport	78
2.3.1	The Electric Field Effect	79
2.3.2	Landau Quantization	86
2.3.3	Shubnikov-de Haas Oscillations	92
2.4	Summary	94
3	Experimental Techniques and Apparatus	97
3.1	Graphene Flakes: Preparation and Optical Detection	98
3.2	Lithography: Etching and Electrical Contacts	105
3.3	Atomic Force Microscopy	110
3.3.1	Working Principles	110
3.3.2	Operation Modes and Data Channels	117
3.3.3	Imaging Artifacts	121
3.4	Magnetotransport: Cryogenic Setup and Measuring System	128
3.5	Summary	132

4	Structural Studies on Twisted Bilayer Graphene	133
4.1	Preparation of Twisted Graphene Bilayers	134
4.2	Morphology of Twisted Graphene Bilayers	149
4.2.1	Angular Distribution	150
4.2.2	Interlayer Distance	159
4.2.3	Folded Edge	165
4.2.4	Friction on TBG	177
4.3	Summary	182
5	Magnetotransport in Twisted Bilayer Graphene	185
5.1	Berry Phase Transition in a Twisted Graphene Bilayer	186
5.1.1	Sample Properties	186
5.1.2	Low Fermi Energy	189
5.1.3	High Fermi Energy	201
5.2	Satellite Landau Fans in Twisted Graphene Bilayers	214
5.2.1	Sample A	214
5.2.2	Sample B	225
5.3	Summary	234
6	Conclusions	237
	Appendix	245
	Bibliography	253
	CV/ Publications/ Scientific Conferences	277
	Credits	282

List of Constants, Symbols, and Abbreviations

List of Constants

Φ_0

Magnetic flux quantum $\frac{h}{e}=4.135\,667\,506 \times 10^{-15}$ Wb

e

Elementary charge of $1.602\,176\,62 \times 10^{-19}$ C

h, \hbar

Planck constant of $h=6.626\,070\,040 \times 10^{-34}$ J s,
reduced Planck constant of $\hbar=1.054\,571\,800 \times 10^{-34}$ J s

k_B

Boltzmann constant of $1.380\,648\,52 \times 10^{-23}$ J K⁻¹

m_0

Electron rest mass of $9.109\,382\,15 \times 10^{-31}$ kg

List of Symbols

ΔK

Distance between the two twisted graphene layers' rotationally displaced K -points (K' -points) in reciprocal space

Δb

Magnitude of elevation with respect to the plane of the top layer at the bended edge of folded graphene

$\Delta h_{(\text{AB})}$

Interlayer distance in a graphene bilayer of general (Δh) and AB-stacking configuration (Δh_{AB})

β

Berry phase

$\lambda_{\text{M,C,hBN}}$

Wavelength λ of superstructure between two lattices, describing continuous Moiré pattern (λ_{M}) and commensurate superlattice (λ_{C}) respectively. λ_{hBN} refers to the superstructure between graphene and hexagonal boron nitride

$\mu_{\text{e,h}}$

Charge carrier mobility μ , specific to electrons (μ_{e}) and holes (μ_{h})

ν

Filling factor of Landau levels

ω_{c}

Cyclotron frequency $\omega_{\text{c}} = \frac{eB}{m^*}$

θ

Angle of rotational mismatch between lattices in a twisted graphene bilayer

a_{G}

Lattice constant of graphene, measuring 246 pm

$\mathbf{a}_{1,2}$

Lattice vectors of graphene:

$$\mathbf{a}_1 = a_G \begin{pmatrix} 1/2 \\ \sqrt{3}/2 \end{pmatrix}, \mathbf{a}_2 = a_G \begin{pmatrix} -1/2 \\ \sqrt{3}/2 \end{pmatrix}$$

$\hat{\mathbf{a}}_{1,2}$

Reciprocal lattice vectors of graphene:

$$\hat{\mathbf{a}}_1 = \frac{2\pi}{a_G} \begin{pmatrix} 1 \\ 1/\sqrt{3} \end{pmatrix}, \hat{\mathbf{a}}_2 = \frac{2\pi}{a_G} \begin{pmatrix} -1 \\ 1/\sqrt{3} \end{pmatrix}$$

b_G

Distance between nearest neighbors/constituents of the two-atomic basis of graphene's lattice, measuring 142 pm

$C^{(*)}$

C : electrical capacitance;

C^* : capacitive coupling constant to an electrical gate, proportionally relating n to U_{BG} (related to C via division by area A and elementary charge e)

E_F

Fermi energy

K

Distance between Γ and K -point (also between K - and K' -point) in graphene's first Brillouin zone

ℓ

Length of the folded edge in twisted bilayer graphene

m^*

Effective (and cyclotron) mass of a charge carrier in the electronic dispersion of a solid state system.

$n_{b,t,tot}$

Charge carrier concentration n ,
specific to bottom layer (n_b),
top layer (n_t),
and sign-sensitive sum of both layers (n_{tot})

r

Radius of curvature in the bended edge of folded graphene

Si(+)

Silicon (Si); p-doped (Si⁺) for the use as electrical backgate

SiC

Silicon carbide

SiO₂

Silicon dioxide

$t_{e,h}^\theta$

Interlayer hopping energy in rotationally faulted systems t^θ ,
specific to electron-like (t_e^θ)
and hole-like (t_h^θ) dispersion

$U_{BG,CNP}$

Backgate voltage as general parameter (U_{BG})
and at the charge neutrality point (U_{CNP})

v_F, \tilde{v}_F

Fermi velocity (v_F)
and reduced Fermi velocity (\tilde{v}_F)

List of Abbreviations

- 2D** two-dimensional
- 2DEG** two-dimensional electron gas
- AC** alternating current
- AFM** Atomic Force Microscope
- CNP** charge neutrality point
- CVD** chemical vapor deposition
- DC** direct current
- DoS** Density of States
- hBN** hexagonal Boron Nitride
- LEED** Low Energy Electron Diffraction
- LL** Landau level
- mBz** mini-Brillouin zone
- MLG** Monolayer Graphene
- PMMA** polymethyl methacrylat
- QHE** Quantum Hall Effect
- SC** single crystal
- SdH** Shubnikov-de Haas
- SE** sublattice exchange
- SEM** Scanning Electron Microscope

- STM** Scanning Tunneling Microscope
STS Scanning Tunneling Spectroscopy
TBG Twisted Bilayer Graphene
TEM Transmission Electron Microscope
vdW van der Waals
vHs van Hove singularity

1 Introduction

Twisted bilayers of folded graphene are best introduced by taking a look at the latter first:

Graphene has drawn massive scientific attention during the past decade and exhibits - mechanically as well as electronically - a multitude of fascinating properties[1]:

To begin with, its mere stable existence was long thought impossible, as thermal fluctuations should melt a **two-dimensional (2D)** crystal at any finite temperature¹. Nevertheless, isolation of single-atomic graphite planes was achieved as early as 1962 by Boehm[3], who later also coined the term of graphene[4]. Geim and Novoselov established the study of the material 's electronic properties in 2004[5], awarding them the Nobel price in physics in 2010. Corresponding avenue to the rich electronic spectra of graphene enabled first-time observation of several fundamental physical concepts in practice:

In consequence of its two-sublattice structure, description of the hosted electronic wave functions in graphene requires an additional degree of freedom, which is often referred to as pseudospin. This manifests in a nonzero Berry phase of π and the observation of an anomalous, half-integer **Quantum Hall Effect (QHE)** for **Monolayer Graphene (MLG)**[6, 7]. Low-energy **MLG** bands are furthermore linear, mimicking a relativistic scenario with zero rest mass and constant Fermi velocity $v_F \approx 1 \times 10^6 \text{ m s}^{-1}$ as effective speed of light.

¹a stable quasi-2D configuration is achieved via out-of-plane corrugation[2].

From a top-down point of view, **Twisted Bilayer Graphene (TBG)** constitutes the most elementary example of turbostratic graphite; in a bottom-up perspective it provides the ultimate model system for **van der Waals (vdW)** interaction between **2D**-crystals.

In many ways, **TBG** may be seen as a scaled reflection of **MLG**; multiple characteristic aspects of the constituting layers reappear - magnified in real-space; reduced in momentum as well as energy - in the bilayer system:

The following section **2.1** treats the real-space to begin with: Rotationally misaligned superposition of two lattices generally leads to the formation of Moiré pattern, reflecting the original periodic structure on a larger scale. For a discrete set of interlayer twist angles, rotated lattices furthermore become commensurate, rendering the superstructures strictly periodic. Section **2.1.3** provides an in-depth review of the underlying geometrical principals.

In addition, twisted layers will corrugate and distort in response to varying interlayer lattice registry across a superstructure's unit cell; according impact on **TBG** morphology in different substrate environments is discussed in [sec. 2.1.4](#).

Section **2.2** reviews electronic dispersion, starting with a most established interlayer coupling scenario: Individual rotationally displaced bands of twisted layers persist in small energies until merging in avoided crossing, forming a **van Hove singularity (vHs)**[[8](#), [9](#)]. Fermi velocity is herein reduced with respect to **MLG**.

An alternative coupling model predicts the generation of secondary Dirac singularities instead[[10](#)], which is a reflection of the above introduced **MLG** pseudospin structure in the **TBG** dispersion.

In momentum-space, the superlattice periodicity is reflected in an accordingly small Brillouin zone, leading to backfolding of the dispersion, which constitutes a further mechanism behind the generation of secondary Dirac singularities at higher energy[[11](#), [12](#)].

In general, the scenario of two conducting layers in closest possible vicinity is associated with phenomena like excitonic condensation, Coulomb drag or quantum capacitive screening of charge[13–15]. This renders the twisted graphene bilayer system a highly promising platform for fundamental research and encourages its thorough understanding which may furthermore be translated to stacked vdW-heterostructures[16] for electronic devices.

The here presented findings are based on experimental studies of TBG morphology as well as electronic structure.

Techniques and apparatus needed on the here taken route from a piece of graphite to the resolution of Moiré superlattices in TBG - or to electrical measurements on a sample in high magnetic fields - are introduced in chapter 3. Special focus is herein directed to the Atomic Force Microscope (AFM), on one hand serving for the lithographic task of micromechanical manipulation, on the other for imaging and detailed investigation of TBG morphology.

Section 4.1 continues with the topic of TBG preparation: The method of choice for the present work lies in the folding of a MLG sheet onto itself, thereby creating TBG with top and bottom layer connected via a bended edge.

A here investigated method induces folding via AFM nanoindentation. A recently proposed thermally activated growth mechanism[17] is identified in driving TBG expansion after mechanical initiation; two classes of folded geometry can herein be distinguished and are shown to follow individual growth dynamics.

Section 4.2 provides a systematic AFM study of sample morphology for thusly prepared TBG samples:

In sec. 4.2.1, two methods for determining interlayer twist are introduced and applied; the according distribution of twist angles is discussed with respect to the above mentioned classes in folded geometry.

Section 4.2.2 investigates TBG interlayer distance, finding large variations over a span of $\sim 3 \text{ \AA}$ and a pronounced twist-angle dependence. The results are discussed with respect to lattice corrugation as well as interlayer commensuration.

A unique characteristic in here investigated TBG of folded MLG, the connecting bended edge is shown to correlate with the parameters of interlayer distance and twist angle in terms the folded length. In the frame of the above introduced dynamic growth model[17], these findings allow for inference of interlayer interaction energy, as presented in sec. 4.2.3. Given its rounded cross-sectional shape moreover, the folded edge may be viewed as half a carbon nanotube. The fold's radius of curvature is found to scale with the folded length, in fact reflecting earlier theoretical nanotube studies.

In sec.4.2.4, enhanced AFM-measured friction on the TBG surface is furthermore discussed with respect to superlubricity in between incommensurate layers[18]. The bended edge is herein found to have a stabilizing effect.

Chapter 5 finally investigates the electronic structure of TBG in magnetotransport experiments, finding indications for three distinct scenarios as introduced in sec. 2.2.

In section 5.1 the spectra of two decoupled MLG dispersions with reduced Fermi velocity are observed in low energies. The signatures are enriched by the induction of layer asymmetries via a capacitive gate, which is described by a screening model accounting for electron-hole asymmetry and Fermi velocity renormalization.

In high energies, a theoretically anticipated change in Berry phase is detected[19, 20]; magnetic-field dependence in the phase transition is discussed in terms of Fermi-energy pinning to different Landau levels.

Section 5.2 reports on additional Landau fans in longitudinal magnetoresistance which arise in two distinct electronic scenarios:

In case of the first-presented TBG transport signature, different degrees of degeneracy are found between the respective Landau fans, which - in conjunction with the analysis of their occurrence in different charge carrier concentration - indicates manifestation of the alternative coupling model from ref.[10].

In two further samples, the generation of additional Dirac singularities can be attributed to backfolding at the mini-Brillouin zone boundary of the TBG superlattice. A special sample geometry is herein found to promote an effective electronic scenario which is similar to the one in heterostructures of graphene on a substrate of hexagonal Boron Nitride (hBN)[11].

Observation of the above variety in electronic scenarios is discussed with respect to different degrees of rotational mismatch. Moreover, the oftentimes neglected role of lattice corrugation and distortion will be a recurrent theme in explanation of here found as well as elsewhere reported TBG spectra, which ties together the two investigated aspects of morphology and electronic structure.

2 Graphene and its Twisted Bilayer: Theoretical Background

The following chapter is designed to provide theoretical background for the main experimental findings presented in [chap. 4](#) and [chap. 5](#). Furthermore it should be considered as review and compendium of the current state in [TBG](#)-research.

Organized in three sections building on each other, this chapter starts with the lattice structures of [MLG](#) and [TBG](#) ([sec. 2.1](#)), continues with the corresponding electronic dispersions ([sec. 2.2](#)) and ends with the expected magnetotransport behavior ([sec. 2.3](#)). Theoretical prediction is compared to experimental studies on [TBG](#), in some aspects extending to the related field of graphene on a substrate of [hBN](#).

Special attention is given to the angle-dependent superstructures between rotated lattices in the first section [2.1](#): Making for a fascinating geometric study in their own right, Moiré pattern ([sec. 2.1.2](#)) and commensurate superlattices ([sec. 2.1.3](#)) sensitively determine [TBG](#) band structure and quantization in magnetic field; subtle nuances in real-space structure may significantly influence electronic features ([sec. 2.2.3](#)). Furthermore, periodic long-range corrugations provide accurate means to determine interlayer rotation via scanning probe microscopy ([sec. 4.2](#)). A thorough understanding of the underlying structures is therefore of central importance and will be developed in the following.

2.1 Lattice Structure

The basis of a crystal's physical properties lies in its chemical composition and lattice structure. The present section will therefore start with the element of carbon and one of its allotropes, the two-dimensional sp^2 -network also known as a single layer of graphene[4, 21] (sec. 2.1.1).

A geometrical view is then taken on the interposition of two such identical honeycomb lattices under an arbitrary angle of rotation, which is the structure of the twisted graphene bilayer. In sec. 2.1.2 and sec. 2.1.3, corresponding angle-dependent superstructures[22–25] are reviewed and classified in terms of lattice commensurability: Incommensurate Moiré pattern have been detected in early **Scanning Tunneling Microscope (STM)**-studies on the surface of turbostratic graphite[26]. Later, band structure calculations for **TBG** generally required consideration of commensurate superlattices for the application of Bloch's theorem.

Beyond this important distinction, the **TBG** structure is currently disclosing further aspects of considerable complexity:

In progress for decades[27, 28], research on the geometry of superlattices continues to reveal novel phenomena: Characterized by their sublattice exchange symmetry, two different commensuration classes in **TBG** were pointed out in ref.[29] and most recently proved to be of experimental relevance[30]. The corresponding intricate geometries are illustrated towards the end of sec. 2.1.3.

Finally, a most recent development goes beyond the purely geometric approach of rigidly interposed lattices: the presently evolving focus on lattice distortion in stacked **2D**-materials with periodic superstructures is discussed in sec. 2.1.4. Out-of-plane corrugation and in-plane distortion arise due to relaxation of atomic positions in response to periodic variation in local stacking configuration[25, 31], which may have significant impact on the properties of **TBG** (cf. sec. 2.2 and chap. 5).

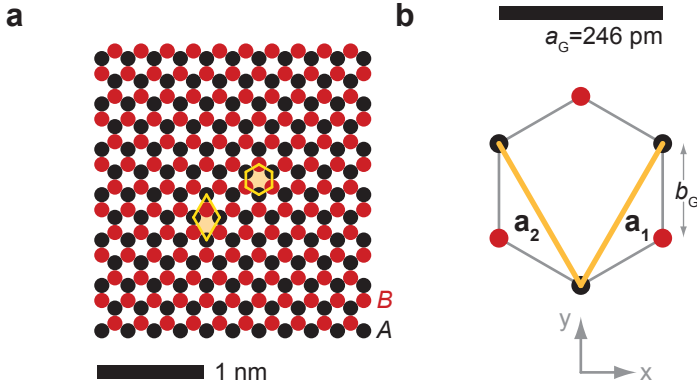
2.1.1 Monolayers and *AB*-stacking

Figure 2.1 a: Graphene's honeycomb structure with dots as sp^2 -hybridized carbon atoms at lattice positions. Sublattices *A* and *B* are marked in black and red respectively. Two representations of a primitive unit cell are drawn in yellow. **b:** Primitive unit cell with two-atomic base of atoms *A* (black) and *B* (red) and lattice vectors $\mathbf{a}_{1,2}$. The scalebar to the top spans one lattice constant, the coordinate system to the bottom provides a frame for eq. 2.1.

In its ground state, the carbon atom's electronic configuration is $1s^2 2s^2 2p^2$ with two singly occupied orbitals $2p_x, 2p_y$ according to Hund's second rule. Excitation of an electron from the doubly occupied $2s^2$ -orbital to the $2p_z$ -orbital thus increases the number of possible bonds by a factor of two, which is energetically favorable in the presence of available bonding partners. An even lower energetic state is achieved in mixing between the four valence shell orbitals by linear combination of the corresponding wave functions: The $2s$ and three $2p$ -orbitals hybridize to four equivalent sp^3 -orbitals

in tetrahedral symmetry, leading to the diamond cubic crystal structure[32]. The p_z -orbital may be excluded from mixing, hybridizing the remaining $2p_x$ - $2p_y$ - and $2s$ -orbitals in three sp^2 -orbitals. These lie in the xy -plane, separated by angles of 120° in C_3 -symmetry and are responsible for the graphitic lattice structure (fig. 2.1): the building block of graphite, fullerenes[33], carbon nanotubes[34] and graphene[1].

The honeycomb pattern arising from σ -bonds between sp^2 -hybridized carbon atoms is not a Bravais lattice. A bi-atomic basis of neighboring atoms A and B (fig. 2.1, black and red respectively) is therefore needed to describe the hexagonal structure via a trigonal lattice. The carbon-carbon bond length in graphene lies at $b_G = 142 \text{ pm}$ [2], primitive translations follow from geometry as

$$\begin{aligned} \mathbf{a}_1 &= a_G \begin{pmatrix} 1/2 \\ \sqrt{3}/2 \end{pmatrix} \\ \mathbf{a}_2 &= a_G \begin{pmatrix} -1/2 \\ \sqrt{3}/2 \end{pmatrix} \end{aligned} \tag{2.1}$$

with lattice constant $a_G = 246 \text{ pm}$ and in the coordinate system to the bottom of fig. 2.1 b.

In structures built of multiple graphene sheets (i.e. graphite or fewlayer graphene), the most common configuration lies in Bernal- or AB -stacking. Layers are weakly bound by vdW -interaction; the interlayer distance is $\Delta h_{AB} = 3.35 \text{ \AA}$ [35]. Figure 2.2 shows the lattice of an AB -stacked graphene bilayer with its name-giving coincident A - and B -sites in bottom and top layer respectively (see legend to the bottom). Starting at overall congruent AA -stacking, there are two ways to achieve Bernal-stacking: The first lies in a translation along b_G to the site of a nearest neighbor as indicated by the blue arrow in fig. 2.2, the second in a 60° -rotation around an arbitrary lattice site as indicated in green (top left, fig. 2.2).

In terms of TBG, AA-stacking and AB-stacking may thus be understood as the extreme cases of 0° - and 60° -rotation angle. The general cases of rotational mismatch angles $0^\circ < \theta < 60^\circ$ are discussed in the following [sec. 2.1.2](#).

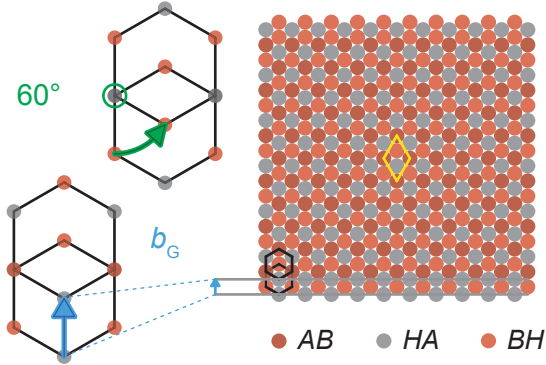


Figure 2.2 Right: Two hexagonal lattices interposed in AB-stacking configuration. Sublattices are marked in gray (A) and red (B), interpositions of bottom and top layer are AB, HA and BH as indicated in the legend to the bottom, where H marks a hexagon center. Left: Two hexagonal unit cells, interposed in Bernal-stacking, achieved from AA-stacking by rotation (top) and translation (bottom) respectively.

2.1.2 Twisted Bilayer Graphene: Moiré Superstructures

Superposition of identical geometric structures under an angle of rotational mismatch will give rise to an apparent reflection of the original pattern at a larger scale (also applicable to aligned structures of slightly different periodicity). These long-range modulations are known as Moiré superstructures[36–38], the denomination deriving from the french expression for a special treatment of cloth[37, 38].

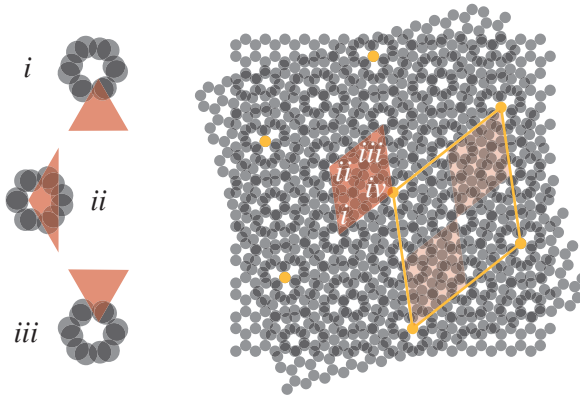


Figure 2.3 Two hexagonal lattices, twisted against each other by an angle of 16.426° . Most notable to the eye is a Moiré pattern with unit cell marked in red. Three of its corners (*i* – *iii*) are magnified in the inset to the left. The fourth corner (*iv*) coincides with lattice sites of both twisted layers. Marked in yellow is a strictly commensurate superstructure of twice the Moiré wavelength (notice two red transparent rhombi fitting into the yellow one).

Perceivable by the human eye in graphical representation (fig.2.3), the Moiré pattern also manifests itself on the nanoscale between

rotated atomic lattices: Periodic real-space variations observed in **STM**-measurements on the surface of graphite were first connected with rotational mismatch of an atomic top layer in ref.[26]. Since then, superstructures have been routinely resolved via **Transmission Electron Microscope (TEM)**[24], **Low Energy Electron Diffraction (LEED)**[39] and **AFM**[40] (see also [sec. 4.2.1](#) for the latter).

It shall be noted that the perceived periodicity λ_M of detected Moiré modulations (e.g. in optical contrast, density of states or height) does, in general, not reflect a commensurate lattice on the atomic scale: Figure 2.3 shows a **TBG**-schematic featuring bright and dark rings, which alternate in an apparently periodic fashion (marked in red). As evident from the atomically nonequivalent corner positions of the Moiré unit cell however (fig. 2.3, inset to the left), the corresponding superstructure is not strictly periodic. In the depicted example, a true, commensurate lattice may be found at wavelength $\lambda_C = 2 \cdot \lambda_M$ (fig. 2.3, indicated in yellow).

The existence and wavelength of commensurate structures at a given rotational mismatch will be discussed in [sec. 2.1.3](#); a mathematical description of the visually dominant Moiré pattern is provided in the following.

Various approaches lead to an expression for the Moiré superstructure between two given lattices[36–38, 41]. Here, the superposition of trigonometric functions and simple relations in reciprocal space are employed to sketch out the principles involved: Consider two identical line grids, rotated against each other by an angle of θ . Line spacing a and orientation shall be given by wave vectors

$$\mathbf{k} = \frac{2\pi}{a} \begin{pmatrix} \cos(0) \\ \sin(0) \end{pmatrix}, \quad \mathbf{q} = \frac{2\pi}{a} \begin{pmatrix} \cos(\theta) \\ \sin(\theta) \end{pmatrix}$$

respectively. To describe the lines and gaps via an intensity $0 \leq I_G \leq 1$ in dependence on position vector \mathbf{x} , squared cosine functions

$$\cos^2(\mathbf{kx}/2), \quad \cos^2(\mathbf{qx}/2)$$

are chosen as an approximation of grids (the denominator of 2 in the cosines' arguments compensating for the effective doubling of wave number upon squaring). Panels a and c of [fig. 2.4](#) show the above functions as maps of intensity for an example rotation of $\theta=30^\circ$.

The two grids are superposed by summation of the corresponding functions (left-hand side of [eq. 2.2](#)), giving rise to the Moiré pattern depicted in [fig. 2.4 b](#). Mathematically, trigonometric identity[42] yields:

$$\cos\left(\frac{\mathbf{k}\mathbf{x}}{2}\right)^2 + \cos\left(\frac{\mathbf{q}\mathbf{x}}{2}\right)^2 = 1 + \cos\left(\frac{\mathbf{k}-\mathbf{q}}{2}\mathbf{x}\right) \cdot \cos\left(\frac{\mathbf{k}+\mathbf{q}}{2}\mathbf{x}\right). \quad (2.2)$$

The cosine functions in the product on the right-hand side of [eq. 2.2](#) are depicted in [fig. 2.4 d,e](#). Apparently, there is a long-wavelength intensity modulation of wave vector

$$\mathbf{G}/2 = \frac{\mathbf{k}-\mathbf{q}}{2}, \quad (2.3)$$

effectively acting as an envelope for a perpendicularly propagating modulation of smaller wave number

$$\frac{|\mathbf{k}+\mathbf{q}|}{2} \approx |\mathbf{k}| = |\mathbf{q}| \quad (2.4)$$

at reasonably small θ .

The former, envelope function of wavelength $\lambda_{\mathbf{G}/2} = 4\pi|\mathbf{G}|^{-1}$ is responsible for the perceived Moiré periodicity $\lambda_{\mathbf{M}}$ which is half of $\lambda_{\mathbf{G}/2}$ (compare black arrow and green bar, [fig. 2.4 b](#)). The two wavelengths may be reconciled by looking at the average intensity along the dashed parallel lines in [fig. 2.4 b](#), integrating over the much smaller features described by [eq. 2.4](#): Evidently the only difference between intensity modulations along black and white line is an effective phase shift of π (see black and white ovals, [fig. 2.4 b](#)) which is not significant to the human eye (and likewise a microscope of limited resolution) at $|\mathbf{G}| \gg |\mathbf{k}|$.

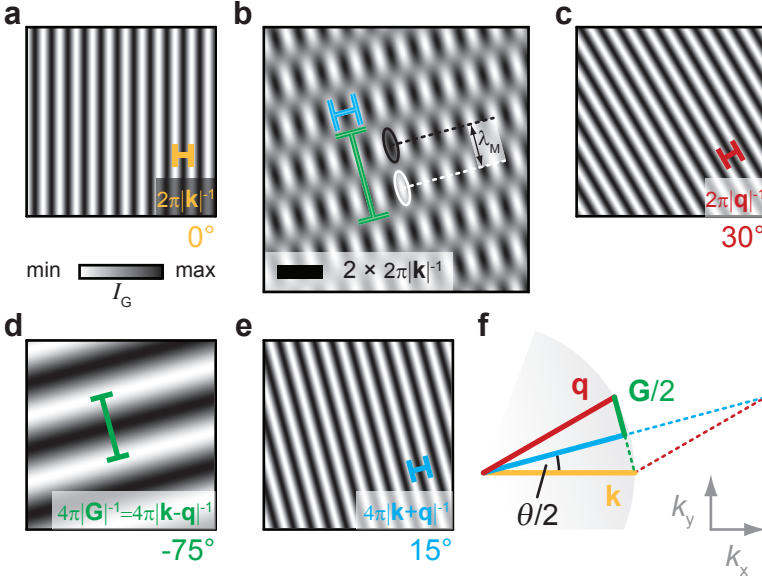


Figure 2.4 **a:** Periodic line pattern; first summand on the left-hand side of eq. 2.2. The wavelength is indicated in yellow. **b:** Sum of line patterns in **a** and **c**. Periodicities are marked in blue and green. Ovals mark nonequivalent features in the pattern, dashed lines indicate paths of equal average intensity I_G . **c:** Periodic line pattern; second summand on the left-hand side of eq. 2.2. The wavelength is indicated in red. **d:** Envelope and first factor of the product on the right-hand side of eq. 2.2. The wavelength is marked in green. **e:** Average of **a** and **c** in terms of wave vector (wavelength marked in blue) and second factor of the product on the right-hand side of eq. 2.2. **f:** Schematic of reciprocal space: wave vectors of the four cosine functions in eq. 2.2 are depicted according to the color code used in panels **a-e**.

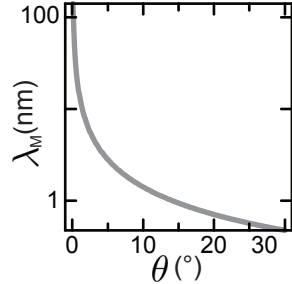
Analog to the perceived volume modulations in acoustic beat[43], the Moiré wavelength in rotated grids of reasonably small twist angle θ is therefore given by the difference \mathbf{G} between the original wave vectors \mathbf{k} and \mathbf{q} as $\lambda_M = 2\pi/|\mathbf{G}|$. Alternative to eq. 2.3, $|\mathbf{G}|$ is readily derived via trigonometry as suggested in fig. 2.4 f, yielding

$$\lambda_M(\theta) = \frac{a}{2 \cdot \sin(\theta/2)}, \quad (2.5)$$

with the one-dimensional relation $|\mathbf{k}| = \frac{2\pi}{a}$.

The above reasoning can analogly be extended to more complex two-dimensional lattices[36, 37] like graphene, ultimately reaching the same relation, expressed in eq. 2.5. Because of graphene's C_6 -symmetry, twist angles $30^\circ \leq \theta \leq 60^\circ$ are equivalent to $60^\circ - \theta$ in terms of Moiré wavelength. Therefore, only angles $0^\circ \leq \theta \leq 30^\circ$ need to be considered for all possible λ_M as depicted in fig. 2.5.

Figure 2.5 Moiré wavelength λ_M in dependence on rotational mismatch θ between two rotated lattices. The wavelength reaches its minimum of $\lambda_M = 475$ pm at $\theta = 30^\circ$ and diverges to infinity as $\theta \rightarrow 0^\circ$. In between there is a rapid increase of wavelength for $\theta \lesssim 10^\circ$ towards smaller angles (notice the logarithmic scale).



While Moiré modulations are visually dominant (fig. 2.3), a convenient indicator of interlayer rotation[9, 12, 44, 45] and in large parts responsible for TBG-electronic structure[41, 46–48] (see also sec. 2.2), there are phenomena in TBG-physics which can only be understood in terms of lattice commensuration[29, 30, 49]. The conditions for the emergence of these strictly periodic superlattices are investigated in the following sec. 2.1.3.

2.1.3 Twisted Bilayer Graphene: Commensurate Superlattices

In the following, an expression for all possible commensurate superstructures between two identical trigonal lattices shall be derived. Notation mostly follows ref.[23]; aspects of perspective and ideas of visualization were furthermore inspired by refs.[22, 25, 29, 50–52].

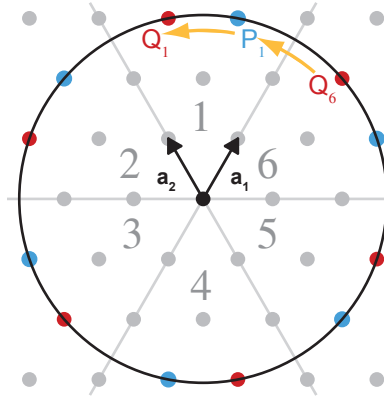


Figure 2.6 Representation of one of the two trigonal sublattices of graphene (dots) with unit vectors \mathbf{a}_1 and \mathbf{a}_2 (black arrows). The circle defines a shell of lattice sites (colored dots) equidistant to the center (black dot). C_6 -periodic sectors with one P- (blue) and Q- (red) lattice site each are marked by numbers 1-6. Curved yellow arrows indicate possible commensurate lattice rotations.

A sensible approach to the problem starts with two congruently aligned trigonal lattices with the center of rotation set to a lattice position (fig. 2.6). This defines an origin around which lattice sites may be rotationally displaced on equidistant shells (e.g. black circle, fig. 2.6). Because of the trigonal lattice's C_6 -symmetry, 60° -rotation

is equivalent to unity; each C_6 -periodic sector (1 to 6, [fig. 2.6](#)) houses two lattice sites P^c and Q^c for every shell c (blue and red dots in [fig. 2.6](#)). All commensurate rotations are therefore described by two maps $M : P_1 \mapsto Q_1$ and $M' : Q_6 \mapsto P_1$ as marked by the yellow arrows in [fig. 2.6](#).

Corresponding superlattice wavelengths are $\lambda_C = \lambda_{C'}$, rotation angles $\theta = 60^\circ - \theta'$ within a given shell. Parameters may generally be expressed via the scalar product

$$\mathbf{p}_i \cdot \mathbf{q}_j = \cos(\theta) \cdot \lambda_C^2 \quad (2.6)$$

of vectors \mathbf{p}_i , \mathbf{q}_j from the center of rotation to lattice sites P_i , Q_j (black dot to colored dots, [fig. 2.6](#)), where

$$\begin{aligned} \lambda_C &= |\mathbf{q}_1| = |\mathbf{q}_6| \\ &= |\mathbf{p}_1| = |m \cdot \mathbf{a}_1 + n \cdot \mathbf{a}_2| = \sqrt{m^2 + mn + n^2} \cdot a_G \end{aligned} \quad (2.7)$$

with integers n, m . Using the above relations, [eq. 2.8](#) finds the expressions for commensurate rotation angles which may be indexed by a pair of integers $\theta(m, n)$ and $\theta'(u, v)$, according to the number of unit vectors \mathbf{a}_1 , \mathbf{a}_2 needed to build the corresponding \mathbf{p}_i , \mathbf{q}_j . Note that only coprime pairs of indices m, n (u, v) have to be considered for the full set of commensurate structures, as all else describes mere integer multiples of a smallest possible wavelength correspondent to the primitive superlattice unit cell. Furthermore, indices m, n (u, v) commute with respect to superlattice wavelength and a twist angle between 0° to 60° , so only $n < m$ ($v < u$) need to be considered.

$$\begin{aligned}
 \mathbf{P}_1 &\mapsto \mathbf{Q}_1 \\
 \mathbf{p}_1 \cdot \mathbf{q}_1 &= [m \cdot \mathbf{a}_1 + n \cdot \mathbf{a}_2] \cdot [n \cdot \mathbf{a}_1 + m \cdot \mathbf{a}_2] \\
 &= \left(\frac{1}{2} m^2 + 2mn + \frac{1}{2} n^2 \right) \cdot a_G^2 \quad (2.8a) \\
 \Rightarrow \cos(\theta) &= \frac{1/2 \cdot m^2 + 2mn + 1/2 \cdot n^2}{m^2 + mn + n^2}
 \end{aligned}$$

$$\begin{aligned}
 \mathbf{Q}_6 &\mapsto \mathbf{P}_1 \\
 \mathbf{q}_6 \cdot \mathbf{p}_1 &= [(u + v) \cdot \mathbf{a}_1 - v \cdot \mathbf{a}_2] \cdot [u \cdot \mathbf{a}_1 + v \cdot \mathbf{a}_2] \\
 &= \left(u^2 + uv - \frac{1}{2} v^2 \right) \cdot a_G^2 \quad (2.8b) \\
 \Rightarrow \cos(\theta') &= \frac{u^2 + uv - 1/2 \cdot v^2}{u^2 + uv + v^2}
 \end{aligned}$$

Figure 2.7 visualizes the results from eq. 2.8 in a plot of wavelength vs. twist angle: Commensurate parameter pairs from map M are depicted in yellow shifting to red for rising index n (eq. 2.8a), results from map M' are color-coded in blue growing darker for rising index v (eq. 2.8b).

Notably, the lower bound of commensurate wavelengths λ_C falls together with the continuous Moiré relation at discrete angles growing increasingly dense for $\theta \rightarrow 0^\circ$ and $\theta' \rightarrow 60^\circ$. Corresponding structures are described by $(m - n) = 1$ and $(u - v) = 1$ (see examples in fig. 2.7), which can be understood mathematically by combining equations 2.6, 2.7 and 2.8a to

$$\lambda_C^2 - \frac{1}{2} (m - n)^2 a_G^2 = \cos(\theta) \lambda_C^2$$

and using the trigonometric identity[42] $1 - \cos(\theta) = 2 \sin^2(\theta/2)$, to get:

$$\lambda_C = \frac{|m - n| a_G}{2 \sin(\theta/2)}.$$

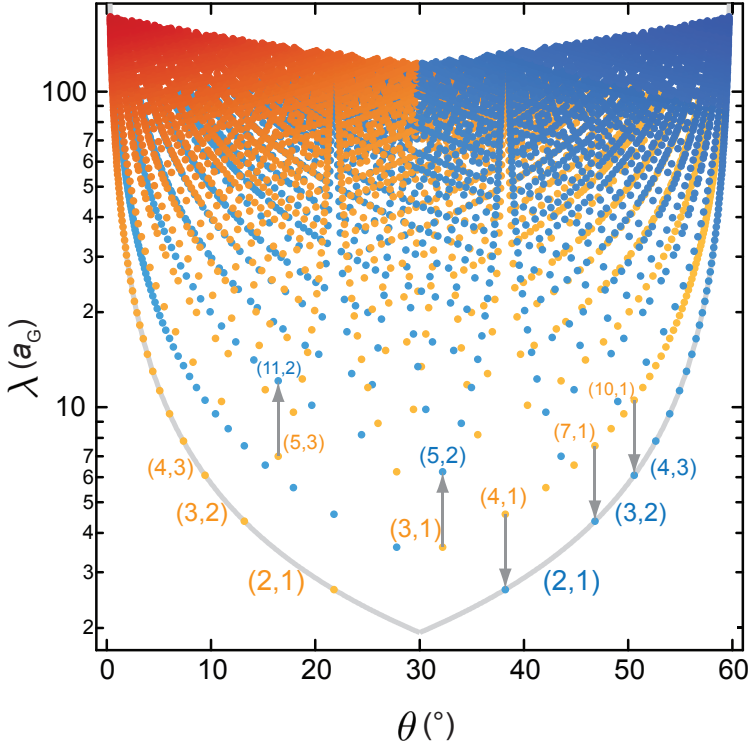


Figure 2.7 Superlattice wavelength λ_C in units of graphene's lattice constant a_G vs. interlayer twist angle θ for commensurate structures of indices $(m, n) \leq (100, 100)$ corresponding to map M (eq. 2.8a, orange dots) and $(u, v) \leq (100, 100)$ corresponding to map M' (eq. 2.8b, blue dots). Gray line: Moiré wavelength λ_M in units of graphene's lattice constant a_G vs. interlayer twist angle. Gray arrows mark selected commensurate pairs of identical twist angle with M - and M' -origin respectively.

The above results are often regarded as conclusive in describing all possible commensurate superstructures by an angle of rotational mismatch and the correspondent wavelength of a primitive unit cell[22, 25, 41, 50]. However there still appear to be angles of rotational mismatch with doubly defined wavelengths $\lambda_{\mathbf{C}}(\theta) \neq \lambda_{\mathbf{C}}(\theta')$ (examples indicated by gray arrows in fig. 2.7), the larger of which thus characterize non-primitive unit cells by definition.

Where a single map M on its own acts as a proper function $\theta \mapsto \lambda_{\mathbf{C}}(\theta)$ by restriction to coprime index pairs m, n (same for map M' and indices u, v), there is an ambiguously defined subset of wavelengths between both maps. Combining M and M' to one function and determining criteria for the elements of this subset, the following pages provide analytical expression and geometrical understanding inspired by refs.[23, 29, 52]: It will prove useful to introduce indices $r = m - n$ and $s = u - v$ and rewrite the results of eq. 2.8 as

$$\begin{aligned} \cos(\theta) &= \frac{1/2 \cdot n^2 + 2(r+n)n + 1/2 \cdot (r+n)^2}{n^2 + (r+n)n + (r+n)^2} \\ &= \frac{3n^2 + 3nr + 1/2 \cdot r^2}{3n^2 + 3nr + r^2} \\ &= \frac{3(n+r/2)^2 - (r/2)^2}{3(n+r/2)^2 + (r/2)^2} \end{aligned} \tag{2.9a}$$

$$\begin{aligned} \cos(\theta') &= \frac{(s+v)^2 + (s+v)v - 1/2 \cdot v^2}{v^2 + (s+v)v + (s+v)^2} \\ &= \frac{s^2 + 3vs + 3/2 \cdot v^2}{3v^2 + 3vs + s^2} \\ &= \frac{(s+3v/2)^2 - 3(v/2)^2}{(s+3v/2)^2 + 3(v/2)^2} = \frac{3(s+3v/2)^2 - (3v/2)^2}{3(s+3v/2)^2 + (3v/2)^2} \end{aligned} \tag{2.9b}$$

Evidently, maps M and M' may be expressed in equivalent form, where s and $3v$ in map M' take the place of n and r in map M . All commensurate angles are therefore given by map M alone where at every r equivalent to $3v$ with

$$r \bmod 3 = 0,$$

the wavelength λ_C , expressed in eq. 2.7 is reduced by a factor of $\sqrt{3}$ (note that in the last step of eq. 2.9b, the fracture gets enhanced by 3, making the denominator equal to $3 \times \lambda_C^2$).

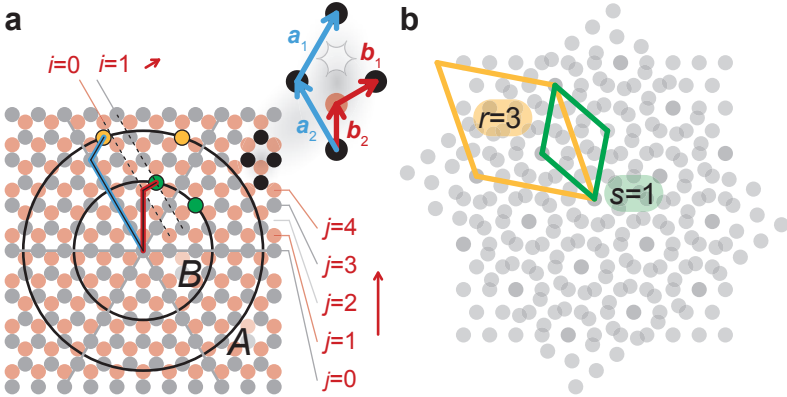


Figure 2.8 a: Honeycomb structure of graphene with two shells A $((m, n) = (4, 1) / (r, n) = (1, 1))$ and B $((u, v) = (2, 1) / (s, v) = (1, 1))$ marked as concentric circles. $\sqrt{3} \times \sqrt{3}$ - and primitive structure are marked in yellow and green respectively. Red indices i, j describe shell B in terms of nearest-neighbor vectors. Inset: Magnified unit cell with vectors $\mathbf{a}_{1,2}, \mathbf{b}_{1,2}$. **b:** Two lattices twisted by 38.213° . Primitive and $\sqrt{3} \times \sqrt{3}$ -non-primitive commensuration cell are indicated in green and yellow respectively.

The significance of " $r \bmod 3 = 0$ "-structures is inherently rooted in graphene's trigonal lattice and may be understood geometrically in the example of [fig. 2.8](#): A vector $\mathbf{q}_1^b = m^b \mathbf{b}_1 + n^b \mathbf{b}_2$ (with $\mathbf{b}_1, \mathbf{b}_2$ connecting nearest neighbors as indicated in the inset to the top) relates to vector $\mathbf{q}_1 = n \mathbf{a}_1 + m \mathbf{a}_2$ of map M by -30° rotation and scaling by $\frac{1}{\sqrt{3}}$ for $(m^b, n^b) = (n, m)$. The following table lists indices m^b, n^b and their difference $r^b = n^b - m^b$, at which \mathbf{q}_1^b connects two sites of the same sublattice (gray dots in the example of [fig. 2.8](#)), where i, j are auxiliary integers.

m^b	n^b	r^b
$3i$	$3j$	$3(i-j)$
$1+3i$	$1+3j$	$3(i-j)$
$2+3i$	$2+3j$	$3(i-j)$

Table 2.1: List of possible index pairs m^b, n^b and corresponding $r^b = n^b - m^b$ for which \mathbf{q}_1^b connects two sites of the same trigonal sublattice.

The factor of 3 stems from the repeating threefold sequence of two sublattices sites (gray, red) and a vacancy (empty hexagon center) along the direction of both \mathbf{b}_1 and \mathbf{b}_2 . Therefore, \mathbf{q}_1^b is a lattice translation vector for every r^b with $r^b \bmod 3 = 0$, rendering the larger vector \mathbf{q}_1 non-primitive for every r with $r \bmod 3 = 0$. Note that lattice translation, \mathbf{q}_1^b may also be described in terms of $\mathbf{a}_1, \mathbf{a}_2$ by map M' as in [eq. 2.9b](#), where $(u, v) = (2, 1)$, reconciling algebraic with geometrical approach.

With the above corrections, the complete set of primitive superstructures between two twisted graphene lattices has been attained. [Figure 2.9](#) depicts the results in terms of wavelength λ_C vs. twist angle θ for indices $(r, n) \leq (500, 500)$; " $r \bmod 3 = 0$ "-structures are plotted in blue.

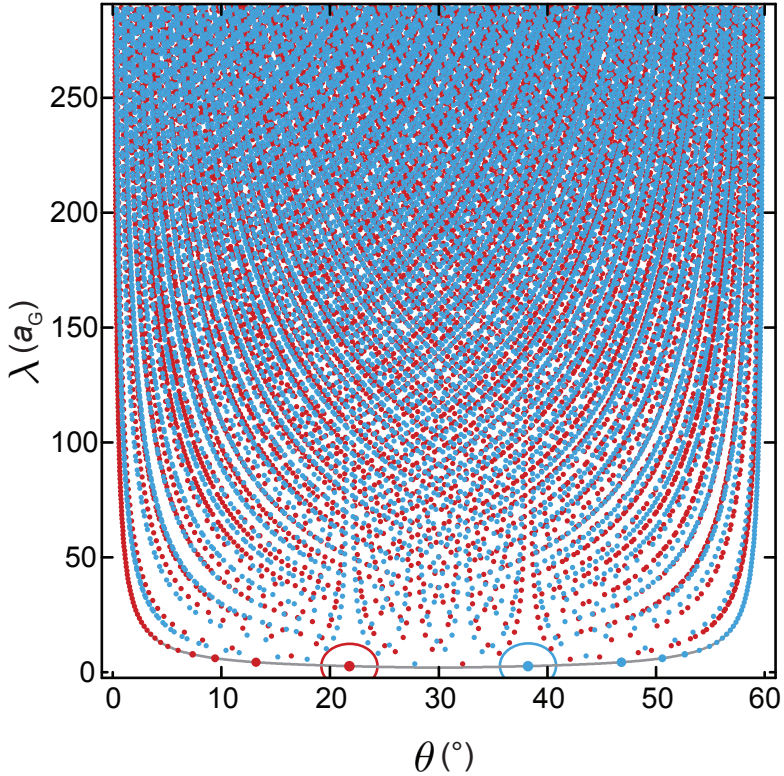


Figure 2.9 Colored dots: Superlattice wavelength λ_C in units of graphene's lattice constant a_G vs. interlayer twist angle θ for commensurate structures of indices $(r, n) \leq (500, 500)$. Structures are plotted in blue for $r \bmod 3 = 0$ and red for $r \bmod 3 \neq 0$. Characteristic positions at 21.787° and 38.213° are emphasized. Gray lines: Moiré wavelength λ_M in units of graphene's lattice constant a_G vs. interlayer twist angle θ .

In analysis of [fig. 2.9](#) it shall be noted that twist angles of 21.787° and 38.213° respectively appear to have a prominent position in the commensurate parameter space, occupying exclusive spots within a radius of more than 2.5° and $10 a_G$ as indicated by colored ellipses. This is explained by many non-primitive superstructures in the vicinity of the corresponding, very elemental index pairs of $(r, n) = (1, 1)$ and $(r, n) = (1, 3) \rightarrow (s, v) = (1, 1)$ and will be of significant importance for the understanding of measured interlayer spacing Δh in [TBG](#), presented in [sec. 4.2.2](#).

With respect to twist angle and wavelength, the commensurate structures are strictly symmetric around 30° , with symmetry pairs being of " $r \bmod 3 = 0$ "- and " $r \bmod 3 \neq 0$ "-origin respectively ([fig. 2.9](#), displayed in red and blue). Taking into account the second sublattice however, significant structural difference in between each symmetry pair becomes evident, rendering all structures antisymmetric around 30° with respect to their inherent [sublattice exchange \(SE\)](#) symmetry. The distinction was pointed out as late as 2010 by Mele[[29](#)] and has important consequences in the electronic dispersion of [TBG](#)[[30](#)] (see also [sec. 2.2](#)). In the following, [SE](#)-odd and [SE](#)-even superstructures are introduced and compared in a visual example. A brief geometrical consideration then identifies the root of a particular [SE](#)-symmetry in the map M or M' behind the according structure.

[Figure 2.10](#) shows an example of two [TBG](#)-structures, which are commensuration partners. The term was coined in ref.[[29](#)] and describes two commensurate superlattices arising at θ and $60^\circ - \theta$ respectively. As shown above and evident from graphical representation, the wavelengths are of equal length in both structures.

However, where the long diagonal of the superlattice unit cell (yellow rhombus, fig. 2.10) crosses two mixed sites of sublattice B and hexagon center H at $\theta=21.787^\circ$, equivalent positions are occupied by coinciding BB and HH spots at $\theta=38.213^\circ$.

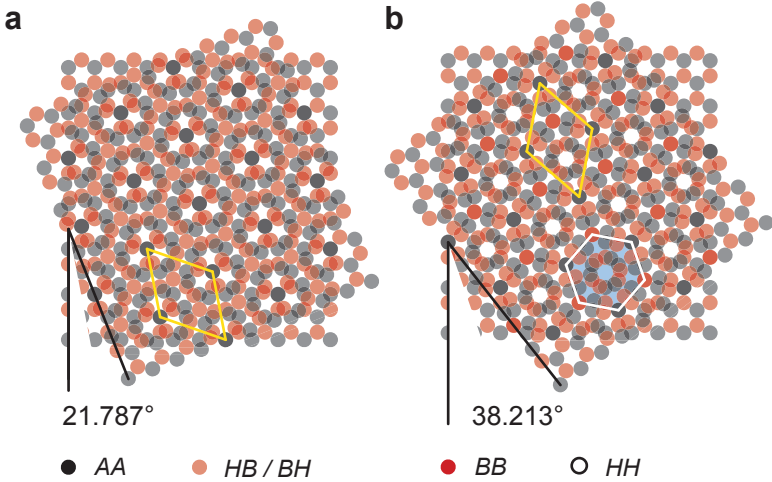


Figure 2.10 Schematic of *TBG*-structures with identical wavelength λ_C (unit cell marked in yellow) at different twist angles θ and $60^\circ - \theta$ respectively. Transparent black and red dots represent sublattice A and B respectively. **a:** *SE*-odd structure at rotational mismatch angle $\theta=21.787^\circ$. Only sites of sublattice A coincide. **b:** *SE*-even structure at rotational mismatch angle $\theta=38.213^\circ$. Coinciding sites of both sublattices (AA , BB) and hexagon centers (HH) reconstruct the hexagonal lattice structure of a graphene mono- or *AA*-stacked bilayer (marked in white).

Coincident H -sites lend the latter structure its lighter appearance;

coincident B -sites render it symmetric in terms of the two sublattices. The superlattice to the right-hand side is therefore described as **SE-even**, where its counterpart is **SE-odd**. In fact, the complementary structures may be viewed as superlattice representation of AA - and AB -stacking respectively[29], also comprehensible from the sensible representation of the **SE-even** unit cell in hexagonal form (fig. 2.10 b, marked in white).

The emergence of **SE-even** structures with coincident sites in both sublattices may be understood via consideration of linear combinations in \mathbf{b}_1 and \mathbf{b}_2 (cf. the geometrical approach to " $r \bmod 3 = 0$ "-structures on p. 39). Encircled in black, fig. 2.11 shows pairs of lattice sites to be rotationally superposed according to map M (panel a) and map M' (panel b) respectively. Vectors between rotation center and according A -sublattice sites are indexed by integers (m, n) and (u, v) respectively acting as prefactors to lattice vectors $\mathbf{a}_1, \mathbf{a}_2$. Encircled in red are sites of sublattice B , described by indices $(m^b, n^b) = (m, n)$ and $(u^b, v^b) = (u, v)$ respectively, serving as prefactors to vectors between nearest neighbors $\mathbf{b}_1, \mathbf{b}_2$ (see inset of fig. 2.11).

As evident from symmetry considerations, map M inherently forestalls rotational superposition of B -sublattice sites. Instead, B -sites will be mixed with hexagon centers H (fig. 2.11 a, corresponding H -spots are marked by red crosses). Map M -structures and therefore all commensurate superlattices with $r \bmod 3 \neq 0$ (remember eq. 2.9 and following discussion) are therefore to be placed in the **SE-odd** category.

In contrast, map M' superposes B -sublattice sites with their mirror-symmetric equivalent if described by a given index pair $(u^b, v^b) = (u, v)$. The latter condition is evaluated by counting out atomic positions in direction of \mathbf{b}_1 and \mathbf{b}_2 respectively and considering the periodic repetition in threefold sequences of A, B and H .

Results are listed in [tab. 2.2](#); in summary, a sublattice- B site is described by indices (u^b, v^b) for every s^b with

$$s^b \bmod 3 \neq 0. \quad (2.10)$$

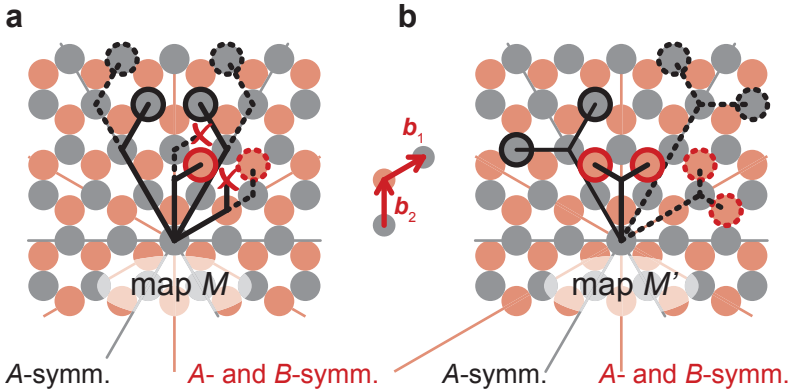


Figure 2.11 Schematics of the graphene lattice with sublattices A (gray) and B (red). The inset shows two vectors, connecting nearest neighbors. **a**: Encircled in black are A -sublattice sites to be superposed by map M (leading to alternative commensurate structures for solid and dashed lines respectively). Encircled in red are B -lattice sites which will be mapped to hexagon centers (marked by red crosses) due to the lack of sublattice mirror symmetry around the axis marked in black. **b**: Encircled in black are A -lattice sites to be superposed by map M' (again with alternative structures for solid and dashed lines). Encircled in red are B -lattice sites which will be mapped onto each other by the same rotations as the A -lattice sites.

In the context of the combined map introduced on p.38, map M' is only needed when map M produces non-primitive structures

at $r \bmod 3 = 0$. In that case, indices (r, n) of map M translate to indices $(s, v) = (n, r/3)$ in map M' . From definition of n and r as coprime and $r \bmod 3 = 0$ follows $s \bmod 3 \neq 0$ with $s = n$. As $s^b = s$ (initial assumption: $(u^b, v^b) = (u, v)$), eq. 2.10 is fulfilled leading to the ultimate statement that every " $r \bmod 3 = 0$ "-structure is in fact **SE**-even.

u^b	v^b	s^b
3i	1+3j	-1+3(i-j)
1+3i	2+3j	-1+3(i-j)
2+3i	3j	2+3(i-j)

Table 2.2: List of possible index pairs u^b, v^b describing vectorial interconnection between sublattices. The difference $s^b = u^b - v^b$ is denoted to the right, i and j are auxiliary integers.

The full set of commensurate structures is therefore divided in two halves of opposite **SE**-symmetry, as visually evident from fig. 2.9 with **SE**-odd structures plotted in red and **SE**-even commensuration partners marked in blue.

Notice however that rotational symmetry is dependent on the choice of rotation axis: Figure 2.12 shows stacks of two lattices, rotated against each other by θ and $\theta' = 60^\circ - \theta$ in top and bottom panels respectively. In panels **a** and **d**, the center of rotation pins together a common lattice site, giving rise to commensuration partners as introduced above. In panels **b** and **e**, a lattice site in the top layer is pinned to a hexagon center in the bottom lattice, giving rise to **SE**-odd structures at both angles. Panels **c** and **f** illustrate rotation around a common hexagon center, which leads to **SE**-even symmetry at θ and θ' . Evidently, C_3 -symmetry with nonequivalent structures at θ and $\theta' = 60^\circ - \theta$ is given at only one of three commensurate rotation centers. The C_6 -symmetry of the trigonal sublattice is restored in both other cases.

Notice further, that translation along one binding length b_G between layers may change **SE**-symmetry from odd to even and vice versa, as suggested by the red lines in [fig. 2.12](#), indicating translations of the bottom in relation to the top layer with respect to the corresponding left-hand side panel. Not being inherently linked to rotational mismatch, **SE**-symmetry is therefore not a robust feature.

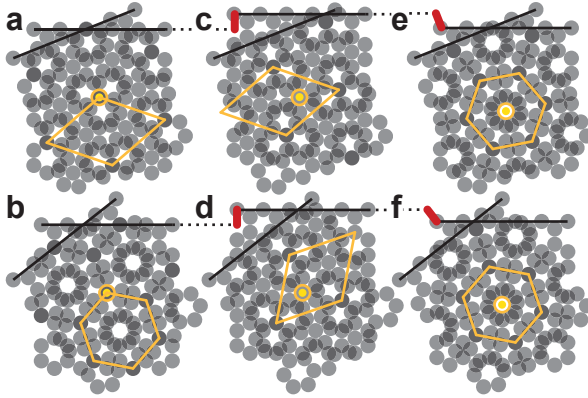


Figure 2.12 Schematic of twisted bilayers with $\theta=21.787^\circ$ (top panels) and $\theta=38.213^\circ$ (bottom panels). The axis of rotation has been fixed at a common lattice site (left panels), a site of coinciding lattice site and hexagon center (middle panels) and a common hexagon center (right panels) respectively. **SE**-odd structures are identified by a rhombic, **SE**-even structures by a hexagonal unit cell.

Furthermore, commensuration partners resemble each other closely for small θ (large $\theta'=60^\circ-\theta$): Where at large angles, coinciding hexagon centers distinguish the **SE**-even structure's appearance ([fig. 2.10](#)), coincidence of *A*-sites at small interlayer twist leads to areas of overlapping hexagon centers in **SE**-odd structures as well (see [fig. 2.13](#)).

Furthermore, where coinciding B -atoms and hexagon centers closely approximate AB -stacking at θ close to 0° in the SE -odd structure, the same goes for coinciding A -atoms (AA) and coinciding B -atoms (BB) in the SE -even structure at θ' close to 60° .

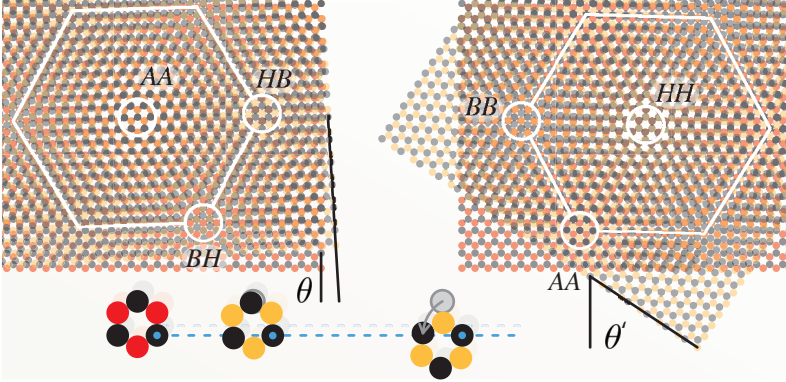


Figure 2.13 Commensuration partners at 3.481° (left) and 56.519° (right). The superlattice unit cell and three nonequivalent commensurate spots are marked in white. Magnifications of the unit cells in bottom layer (left) as well as top layer of the SE -odd structure (middle) and SE -even structure (right) are depicted to the bottom.

Both structures are therefore characterized by alternating approximations of AA -, AB - and BA -stacking in the low-angle range, which raised doubts about the physical relevance of a distinction at the smallest twist angles[23]. At large angles however, distinct signatures in electrical resistance through a rotatable junction of graphite recently provided experimental hints towards an electronic manifestation of the two commensuration classes[30].

2.1.4 Lattice Distortion and Relaxation

Following the geometric considerations for the interposition of two rigid lattices in the previous sections, the following pages will focus on a recent development in the research on superstructures in vdW-heterostructures: the corrugation and distortion of lattice planes in response to alternating local stacking configuration. The motivation behind corresponding efforts derives from the following:

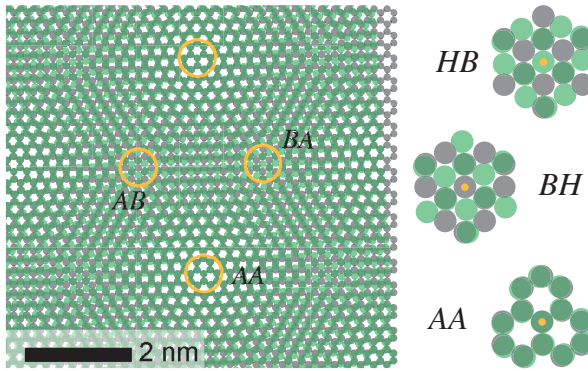


Figure 2.14 Two lattices (green top, gray bottom) interposed under a commensurate angle of 3.150° . Yellow circles mark areas of approximate AA- and AB/BA-stacking around the symmetry spots as magnified to the right (yellow dots mark commensurate position).

Figure 2.14 shows interposed graphene lattices under a relatively small angle of rotational mismatch. The low degree of twist has two important implications: Firstly, there are relatively large areas with slowly changing similar stacking configuration around the symmetry spots (yellow dots, inset to the right) in the unit cell. Secondly, the stacking in these areas closely approximates aligned AA- and AB/BA-stacking respectively, as introduced in context of [fig. 2.13](#).

As *AA*- and *AB*-stacking generally give rise to different interlayer distance[22, 35, 53–55], one can therefore expect a periodic corrugation of the stacked lattices in *z*-direction, following the local registry variations in the superlattice *xy*-plane.

Experimentally, the shape and amplitude of corrugations is difficult to determine. The prevalent technique for superlattice resolution lies in *STM* measurements. Height profiles at constant tunneling current are highly sensitive to variations in the electronic **Density of States (DoS)** however, which can be expected to depend on local stacking configuration. Therefore *STM*-measured corrugation amplitudes tend to vary strongly with tunneling condition and cannot be trusted easily[56, 57].

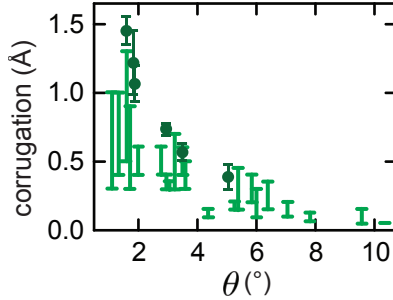


Figure 2.15 *STM*-measurements of corrugation (expressed as difference between corrugation maxima and minima) in **chemical vapor deposition (CVD)**-grown *TBG* of various twist angles. Depicted in light green are data from ref.[56], in dark green from ref.[58]. Range of corrugation for a given θ stems from different tunneling conditions.

One universal behavior is found unanimously though: Corrugation amplitudes grow with the size of the superlattice unit cell towards smaller interlayer twist as shown in fig.2.15 (data from refs.[56, 58]).

This is understood intuitively, as bending associated to a local elevation will require less energy when distributed over a longer distance. Furthermore, local stacking registry will resemble perfect *AA*- or *AB*-stacking more closely at smaller rotational mismatch.

A straightforward way to theoretically model superlattice corrugation lies in considering out-of-plane relaxation in atomic positions as simulated via quantum chemistry methods in ref.[54] and via large scale density functional theory in ref.[53]. Moiré pattern corrugation is hereby found to take sinusoidal shape[53] which is qualitatively confirmed via an analytical approach in elasticity theory[58].

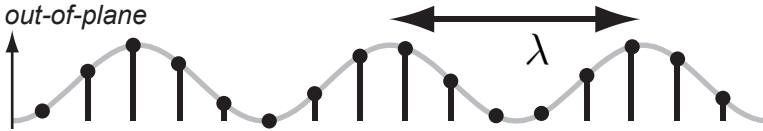


Figure 2.16 Sinusoidal shape taken on by superlattice corrugations. Black dots signify carbon atoms which may relax in the out-of-plane direction.

Experimental findings on graphene lying closely aligned atop a substrate of **hBN** however[59], gave the research on lattice relaxation and distortion a new direction: As depicted in **fig. 2.17 a**, a Moiré pattern arises between graphene and **hBN** due to a lattice mismatch of $\delta = a_{\text{hBN}}/a_{\text{G}} - 1 \approx 1.8\%$, where the wavelength of the superstructure λ_{hBN} reaches its maximum at perfectly aligned lattices[60]. In such a structure, graphene's lattice constant was detected to spatially vary by $\sim 2\%$ as depicted in **fig. 2.17 b,c**[61]. As theoretically understood in refs.[31, 62], areas of energetically favorable *BA*-stacking (aligned carbon and boron atoms, see **fig. 2.17 d**) will strive to widen, the corresponding strain in graphene being energetically counterbalanced by a gain of interaction energy with the substrate.

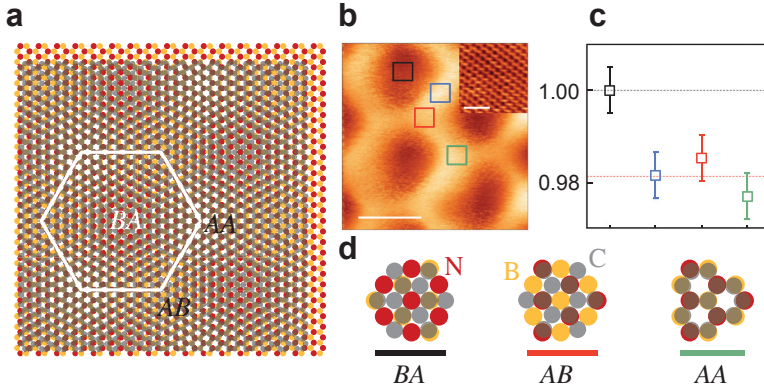


Figure 2.17 a: Two superimposed hexagonal lattices signifying *hBN* (yellow for boron, red for nitrogen) and graphene (gray). The mismatch in lattice constant (exaggerated for clarity) leads to a Moiré pattern. **b:** From ref.[61]: *STM*-resolution of the superstructure in graphene lying on top of an *hBN* substrate. **c:** Lattice constants as measured in the color-coded areas indicated in **b**. **d:** Magnified atomic constellations, extracted from the spots indicated in **a**.

Apparently, in-plane distortions have to be considered for an accurate picture of the atomic arrangement along a superlattice in layered *vdW*-structures. Applied to *TBG* of large interlayer twist, this principle does not much alter the sinusoidal shapes attained from out-of-plane relaxation only[25, 63]. At small angles $\theta \lesssim 2^\circ$ and large superlattice unit cells however, corrugation is predicted to concentrate in localized bumps at compressed *AA*-like spots with maximized areas of approximated *AB*-stacking in between[25]. Going further, ref.[63] most recently found an alternative so-called "bending-mode" of local stacking optimization and strain release, featuring large

in-phase corrugation of top and bottom layer into the same direction at smaller variations in local interlayer distance. Curiously, the predicted structures would lower the effective lattice symmetry and double the wavelength with respect to the original rigid interposition; according phenomena are expected at $\theta \lesssim 1.6^\circ$.

The above retrace of development in the theory of interlayer configuration highlights the complexity of the problem: Especially at small twist angles and long-wavelength superstructures, every possible degree of freedom seems to be relevant in the relaxation of constituting carbon atoms. Furthermore, optimized structures may even depend on the initial conditions used upon relaxation and co-exist in metastable phases[63].

On a very basic note moreover, consideration of the substrate is of utmost experimental relevance for TBG-structures. Especially with respect to symmetry between top and bottom layer, the structure of and interaction with the environment a TBG sample is placed in can be expected to have significant impact on the detailed manifestation of lattice relaxation.

Four commonly found scenarios are discussed in the following:

1. The sample may be suspended[2, 64, 65]. In TBG this has e.g. been realized by transfer to a copper grid for subsequent TEM-analysis[24]. In this scenario, corrugation is unimpeded and may unfold symmetrically in top and bottom layer.
2. The sample may lie on an atomically flat substrate like hBN[59], which will lead to a stabilization of the bottom layer in flat attachment to the substrate through homogenous vdW-interaction (provided that Moiré pattern interaction with hBN is minimized by rotational misalignment[60]). The major part of registry-optimization will therefore be carried by the top layer in this second scenario.

3. The sample may be embedded in a vdW-heterostructure[16, 66]. Providing an atomically flat substrate, protection from environmental influence and serving as gate dielectric, encapsulation of graphene in between layers of hBN has become common experimental practice in the recent past[67]. In this scenario, interaction with atomically flat top and bottom dielectric and compression via next-nearest neighbor interaction within the layered structure can intuitively be expected to damp any out-of-plane corrugation. In fact, an additional top layer of hBN was found to suppress the relaxed commensurate state of graphene, discussed in fig. 2.17[61].
4. Finally, TBG on a substrate of SiO₂ is the system under investigation for the present dissertation. As found in ref.[68], graphene should in fact be viewed as partly suspended over (rather than neatly conformed to) the roughness of the substrate, which would allow for a certain degree of corrugation in the bottom layer. Effectively, samples on SiO₂ will therefore exhibit higher symmetry between layers than on hBN but corrugate less freely than in the suspended case, placing them in between scenarios 1.) and 2.).

Ref. [25] confirms the relevance of the above qualitative considerations for TBG: Major differences in strain and corrugation profiles of graphene are found between the case of either a rigid graphite substrate or a symmetrically relaxed graphene layer as twisted counterpart: Figure 2.18 shows calculated height profiles for both cases at a rotational mismatch angle of $\theta = 1.2^\circ$. Where at a rigid bottom layer, the corrugation profile appears approximately sinusoidal with elevation in areas of AA-stacking, a much more intricate pattern with sixfold ridges around AA-spots arises between two symmetrically contorted lattices, which is also confirmed in ref.[63].

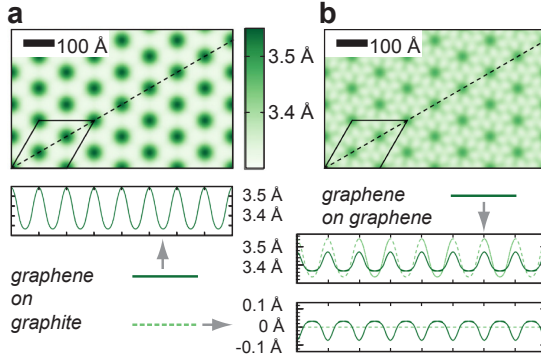


Figure 2.18 a: From ref.[25]: Calculation of lattice distortion in a layer of graphene lying on top of a graphite substrate under rotational mismatch angle of $\theta=1.2^\circ$. The color plot in top shows interlayer distance over the xy -plane, the graph to the bottom a cross-section through the above map along the there indicated line. **b:** Calculated lattice distortion for two graphene layers twisted by $\theta=1.2^\circ$ and unperturbed by any substrate. The map in top shows the distance between top layer and the plane, a flat bottom layer would assume; the upper one of the graphs to the bottom shows an according cross-section. The lower graph depicts corrugation in the bottom layer. Dashed light-green lines indicate the same for graphene on a graphite substrate for comparison.

In many cases, the above listed practical distinctions are not (consciously) considered in theoretical work. For example, ref.[53] performs TBG band structure calculations for symmetrical out-of-plane relaxation, emulating the first scenario. In contrast, the tight-binding approach employed in ref.[69] is technically restricted to in-plane shear and strain only, which most resembles the scenario of an encapsulated device.

In such cases, it is up to the experimentalist, to find the model in best approximation of a given experimental condition.

The above considerations will frequently appear in review of the TBG band structure: relation between different interlayer coupling terms can be expected to vary in response to lattice corrugation (see [sec. 2.2.2](#)) and has been shown to sensitively affect merging of dispersions[10]. Related phenomena in magnetotransport measurements are discussed in [sec. 5.2](#).

Furthermore, the discussed sample environment may play a crucial role in the effect of the superlattice mini-Brillouin zone boundaries on electronic dispersion as discussed in [sec. 2.2.3](#). According considerations are central in the understanding of transport signatures presented in [sec. 5.1](#).

2.2 Electronic Dispersion

Where the mechanical properties of graphene are mostly dictated by the in-plane σ -bonds between sp^2 -orbitals, the p_z -orbital forms π -bonds to three nearest neighbor atoms in the graphene lattice, thereby increasing the bond order to $1\frac{1}{3}$ for every carbon-carbon bond[70]. The energy of the system is further lowered by delocalization of the corresponding states and formation of π -bands; it is these bands that give rise to the rich and unprecedented physics observed in electronic transport and optical spectroscopy on graphene.

The following section provides an introduction to the electronic dispersions of monolayer, AB -bilayer and twisted bilayer graphene:

In [sec. 2.2.1](#), the results of a tight-binding approximation for [MLG](#) are discussed with focus on the linear low-energy dispersion around K and K' -symmetry points; the emergence of a topological Berry phase of $\beta = \pi$ is noted and discussed in terms of the two sublattices.

Furthermore, the electronic dispersion of an AB -bilayer is briefly presented, focusing on differences to [MLG](#).

Predictions and experimental findings on the low-energy band structure in [TBG](#) are reviewed in [sec. 2.2.2](#). Principals and consequences of a well-established interlayer coupling model, involving a low-energy [vHs](#) as well as reduction of Fermi velocity, are discussed.

Finally, [sec. 2.2.3](#) touches on electronic phenomena directly linked to interlayer superlattices: The according [mini-Brillouin zone \(mBz\)](#) is introduced; as associated backfolding occurs at an angle-dependent larger k , this subsection mainly treats corresponding higher-energy [TBG](#) phenomena, thereby complementing [sec. 2.2.2](#).

2.2.1 Monolayer and AB-bilayer

To establish a frame of reference for graphene's electronic dispersion, the first Brillouin zone is constructed from the real-space unit cell introduced in [sec. 2.1.1](#):

Reciprocal unit vectors are

$$\begin{aligned}\hat{\mathbf{a}}_1 &= \frac{2\pi}{a_G} \begin{pmatrix} 1 \\ 1/\sqrt{3} \end{pmatrix} \\ \hat{\mathbf{a}}_2 &= \frac{2\pi}{a_G} \begin{pmatrix} -1 \\ 1/\sqrt{3} \end{pmatrix}.\end{aligned}\tag{2.11}$$

Figure 2.19 shows a schematic of the hexagonal structure. In analogy to the two sublattices in real space, there are two nonequivalent symmetry spots in the corners of the Brillouin zone, which are denoted as K and K' (blue and red respectively).

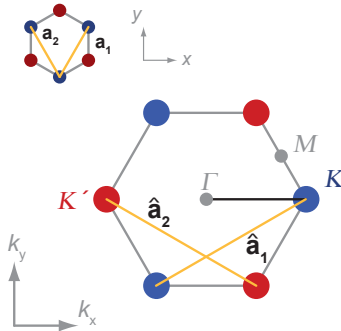


Figure 2.19 First Brillouin zone of graphene; the inset to the top left shows the real-space unit cell for reference. Three K - and K' -symmetry points each are marked by blue and red dots respectively; Γ - and M -points are indicated in gray.

The electronic dispersion of the π -band in graphene's honeycomb structure was derived as early as 1947 by Wallace[71], using a tight-binding approach. Here, the wave function is a linear combination of equivalent Bloch functions for sublattices A and B . In nearest-neighbor approximation (every A atom has three B neighbors and vice versa), the energetic dispersion derives as[72]

$$E(\mathbf{k}) = \pm\gamma_0 \left(1 + 4 \cos \frac{\sqrt{3}a_G k_x}{2} \cos \frac{a_G k_y}{2} + 4 \cos^2 \frac{a_G k_y}{2} \right)^{1/2} \quad (2.12)$$

with $\gamma_0 \approx 3\text{eV}$ as nearest-neighbor hopping term and $k_{x,y}$ as Cartesian components of the momentum-space vector \mathbf{k} .

Equation 2.12 is plotted in fig. 2.20. Panel a shows a 3D illustration of the energetic dispersion, where a symmetric structure around zero energy (according to the plus/minus sign in eq. 2.12) as well as touching of bands at the K - and K' -points of the Brillouin zone (gray hexagon) becomes evident. In undoped graphene, this is also the level of Fermi energy E_F .

Panel b shows the positive halve of the bandstructure in terms of equi-energy contours. The dispersion appears radial-symmetric around the Γ -point at $\mathbf{k} = (0, 0)$. Vicinity of the K/K' -points approximates C_3 -symmetry at high energies; radial symmetry is assumed for $E \lesssim 0.5\text{eV}$, as evident from the close-up in the inset to the top right.

As the low-energy part of a dispersion is of special interest for electronic transport, special focus is taken on the corners of the Brillouin zone: Taylor expansion in small $\mathbf{q} = \mathbf{k} - \mathbf{K}$ around the K/K' -points yields a good approximation of eq. 2.12 in

$$E(\mathbf{q}) = \pm \frac{\sqrt{3}}{2} \gamma_0 a_G q = \pm v_F \hbar q \quad (2.13)$$

with $q = |\mathbf{q}|$ and a constant Fermi velocity of $v_F \approx 1 \times 10^6 \text{ m s}^{-1}$.

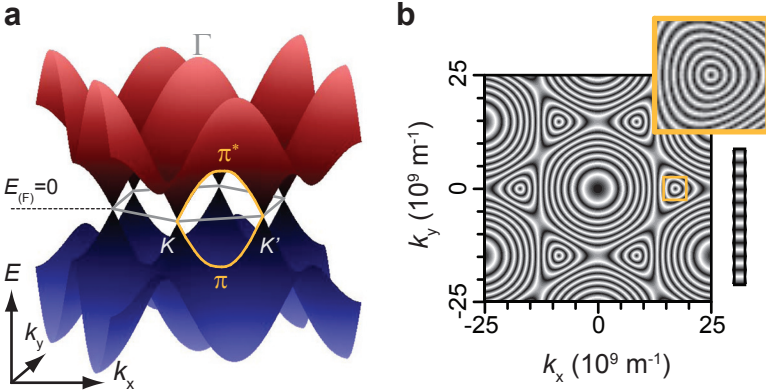


Figure 2.20 a: Energetic dispersion from eq. 2.12; the Brillouin zone from fig. 2.19 with according symmetry points is marked in gray, π - and π^* -bands are indicated in yellow. **b:** Positive (red) band from a, plotted in terms of equi-energy contours. The inset to the right shows a close-up of the $5 \times 10^9 \text{ m}^{-2} \times 5 \times 10^9 \text{ m}^{-2}$ -area around the K -point, indicated by the yellow square in the main panel. Energy (scale to the right) spans 9 eV and 2.4 eV for main panel and inset respectively.

The above findings bespeak one of graphene's unusual electronic properties: Low-energy carriers mimic a relativistic electron gas with v_F as ~ 300 times smaller equivalent to the speed of light. Direct practical consequences are a linearly increasing density of states

$$D(E) = \frac{2E}{v_F^2 \hbar^2 \pi}, \quad (2.14)$$

where twofold spin and (due to inequivalent K - and K' -points) twofold valley degeneracy are taken into account.

The relation between Fermi energy E_F and charge carrier density n is correspondingly given by

$$n = \frac{E_F^2}{v_F^2 \hbar^2 \pi}. \quad (2.15)$$

Notice the difference to the common **two-dimensional electron gas (2DEG)**, usually realized in GaAs-based heterostructures, where classical quadratic dispersion and according energy-independent density of states as well as linear increase in carrier density are found.

Figure 2.21 depicts the Dirac cone (named after the hosted Dirac fermions) which is commonly used in description of the linear approximation for graphene's low-energy dispersion.

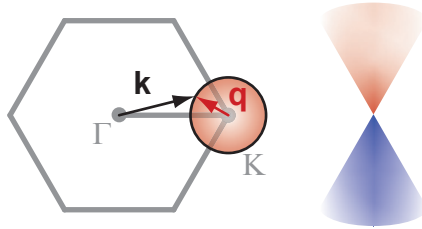


Figure 2.21 *Left: Brillouin zone of graphene; momentum \mathbf{k} is expressed via the K -point and a vector \mathbf{q} as indicated in red. Right: Schematic of the isotropically linear low-energy dispersion around the Brillouin-zone corners.*

A second important peculiarity in graphene's electronic structure is rooted in its two-atomic base, which requires vectorial description of the electronic wave function. At the center of the associated problem is the relation of quantum mechanical phase between sublattices.

Figure 2.22 shows two simple examples for the Γ - (upper panels) and K -point (lower panels) respectively: At $k = 0$, the electronic wave function is of the same phase for all atoms of a given sublattice. Inter-sublattice configuration may now be either in bonding or antibonding state, which corresponds to phase-shifts of zero and π respectively. In the band structure, this manifests in formation of a negative and positive branch respectively (blue, red in fig. 2.20).

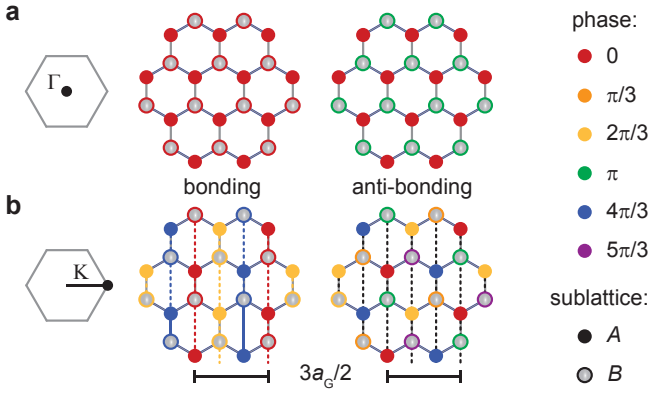


Figure 2.22 Color-coded phase of wave function in (real-space) sublattices A (solid dots) and B (empty circles) for bonding (left) and anti-bonding state (right). **a:** Γ -point **b:** K -point. Wavelength corresponding to K is indicated by black scales.

At the K -point, momentum is given by

$$K = \frac{4\pi}{3a_G} \quad (2.16)$$

which corresponds to a wavelength of $3a_G/2$. According phase relations between atomic planes are indicated in fig. 2.22 b for bonding and anti-bonding states respectively.

Mathematical description of the above problem within the low-energy Dirac cone around the K -point is given by

$$\mathcal{H}(\mathbf{q}) = \hbar v_F \boldsymbol{\sigma} \mathbf{q} = \hbar v_F \begin{pmatrix} 0 & q_x - iq_y \\ q_x + iq_y & 0 \end{pmatrix}, \quad (2.17)$$

where i is the imaginary unit and $\boldsymbol{\sigma}$ is a vector of Pauli matrices σ_x, σ_y [72].

Eigenvectors are found in

$$\boldsymbol{\psi}(\mathbf{q}) = \frac{1}{\sqrt{2}} \exp(ikr) \begin{pmatrix} \pm \exp(-i\theta_q/2) \\ \exp(i\theta_q/2) \end{pmatrix}, \quad (2.18)$$

where $\theta_q = \arctan(q_y/q_x)$. The two components of $\boldsymbol{\psi}(\mathbf{q})$ herein describe the phase in two respective sublattices; the plus/minus-sign in the upper entry decides between description of lower and upper band respectively.

The described phase relation can be interpreted as a pseudospin degree of freedom. It becomes evident that a 180° rotation of momentum \mathbf{q} in a Dirac cone flips the pseudospin vector (switches the phase difference by an amount of π).

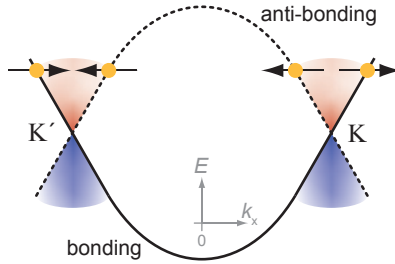


Figure 2.23 Dirac cones of opposite valleys; carriers of opposite pseudospin are marked via orientation of arrows.

Interestingly, the relation between \mathbf{q} and the pseudospin vector is opposite between Dirac cones around K - and K' -points[72], as illustrated in fig. 2.23. In consequence, a sign-reversal in momentum at preserved pseudospin is only possible between opposite valleys; backscattering within a single Dirac cone is forbidden, giving rise to Klein tunneling in graphene[73].

Another interesting phenomenon becomes evident when setting $\theta_{\mathbf{q}} = 2\pi$, which corresponds to a round-trip in momentum \mathbf{q} : Where the pseudospin returns to its original orientation, the phase within each sublattice has changed by an amount of π , which defines the Berry phase β in monolayer graphene. Direct consequences become evident in the anomalous half-integer QHE[6, 7], as described in the upcoming sec. 2.3.2 on magnetotransport.

Electronic Structure of the Bernal-stacked Bilayer

The Brillouin-zone of the Bernal-stacked bilayer is identical to the one of monolayer graphene (see fig. 2.19). In fact, the electronic dispersion of the bilayer displays an equivalent valley structure too[74, 75].

The lowest band (for electron and hole side each) in the vicinity of K - and K' -points is approximated by

$$E \approx \pm \frac{1}{2} \gamma_1 \left(\sqrt{1 + \frac{4v^2 \hbar^2 q^2}{\gamma_1^2}} - 1 \right) \quad (2.19)$$

where $\gamma_1 \approx 0.4 \text{ eV}$ is the interlayer hopping term and $v \approx 8 \times 10^5 \text{ m s}^{-1}$ [74].

At low $q \lesssim 3.7 \times 10^8 \text{ m}^{-1}$, eq. 2.19 is approximated by a quadratic dispersion

$$E \approx \pm \frac{\hbar^2 q^2}{2m^*} \quad (2.20)$$

where $m^* = \gamma_1/(2v^2) \approx 0.054 m_0$ [74].

Figure 2.24 shows plots of equations 2.19 and 2.20, where the latter is depicted in dashed lines. The hyperbolic nature of bands at higher energies is examined e.g. in ref.[76], where a detailed view is taken on the energy-dependence of m^* .

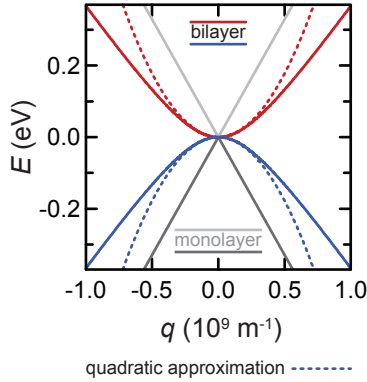


Figure 2.24 Lowest-energy band of the *AB*-stacked graphene bilayer. Dashed lines indicate small-energy quadratic approximation, the monolayer dispersion is displayed in gray for comparison.

Interestingly, the *AB*-bilayer displays a Berry phase of 2π [74] corresponding to a winding number of two (i.e. two turns of 2π rotation in the pseudospin, over the path of one closed circle in momentum space)[75]. This gives rise to yet another anomalous QHE sequence in a graphene system[77], as will be discussed in sec. 2.3.2.

2.2.2 Twisted Bilayer: Low-Energy Dispersion

In the low-energy range, the electronic dispersion of the twisted graphene bilayer is best understood via a perturbative model:

In the absence of interlayer coupling, rotational mismatch in real-space directly translates to a twist between the individual monolayer dispersions around a joint Γ -point at zero momentum. As marked in [fig. 2.25](#), rotation displaces the individual layers' Dirac cones by an amount of

$$\Delta K = 2 \sin(\theta/2)K, \quad (2.21)$$

where θ is the interlayer twist angle and K the magnitude of momentum in the Brillouin-zone corners (see [eq. 2.16](#)).

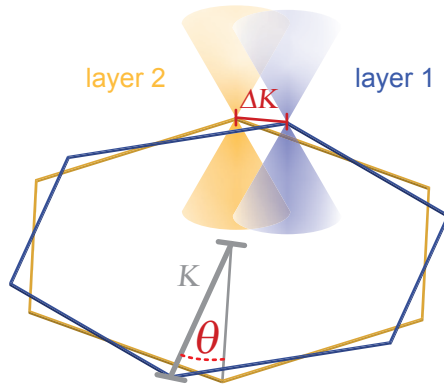


Figure 2.25 Brillouin-zones and a representative Dirac cone in one corner each, for two twisted MLG dispersions. Rotational mismatch θ around the joint Γ -point is indicated in red; individual Dirac cones are displaced by an amount of ΔK via the lever of magnitude K (indicated in gray).

At sufficiently small angles, where interlayer registry smoothly evolves between AA - and AB -stacking (see fig. 2.13), continuum models[8, 10, 41] find merging between Dirac cones in van Hove singularities, midway between the rotationally offset K -points. Energetic position of the vHs is given by the crossing of uncoupled MLG dispersions and the interlayer hopping energy t^θ , as illustrated in fig. 2.26. The coupling process can herein be understood as avoided crossing between individual dispersions, leading to splitting and re-merging of bands[41].

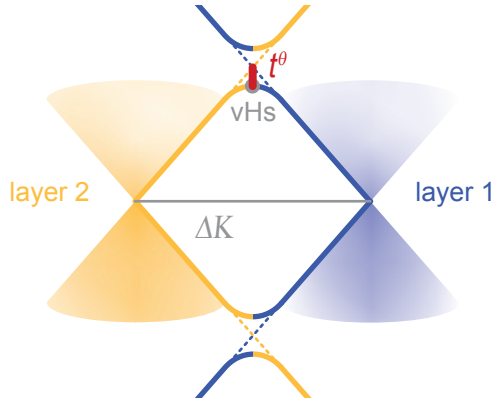


Figure 2.26 Rotationally displaced Dirac cones of the two layers; crossing of bands (dashed lines) is avoided by splitting and re-merging. Energy t^θ between anticrossing and the vHs is indicated in red.

At low energy, between vHs , the TBG therefore has a layer-degenerate spectrum, contributing another factor of two to the four-fold degeneracy of MLG . Interestingly, an electric field between layers is found to merely offset the two layers Dirac cones in energy,

while the principal picture of the coupled dispersion remains the same[8]. It is therefore possible to detune layer degeneracy; access to the phenomenon via asymmetric gating is discussed in [sec. 2.3.1](#).

The above picture is well established in the intermediate angular range between $\sim 3^\circ$ and $\sim 15^\circ$; **vHs** have been confirmed as peak in the density of states as measured via **Scanning Tunneling Spectroscopy (STS)**[9, 44, 56, 78, 79]. The parameter of hopping energy is herein most commonly found at $t^\theta \sim 0.1$ eV, although a wide span from 0 eV to 0.13 eV has recently been observed in a broader study[44].

In direct consequence of the energetically lowered meeting point between the two layers' dispersions, the Fermi velocity v_F is renormalized. Ref.[8] predicts

$$\tilde{v}_F = v_F \left(1 - 9 \left(\frac{t^\theta}{\hbar v_F \Delta K} \right)^2 \right), \quad (2.22)$$

via the continuum model. The expression is plotted in [fig. 2.27](#); similar evolution is found in tight-binding approaches[52, 53].

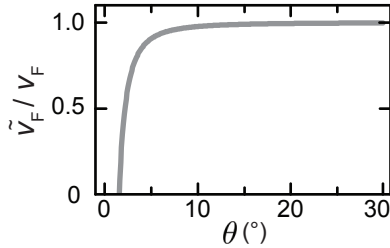


Figure 2.27 Reduction in Fermi velocity with respect to the native value, as expressed in [eq. 2.22](#) with $v_F = 1 \times 10^6$ m s $^{-1}$, $t^\theta = 0.1$ eV.

Again, there is abundant experimental proof for the angular range between $\sim 3^\circ$ and $\sim 15^\circ$: clear reduction in carrier velocities is found via different techniques, e.g. STS[56, 78] and transport experiments[45, 80], confirming the applicability of the above model in TBG from different sources (see sec. 4.1).

At the smallest rotational mismatch though, eq. 2.22 has obvious limitations: the predicted \tilde{v}_F crosses zero at $\theta \sim 1.5^\circ$. Fig. 2.28 illustrates the inevitability of this happening in a simple model; panel b suggests approximation of \tilde{v}_F via the slope of straight lines (dashed black) connecting the Dirac points at zero energy with the vHs, the latter lying t^θ below the crossing of uncoupled bands (solid black).

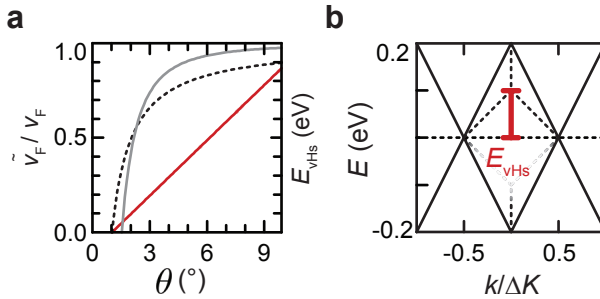


Figure 2.28 a: Reduction factor in Fermi velocity according to eq. 2.22 (solid gray line) and from geometrical approximation (dashed black line, see main text). Red line indicates energy E_{vHs} between zero and the van Hove energy as marked in **b**; parameters are $v_F=1 \times 10^6 \text{ m s}^{-1}$ and $t^\theta=0.1 \text{ eV}$. **b:** Schematic of the TBG dispersion at 2° ; momentum axis is normalized by magnitude of rotational displacement ΔK . Dashed lines indicate straight connections between Dirac points and the vHs position; the slope of lines is plotted angle-dependently in **a**.

The according approximation is depicted as dashed line in eq. 2.22 a and shows a similar evolution to eq. 2.22. Importantly, the accordingly estimated band velocity will cross zero at E_{vHs} (red, panels a and b).

As a negative Fermi velocity does not make sense in the here considered frame, the behavior of TBG dispersion at the smallest interlayer twist needs alternative description.

Ref.[81] finds oscillating densities of state with multiple instances of $\tilde{v}_{\text{F}}=0$ as θ progresses below 1° (similar in ref.[47] via tight-binding approach); punctual flattening of bands at so called magic angles around 1.5° is also found under consideration of sinusoidal lattice corrugation[53] and has been hinted towards in an experimental STS study[79].

In analogy to findings on lattice-relaxed graphene on hBN[31], the opening of a bandgap constitutes another presumable scenario for the low-energy dispersion of TBG with very small twist angles, where lattice corrugation and distortion reach their maximum (see sec. 2.1.4).

Lastly, a major alternative to the above described, well established model is pointed out: In conjunction with the geometrical identification of opposite commensuration classes (see sec. 2.1), Mele finds according differences in the electronic spectra, where SE-odd structures resemble the dispersion in AB-stacking, and SE-even configuration leads to AA-bilayer-like electronic behavior[29]. The distinction applies to TBG of large interlayer twist only, which are not in the focus of here presented experimental studies (chap. 5).

For small angles however, and in a continuum approach similar to the ones described above[8, 41], it is again Mele who points out interesting (and possibly crucial) details in interlayer coupling[10]: Within the Slonczewski-Weiss-McClure theory for graphite (reviewed for example in ref.[82]), there are three important parameters expressing different hopping processes:

As depicted in [fig. 2.29 a](#), γ_1 stands for coupling between aligned sublattices; γ_3 expresses unaligned-unaligned hopping, where γ_4 measures transfer between an unpartnered and an aligned atom in the respective layers.

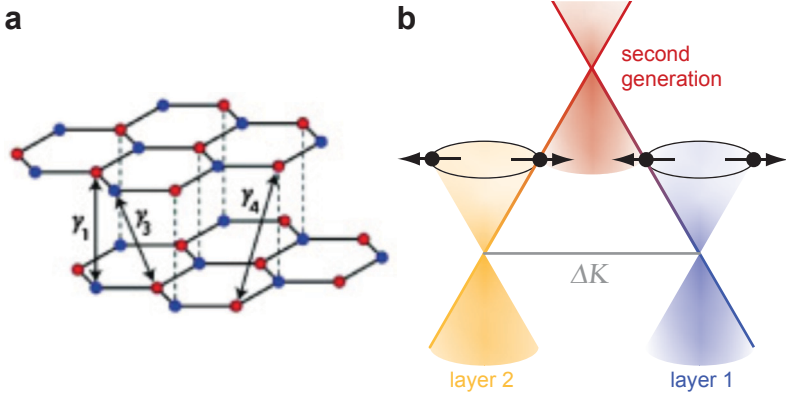


Figure 2.29 a: From ref.[10]: in the example of *AB*-stacking, different hopping processes are indicated. **b:** Rotationally displaced Dirac cones: at equal helicity, pseudospins (black arrows) of different orientation meet at the intersection between dispersions. In analogy to the original singularities, a second generation Dirac cone arises.

In the commonly applied model leading to **vHs** formation, γ_3 and γ_4 are set to zero; as only one sublattice per layer is thus involved, the pseudospin degree of freedom becomes irrelevant.

For $\gamma_1 \approx \gamma_3$ and $\gamma_4 \approx 0$ Mele finds a so called compensated class, effectively arising due to coupling between Dirac cones of opposite helicity (like in K - and K' -points). Here too, a **vHs** and higher subband arise, though details of the dispersion vary with respect to the common model.

In contrast, the uncompensated class is rooted in coupling between cones with the same sign of winding number. As depicted in [fig. 2.29 b](#), this leads to the formation of second generation Dirac cones. The process may be understood in analogy to the situation around original singularities, where branches of opposite pseudospin are crossing and the absence of backscattering preempts the opening of a gap[[10](#), [83](#)]. In the uncompensated scenario, Fermi velocity remains unaffected; possible evidence has been found in refs.[[84](#), [85](#)] and will be discussed for a here measured example in [sec. 5.2](#).

It is obvious that, especially in dependence on the degree of lattice relaxation, the relation between different hopping amplitudes will vary greatly. As speculated in ref.[[10](#)], corrugation and related delamination of *AA*-stacked regions will for example favor the compensated class. With the whole spectrum of possible lattice contortion discussed in [sec. 2.1.4](#), there is consequently ample possibility for either of the two pseudospin-sensitive classes. Consideration of the [TBG](#) sample's environment and corresponding degree of lattice relaxation ([sec. 2.1.4](#)) gains importance in the light of the reviewed considerations.

2.2.3 The Superlattice mini-Brillouin zone

The unit cell of a TBG superstructure in momentum space scales reciprocally to the one in real space and is thus often termed as mini-Brillouin zone (mBz). As suggested in fig. 2.4 f, in the section on Moiré theory, the reciprocal superlattice wavelength is constructed as

$$G = 2\hat{a} \sin(\theta/2), \quad (2.23)$$

where $\hat{a} = \frac{4\pi}{\sqrt{3}a_G}$ is the magnitude of reciprocal unit vectors $\hat{\mathbf{a}}_{1,2}$ and θ the interlayer twist.

Comparison of ΔK from eq. 2.21 to G from eq. 2.23 reveals a difference in factor $\sqrt{3}$, which mirrors the real-space relation between b_G and a_G . The underlying picture is depicted in fig. 2.30 a, where G is the span between rotated vectors $\hat{\mathbf{a}}$ (dashed blue and yellow) and ΔK the one between rotated K (black).

The differences between Moiré pattern and commensurate superlattice in real space (sec. 2.1.2 vs. sec. 2.1.3) are reflected in the reciprocal, as shown in the comparison between fig. 2.30 a and b: In the commensurate case at $\theta = 9.43^\circ$, the mBz around individual double-corners of the original Brillouin zones (at outer red hexagons) may be extrapolated to a single congruent one in the center of momentum space (i.e. around the Γ -point in fig. 2.30 b). Only $\sim 0.5^\circ$ of twist angle more however, and a severe mismatch between expanded mBz-lattices becomes evident (fig. 2.30 a).

While commensuration is irrelevant in the above mentioned effective continuum model for twist angles $\theta \lesssim 10^\circ$ [48], generation of mini-bands formally requires exact periodicity in the Bloch formulation. At large interlayer twist, the exact rotational mismatch will therefore be relevant to the TBG electronic dispersion;

due to increasingly high density of commensurate states in smaller angles however (fig. 2.7, fig. 2.9), the discussed rearrangements of individual lattices (also increasingly pronounced in the small-angle range, see sec. 2.1.4) will likely become the dominant factor in the stringency of **mBz**-related backfolding phenomena.

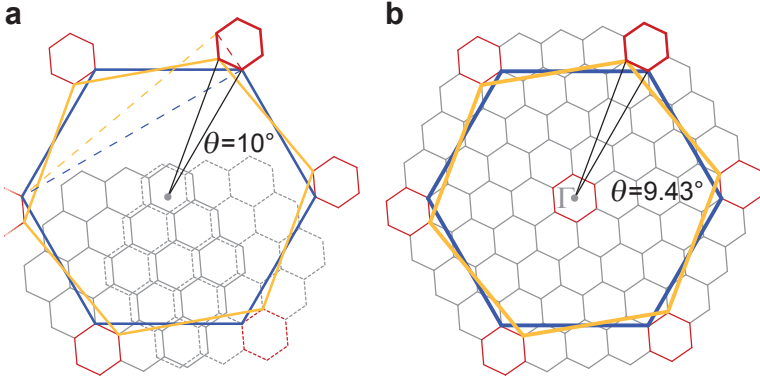


Figure 2.30 Schematic of reciprocal space with Brillouin zones of twisted layers (blue and yellow respectively). Red and gray hexagons indicate the corresponding **mBz**. **a:** Incommensurate structure of $\theta = 10^\circ$; relations of eq. 2.21 and eq. 2.23 are suggested by solid black and dashed colored lines respectively. Expansion of **mBz** around different pairs of rotationally displaced Dirac cones (red hexagons) reveals a mismatch. **b:** Commensurate structure at $\theta = 9.43^\circ$; reciprocal superlattice matches both original Brillouin zones.

Instances of rigorous backfolding into a **vdW**-interlayer **mBz** have been impressively demonstrated for the case of graphene on hexagonal boron nitride (**hBN**) [86–88], which creates an instructive example for possible outcomes in **TBG**.

As introduced in [sec. 2.1.4](#) ([fig. 2.17](#)), a superlattice arises between graphene and [hBN](#) due to a mismatch of lattice constants, where λ_{hBN} reaches its maximum around 14 nm at rotational alignment between lattices[86].

[Figure 2.31](#) a shows the according k-space scenario with a net of superlattice [mBz](#); a Dirac cone (red circle) arising at the center of the zone (red dot) will cross six others (green circles) from the neighboring [mBz](#) at midpoint (yellow dots) between the mini zone's K - and K' -points. In argumentation analog to the above description of Mele's uncompensated class ([fig. 2.29](#))[89], secondary Dirac points arise at the crossing, as calculated in [ref.\[88\]](#) and depicted in [fig. 2.31](#).

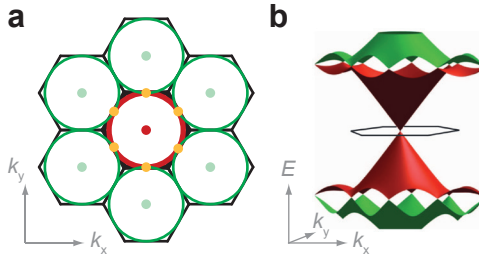


Figure 2.31 a: Reciprocal-space situation in graphene on [hBN](#). Multiple hexagonal [mBz](#) are depicted in black lines. The red dot indicates the Dirac point at the K -point of the original [MLG](#); the green dots signify copies evoked by the long-range periodic superlattice potential; the yellow dots indicate second generation Dirac points at the crossing between Dirac cones in first and further [mBz](#). **b:** From [ref.\[88\]](#): band structure in the [mBz](#), calculated for the scenario in [a](#).

The superlattice Dirac points arise at the border of the **mBz** with all of the contained states occupied, which may be described via the relation

$$n \frac{\sqrt{3}}{2} \lambda^2 = 4, \quad (2.24)$$

where the factor to carrier concentration n is the area of the superlattice unit cell in real space and the number of four on the right-hand side accounts for graphene's fourfold degeneracy[86–88, 90].

Accordingly, copies of the Dirac point signature can be observed at a few $n \sim 1 \times 10^{16} \text{ m}^{-2}$ in electronic transport on closely aligned graphene-**hBN** heterostructures; a change of effective carrier polarity is observed about midway between singularities, as reflected in corresponding Hall measurements[86–88].

In **TBG**, the situation is complicated by the involvement of two rotationally displaced Dirac cones. Three different scenarios are reviewed in the following:

Firstly, commensuration effects may be assumed negligible[19, 20, 91]. In this case the dispersion, merged in a **vHs** at midpoint between the rotated layers' Dirac points (fig. 2.26), continues as one beyond the borders of the **mBz**.

Ref.[92] provided hints towards the experimental relevance of the corresponding scenario; magnetotransport signatures found in context of the present work[45] solidify the validity of the underlying model (see sec. 5.1).

In ref.[91] too, observations of Landau quantization (see sec. 2.3.2) across states beyond the borders of the **mBz** indicate absence of zone folding.

Secondly, the major coupling scenario of the low-energy **vHs** (sec. 2.2.2) is combined with the folding mechanism found for the **hBN**-related phenomena (fig. 2.31):

Figure 2.32 a shows the according k-space scenario: the two layers' dispersions, originated at the positions marked by red dots, have merged in a **vHs** at the Γ -point of the **mBz** (black star) and continue as one towards the border of the mini zone. Here, the same backfolding process as in fig. 2.31 occurs, as calculated in ref.[93] and depicted in fig. 2.32 b.

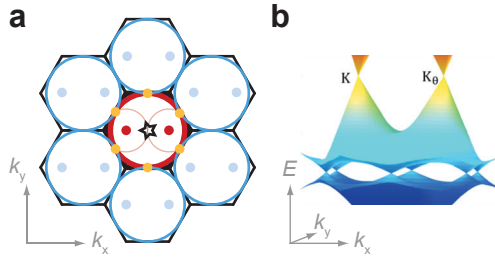


Figure 2.32 a: Reciprocal-space situation in **TBG** according to ref.[93]: Multiple hexagonal **mBz** are depicted as black lines. The red dots indicate Dirac points of twisted layers at the K - and rotated K^θ -points, where the black star indicates the position of a **vHs**; the blue dots signify Dirac-point copies in further **mBz**; the yellow dots indicate second generation Dirac points at the crossing between merged dispersions in first and further **mBz**. **b:** From ref.[93]: band structure in the **mBz**, calculated for the scenario in **a**.

Thirdly, the model applied in ref.[50] likewise finds low energy **vHs** but an alternative representation of the backfolding process: As depicted in fig. 2.33 a, the rotationally displaced Dirac points are positioned in the corners of the **mBz** in semblance to the K - and K' -points of **MLG**; neighboring mini zones supply Dirac cones for the remaining four corners to complete the analogy.

Figure 2.33 b shows the calculated dispersion[50, 90]; above the vHs (black stars in panel a) it features a charge inversion and transition to a Berry phase of zero in a hole-like pocket originated in the Γ -point, where a gap opens to the next-highest subband.

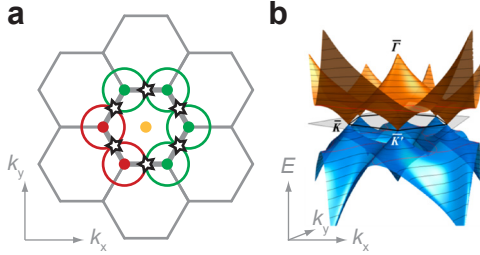


Figure 2.33 a: Reciprocal-space situation in TBG according to refs.[50, 90]: Multiple hexagonal mBz are depicted as gray lines. The red dots indicate Dirac points of twisted layers at the rotated \bar{K} - and \bar{K}' -points; the green dots signify copies from further mBz ; black stars indicate the position of vHs ; the yellow dot indicates the highest-energy point and upper end of the mini-band at the Γ -point. **b:** From ref.[90]: band structure in the mBz , calculated for the scenario in a.

The second and third of the three above presented alternatives are similar (in principle, only the frame of reference is shifted), differ however in the number of newly created band origins and the expected topology.

Experimental evidence for the latter scenario was found in ref.[90]; possible origin for the applicability of one or the other high-energy coupling model may be found in the particular degree of lattice corrugation in the measured sample as discussed in the beginning of this section and introduced in sec. 2.1.4.

2.3 Magnetotransport

A powerful tool to probe the electronic properties of a material system lies in magnetotransport measurements. The behavior of charge carriers at different Fermi energy as well as particular sequences of quantization in magnetic field hold information about the electronic dispersion and topology of a probed material.

Transport in the absence of magnetic field alone already gives access to a variety of sample parameters. As discussed in the first section 2.3.1, carrier mobility and doping concentration may be extracted from field effect resistance under variation of a gate voltage.

Individual TBG layers' Dirac cones are decoupled at low energy as introduced in sec. 2.2.2. Here, asymmetric gating creates an electric field and energetic offset between layers, as quantitatively described by a screening model introduced in the second part of sec. 2.3.1.

A perpendicular magnetic field quantizes in-plane electronic momentum and energy. The topological winding number pours into quantization criteria and leads to distinct Landau level sequences in MLG, Bernal-stacked bilayer graphene, and different coupled varieties of TBG as discussed in sec. 2.3.2.

Landau quantization as introduced in sec. 2.3.2 manifests in a modulated density of states in the presence of disorder, where Shubnikov-de Haas oscillations are witnessed in longitudinal resistance. Quantitative description of these is provided in sec. 2.3.3; informative value with respect to parameters of the underlying electronic dispersion is discussed.

2.3.1 The Electric Field Effect

Due to the atomic thickness of graphene, charge induced via a capacitive gate is delocalized over the whole conducting sample; the carrier density is continuously tuneable between the regimes of electron and hole conduction due to the gapless dispersion. This manifests in the observation of an ambipolar field effect with Drude conductivity

$$\sigma = \mu en \quad (2.25)$$

where μ is charge carrier mobility, e is the elementary charge and n is charge carrier concentration. The latter is proportionally related to a gate voltage U_{BG} (global backgate in this work) via capacitance C which leads to proportional dependency of σ in U_{BG} as illustrated by gray lines in [fig. 2.34](#). Four major factors however commonly give rise to alterations from this simple picture:

- A doping charge constitutes a constant offset in the gate-induced carrier density. The **charge neutrality point (CNP)** shifts to positive U_{CNP} for p-doping (as depicted in [fig. 2.34](#)) and negative U_{CNP} for n-doping.
- Substrate influence as well as intrinsic corrugation induce potential disorder in a graphene sheet, giving rise to so called electron-hole puddles, i.e. local variation of n over as much as $1 \times 10^{15} \text{ m}^{-2}$ [[94](#)]. From this follows a finite minimal conductivity in the range of $1 e^2/h$ to $10 e^2/h$ [[95](#)], as depicted to the bottom of [fig. 2.34](#).
- Electron-hole asymmetry in μ will proportionally lead to different slopes in σ as evident from [eq. 2.25](#).
- Finally, short-range scattering has been shown to manifest in sublinear evolution of conductivity over carrier density [[96](#)]; a phenomenon which may also arise in consequence to contact resistance.

A recorded field effect curve thus allows for the extraction of basic electronic parameters like carrier mobilities $\mu_{e,h}$ and doping charge as well as inference of potential disorder and scattering mechanisms.

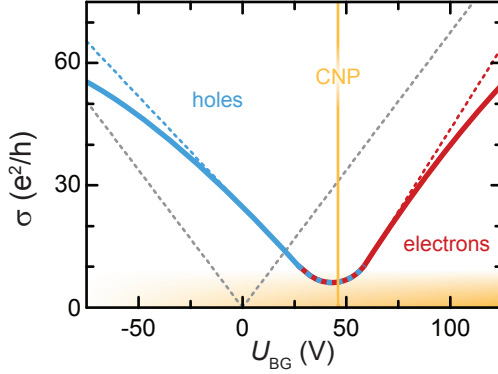


Figure 2.34 Conductivity vs. backgate voltage. Dashed gray line is eq. 2.25 with $\mu=2500\text{ m}^2\text{V}^{-1}\text{s}^{-1}$ and a capacitive coupling of $C^*=6.53 \times 10^{14}\text{ V}^{-1}\text{m}^{-2}$. The CNP (vertical yellow line) is shifted due to a doping charge of $3 \times 10^{16}\text{ m}^{-2}$; finite minimal conductivity due to potential disorder rounds off conductivity at some e^2/h (shaded yellow area). Asymmetric $\mu_e=3000\text{ m}^2\text{V}^{-1}\text{s}^{-1}$ and $\mu_h=2000\text{ m}^2\text{V}^{-1}\text{s}^{-1}$ lead to different slopes in regimes of electron and hole conduction; sublinear evolution at larger absolute n may arise due to short-range scatterers as well as contact resistance.

In TBG however, gate-induced carrier density distributes over two potentially decoupled layers. A quantitative discussion of the involved screening-mechanism in dependence on sample parameters like interlayer distance and twist angle is provided in the following.

Screening

The energetic offset ΔE between Dirac points in top and bottom layer is generally described via the following equation:

$$\begin{aligned}\Delta E &= \frac{\Delta h e^2}{\epsilon_0} (n_t - \delta n) \\ &= v_F \hbar \sqrt{\pi} \left(\text{sgn}(n_b) \sqrt{|n_b|} - \text{sgn}(n_t) \sqrt{|n_t|} \right)\end{aligned}\tag{2.26}$$

The upper part accounts for the fact, that every electron induced in the top layer via the backgate contributes to an electric field between layers. Interlayer capacitance is derived in the model of a parallel plate capacitor with distance Δh and the interlayer dielectric constant ϵ_0 of vacuum. The carrier concentration δn accounts for contributions to n_t which are not backgate-induced but due to an offset in Fermi energy E_F e.g. through doping.

The lower part of eq. 2.26 expresses the difference between E_F as measured from the Dirac points of bottom and top layer respectively (see eq. 2.15), which is a measure for ΔE under the assumption of a joint Fermi level between layers (e.g. due to joint electrical contacts).

Figure 2.35 depicts the above scenario, where the vertical signifies energy and the horizontal real-space extension (as well as reciprocal space in case of the depicted electronic dispersions). Opposite amounts of charge are induced in backgate and TBG; contributions in the top layer have a sign-reversed counterpart in the sum of charge induced in bottom layer and backgate, which constitutes a parallel-plate-capacitor situation with effective plate separation Δh and charge $n_t - \delta n$ between TBG layers. Note that in the interpretation of δn as doping charge in the top layer, an equal amount of doping follows for the bottom layer as evident from energetic equality $\Delta E = 0$ between layers at $n_t = \delta n$ (i.e. at zero backgate-induced charge); alternative interpretations correspond to layer-asymmetric

doping charge. In practice, fitting of the above model to TBG-data requires further offset in relation to the gate voltage U_{BG} ; a final interpretation of δn and its relation to overall doping Δn can then be read of carrier concentrations at $U_{\text{BG}} = 0$ as described in point 4.) on p. 83.

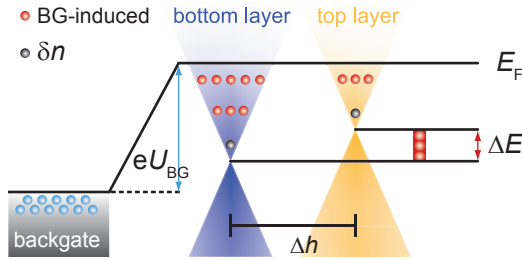


Figure 2.35 Schematic of gated TBG: a voltage U_{BG} between backgate (gray bar, bottom left) and TBG separates holes (blue dots) and electrons (red dots); part of the latter are induced in the top layer (yellow) and lead to energetic raise ΔE with respect to the bottom layer (blue) due to an electric field integrated over interlayer distance Δh . Gray dot in top layer indicates doping charge δn ; in the specific formulation of eq. 2.26, this requires the same doping in the bottom layer.

Equation 2.26 describes screening in TBG of symmetrical Fermi velocity as applied in [15, 97]. Increased flexibility and implicit account for interlayer twist is achieved in a here applied extension of the model which calculates the electronic situation in a TBG sample in dependence on eight basic system parameters as described in the following four steps:

1.) Carrier concentration in the top layer is calculated as

$$n_t = \epsilon_0 \Delta E / (e^2 \Delta h) + \delta n$$

in dependence on the variable of ΔE . TBG system parameters are Δh and δn .

2.) Reduced Fermi velocities in the top and bottom layer are calculated from eq. 2.22 as

$$\tilde{v}_F^t = v_F^t \left(1 - 9 \left(\frac{t_{e,h}^\theta}{\hbar v_F^t \Delta K} \right)^2 \right) \quad \tilde{v}_F^b = v_F^b \left(1 - 9 \left(\frac{t_{e,h}^\theta}{\hbar v_F^b \Delta K} \right)^2 \right).$$

TBG system parameters are the native Fermi velocities v_F^t and v_F^b of top and bottom layer respectively; interlayer hopping energies t_e^θ and t_h^θ account for electron-hole asymmetry; ΔK implies interlayer twist θ via eq. 2.21.

3.) As a preparatory step, the Fermi energy E_F as measured from the top layer's Dirac point is calculated as

$$E_F^t = \tilde{v}_F^t \hbar \cdot \text{sgn}(n_t) \sqrt{\pi |n_t|}.$$

The bottom layer's carrier concentration follows as

$$n_b = \text{sgn}(E_F^t + \Delta E) \frac{(E_F^t + \Delta E)^2}{(\tilde{v}_F^b \hbar)^2 \pi}.$$

4.) Carrier concentrations are related back to the gate voltage via

$$n_b + n_t - 2\delta n = C^* (U_{BG} - U_\Delta)$$

where TBG parameter U_Δ accounts for deviations from symmetric doping. The capacitance per unit area and elementary charge is set to $C^* = 6.53 \times 10^{14} \text{ V}^{-1} \text{ m}^{-2}$ for the calculations in fig. 2.36.

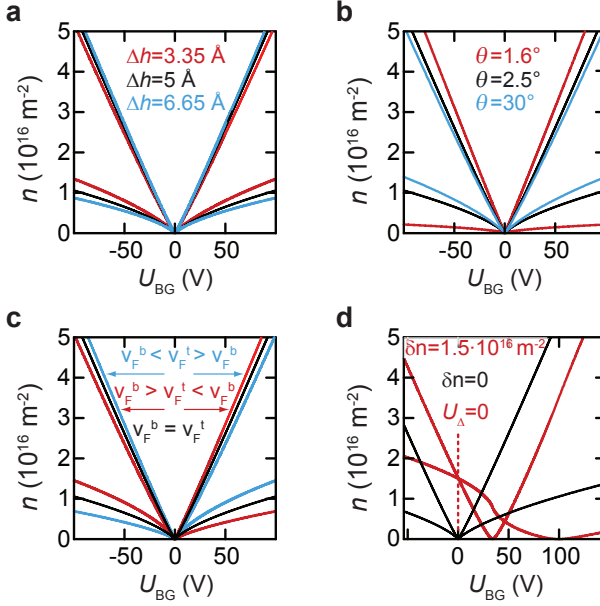


Figure 2.36 Carrier densities in bottom and top layer (stronger curving and lower n in the latter) as calculated via the extended screening model. *TBG* parameters for black curves are $\Delta h = 5 \text{ \AA}$, $\delta n = 0$, $v_F^{t,b} = 1 \times 10^6 \text{ m s}^{-1}$, $t_{e,h}^\theta = 0.1 \text{ eV}$, $\theta = 2.5^\circ$ and $U_\Delta = 0$. **a:** Varied parameter Δh : larger interlayer distance leads to more effective screening of the top layer from backgate influence. **b:** Varied parameter θ : smaller interlayer twist leads to further reduction in Fermi velocity and corresponding rise in density of states which enables more effective screening. **c:** Varied parameter $v_F^{t,b}$: argumentation via the densities of state applies similar to **b**. **d:** Varied parameter δn : top and bottom layer do not share the same *CNP* any more but are equally doped as evident from $n_b = n_t$ at $U_{BG} = 0$.

Figure 2.36 shows accordingly modeled distributions of carrier density for top and bottom layer in response to variation in five key parameters:

As intuitively expected, less charge is induced in the top layer for larger interlayer separation Δh as illustrated in panel a.

As evident from panel b, interlayer twist has significant influence on charge distribution in the backgated TBG: Due to the corresponding reduction in Fermi velocity \tilde{v}_F , layers in small-angle systems have larger densities of state which allows for more effective screening of charge. A similar effect is observed for increasing hopping energies $t_{e,h}^\theta$.

Panel c shows the effects of asymmetric native Fermi velocities $v_F^{t,b}$ between top and bottom layer as indicated by corresponding arrows and legend: Lower velocity and corresponding higher density of state in the bottom layer allows for more effective screening of backgate influence in the top layer.

Finally, panel d depicts the effect of backgate voltage on a dispersion with energetic offset. Charge neutrality is split between layers; the carrier density evolution is highly asymmetric in gate voltage.

2.3.2 Landau Quantization

In a magnetic field perpendicular to a two-dimensional electronic system, the energetic spectrum of carriers becomes discrete. Rooted in the acquisition of phase on a path enclosing a magnetic flux, this may be understood in a semiclassical description: Ref.[98] states the condition

$$\pi k^2 = 2\pi eB \left(N + \frac{1}{2} - \frac{w}{2} \right) / \hbar, \quad (2.27)$$

where k is the radius of a circular cyclotron orbit in reciprocal space and N an integer. The mismatch of $\frac{1}{2}$ expresses the usual offset from the quantum mechanic harmonic oscillator; the winding number w accounts for the additional acquisition of topological phase upon full-circle rotation (e.g. $w = 1$ for MLG, eq. 2.18).

Equation 2.27 yields the so called **Landau level (LL)** spectrum in energy for a given electronic system via the according dispersion relation. For a non-relativistic **2DEG**, the spectrum is

$$E_N = \hbar\omega_c (N + 1/2) \quad (2.28)$$

with cyclotron frequency $\omega_c = \frac{eB}{m^*}$.

In contrast, a graphene monolayer exhibits

$$E_N = \pm v_F \sqrt{2e\hbar BN}, \quad (2.29)$$

where the square-root dependence is linked to the linear dispersion and the unusual zero-energy mode arises in consequence of the topological Berry phase[6, 7].

Ref.[74] finds the *AB*-bilayer spectrum as

$$E_N = \pm \hbar\omega_c \sqrt{N(N-1)}; \quad (2.30)$$

the according double zero-energy mode constitutes a major variation with respect to the similar **2DEG** spectrum[77].

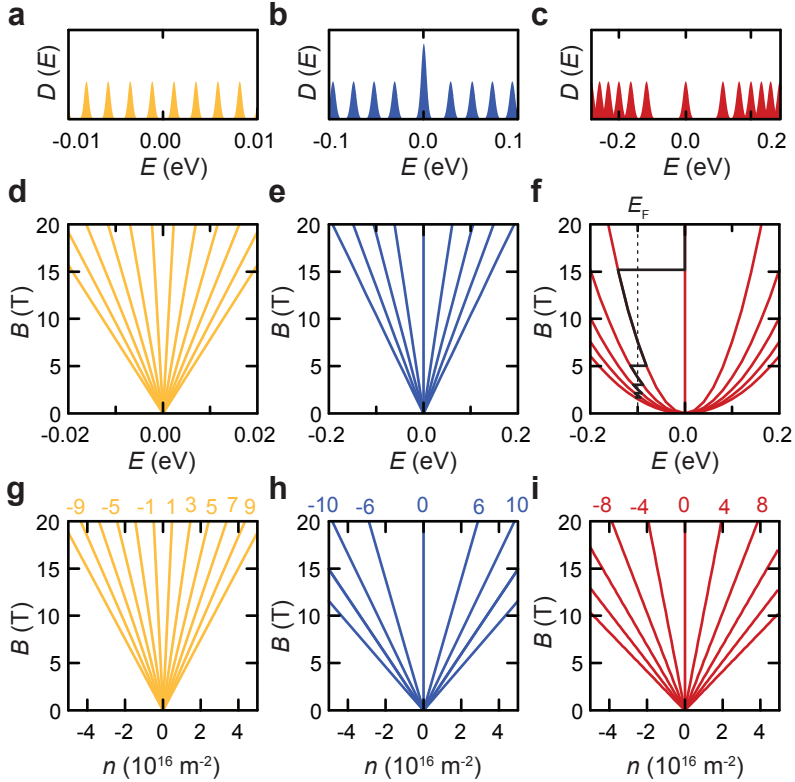


Figure 2.37 LL in 2DEG (left, $m^*=0.5 m_0$), Bernal bilayer (middle, $m^*=0.054 m_0$), and MLG (right, $v_F=1 \times 10^6 \text{ m s}^{-1}$). Upper panels show density of states at $B=10 \text{ T}$ (disorder-broadened). Middle panels mark dependence of LL on energy and perpendicular magnetic field. Lower panels show LL in dependence on charge carrier density, where degeneracy is two in the 2DEG and four in graphene.

Figure 2.37 shows the relations from eq. 2.28 (left panels), eq. 2.30 (middle panels), and eq. 2.29 (right panels) with the parameters stated in the figure caption.

The spreading shape of LL in energy and magnetic field is often referred to as Landau fan. Where square-root dependence from eq. 2.29 leads to curved slopes in the energy diagram for MLG (fig. 2.37 f), Landau fans are generally straight in charge carrier concentration n (fig. 2.37 i) as described in the following:

A single LL holds

$$\frac{2\pi eB/\hbar}{4\pi^2} = \frac{B}{\Phi_0}, \quad (2.31)$$

where the numerator expresses the k-space volume of a circular ring between N and $N+1$ according to eq. 2.27; the denominator stems from the volume of a single state in reciprocal space and $\Phi_0 = h/e$ is the magnetic flux quantum. From this, one can define a filling factor

$$\nu = \frac{n}{B/\Phi_0} \quad (2.32)$$

which linearly relates carrier concentration n and magnetic field B via the flux quantum.

As marked in fig. 2.37 g-i, the filling of Landau levels is further dependent on the degeneracy g of a given electronic system: The carrier concentration corresponding to a LL with index N is herein given by

$$n = 4N \cdot B/\Phi_0 \quad (2.33a)$$

$$n = 0 \quad \text{and} \quad n = 2 + 4N^\pm \cdot B/\Phi_0 \quad (2.33b)$$

for MLG (eq. 2.33a) and AB -bilayer (eq. 2.33b) respectively, where N^\pm is a nonzero integer. The offset of two in the Bernal-stacked case is due to the double zero-energy mode (fig. 2.37 b) which houses $4 \times \frac{B}{\Phi_0}$ states in electron and hole branch of the dispersion each.

In the low-energy range below the ν Hs (sec. 2.2.2), the above principals may be directly transferred to TBG:

In the layer-symmetric case, degeneracy is elevated to $g = 8$; LLs are found at filling factors $\nu=8N$, as illustrated in fig. 2.38 a.

In an asymmetrically gated sample, screening of charge lifts layer degeneracy as described in sec. 2.3.1. Evolution of LLs in B is given by eq. 2.33a for bottom and top layer each; an example of corresponding Landau fans is depicted in fig. 2.38 b for the screening scenario presented in fig. 2.36 d (red curves).

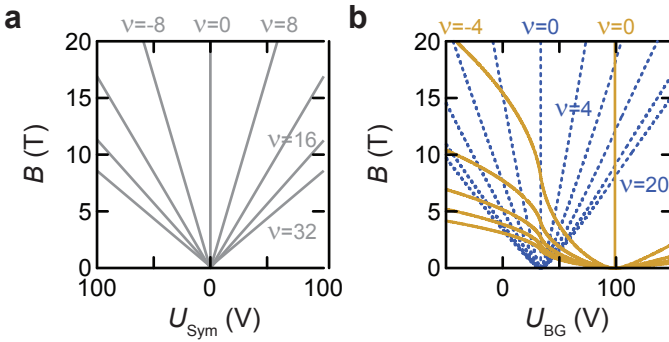


Figure 2.38 a: LL evolution in TBG below the ν Hs in dependence on magnetic field and a layer-symmetric gate voltage U_{Sym} ; capacitive coupling is $C^* = 6.53 \times 10^{14} \text{ V}^{-1} \text{ m}^{-2}$. Filling factors at respective LLs are indicated in gray. **b:** LLs in TBG below the ν Hs; here, an asymmetric backgate voltage U_{BG} (same coupling as in a) has greater influence on the bottom layer (blue) than the screened top layer (yellow). Filling factors are indicated in corresponding color code. Screening parameters are found in fig. 2.36 d.

At higher energy, when Fermi energy crosses the νHs and the different coupling scenarios from [sec. 2.2.3](#) come into play, spectra become more complicated:

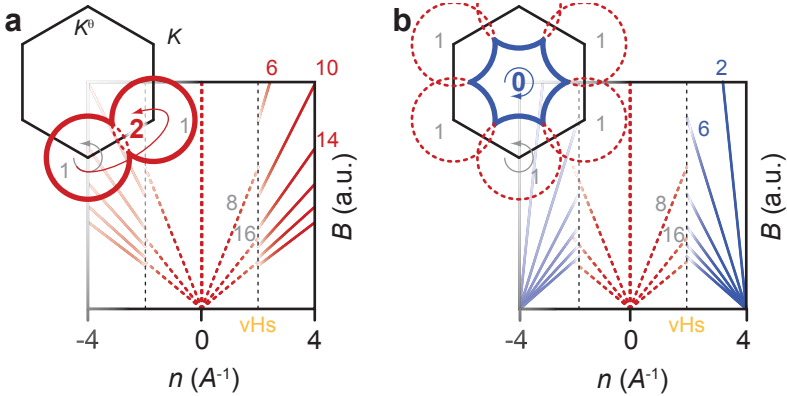


Figure 2.39 a: *LL spectrum of TBG across the νHs (dashed black line) in neglect of backfolding: At low carrier concentration, an eightfold degenerate sequence of LL (red dashed) is expected in the layer-symmetric scenario. High-energy carriers are quantized in the Bernal-bilayer sequence of filling factors at fourfold degeneracy (solid red). The inset shows a cyclotron orbit in the merged dispersion above the νHs in relation to the $m\text{Bz}$; winding numbers are indicated in gray and red for low and high energy cyclotron orbits respectively. **b:** Analog to **a** but in the rigorous backfolding scheme, cyclotron orbits in the six corners of the $m\text{Bz}$ merge and change sign of rotation (inset, bold blue). Corresponding LLs originate in carrier concentrations corresponding to a filled $m\text{Bz}$, sequence is fourfold degenerate and without zero-energy mode in the scenario from [fig. 2.33](#).*

The inset of [fig. 2.39 a](#) shows semiclassical cyclotron orbit trajectories in reciprocal space in relation to the **mBz**. If backfolding effects are neglected, the two rotationally displaced Dirac cones merge in the **vHs** and continue as a single dispersion. Accordingly, the topography of the Fermi surface changes; cyclotron orbit now enclose two Dirac points (bold red), which doubles the winding number[[98, 99](#)] and manifests in an *AB*-bilayer-like sequence of filling factors ([eq. 2.33b](#)) as illustrated in the main panel[[19, 20](#)].

The inset of [fig. 2.39 b](#) shows cyclotron orbits in the scenario from [fig. 2.33](#)[[50, 90](#)]. Here, bands are folded back into the **mBz** and cyclotron orbits around the six corners merge into one around the Γ -point. As the enclosed band is now hole-like, the original Landau fan (dashed red) stops at the **vHs** (dashed black) and meets a secondary one (blue), which originates from where all states in the **mBz** are occupied (see [eq. 2.24](#)).

The spectrum becomes even more complex, when the magnetic flux through the superlattice unit cell becomes comparable to Φ_0 . Here, rich fractal spectra were predicted which are often referred to as Hofstadter's butterfly in appreciation of their theoretical creator[[100](#)].

As the flux through a hexagonal unit cell $B\sqrt{3}/2\lambda^2 \sim \Phi_0$ at $\lambda \sim 15$ nm for an experimentally accessible magnetic field of 20 T, supercells in aligned graphene-**hBN** heterostructures proved large enough to witness traces of the self-similar fractal pattern in magnetotransport experiments[[86, 87, 99](#)].

Similar sizes of the superlattice unit cell are reached in **TBG** at an interlayer twist of $\theta \lesssim 1^\circ$. The rich spectra to be beheld, are formulated in refs.[[46, 50, 101](#)].

2.3.3 Shubnikov-de Haas Oscillations

In principal, longitudinal resistance as well as conductivity vanish between LL due to the absence of free states and a current carried by edge channels[102]. In perpendicular resistance, the Quantum Hall effect (QHE) is witnessed in discrete plateaus of

$$R_{xy} = \frac{e^2}{h\nu} \quad (2.34)$$

with $\frac{e^2}{h}$ the von Klitzing constant and ν indicating the integer number of filled LL below Fermi energy.

At intermediate magnetic fields, limited sample quality or elevated measuring temperatures, the density of states is no longer discretized but modulated by Landau quantization. Here, so called **Shubnikov-de Haas (SdH)** oscillations are witnessed in the longitudinal resistance.

Description in magnetic field is given by[7, 76]

$$\Delta R = R_{\text{env}}(B, T) \cos\left(\frac{2\pi}{\Delta B^{-1}} B^{-1} + \pi + \beta\right), \quad (2.35)$$

where β is the Berry phase.

In direct correspondence to the relations in eq. 2.33, ΔB^{-1} (gray bar, fig. 2.40) is related to the charge carrier concentration via

$$n = \frac{eg}{h\Delta B^{-1}}. \quad (2.36)$$

$R_{\text{env}}(B, T)$ is an envelope to the sinusoidal oscillations and proportional to the product of two factors: the magnetic-field-dependent Dingle factor

$$R_{\text{D}}(B) = \exp\left(-\pi\omega_{\text{c}}^{-1}\tau_{\text{q}}^{-1}\right) \quad (2.37)$$

with quantum scattering time τ_q , as well as an expression for temperature-dependent damping[6, 7, 76]

$$R_T(B, T) = \frac{2\pi^2 k_B T / (\hbar\omega_c)}{\sinh(2\pi^2 k_B T / (\hbar\omega_c))}, \quad (2.38)$$

where k_B is the Boltzmann constant. Note that the effective mass in the parameter ω_c is energy-dependent in MLG and relates to the Fermi velocity as

$$v_F = \sqrt{\frac{\hbar^2 n \pi}{m^*}}. \quad (2.39)$$

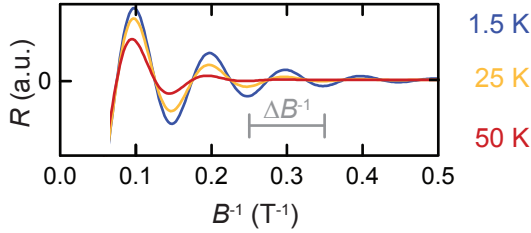


Figure 2.40 SdH-oscillations in monolayer graphene according to eq. 2.35 with the typical parameters of $m^*=0.025 m_0$ and $\tau_q = 50$ fs for three different temperatures according to the legend.

The above relations enable the extraction of a wide range of sample parameters: The Berry phase is readily derived from the offset in inverse magnetic field; equation 2.36 gives access to the charge carrier concentration n involved in a given oscillation. Temperature-dependent fits of eq. 2.38 furthermore yield effective mass m^* (and corresponding Fermi velocities v_F), where quantum scattering times τ_q are extracted from magnetic-field dependence via eq. 2.37.

2.4 Summary

The above chapter laid important foundations for the experimental findings presented in the following.

Starting with monolayer graphene and following this thread through the three sections of this chapter, the two-sublattice structure of graphene is introduced in [sec. 2.1.1](#). The direct electronic consequence, namely a pseudospin degree of freedom and acquisition of a Berry phase of $\beta=\pi$ over a closed circle in momentum space, is discussed in [sec. 2.2.1](#). Within Landau quantization of [MLG](#)-states, the introduced phase gives rise to a zero-energy mode as presented in [sec. 2.3.2](#).

Bernal- or *AB*-stacking configuration is introduced; the merged dispersion is presented to possess $\beta=2\pi$ topology and a double zero-energy mode.

In [sec. 2.1](#), [TBG](#) real-space structure is reviewed in detail; distinction between continuous Moiré superstructures ([sec. 2.1.2](#)) and rigorously periodic superlattices ([sec. 2.1.3](#)) is pointed out. Criteria for commensurability are derived; high density of accordingly periodic structures is found in low twist angles while exclusive commensurate spots exist at large rotational mismatch above $\sim 20^\circ$

Applicability of a continuum model for electronic coupling in both cases is presented in [sec. 2.2.2](#) for the low-energy dispersion of [TBG](#). Here, the two layers' dispersions are effectively decoupled before they merge in low-energy van Hove singularities. Detuning of individual Dirac cones via an electric field arising upon asymmetric gating (e.g. via a backgate) is described and modeled in [sec. 2.3.1](#). Accordingly offset and superposed evolution of Landau levels in the two layers is suggested in [sec. 2.3.2](#).

In a less explored interlayer coupling alternative, merging occurs in second generation Dirac singularities.

At high energies, different scenarios are reviewed (sec. 2.2.3). Back-folding into the superlattice mini-Brillouin zone is introduced in the example of graphene on hBN and extended to TBG. Corresponding topology of cyclotron orbits in magnetic field is reviewed towards the end of sec. 2.3.2.

Finally, lattice relaxation, manifesting in corrugation of layers with maximized interlayer distance in AA-stacked regions as well as more complex in-plane distortions, is introduced in sec. 2.1.4.

As discussed in sec. 2.2.2, such contortions could severely alter TBG electronic structure to the point of a changed effective helicity in the coupling Dirac cones[10].

For high energy, free lattice conformation is discussed with respect to its role in band-folding into the superlattice's mini-Brillouin zone (sec. 2.2.3).

The above review highlights the riches in graphene and TBG physics; where theoretical understanding of interlayer interaction grows more and more refined, there still are little discovered fundamentals. The seemingly simple system of two graphene sheets stacked on top of each other holds geometrical (sec. 2.1.3) and electronic (sec. 2.2.2, sec. 2.2.3) intricacies which make the twisted graphene bilayer a subject of ongoing scientific relevance[17, 30, 45, 49, 63, 90, 103].

3 Experimental Techniques and Apparatus

An intriguing quality of curriculum and work in the *Department for Nanostructures*, facilitating this dissertation, is the depth of operations, ranging from sample preparation to data analysis and scientific writing. On this path, a variety of techniques and apparatus are needed at the different stages of experimental progress. The present chapter provides an overview of the typical steps, from exfoliating graphene to magnetotransport measurements in **TBG**.

Micromechanical cleavage of natural graphite as method of preparation for graphene is introduced in **sec. 3.1**; the optical detectability on a substrate of **SiO₂** is discussed.

A special focus of this chapter lies on the **AFM** which is treated in terms of working principals and imaging artifacts specific to measurements on **TBG** in **sec. 3.3**.

Processing of **TBG** samples in preparation for electrical measurements is described in **sec. 3.2**; the subsequent steps of **Scanning Electron Microscope (SEM)**-lithography, involving etching into suitable sample geometries and definition of electrical contacts are illustrated.

Finally, the cryogenic setup enabling measurements at temperatures down to 1.5K is introduced together with the basic modus operandi for electrical measurements on graphene in **sec. 3.4**.

3.1 Graphene Flakes: Preparation and Optical Detection

Graphene, if understood in the more general sense of graphitic fewlayers in liquid suspension or in attachment to a substrate, has been subject of experimental studies for over 50 years: In 1962, Boehm et al. reported on thin carbon films achieved alternatively by chemical reduction or rapid heating of graphite oxide[3]. Thin layers of graphite were achieved by thermal decomposition on the surface of SiC in 1975[104]. Later, CVD-growth on the surface of transition metals enabled investigation of mono-atomic carbon overlayers[105]. Finally, Geim and Novoselov demonstrated the successful isolation of graphene by mechanical cleavage of graphite via a strip of adhesive tape in 2004[5].

The above techniques have since been refined, while additional, more specialized approaches developed over the years[106]. Central to the thesis at hand is first and foremost mechanical exfoliation, which is the basis for the presented experimental work and will be described in the following. Preparation of TBG via folding of exfoliated flakes is discussed in depth in chap. 4 together with a brief review on alternative approaches, namely mechanical transfer as well as growth from SiC and via CVD. The present section closes with explanation and evaluation of the high optical contrast of graphene on a substrate of SiO₂, which is crucial to the handling of exfoliated samples in further processing steps.

Mechanical exfoliation

The concept of micromechanical exfoliation makes use of the laminar structure in certain materials like graphite or hBN-crystals (see fig. 3.1), where interlayer binding is given by vdW-interaction. The binding energy between two layers in graphite lies around 0.3 Jm^{-2}

or 50 meV per carbon atom[107], which is two orders of magnitude lower than the in-plane carbon-carbon bond of 4.3 eV. Therefore, the basal planes of a crystal are easily torn apart while staying intact over relatively large areas, which usually measure several μm^2 at the monolayer level, after multiple exfoliation steps.

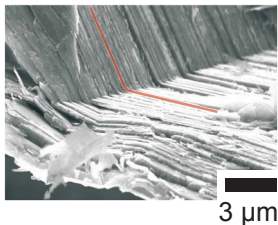


Figure 3.1 From ref.[108]: SEM-recording of a graphite crystal. The laminar structure shows in clusters of basal planes (parallel to red lines), lending the crystal a faceted structure.

For this work, pieces of natural graphite, measuring one to a few millimeters are used as starting material. Exfoliation is performed by repeatedly folding and drawing back a strip of adhesive tape over the graphite, thereby covering the tape with increasingly smaller fragments, ultimately reaching graphene after $\sim 10 - 50$ cycles. The graphene-covered tape is then pressed to a clean substrate (in this work SiO_2) and removed after a certain time. Through *vdW*-interaction, a subset of flakes from the tape will stick to the substrate surface; suitable graphene samples may then be chosen via the optical microscope (see [sec. 3.1](#)).

Variation in a number of exfoliation parameters was evaluated with respect to the yield in terms of number and size of graphene flakes. Different tapes, amounts of pressure onto the substrate as well as rest times before removal of the tape were tested to no significant avail. However, sensitivity to an environmental parameter could be observed: Backed up by limited statistics but nevertheless noteworthy, the yield of exfoliation in a low-humidity environment appears to be superior. This observation was made by comparing

results from winter months, where relative humidity in the cleanroom air may drop down to $\sim 20\%$, to results from warmer outside climates with up to $\sim 70\%$ humidity in the cleanroom. From this, it is tempting to draw a connection to the hydrophobic nature of graphene[109, 110]. A water film on the surface of the substrate may inhibit efficient attachment of graphene flakes. To explore this, the effect of hydrophobic functionalization on the SiO_2 surface was studied in cooperation with the group of Prof. Behrens from the inorganic chemistry department of the Leibniz University of Hanover. As reported in the master's thesis of Benedikt Brechtken however, no significant improvement in exfoliation yield could be noted[111]. Water clusters on the graphitic surface itself[109] may also be a limiting factor for the interaction with a substrate. Baking out of the graphene-covered tape (at low enough temperatures to avoid its decomposition) or the use of a hydrophilic substrate, in an opposite approach to the one described above, are therefore possible routes of further exploration.

Optical detection

While graphene has been shown to absorb significant, wavelength-independent 2.3% of incident light (i.e. $\pi\alpha$ with $\alpha = e^2/(\hbar c)$ as fine structure constant and c as speed of light)[112], even higher optical contrast can be achieved in reflection on a suitable substrate. Ref.[113] provides experimental study and theoretical description for the following scenario: A graphene sample of thickness d_{Gra} is lying in air on top of a substrate of SiO_2 grown over depth d_{SiO_2} on a base of silicon which is considered semi-infinite in thickness (see fig. 3.2). According to Fresnel's equations, incident light is reflected and transmitted at every junction in dependence on corresponding indices of refraction η_0 to η_3 . Moreover, in passing a given material layer, fractions of light get absorbed according to the imaginary part

of corresponding η ; different reflections interfere based on their respective optical path length modulated by the real part of η .

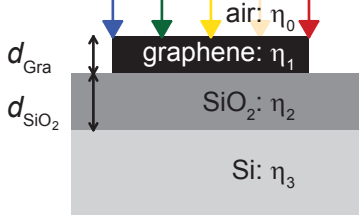


Figure 3.2 Side-view schematic of a graphene flake on a substrate of SiO_2 and Si . The sample lies in air. White light is irradiated from the top.

Based on the above considerations, ref.[113] finds an expression (equation 1 in the publication) for the intensities I_{Sub} and I_{Gra} of light coming back from an uncovered substrate and a graphene sample respectively. Accordingly, I_{Sub} is plotted in fig. 3.3 a as a function of the light's wavelength Λ and thickness of the oxide d_{SiO_2} with indices of refraction $\eta_0 = 1$ and $\eta_2(\Lambda = 400 \text{ nm}) = 1.47$ as well as $\eta_3(\Lambda = 400 \text{ nm}) = 5.6 - 0.4i$ in approximation of the Λ -dependent η_2 and η_3 [113], where i is the imaginary unit.

In the work leading up to this dissertation, a SiO_2 -thickness of 330 nm was employed and is marked as a white line in fig. 3.3 a. Minima and maxima in intensity are marked by colored circles at respective wavelengths and lend the substrate a greenish appearance in a white light source as illustrated in fig. 3.3 b, v.

The optical contrast between a graphene layer and the substrate may be defined as

$$C_{opt} = \frac{I_{Sub} - I_{Gra}}{I_{Sub}}.$$

For the plot in fig. 3.3 c, MLG is assigned a thickness of $d_{Gra} = 3.35 \text{ \AA}$ (sec. 2.1.1) and the refractive index $\eta_1 = 2.6 - 1.3i$ of bulk graphite[113].

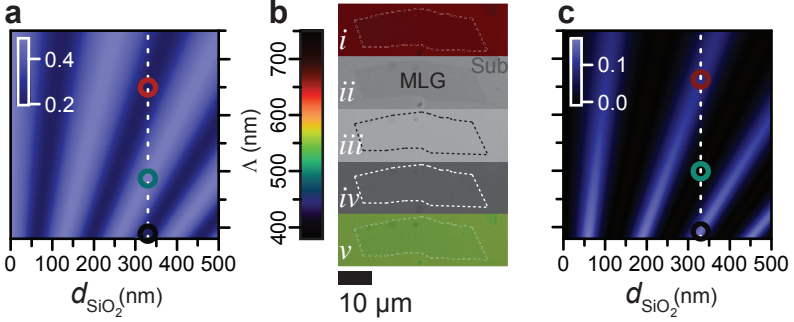


Figure 3.3 a: Wavelength (Λ)-dependent relative intensity I_{Sub} of light returning from a substrate of SiO_2 grown over variable thickness d_{SiO_2} onto a bulk of silicon ($1 \hat{=} 100\%$ of incident light). **b:** Photographs of MLG on a 330-nm- SiO_2/Si substrate: *i*: shot through optical red filter, *ii*: red channel RGB-split of *v*, *iii*: green channel RGB-split of *v*, *iv*: blue channel RGB-split of *v*, *v*: shot at white incident light. **c:** Calculated optical contrast C_{opt} of MLG on top of the substrate considered for panel a.

Maxima in C_{opt} are found near the UV-spectrum at $\Lambda = 394$ nm and in the red spectrum at $\Lambda = 660$ nm. The latter can be used to significantly enhance the visibility of MLG which is still quite low in white light (see fig. 3.3 b *v*): As seen in the topmost sub-panels of fig. 3.3 b, both an optical red filter and the red channel of an RGB-split in a digital photograph will render a monolayer flake easily discernible from the substrate, while green and blue channel of the RGB-split show almost no contrast.

With the equipment and substrate used for the present work, the highest contrast is attained in the red channel of an RGB-split photograph taken through an optical red filter, thus narrowing down the spectral range close to the wavelength of maximal contrast. Exper-

imental values lie at $C_{opt} \approx 7.5\% \pm 1.5$, where the calculated maximum at $\Lambda = 660 \text{ nm}$ is 10% ; the deviation is explained by approximations in the employed model as well as spectral mismatch between experimentally filtered and optimal wavelength. The bottom panel of [fig. 3.4](#) shows an example histogram of pixel frequency vs. intensity in 8-bit encoding (intensity maximum at 255) for a **MLG** picture which has been spectrally optimized as described above. The sum of two Gaussian distributions is fit to the data in good accuracy. For more clarity, the intensity range of the photograph to the top is compressed around the peak positions in the frequency distribution. In the following, such optimized visualization will have been applied to all optical pictures of presented graphene samples.

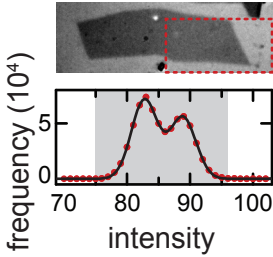


Figure 3.4 *Top: Red channel of RGB-split performed on **MLG**-photograph through optical red filter. Contrast is enhanced by compression of intensity to the gray shaded area in bottom panel. Bottom: Histogram over area indicated by dashed lines in top. Black line is a double-Gaussian fit.*

Optical contrast may also serve in telling apart graphene and graphite samples in terms of thickness. [Figure 3.5](#) shows calculations for variable layer numbers in the model described above[[113](#)]. At the wavelength $\Lambda = 660 \text{ nm}$, optimal for **MLG** detection, contrast C_{opt} rises slightly sublinear for the first few layers (see inset of panel b). At $n_{layer} \gtrsim 5$, the slope decreases and changes sign at $n_{layer} = 24$, finally leading to inverted contrast above 77 layers, where samples will start to appear light rather than dark with respect to the substrate. After a local absolute contrast minimum at $n_{layer} = 382$, C_{opt} converges where interference of rays return-

ing from the different material junctions becomes irrelevant due to absorption in the graphite sample.

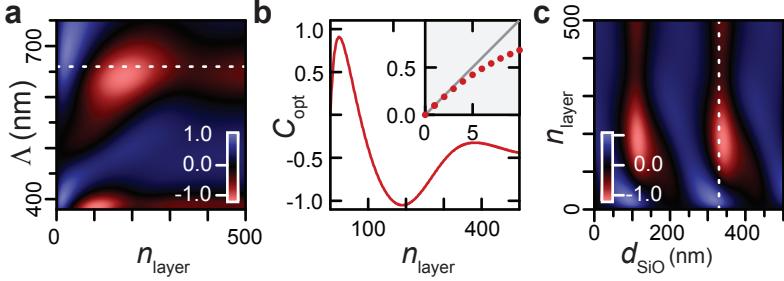


Figure 3.5 a: Calculated optical contrast C_{opt} for graphite on a 330 nm- SiO_2/Si substrate in dependence on optical wavelength Λ and number of graphene layers n_{layer} . **b:** Cross section along dashed white lines in both panels **a** and **c**. The inset shows C_{opt} for the first ten layers; the gray line extrapolates the contrast step from zero to one layer. **c:** C_{opt} for graphite at optical wavelength $\Lambda = 660$ nm in dependence on oxide thickness d_{SiO_2} and number of graphene layers.

In summary, the above described model serves as a convenient means to estimate the number of layers in a graphene sample via optical contrast on a substrate of SiO_2 grown on top of Si . As the interlayer distance $\Delta h_{AB} = 3.35 \text{ \AA}$ in AB -stacking and the refractive index $\eta_1 = 2.6 - i$ of bulk graphite are assumed, calculations should be most accurate at large layer numbers arranged in Bernal-stacking.

In this work, qualitative applicability to TBG can be confirmed; more detailed studies on the effect of variable Δh (see sec. 4.2.2) as well as twist-dependent optical absorption[114] in rotated stacking may constitute an interesting direction of research however.

3.2 Lithography: Etching and Electrical Contacts

To probe the electronic transport properties of **TBG**, electrical contacts need to be applied. Furthermore, sample geometries like a Hall bar shape may be defined by etching; in the case of **TBG**-areas surrounded by **MLG** (when the bottom layer is larger than the top layer, as depicted in [fig. 3.6](#)), isolation of the twisted bilayer may be achieved by etching away undesired portions in the vicinity.

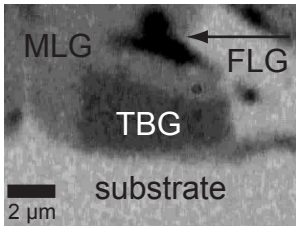


Figure 3.6 *Optical picture of a twisted bilayer produced by folding of **MLG**. The **TBG** area is surrounded by monolayer- as well as thicker fewlayer graphene (**FLG**) to the top and left.*

As **TBG** samples usually measure in the low μm -range, desired structures and electrical contacts need to be defined at sub-micron precision. The obvious method of choice for this task lies in electron beam lithography (e-beam lithography) which involves a number of steps, followed by oxygen plasma etching, application of metal contacts via physical vapor deposition and electrical connection to a chip carrier as summarized in [fig. 3.7](#):

- As a first step ([fig. 3.7 a](#)), **polymethyl methacrylat (PMMA)** is applied as e-beam resist. For this work, a double coating of 4% 200K **PMMA** in a solvent of ethyl lactate and 2% 950K **PMMA** in anisole is subsequently spun onto the sample at 4000 rpm and baked out on a hot plate at 185 °C for 10 min each (1K indicating 1000 g mol⁻¹ of the respective molecule).

3 Experimental Techniques and Apparatus

- Desired lithographic structures are designed with the software ELPHY of the company RAITH which enables a direct translation to movement of the electron beam of an SEM. E-beam lithography takes place at an accelerating voltage of 30 keV and an electron dose of $\sim 250 \mu\text{C}/\text{cm}^2$ (exact values vary slightly for different samples) to depolymerize irradiated portions of the PMMA-resist for a positive lithographic process. The undercut (trapeze shape of light blue areas, fig. 3.7 b) is due to forward scattering of electrons.

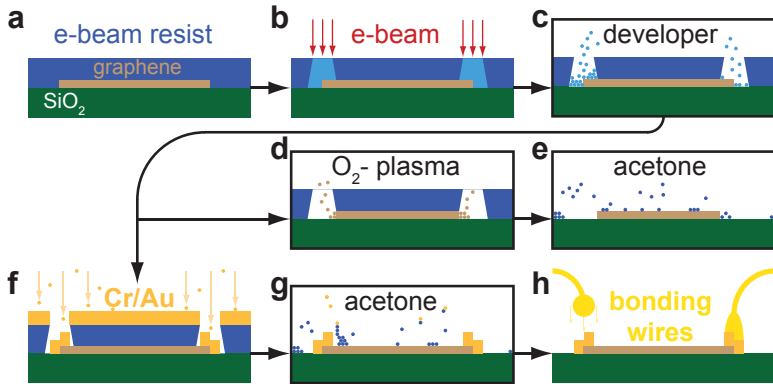


Figure 3.7 Schematic of different processing steps. **a:** PMMA (blue bar) is spun onto the sample. **b:** Areas of the resist are irradiated via SEM. **c:** The structures depolymerized in **b** are dissolved in a developer. **d:** Uncovered graphene is etched away. **e:** The resist is dissolved in acetone. **f:** Alternative to **d**, the sample is exposed to physical vapor deposition. **g:** e-beam resist and covering metal are removed via acetone. **h:** Bond wires are drawn between contacts evaporated in **f** and a chip carrier (not depicted).

- Irradiated **PMMA** is dissolved in a developer of methyl isobutyl ketone (MIBK) and isopropanol (1:3) (fig. 3.7 c).
- The structure created in steps **a-c** may now be used as an etching mask (fig. 3.7 d). The sample is exposed to oxygen plasma generated from oxygen gas through ionization by microwaves. With the used incinerator (PVA TEPLA AG, type 100-E) at parameters of 1 mbar and 100 W, an etching duration of 100 s has been found to remove a monolayer of graphene. Double layers are reliably etched at ~ 220 s. For thicker graphene samples and graphite, multiple etching steps with fresh **PMMA** are advisable, due to degradation of the etching mask in O_2 -plasma.
- As illustrated in (fig. 3.7 e), the **PMMA**-mask may be removed by dissolution in acetone.
- Alternative to etching (step **d**), the mask created in steps **a-c** can be used for locally selective physical vapor deposition (fig. 3.7 f). In low-pressure atmosphere ($< 10^{-6}$ bar), a metal of choice is evaporated via an electron beam; the sample is installed upside-down in a distance of ~ 1 m above the crucible. Thereby, metal atoms settle on the sample surface under near normal angle of incidence, not filling out the voids below the undercut.

For this work, 8 nm to 10 nm chromium (Cr) and 30 nm to 60 nm gold (Au) were subsequently deposited as adhesive layer and conductor respectively.

- Resist and covering metal are removed by dissolution of **PMMA** in acetone (fig. 3.7 g); the above mentioned undercut enables bypassing of the unreactive metal layer. The contacts deposited directly onto substrate and sample stay unaffected.

3 Experimental Techniques and Apparatus

- Finally, the contacts deposited in step **g** are connected to a chip carrier (see **fig. 3.8 h**). Large bond pads (see **fig. 3.8 g**), defined following the above steps serve as contact area to thin gold wires. Connection is achieved by thermosonic bonding with a ball bond at the pads and a wedge bond at the chip carrier. The silicon base (**fig. 3.2**) of the used substrate has been rendered conductive by p-doping and is secured to the base of the chip carrier by conductive glue to establish a backgate contact, prior to bonding.

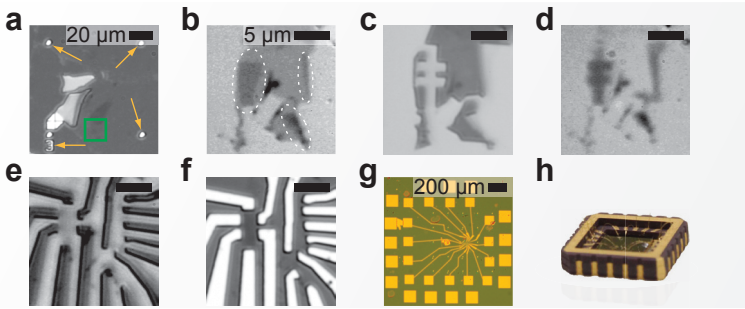


Figure 3.8 a: Optical picture of graphite (white) and graphene (dark, marked by green square). Cr/Au-markers have been applied in the vicinity, as indicated by yellow arrows. **b:** Magnification of area marked by green square in **a**. TBG are marked by white ellipses. **c:** Developed etching mask: light areas are covered by PMMA. **d:** Etching result: only structured TBG remains. **e:** Developed mask for definition of contacts via vapor deposition. **f:** Contacted samples: the gold leads appear white due to high reflectance. **g:** Larger area of the contacted sample: electrical contacts lead to large pads for bonding. **h:** From ref.[115]: Photograph of a bonded sample in a chip carrier.

Figure 3.8 illustrates the above processing steps in a real example. In practice, a first lithography step is needed for the application of a marker field (see fig. 3.8 a) to provide means of accurate alignment between SEM- and sample-coordinates for the subsequent steps of defining masks for etching (see fig. 3.8 c) and electrical contacts (see fig. 3.8 e). On average, three cycles of the e-beam lithography process are therefore needed to prepare a sample for electrical measurement.

As undesirable consequence of the described processing steps, residues of e-beam resist will inevitably stick to the sample surface even after the subsequent cleaning procedure in acetone, isopropanol and drying in nitrogen gas flow. PMMA contaminants act as dopant and reduce electronic mobility. Possible cleaning steps are annealing in inert atmosphere via external or Joule heating[116]. These methods may lead to sample damage however and have been shown to reduce the intrinsic electronic quality of graphene on SiO₂ by conforming the former to the inherent surface roughness of the latter[117]. A potent alternative lies in mechanical cleaning[118, 119], which is discussed as part of the following section on principals and application of the AFM.

3.3 Atomic Force Microscopy: Imaging and Mechanical Manipulation

A particularly important experimental tool for the thesis at hand is the **AFM**: On one hand it served for a variety of tasks in imaging, ranging from the recording of basic topography information and the probing of frictional behavior to the resolution of Moiré superstructures (sec. 4.2). On the other hand, the **AFM** was employed as a tool for micromechanical manipulation; the scanning probe may e.g. serve as microscale broom in brushing away residues of processing chemicals, thereby improving overall electronic quality of the investigated sample. A central lithographic task for the present work is furthermore the preparation of **TBG** via folding of single layer graphene as presented in sec. 4.1.

The present section starts with a short tract on the **AFM**'s essential components and basic working principles; it follows an overview of operation modes and parameters for the various imaging and lithographic tasks performed in the context of this work. Finally, overview and discussion are provided on a number of imaging artifacts and intricacies in **AFM** operation, specific to the work with flakes of two-dimensional crystals.

3.3.1 Working Principles

The **AFM** as a means to measure forces with aN-precision was initially presented in 1986 by Binnig et al.[120] as an extended application of the scanning tunneling microscope[121]. Binnig and Rohrer were awarded the Nobel price in physics for their design of the latter in the same year.

The AFM's working principle may be understood in terms of five basic components, as illustrated in [fig. 3.9](#): In proximity to a sample surface, a small probe (1) senses interaction forces which translate to deflection and change of effective resonance frequency in a supporting cantilever (2). Deflection or behavior under resonant excitation are read out by a detection system (3) and processed in a feedback loop (4), controlling a piezoelectric actuator (5). The latter adjusts probe-sample distance and enables lateral relative positioning, thereby allowing for a spatial scan of e.g. topographic features.

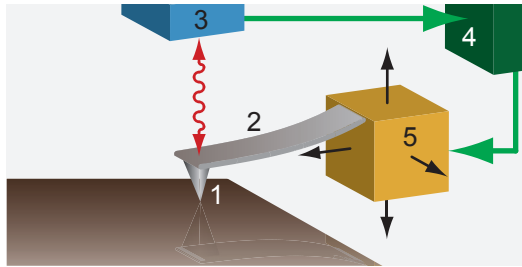


Figure 3.9 Schematic of the essential components of an AFM and their interrelation: The tip of a scanning probe (1) senses the force field at a sample surface (brown). Deformation of the cantilever (2) is probed (red arrow) by a detection system (3, blue box). Detected information is fed to a control unit (4, green box) driving the scanner (5, yellow box) which moves the scanning probe relative to the sample.

The AFM primarily used for the present work is of type MULTIMODE-2 (DIGITAL INSTRUMENTS), operated in combination with a NANOSCOPE IIIa controller. Furthermore, a DIMENSION V controlled by a NANOSCOPE V unit was employed for special tasks.

Focusing on their implementation in these AFM models, the five above introduced components are discussed in the following:

1.) Tip-sample interaction is of Lennard-Jones type, with short-range Pauli repulsion and long-range attractive vdW-forces. Furthermore, water capillary forces might significantly add to the attractive potential when imaging in ambient conditions[122]. Especially in the repulsive regime, lateral resolution is limited by the sharpness of the tip which determines the effective contact area. For the major part of imaging tasks, Si₃N₄-probes of type PNP-TR (NANOWORLD) with a tip radius of curvature $\lesssim 10$ nm were employed. At the cost of a larger radius (100 nm to 200 nm in DT-NCHR from NANOSENSORS), diamond coating renders a tip more wear-resistant, which was exploited for the lithographic task of scratching into graphene (p. 120).

2.) The cantilever beam supporting the tip is fixated at its rear and behaves as a spring bar approximately following Hooke's law within sensible degrees of deformation. Dependent on its effective mass the scanning probe is furthermore described by a characteristic resonance frequency.

For the above described imaging probes, the spring constant lies at $\kappa = 0.32 \text{ N m}^{-1}$. This value proves high enough to overcome the attractive force gradient at the sample surface thus preventing sticking of the tip in the given experimental conditions (namely SiO₂ and graphene in ambient conditions), while being preemptive to spring loads which could damage a graphene flake. The lithography probes have an average spring constant of $\kappa \sim 80 \text{ N m}^{-1}$ which enables exertion of larger tip-sample force.

Significant for different imaging modes (see p. 117) as well as the major scanning artifact of mechanical crosstalk (see p. 122), a cantilever may generally contort in three bending modes depending on the direction of force applied at the scanning probe's tip, which is illustrated in fig. 3.10.

Most important to the basic operation mode of probing sample topography, the cantilever will deflect up- or downwards in response to a respective normal force, as suggested in [fig. 3.10 b](#). Secondly and crucial to frictional measurements, lateral forces in the y -direction ([fig. 3.10 c](#)) lead to torsion of the cantilever around its long axis. Finally, as shown in panel d, lateral forces in the x -direction promote buckling which leads to a similar tilt at the cantilever's front as in the case of deflection (compare panel a).

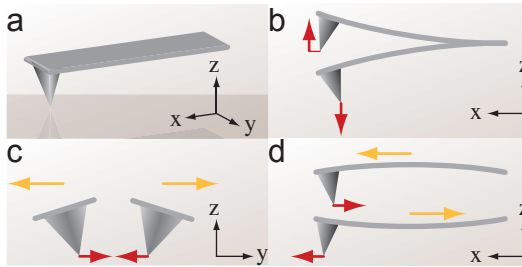


Figure 3.10 *Bending modes of a scanning probe. a:* 3D-view of a bar-shaped cantilever and tip. The coordinate system to the bottom provides a frame of reference for the rotated views in panels **b-d**. **b:** Side-view of the scanning probe; the cantilever deflects up- or downwards in response to a respective force acting on the tip (red arrows). **c:** Front-view of the scanning probe moving relative to the sample in direction of yellow arrows; frictional forces at the tip (red arrows) lead to torsion of the cantilever. **d:** Side-view of the scanning probe; the cantilever buckles up- or downwards in response to lateral forces (red arrows).

Where the above considerations focus on static deformation, surface forces also affect a cantilever's dynamic properties; the corresponding resonance frequency f_0 is effectively shifted in dependence

on the tip-sample force gradient[123]. Eigenfrequencies of here employed types lie at $f_0 = 67$ kHz and $f_0 \sim 400$ kHz respectively.

In summary, deformation of the cantilever in three bending modes as well as alteration of the effective resonance frequency may therefore serve as indicator for interaction forces between tip and sample.

3.) To access tip-sample interaction, the above described effects on the cantilever need to be detected. Initially, the detection system was implemented via an STM-tip hovering above the cantilever[120]; tunneling current between this tip and a conductive cantilever would be distance-dependent and thus sensitive to cantilever deflection.

In the majority of modern AFMs including the here employed models, an optical detection system is used: As illustrated in fig. 3.11, the reflection of a laser beam at the cantilever is read out in a photodetector consisting of four separate elements. Difference U_{vert} between the sum signals of upper (A,B) and lower (C,D) segments gives a measure for the slope of the cantilever front in x -direction and thus deflection and buckling, difference U_{lat} between the sum of left (A,C) and right (B,D) signals for torsion i.e. tilting in y -direction.

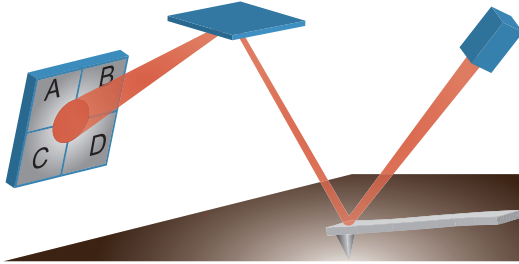


Figure 3.11 Schematic of the optical detection system in an AFM. A laser (right blue box) emits a beam onto the cantilever; the beam is reflected via a mirror (middle blue box) to a four-segment photodetector.

4.) Signals of the photodetector are fed into a control unit. Depending on the mode of operation, a static U_{vert} (corresponding to deflection and thus tip-sample force) or the root mean square of an alternating $U_{\text{vert}}(\mathbf{t})$ (depending on the match between excitation frequency and effective resonance frequency of the scanning probe) are used as feedback signal. If the latter deviates from a certain setpoint value, the scanner is instructed to adjust tip-sample distance (the sign of adjustment depends on mode of operation).

A parameter for immediacy and severity of these adjustments are the feedback gains: if chosen high, the AFM will operate at near constant tip-sample force; if set close to zero, topographic features will fully translate to deflection or change in oscillation amplitude at unchanged vertical extension of the scanner. Both modes have their area of application as discussed in the next subsection on AFM operation modes.

5.) Lastly, the scanner closes the loop of essential AFM-components: As described in point 4.), it adjusts tip-sample distance by vertical extension or contraction; furthermore it allows for point-by-point probing of a given area i.e. scanning of a sample by lateral tip-sample displacement. Sub-Ångström spatial resolution is achieved via exploitation of the converse piezoelectric effect: The most common technical realization lies in a tube-shaped piezo crystal with one electrode at the inside and four at the outside (see fig. 3.12 a). Symmetrical application of a voltage between inner and outer electrodes leads to unison contraction or expansion in the z -direction. Antisymmetric bias between inside and two opposite outside electrodes will bend the tube laterally (in x - or y -direction, depending on the choice of the outside electrode pair). The scanners employed for this work thereby achieve a vertical range of $\sim 6 \mu\text{m}$ and horizontal displacements around $100 \mu\text{m}$. On one hand, this relatively wide range is of advantage in locating graphene flakes on a more or less featureless substrate and imaging large samples.

Of disadvantage are a lessened resolution, piezo creep[124] and the high mass of the scanner which may lead to resonance phenomena at relatively low scanning frequencies (see p. 125).

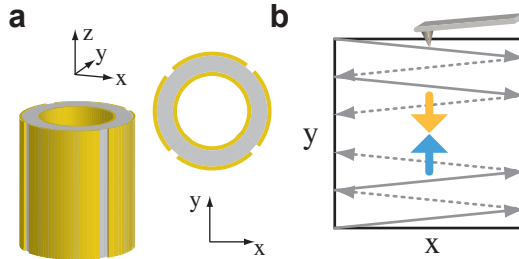


Figure 3.12 a: Side- and top-view schematic of a tube scanner with piezo crystal (gray) and four outer as well as one inner electrode (gold). **b:** Illustration of the scanning process with fast scanning in x -direction (solid gray arrows: trace; dashed: retrace) and slow scanning in y -direction (blue arrow: upscan, yellow: downscan).

The scan of a given area takes place point-by-point and line-by-line (fig. 3.12 b), which leads to an inherent time component. Especially for the understanding of topographic changes during a scan (sec. 4.1) it is therefore crucial to distinguish between up- and downscan. Furthermore, lines can be recorded in opposite directions. Distinction between so-called trace and retrace scans is of utmost importance because of a corresponding change of sign in torsional and buckling response (cf. fig. 3.10).

Finally, the angle between a line scan and the long axis of the cantilever may be chosen freely and is referred to as scanning angle in the following. Scanning under zero degree creates no significant frictional forces in y -direction, thereby minimizing cantilever torsion; a 90° scanning angle maximizes torsional response.

3.3.2 Operation Modes and Data Channels

A most significant distinction in AFM operation lies in the probing of either dynamic or static response: For the former, the scanning probe is excited near its eigenfrequency via a piezoelectric actuator; a relatively large tip-sample distance is maintained where the oscillating tip stays in the attractive (non-contact mode) or intermittent regime (intermittent-contact, also tapping mode) of tip-sample interaction. Changes to the oscillation amplitude are monitored. On the plus side, this mode of operation is maximally non-invasive; on the down side, it does not provide access to the full range of bending modes.

In contrast, scanning in contact mode monitors the static response of the scanning probe i.e. deformation in three bending modes. Stable imaging is achieved at repulsive tip-sample interaction; though unstable upon sharp topographic changes or mechanical vibration, imaging in the weakly attractive regime is also possible. All AFM images presented in the following have been recorded in this static mode to harvest the full range of cantilever response.

For different purposes, different data channels may be accessed. In contact mode, these are

- the vertical extension of the scanner, accurately following relative sample height at sufficiently high feedback gains,
- the vertical-difference signal U_{vert} of the photodetector as a measure for deflection and buckling, most pronounced at low feedback gains,
- the lateral-difference signal U_{lat} of the photodetector as a measure for torsion, approximately proportional to frictional interaction.

Figure 3.13 shows examples of the three channels, simultaneously recorded at intermediate feedback gains to balance channels one and two, and a scanning angle of 280° close to perpendicular, to achieve sufficient signal in the torsional channel three. Evidently, each of the channels highlights certain aspects of the sample: Where channel one (fig. 3.13 a) distinguishes the whole range of height from substrate over graphene to contacts, channel two especially brings out topographic change e.g. at sample edges (fig. 3.13 b). Channel three is mostly sensitive to frictional surface properties and thus distinguishes material rather than topographic features (fig. 3.13 c).

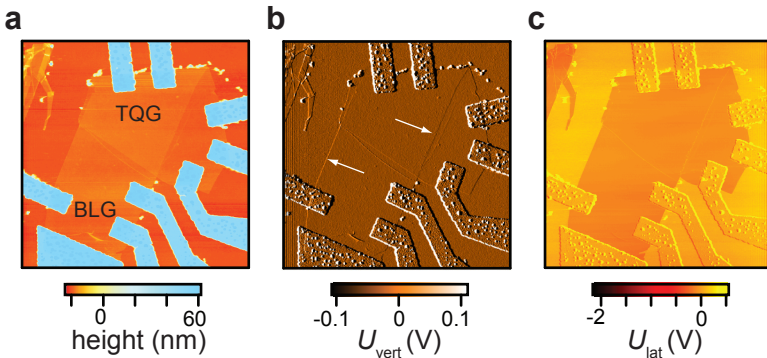


Figure 3.13 Electrically contacted (gold leads) bilayer graphene (BLG) with a fold (“twisted quattrolayer”). At intermediate feedback gains and a scanning angle of 280° an AFM-scan is performed under simultaneous acquisition of three data channels: **a**: Relative vertical extension of the scanner, corresponding to a height profile. **b**: Signal of the photodetector U_{vert} as a measure for deflection and buckling of the cantilever. Sharp sample edges are marked by white arrows. **c**: Signal of the photodetector U_{lat} as a measure for torsion and thus frictional interaction with the surface.

Besides imaging, the AFM may also serve as a tool for lithography. In this, three degrees of invasiveness may be discerned:

The lowest degree preserves the integrity of the graphene lattice. Scanning with a probe of low spring constant (order of magnitude 10^{-1} N m^{-1}) at attractive or repulsive tip-sample forces in the 1-10 nN range[119] has been shown to effectively clean a graphene sample from processing residues and improve its electronic quality in lowering doping and increasing charge carrier mobility[118, 119]. Exertion of higher contact force in the repulsive regime ($\sim 180 \text{ nN}$) is found to limit the gain in carrier mobility by adhering graphene to the roughness of a SiO_2 substrate, measurably evident in higher root mean square values in the topography of a cleaned sample[118]. Figure 3.14 illustrates the effectiveness of micromechanical cleaning

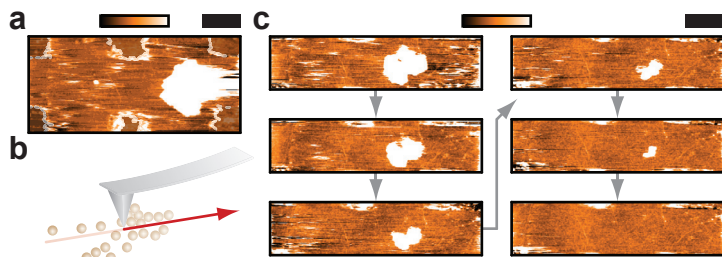


Figure 3.14 Mechanical cleaning of a graphene sample. **a:** Hall bar shape, structured into a TBG sample. A large bulb of PMMA sticks to the sample surface. Color scale spans 10 nm from left to right, the scale bar indicates 1 μm . **b:** Schematic of a scanning probe, brushing away residues. **c:** Cutouts of the hall bar in **a**; every second out of a subsequent series of scans is shown in the order indicated by gray arrows. Time between two subpanels is $\sim 171 \text{ s}$. The color scale to the top spans 5 nm, the scale bar 1 μm .

on the example of a Hall bar structured into a TBG sample via the processing steps introduced in sec. 3.2. The micron-sized bulb of PMMA is brushed away on a time scale of minutes in a continuous scan of the affected sample area in contact mode at ~ 10 nN of repulsive tip-sample interaction.

A second degree of invasiveness has been demonstrated in ref.[125]: Scratching movements of a diamond coated lithography tip (as introduced on p. 112) at several micronewton of spring load left no resolvable topographic marks but led to p-doping in the assaulted area of a monolayer graphene sample. This speaks for the creation of vacancies at the atomic level while preserving the sample's integrity on the microscale.

Finally, invasive topographic alterations can be induced in a graphene sample e.g. in the form of cuts. By repeated tracing (some ten repetitions) along a programmed path at applied forces in the micronewton range (depending on the sharpness of the tip), graphene may be mechanically structured in a controlled way as shown in fig. 3.15 b.

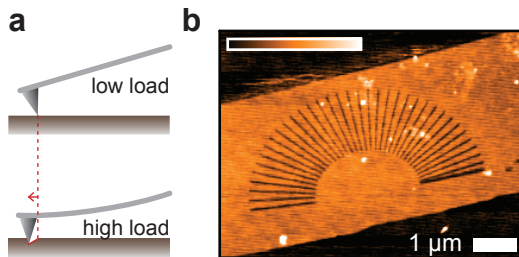


Figure 3.15 a: Schematic of the shift in tip position upon higher spring load in the cantilever. **b:** From the author's bachelor thesis preceding this work: Ray-pattern mechanically scribed into a graphene bilayer via AFM tip. Color scale spans 3.5 nm.

To achieve high accuracy, an offset in the tip position upon higher spring load (see [fig. 3.15 a](#)) has to be accounted for in prior calibration. Note that alternative to the scratching in close contact as applied in this work, lithography has also been successfully implemented in tapping mode[126], yielding similar results.

3.3.3 Imaging Artifacts

The requirement for accurate measurements of TBG interlayer distance as well as the lateral resolution of superlattice structures in the context of this work constitute challenging tasks in AFM operation.

While vertical resolution in the sub-Ångström range is technically given by the scanner and detection system, mechanical crosstalk between the different bending modes (p. 113) gives rise to systematically inaccurate topography measurements in contact mode, potentially to the point of apparent height inversion. Also in tapping mode, step height measurements between different materials are inherently erroneous due to inhomogeneous attractive potentials on different surfaces[127]. As the described artifacts may reach nanometer scale the signal-to-error ratio potentially reaches unacceptable levels for thickness measurements on the atomic scale.

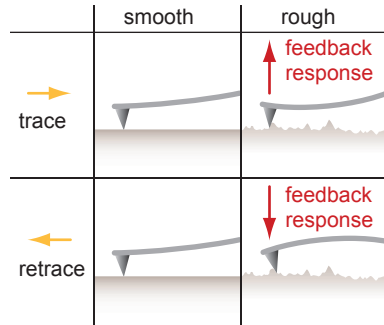
For lateral resolution, high scanning speeds are favorable due to lower impact of thermal noise and drift via reduction of capture timescales. Here, the large mass of the available scanners posed a problem because of their correspondingly low resonance frequencies, leading to artificial features on the lateral scale of interest for Moiré pattern resolution.

The following section provides illustrative examples and remedy for the above described artifacts of mechanical crosstalk and lateral piezo oscillation.

Mechanical Crosstalk

As illustrated in [fig. 3.16](#), scanning in trace or retrace direction leads to different buckling response of the cantilever dependent on the frictional properties of the probed surface. The optical detection system does not differentiate between deflection and buckling as mechanism behind the tilt of the cantilever front however; a rough surface will therefore cause the feedback system to increase probe-sample distance in trace direction, leading to an apparent raise of the topographic plane, while the opposite is the case in retrace direction.

Figure 3.16 Schematic of a scanning probe in reaction to low (left) and high (right) frictional forces. Top and bottom panels illustrate trace and retrace direction respectively. Opposite reaction of the feedback system to the respective buckling response is indicated by red arrows.



Measurements of step height between materials with equal frictional tip-sample interaction are not affected by the described crosstalk effect, as the artificial offset in height applies homogeneously. In the here investigated situation however, graphene is scanned at significantly lower frictional response than SiO_2 [128]. Furthermore, even between graphene samples of different layer number[129, 130] and stacking configuration ([sec. 4.2.4](#)), AFM-measured friction is found to vary.

The severity of the associated error should relate linearly to the frictional tip-sample forces, which are in turn proportional to the normal force. Furthermore, nanoscale stick-slip friction increases

with the logarithm of sliding velocity[128]. Most pronounced buckling response to a given frictional force can moreover be expected for cantilevers of low spring constant.

Figure 3.17 shows topography scans of monolayer graphene on a SiO_2 -substrate. In demonstration of the potentially significant effects of mechanical crosstalk, scanning parameters have been chosen to amplify the effect: A cantilever of low spring constant (0.08 N m^{-1}) is scanned at a relatively high velocity of $100 \mu\text{m s}^{-1}$, while spring load (difference between normal force and an unknown attractive force) is varied. Scanning angle is set to 0° .

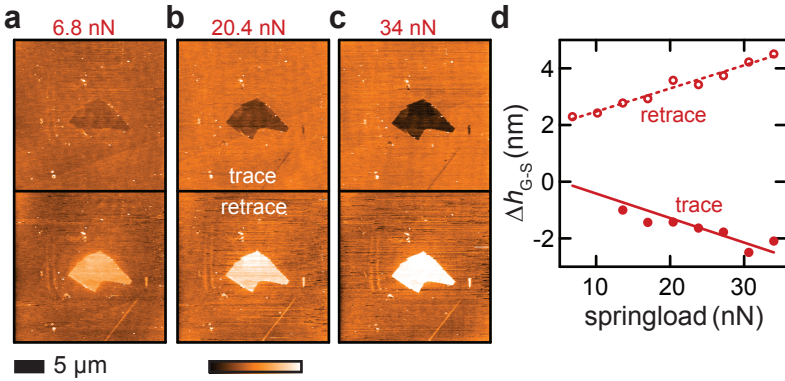


Figure 3.17 Spring-load dependent crosstalk in the height signal of a contact mode AFM scan on monolayer graphene lying on a substrate of SiO_2 . **a-c:** Trace (top) and retrace (bottom) height profiles at cantilever spring loads of 6.8 nN, 20.4 nN and 34 nN respectively. Color scale bar spans 7 nm. **d:** Dots: Extracted height difference Δh_{G-S} between graphene and substrate plane for different spring loads. Lines are linear fits to the data.

At low spring load, the trace scan yields near zero step heights below the range of fluctuation within the graphene sample; higher spring loads lead to a decrease in apparent height difference Δh_{G-S} between graphene and substrate, reaching nanometers into the negative. Retrace topography on the other hand shows an increase in Δh_{G-S} .

These findings are qualitatively understood in terms of the model illustrated in [fig. 3.16](#), where graphene is assumed to provoke near zero buckling response (left) while sliding over rough SiO_2 leads to high cantilever contortion (right).

Quantitatively, the crossing point between linear fits to the data may be viewed as good estimate of the real height and measure for the attractive tip-surface force: At $\Delta h_{G-S} \approx 1$ nm and a spring load of -6.8 nN, the pulling force (negative load) of the scanning probe will compensate attractive tip-surface force, thereby neutralizing normal force as well as frictional buckling response and the related artifact in turn. Note that the value of 1 nm, far exceeding the thickness of a monolayer as expected from graphite's interlayer spacing, is explained by an adlayer of water between sample and substrate and conforms to recent findings in [ref.\[131\]](#).

Besides the above demonstrated method of extracting the real step height via extrapolation of the artifact's effect to a cause of zero, a number of more or less complicated calibration procedures[\[132–134\]](#) and corrections to the feedback loop[\[134\]](#) have been proposed. More recently, the PEAKFORCE technique (BRUKER) which combines tapping and contact mode principles has been found to produce results of high accuracy[\[131\]](#).

A seemingly easy remedy lies in choosing a scanning angle of 90° , which would minimize buckling and give rise to torsion as frictional response. However, slight misalignment of the photodetector usually undermines perfect decoupling of lateral and vertical signals, enabling crosstalk even between torsional and deflection mode[\[135\]](#).

In this work, a reduction to $\lesssim 10$ pm between trace and retrace scans of step heights between graphene layers is achieved by the choice of appropriate scanning parameters:

- A cantilever of intermediate spring constant (0.32 N m^{-1}) is employed.
- If possible, the scanning angle is set to 90° .
- Scanning speed is limited to $2 \mu\text{m s}^{-1}$.
- The contact force is minimized by scanning in the low attractive regime of tip-sample interaction.

In summary, it is highly advisable to always monitor trace and retrace direction at the same time and heed the above optimizations to the scanning parameters and measurement setup.

Piezo Oscillations

In contrast to the vertical, high lateral resolution is needed for measurements of Moiré pattern dimension which holds valuable information about interlayer twist in TBG (sec. 2.1.2). To reduce the blurring of features due to thermal noise and drift, impeding the targeted nanometer resolution, high scanning speeds are necessary.

At about 5 Hz of scanning frequency however, line features appear perpendicular to the fast scanning direction as demonstrated in fig. 3.18. Most pronounced at the beginning (left for trace, right for retrace) oscillations subside in the course of each line scan at moderate scanning frequencies until they completely dominate the obtained image at frequencies above 20 Hz. Occurrence is time- rather than space-dependent as demonstrated in fig. 3.18 which rules out any relation to topographic features; frequencies lie around 1000 Hz.

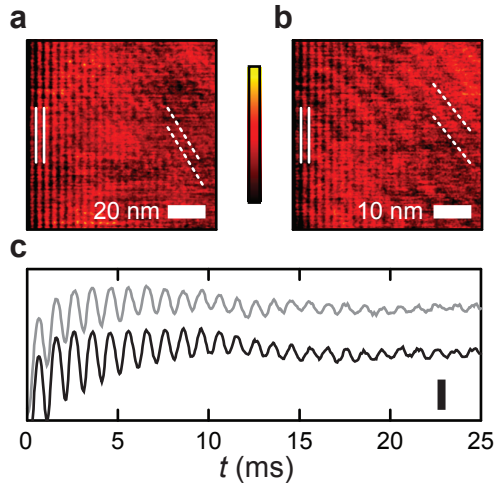


Figure 3.18 a: 100 nm cut-out from a 200 nm map of the torsional signal acquired on a small-angle TBG at 10 Hz. Indicated by dashed white lines are rudimentary features of a Moiré pattern. Solid lines mark piezo oscillations. **b:** Same signal, same sample and frequency as in **a** at half the respective area (50 nm cut-out from a 100 nm scan). Vertical lines to the left have the same spacing as in **a**, revealing their time-dependent nature; diagonal features of the Moiré pattern scale inversely with scanning area, confirming them as rooted in space. **c:** Oscillations marked by solid lines in panels **a** (black) and **b** (gray), plotted on a time-axis. Features from both scans share a frequency of ~ 1000 Hz.

Ref.[136] finds similar lateral resonance in the spectrum of a piezo tube scanner. High excitation frequencies are provided within the broad spectrum associated with the triangular driving signal even though the scanning repetition rate lies orders of magnitude lower.

With the employed scanner (type 5657jv), a scan rate of 10 Hz is found to constitute an optimal compromise between reduction of thermal blurring and lateral piezo oscillation: Firstly, sufficient time passes for the artifacts to have mostly subsided in the second half of each line scan (cut out for the examples in [fig. 3.18](#)). Secondly, the resonance frequency of the scanner is not yet as pronounced in the spectrum of the scanner's driving signal. Heeding this, it is possible to achieve adequate superlattice resolution on the nanometer scale even with a large scanner, capable of $\sim 100 \mu\text{m}$ lateral range, as demonstrated in [sec. 4.2.1](#).

3.4 Magnetotransport: Cryogenic Setup and Measuring System

To resolve the intricate dispersion and topology of TBG's band structure in transport experiments, two major parameters want consideration: Most importantly, the sample temperature has to be controlled. Low temperatures are needed to preclude smearing-out of electronic features. On the other hand, measurements over a wide temperature range are e.g. desirable for the characterization of energy gaps[61]. Secondly, a perpendicular magnetic field enables determination of charge carrier concentration via the Hall effect. Furthermore, the density of states will quantize, forming a gapped energy spectrum (sec.2.3) which may be resolved at high flux density, low temperature and appropriate sample quality, thereby disclosing information about degeneracy, effective mass and Berry phase in the probed sample.

To meet the above requirements a cryogenic setup with a superconducting magnet is employed. Important working principles are summarized in the following: In its essence the used ^4He bath cryostat (OXFORD INSTRUMENTS) is a thermally isolated container filled with liquid helium. The latter serves two purposes, firstly enabling superconductivity in a coil to the cryostat's bottom (fig.3.19), thereby maintaining low power consumption even at high magnetic fields (up to 15 T). Secondly, the helium bath will cool an immersed sample to the liquid helium temperature of 4.2 K.

By installing an inner vacuum chamber (IVC) with a controlled inflow of ^4He through a needle valve, and a pump controlling the pressure, the temperature may be further lowered down to ~ 1.5 K (at ~ 5 mbar). For higher temperatures of 10 K to 300 K, a heater stabilizes the IVC temperature with the help of an automated control unit (ITC 503, OXF. INSTR.). In this, a finite ^4He -pressure should be maintained for sufficient thermal coupling to the sample.

3.4 Magnetotransport: Cryogenic Setup and Measuring System

To guide the sample into the IVC, the chip carrier is fit to the end of a specially designed pole with attached wires to establish electrical connection to measurement apparatus outside the cryostat (yellow line, [fig. 3.19](#)).

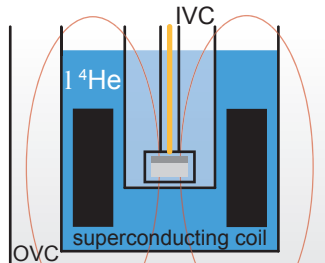


Figure 3.19 Schematic side view of a bath cryostat. A superconducting coil (black rectangles) lies in liquid helium (dark blue). Magnetic field lines (red) flow perpendicular to the sample plane at the bottom of the inner vacuum chamber (IVC), where low ^4He pressure is pumped (illustrated in light blue). Electrical wires (yellow) are led from the chip carrier up a sample pole. The cryostat is isolated by an outer vacuum chamber (OVC).

The requirements for transport measurements presented in this work are comparatively simple: Two out of four input parameters, namely sample temperature and perpendicular magnetic field are introduced above. Furthermore, a voltage U_{BG} between backgate and sample is applied to vary charge carrier concentration. The voltage drop between two given contacts is then measured at a constant source current I_{SD} . A schematic diagram of the measurement setup is given in [fig. 3.20](#).

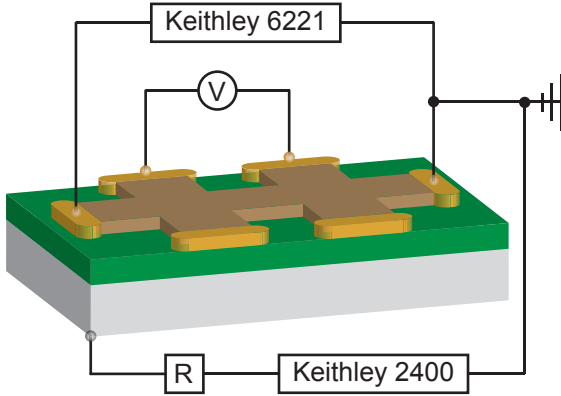


Figure 3.20 Schematic of a sample in Hall bar geometry, lying on a substrate of SiO_2 (dark gray) and Si^+ (light gray). The sample is grounded at the rightmost contact relative to which a voltage is applied to the Si^+ -backgate, using a KEITHLEY 2400 sourcemeter; a series resistor R secures the sample against high backgate current. Via a KEITHLEY 6221, a current is driven between left- and right-most contact. Between the inner contacts voltage drop is measured.

In all here presented electrical measurements, a KEITHLEY 2400 sourcemeter was used for application of the backgate voltage U_{BG} . To limit the charge current of the Si^+ - SiO_2 -graphene capacitor and prevent damaging energy dissipation in case of a dielectric breakdown, a series resistor of $10\text{ M}\Omega$ is integrated additionally to a compliance in the KEITHLEY.

Current is sourced through the sample via a KEITHLEY 6221 which stands out by a high output impedance of $10^{14}\ \Omega$, enabling stable measurements even at high sample resistance.

3.4 Magnetotransport: Cryogenic Setup and Measuring System

Depending on whether measurements are performed under **direct current (DC)** or **alternating current (AC)**, the voltage drop between contacts of interest is detected via KEITHLEY 2000 multi-meter or lock-in amplifier (EG&G 5209, 5210 and 7260) connected to the current source via trigger link.

In general, data were recorded in maps of magnetic field B and backgate voltage U_{BG} for a given temperature T , where B is stepped, U_{BG} is swept and T is set before a given measurement as illustrated in fig. 3.21. Quantitative dependencies on one of these parameters are derived from according cross sections through the recorded maps.

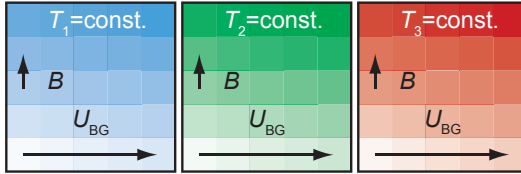


Figure 3.21 Illustration of the temporal order, measurement parameters are varied under. A backgate sweep is performed on a timescale of minutes, followed by a step in magnetic field strength, amounting to multiple hours for a high-resolution map over the full parameter range. If desired, the protocol is repeated for different temperatures T .

Proportional conversion between backgate voltage U_{BG} and charge carrier concentration n is given in the factor $C^* = 6.53 \times 10^{14} \text{ V}^{-1} \text{ m}^{-2}$, which derives from the thickness $d_{\text{SiO}_2} = 330 \text{ nm}$ and dielectric constant $\epsilon_{\text{SiO}_2} = 3.9$ of the oxide layer in the employed substrate following a parallel-plate-capacitor model.

3.5 Summary

In summary of this chapter, mechanical exfoliation of graphene flakes from natural graphite via a strip of adhesive tape was introduced in [sec. 3.1](#). Possible influence of ambient humidity on the exfoliation yield was discussed with regard to graphene's hydrophobic nature.

Optical detectability of graphene on a substrate of SiO_2 grown into a base of Si was demonstrated and theoretically described for the employed oxide thickness. The presented principals were shown to enable identification of layer number and optimized visualization of a given sample.

In [sec. 3.2](#), the processing of a graphene flake into an electrically contacted sample in subsequent steps of e-beam lithography followed by oxygen plasma etching and evaporation of Cr/Au was described.

Section [3.3](#) introduced the working principals of the AFM and established basic terms for the description of important scanning parameters. Application to imaging in different data channels as well as mechanical manipulation ranging from cleaning to cutting of graphene were presented. Finally, the artifact of mechanical crosstalk was traced to its root in a variety of parameters to be tuned for its minimization; the artifact of lateral piezo oscillation was demonstrated and assessed in its impact on the resolution of Moiré pattern in [TBG](#).

In [sec. 3.4](#), the ^4He bath cryostat employed for magnetotransport measurements at temperatures from 1.5 K to 300 K was introduced. Apparatus and protocol for resistance measurements presented in [chap. 5](#) were described.

4 Structural Studies on Twisted Bilayer Graphene

Where [sec. 2.1](#) introduces [TBG](#) structure with respect to lattice geometry on the atomic level and from a mostly theoretical standpoint, the present chapter takes a look at [TBG](#) morphology on the lateral nano- to microscale and is based on experimental study.

Section [4.1](#) starts with a brief review on different approaches to [TBG](#) preparation. The three methods of mechanical transfer, growth from SiC and [CVD](#) are compared with respect to achievable twist angles and lateral dimension. The fourth method, lying in the folding of graphene monolayers, constitutes the source of [TBG](#) examined in this work. On the basis of a broad number of prepared samples, the folding process is examined: mechanical initiation via [AFM](#) is demonstrated; hints towards the underlying dynamic mechanism are evaluated.

In [sec. 4.2](#), folded [TBG](#) are investigated with respect to their most characteristic properties of interlayer twist and interlayer distance. Brought into relation with these, the length of the folded edge ℓ is demonstrated to hold information about interlayer interaction energy and is furthermore found to influence the bending radius in analogy to phenomena in carbon nanotubes. Finally, [AFM](#)-measured friction on the [TBG](#) surface is discussed as a measure for interlayer interaction.

4.1 Preparation of Twisted Graphene Bilayers

To date, there are four established methods of TBG preparation.

The first lies in mechanical transfer, often in conjunction with encapsulation in layers of hBN: Starting with exfoliation to a polymer which would then be upended and aligned over a substrate to position an attached flake onto a substrate-bound bottom layer [67], the method soon evolved to the cleaner dry-pickup, utilizing superior vdW-interaction between two flakes to collect subsequent layers from a substrate via a "stamp"[137]. In principal, the twist angle between two stacked graphene layers can be tuned to an arbitrary value. Relying on straight sample edges (see sec. 4.2.1), accuracy is limited to $\sim 1^\circ$; a novel technique, sectioning and selectively detaching a single flake to transfer it back onto the sample area left on the substrate has been demonstrated to substantially improve accuracy however[138].

Secondly, graphene bilayers may be grown out of SiC. Due to geometrical interplay with the mother material's surface, growth from the Si-face of SiC will give rise to AB-stacking configuration[139], while growth from the C-face preferentially yields TBG of twist angles $\theta = \pm 2.2^\circ$ and $\theta = 30^\circ \pm 2.2^\circ$ [84, 92]. TBG areas reach several microns in lateral dimension but are often limited in electronic quality due to the formation of wrinkles and bubbles upon cooling down after growth.

A third and widely used method is based on CVD growth on transition metal substrates like copper:

Under appropriate nucleation conditions, layers may be subsequently grown onto each other, yielding *AB*-stacked as well as twisted bilayers in the early stages of the process[24]. Typical **TBG** areas measure $1\ \mu\text{m}$ to $10\ \mu\text{m}$ [24, 140]. Distribution of rotational mismatch shows maxima at low and high angles, as illustrated in fig. 4.1.

Though a root cause of this often found distribution is likely to be linked to energetically favorable stacking configurations, a detailed understanding of the preferred arrangement under certain interlayer twist has yet to be developed.

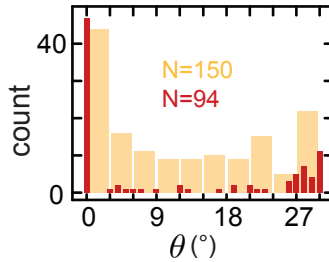


Figure 4.1 Histogram of occurrence in twist angle for **TBG** grown by **CVD**. Data stem from ref.[140] (yellow, low pressure **CVD**) and ref.[24] (red, ambient pressure **CVD**) respectively. The leftmost red bar indicates bilayers in Bernal-stacking.

Lastly, **TBG** can be produced by the folding of monolayer graphene. This is the method of choice for twisted bilayer preparation in the context of this work and will be discussed in the remainder of the present section.

To begin with, folded graphene can occur as byproduct of mechanical exfoliation and is randomly found amongst other flakes. This has early been observed and exploited for a proof of layer number in AFM measurements of the associated step heights[1]. Magnetotransport measurements on contacted flipped-over areas yield quality data indicating high crystalline order in the folded samples (see sec. 5.2).

The attempt to understand and gain control over the folding process brought forth a number of different techniques: Ref.[141] investigated the effects of an additional exfoliation step, peeling away top layers of graphene and graphite already attached to a substrate. Ultrasonic excitation in liquid suspension[142] and flushing flakes on a substrate with water[143] have been shown to yield folded areas in the high nanometer and low micrometer range respectively.

Finally, manipulation via AFM tip has been utilized to create folded regions by scanning at moderately elevated force[144, 145] or selectively invasive nanoindentation[17, 146].

For this work, TBG is prepared via exfoliation as well as two approaches in AFM-manipulation. Figure 4.2 shows examples from exfoliation (panel a), scanning with a hard lithography probe at spring loads around 100 nN (panel b) and cutting into the graphene flake at several micronewton (see diagonal trench in panel c). Results from the two AFM-methods differ in the way that folds originate from native sample edges in the first, and from newly created roughened surfaces in the second case.

In general, folding probability and yield are lowest in random exfoliation and highest in the more invasive AFM approach. In the following, folding results are examined, compared and classified.

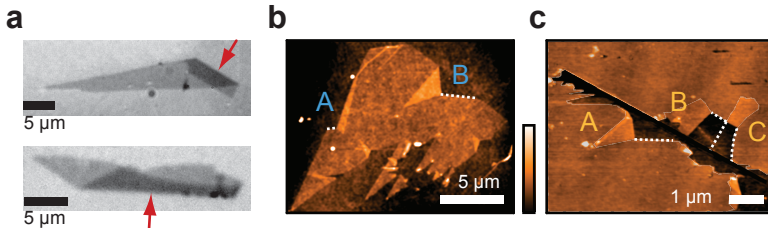


Figure 4.2 a: Optical pictures of graphene monolayers folded over in the areas indicated by red arrows. Folds are a byproduct of exfoliation. **b:** AFM topography of a monolayer graphene flake with multiple folds along the edges. Folding occurred during scanning in hard contact. **c:** AFM topography of a monolayer graphene flake. A diagonal cut has been applied at high contact force; several folds spread from the newly created edges. Color scalebar spans 2 nm and 5 nm for **b** and **c** respectively.

In principal, TBG areas of several micrometers are achievable via all three approaches. Proportionally however, large numbers of small folds below 1.5 μm are created, especially by the invasive AFM method as evident from the histograms in fig. 4.3 a.

A noteworthy distinction between folding sources lies in the produced geometry: Exfoliation flips a flake over as a whole in most cases, causing no rips and tears (both folds in fig. 4.2 a). The majority of TBG created upon scanning are of triangular shape with one edge folded, one edge from the flake's native surface and one edge torn out of the bulk (folds A and B in fig. 4.2 b). Folds originating from a cut trench usually take on a trapeze shape with two rips tapering in distance towards the folded edge (fold C, fig. 4.2 c).

Figure 4.3 b summarizes the described behavior in histograms over the number of tears leading to a fold. In rare cases like the one of fold B, fig. 4.2 c, trapeze shape is taken at a single rip, where the opposite side runs parallel to a sample edge, which is registered under 1* in fig. 4.3 b.

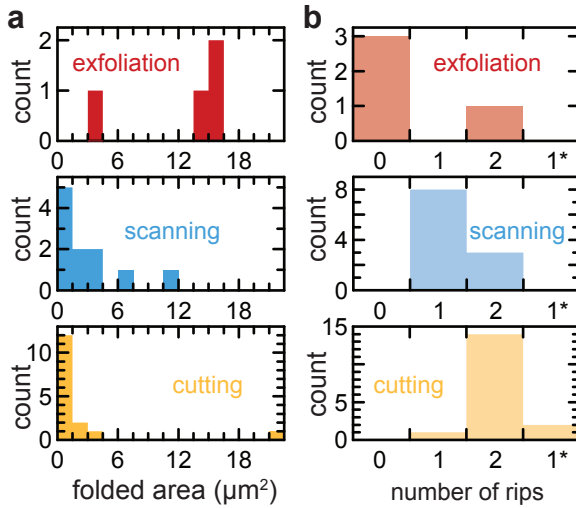


Figure 4.3 a: Histogram of occurrence in folded area for the TBG sources of exfoliation (top, red), AFM-scanning (blue, middle) and AFM-indentation (yellow, bottom). **b:** Histogram of occurrence in the number of rips contributing to a single fold upon exfoliation (top, red), AFM-scanning (blue, middle) and AFM-indentation (yellow, bottom).

For the dynamic process behind the creation of a fold, two scenarios may be envisioned: Firstly, the area to be folded may keep a straight planar shape and flip over rigidly as depicted in fig. 4.4 a.

Secondly, the TBG area may grow in-plane by sliding forward, continuously fed by a rolling motion at the folded edge (fig. 4.4 b).

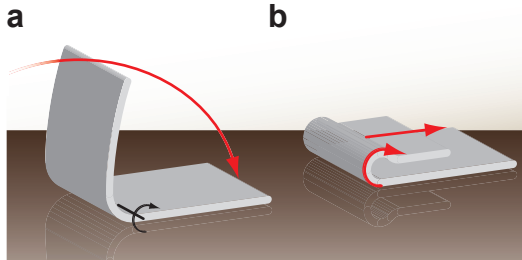


Figure 4.4 Scenarios for the dynamics of a folding process in graphene (gray) on a substrate (brown). **a:** An area of the flake rigidly flips over around a defined axis (marked in black). **b:** The fold grows (straight arrow) coming from a forwards rolling edge (curved arrow).

While the first process should be instantaneous as an unsupported graphene flap in transit will be highly unstable, the second folding process may take place on a finite time scale, depending on a possible driving force (e.g. an AFM-tip) or intrinsic growth dynamics[17]. In the majority of cases, AFM scans do not reveal any time-dependent evolution in fold geometry or size. Due to the inherently limited temporal resolution of AFM scans however, dynamic behavior on time-scales shorter than minutes can not be expected to show in subsequently recorded frames. Distinction between spontaneous or gradual folding processes thus proves difficult.

In spite of the discussed limitations, evolving shapes of freshly created folds could be observed in two instances:

Figure 4.5 e shows an upscan in trace direction, recorded immediately after scribing a trench (dark diagonal line) into a graphene monolayer sample:

An elevated **TBG** area is clearly resolved between the blue and yellow dashed lines; a trapeze-shaped area of bare substrate, as indicated by the blue arrow, suggests folding of the **TBG** out of the according **MLG** vacancy.

Figure 4.5 f depicts the final shape of folded configuration as subsequently recorded with a soft imaging probe (Note that an additional fold, as indicated by the red arrow, is not of primary interest in the current discussion).

A number of correlations in the described scan of panel e suggest the capture of a dynamic, rather than static scenario:

Firstly, the folded area as recorded extends much further than the vacancy it supposedly originates from.

Secondly, the recorded width of the fold stays constant over a long range, where the shape of the final fold as shown in panel f is clearly tapered.

Thirdly, a jump in topography occurs at the height of the white arrow.

Based on these considerations, the scan therefore likely captures the fold as it slides and extends upwards at roughly the velocity of the upscan (39.1 nm s^{-1}):

The upper panels of [fig. 4.5](#) accordingly provide schematic reconstructions of the folding progress based on the scan lines captured locally at selected times, as indicated along the arrow to the left of panel e. The sudden change of growth direction between panels c and d (at the height of the white arrow in panel e) may herein be caused by the fast line-scan motion ($20.1 \text{ } \mu\text{m s}^{-1}$) of the hard **AFM** lithography probe.

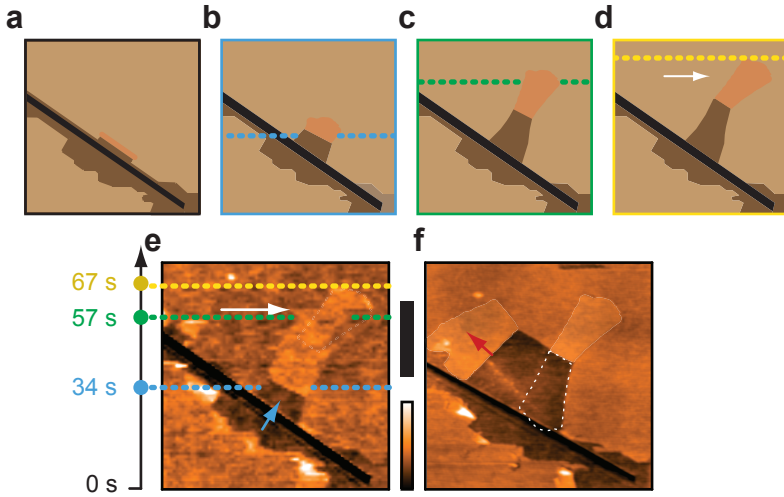


Figure 4.5 *Upper panels:* Suggested temporal evolution of the fold recorded in the lower panels, starting at a narrow flipped-over seed in **a**. **b**: From the vacancy recorded around the position of the blue line in **e**, the folded shape at the corresponding time is reconstructed. **c**: Same as in **b**, based on width and shape of the TBG area around the green line in **e**. **d**: Shape of the final folded configuration (around yellow line in **e**). **Lower panels:** AFM topography of folded graphene. Scale bar indicates $1\ \mu\text{m}$, colorscale spans $3\ \text{nm}$ and $7.5\ \text{nm}$ for left and right panel respectively. **e**: Up-scan in trace direction with a hard lithography probe immediately after application of the diagonal cut, recording the formation of a fold in monolayer graphene. Colored dots along the arrow to the left mark the time since the start of the scan. White arrow marks disruption in topography. **f**: Final folded configuration recorded with a soft imaging probe. (Of secondary interest, the fold indicated by the red arrow has evolved in the meantime.)

A second example is shown in [fig. 4.6](#): Panel c is recorded with a hard lithography probe as upscan (18.75 nm s^{-1}) in trace direction ($19.2 \text{ } \mu\text{m s}^{-1}$) and shows a triangular fold in evolution, where panel d shows the subsequent downscan revealing the final static TBG.

Below the lower dashed white line, [fig. 4.6 c](#) does not reveal any sign of a fold; the contour of the TBG to evolve in further course of the scan is marked in transparent white lines.

Above the upper dashed line, the recorded folding geometry is identical to the final, static one, as depicted in panel d.

These two observations coercively indicate formation of the folded TBG area in a time frame of roughly 30 s, as elapsing between dashed white lines (see time tags at the white dots in [fig. 4.6 c](#)).

The topographic features resolved in the respective local and temporal window furthermore allow for reconstruction of the likely scenario of growth: Two alternative sequences of suggested intermediate configurations are compared in the upper panels of [fig. 4.6](#):

Panel a interpolates three intermediate geometries under assumption of a constant direction in the folded edge. The observed resolution of the torn edge (indicated by the yellow arrow in panel c) is herein accounted for if progress of the upscan is assumed just below the fold (yellow dots, panel a) at any time; the fold itself however would overlap the area in between dashed white lines. As no accordingly elevated features are resolved below the torn edge in panel c, the scenario depicted in panel a provides no satisfactory match to the according scan.

Panel b suggests a counter-clockwise rotation in the direction of the folded edge instead. Here, the folded TBG area would stay above and beyond a given linescan at its lower right corner (yellow dots). In this scenario, the absence of elevated topography below the torn edge is accounted for. Note furthermore that the proposed rotation is associated to different growth velocities along the native sample edge to the top and the torn edge to the bottom (as marked at the

two arrows): Slower progression along the latter is highly sensible, as tearing energy has to be afforded in contrast to the former.

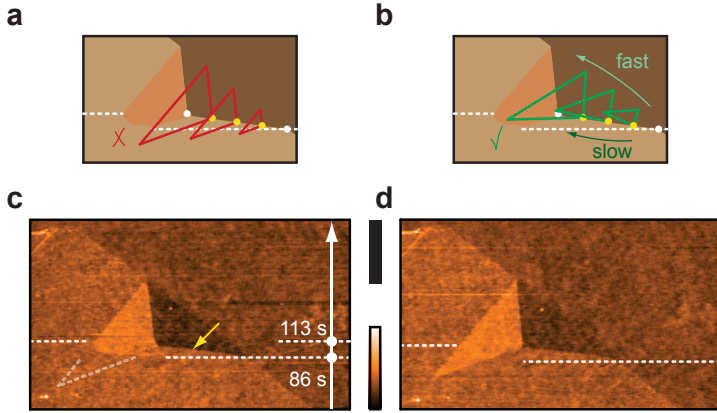


Figure 4.6 Upper panels: Schematic of intermediate folded configurations in the time frame between white dots in **c**. Investigated are two different scenarios of growth: **a**: The angle of the folded edge stays constant; portions of the folded area protrude across the area between dashed white lines and should have been resolved in the topography scan shown in **c**. **b**: The direction of the folded edge rotates counter-clockwise; the area between torn edge and lower dashed white line stays clear. **Lower panels:** AFM topography of folded MLG; scale bar indicates 2 μm, colorscale spans 4.5 nm. **a**: Upscan in trace direction: above the upper dashed white line, main topographic features are identical to the ones in **d**. In between dashed lines, geometry of the torn vacancy to the right appears identical, while the folded area to the left is in evolution. The contour of the final TBG configuration is indicated in transparent white. **b**: Subsequent downscan of the final folded configuration.

As a side note, the vacancy left by the fold in [fig. 4.6 c](#) apparently lies in a lower plane than the surrounding substrate. By panel d, areas are largely planished. Similar "ghosts" of a folded flake are often observed and likely connected to ambient (aqueous) adlayers on the uncovered substrate, where scanning in hard contact will push aside much of the water between graphene and substrate[131].

In summary of the presented examples, dynamic evolution in the configuration of folded areas in graphene is observed upon invasive nanoindentation ([fig. 4.5](#)) as well as scanning in hard contact ([fig. 4.6](#)). Detected growth velocities exceed $\sim 10 \text{ nm s}^{-1}$ and define a narrow time-window below common AFM capture duration. It is therefore highly possible that similar growth processes led to the formation of other TBG produced by AFM-manipulation without being detected, as scanning direction and speed will not match the progression of a newly created fold in most cases. As a working hypothesis, the principals of dynamic growth as deduced from [fig. 4.5](#) and [fig. 4.6](#) are therefore extrapolated to all AFM-induced folds based on their similar shapes and size as well as the above considerations.

Following the hereby established identification of the sliding-scenario from [fig. 4.4 b](#) (opposed to the flipping-scenario) as dynamic mechanism behind folding initiated via AFM, the next question to be answered concerns the driving force behind the associated TBG growth, which may on one hand be external; on the other hand the inherent energetic balance in folded TBG could favor its expansion from a small flipped-over seed to an extended area.

The only possible external trigger in an AFM-scan is the motion of the moving tip. As there is no consistent correlation between the fast scanning direction and the main direction of growth however (around perpendicular in [fig. 4.5](#) vs. parallel in [fig. 4.6](#)), scanning motion as major driving force behind a folding process can be discarded (with the possible exception of small corrections as seen in the disruption of growth direction at the dashed line in [fig. 4.5 e](#)).

Ref. [17] proposes a thermally activated growth mechanism: Starting from a small embryonic structure created via external stimulus and stabilized by vdW-interaction overcoming the strain of the fold, the structure evolves via thermal fluctuation and incrementally progressive assumption of thusly enabled energetically favorable configurations. The energetic gain associated with the binding to another graphene layer over binding to the substrate on a given length dx overcompensates the tearing of bonds, as long as integration over width ℓ yields a large enough area dA (see [fig. 4.7 a](#)).

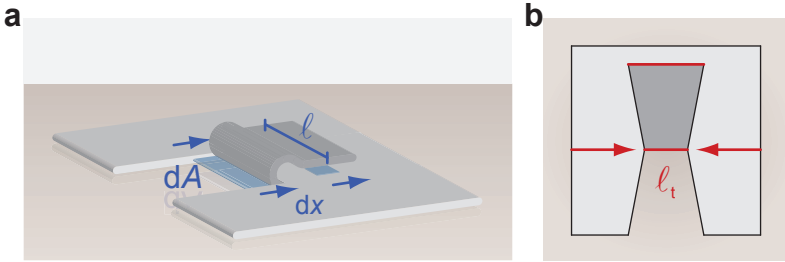


Figure 4.7 a: Schematic of a folding process. Graphene progressively detaches from the substrate in an area dA (blue plane), to gain superior bonding between top and bottom layer over an identical area. Bonds along dx are torn in the process. **b:** Top view of the folded structure. Strain in the folded edge leads to its successive narrowing.

Friction between layers in the sliding motion during growth is found to be a negligible factor, which is ascribed to incommensurate stacking configuration as confirmed via Raman spectroscopy[17]: Incommensurability between graphitic sheets has been demonstrated to give rise to superlubric interaction[18] and is assumed to enable free sliding in the proposed growth scenario.

Strain energy contained in the fold however will enforce successive narrowing of the bended edge and tapering of the torn area (fig. 4.7 b). At a characteristic width ℓ_t the growth is terminated, as energetic gains in $dA_t \leq \ell_t dx$ no longer exceed the bonding energy in two edges along dx .

Experimentally, ref. [17] finds constant ℓ_t in several folds grown in parallel out of a single flake in accord with the theoretical model, which confirms termination width as indicator for the binding energy density between top and bottom layer.

In this work, structures of similar two-rip geometry grown under a variety of interlayer twist angles exhibit termination widths over a wide range between 80 nm and 5 μm . As will be shown in the following sec. 4.2, ℓ_t is in fact found to correlate with rotational mismatch as well as interlayer distance and may thus provide a measure for twist-dependent interaction energy in TBG.

The above described model applies to folded structures with two tears as mostly gained from the invasive indentation method (fig. 4.3 b). For structures grown at one rip however, two important distinctions require alternative explanation:

Firstly, the folded edge may actually grow rather than diminish in width, as evident from fig. 4.6. This rules out the above described termination dynamics, as the corresponding differential area dA (see fig. 4.7 a) and the associated energetic gain are growing accordingly.

Secondly, the considerations discussed on the examples in fig. 4.6 a,b suggest a dynamic behavior in the direction of the folded edge. This translates to a shift in interlayer twist during the growth process, which affects the commensurability of interlayer stacking and in turn alters frictional properties between sliding TBG layers.

Conceivably, a fold growing under rotation may thus lock into a commensurate stacking configuration, thereby increasing friction and abruptly terminating further extension. The validity of this hypothesis for one-rip structures will be put to the test in sec. 4.2.

Most obvious distinctions in folds created as byproduct of exfoliation from those produced via AFM-induced growth are found in relatively large corresponding TBG areas (fig. 4.3 a) as well as the absence of rips in the majority of cases (fig. 4.3 b). Taking a closer look, an important structural effect is furthermore found in TBG areas folded as a whole i.e. at no tearing: Various degrees of rippling on the 10 nm-scale as well as the formation of wrinkles in micrometer intervals are spotted in localized areas of corresponding folds. Examples are shown in fig. 4.8 for a TBG and a folded AB-bilayer not included in the above TBG statistics.

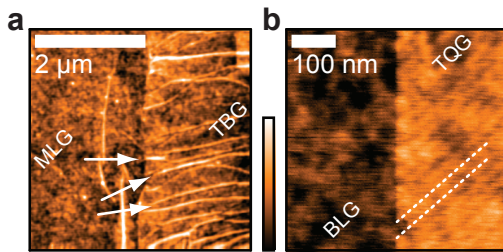


Figure 4.8 a: TBG folded from a monolayer (MLG) during exfoliation. Wrinkles perpendicular to the folded edge (to the right, not depicted) are indicated by arrows. **b:** Twisted quattrolayer (TQL) formed from an AB-bilayer (BLG). Ripples confined to the folded area are indicated by dashed lines. Colorscale spans 2 nm for both panels.

The observed structural distortions are indicative of strain^[147] in the graphene toplayer and thus unlikely to arise during energy-optimized growth as discussed for the AFM-induced folds.

TBG formation during the exfoliation process is therefore likely to be driven externally; as lateral pulling and sliding as illustrated in [fig. 4.4 b](#) has been shown to favor ripped and tapered structures[141], folding in a high arc ([fig. 4.4 a](#), conceivably guided by the adhesive tape) is the most probable scenario.

Note that wide areas of the exfoliated TBG stay unaffected of the discussed distortions and allow for the observation of coherent electronic effects (cf. [sec. 5.2](#)). A likely explanation is energetic and structural optimization in large bulk areas at the cost of localized stress, often found close to the folded edge or the front boundary of the fold.

4.2 Morphology of Twisted Graphene Bilayers

The previous section identified three categories of TBG-preparation via folding: Mechanism behind the majority of folds from exfoliation is mechanical flip-over without introduced tearing; AFM-induced folding is furthermore distinguished by the formation of one or two rips during thermally activated growth.

In the present section, thusly produced structures are examined more closely with the help of various AFM-techniques, focusing on four important parameters:

In [sec. 4.2.1](#), rotational mismatch θ is determined via sample geometry and from Moiré pattern resolution. Distribution of twist angles is correlated to the mechanism of preparation.

In [sec. 4.2.2](#), the interlayer distance Δh is determined in AFM topography measurements and correlated to rotational mismatch and corresponding stacking configurations (cf. [sec. 2.1](#)).

In the above considerations on TBG growth, length of the folded edge ℓ has been pointed out as a possible termination criterion and measure for in-plane interaction. Twist-angle dependence and correlation to interlayer distance are examined in [sec. 4.2.3](#).

Furthermore, the three-dimensional shape of the bended interconnection between top and bottom layer is investigated.

Finally, [sec. 4.2.4](#) presents frictional AFM measurements on the TBG surface which are compared to the behavior on monolayers and single crystal (SC)-fewlayers.

4.2.1 Angular Distribution

As presented in [sec. 2.1](#), rotational mismatch θ is the major parameter for interlayer stacking configuration in TBG:

Firstly, it gives rise to Moiré superstructures of wavelength λ_M , which can be resolved via scanning probe microscopy and monotonously grow with decreasing θ between 30° and 0° (see [eq. 2.5](#)).

Secondly, discrete commensurate angles lead to exact periodicity and overlap of atomic positions at wavelengths λ_C which lie on the Moiré curve of [eq. 2.5](#) as well as potentially far above λ_M for a given commensurate rotation (compare [fig. 2.9](#)).

To determine rotational mismatch experimentally, a number of methods may be applied: Real-space resolution of the Moiré pattern via scanning probe microscopy[26] allows for accurate deduction of θ via [eq. 2.5](#); electron diffraction patterns[24, 39] hold information about the orientation of as well as the superstructure between individual lattices. Furthermore, an indirect measure of θ may be acquired in Raman spectroscopy[148, 149] or in electronic transport measurements.

Means of estimating rotational misalignment are provided in the edges of graphene flakes: Graphene has two nonequivalent symmetry directions which are named after the shape of corresponding edges at the atomic level: the armchair- and zigzag-edge, alternating in 30° -steps upon rotation ([fig. 4.9 a](#)). Exfoliated as well as CVD-grown, samples are found to be terminated by such crystallographic edges in the majority of cases[24, 150].

This is exploited for TBG production in mechanical transfer to align top and bottom layer based on their edges ([sec. 4.1](#)). Note however that an error of up to 30° in 50% of cases is inherent to the method as, lacking atomic resolution, armchair and zigzag edges cannot be distinguished. In a folded sample however, top and bottom layer share the same lattice which eliminates this need of distinction.

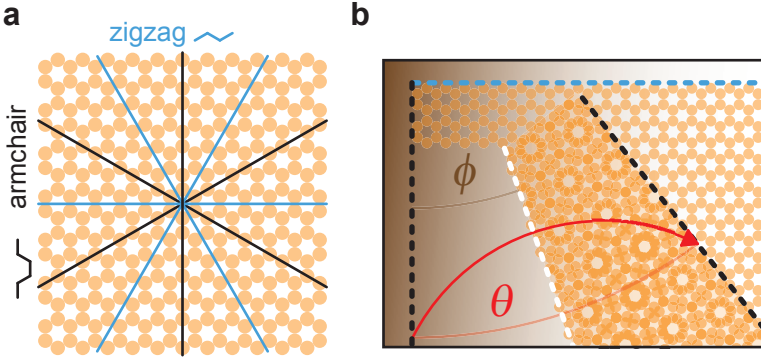


Figure 4.9 a: Graphene’s hexagonal lattice; two crystallographic directions of sixfold rotational symmetry each are indicated in black and blue. Corresponding characteristic edge shapes lead to their captioning as “armchair” and “zigzag”. **b:** Schematic of a graphene lattice folded to a twist angle of 38.213° . The folded edge is marked in white, symmetry directions terminate the flake. The angle ϕ between folded and sample edge as well as the resulting interlayer twist θ are indicated in brown and red respectively.

The twist angle θ is therefore with certainty described by the angle ϕ between orientations found in the sample edges and the folded edge as

$$\theta = 2 \cdot \phi. \quad (4.1)$$

Figure 4.9 b illustrates the above relation. The folded edge may be viewed as acting mirror axis between bottom (black armchair axis to the left) and top layer (black armchair axis to the right). Thusly obtained twist angles are projected into a range of 0° to 30° as a distinction between commensuration partners at the atomic level (see fig. 2.9 and fig. 2.12) is not justified at the given accuracy.

Depending on the quality of straight, undisrupted edges in a sample, accuracy lies in the range of 1° . For statistics over larger numbers of **TBG** as required in the present chapter, the presented methods thus provides a good compromise between experimental effort and informative value. Especially in the low-angle range, electronic spectra in **TBG** may vary on much lower angular scales however (sec. 2.2.2). When important for the interpretation of magnetotransport data (chap. 5), higher accuracies around 0.1° were achieved via Moiré pattern resolution:

As impressively demonstrated for graphene on **hBN**[40], lateral force microscopy is sensitive to a Moiré pattern in giving rise to frictional stick-slip movement of the **AFM**-tip.

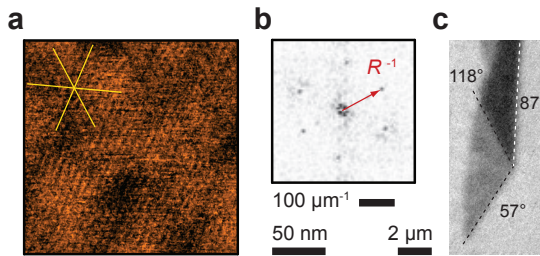


Figure 4.10 a: Lateral signal of the photodetector indicating frictional stick-slip interaction between **AFM**-tip and **TBG** Moiré pattern. The yellow star indicates orientation of the superstructure's periodic planes. The scan is performed around the zero-position of the scanner at 10 Hz under a scanning angle of 50° in the low attractive regime with feedback gains close to zero. **b:** FFT spectrum of **a**. The red arrow indicates the reciprocal Moiré wavelength. **c:** Optical picture of the **TBG** probed for **a**. Orientation of straight edges is indicated by dashed lines and a corresponding angle as measured with respect to the horizontal.

Figure 4.10 a shows AFM-measured friction from the surface of a TBG. Several hours of pre-scanning are advisable to stabilize the AFM setup; room temperature is kept constant via air-conditioning. As a result, features with periodic repetition on the 10 nm-scale are resolved in three orientations as indicated by yellow lines (note that long-range fluctuations on the 50 nm-scale reflect the roughness of the underlying SiO₂-substrate). A corresponding trigonal lattice is confirmed in the fast Fourier transform (FFT) depicted in panel b. The reciprocal lattice vector (i.e. the inverse between subsequent line features in panel a) measures $R^{-1} = 132 \mu\text{m}^{-1}$ as indicated by the red arrow in panel b. The wavelength of the underlying trigonal lattice follows from $\lambda = \frac{2}{\sqrt{3}R^{-1}}$ as $\lambda_M \sim 9 \text{ nm}$. From eq. 2.5, the twist angle may be calculated, yielding $\theta \sim 1.6^\circ$.

As a proof of principle for the above described estimation method, interlayer twist is correspondingly found from fig. 4.10 c and eq. 4.1 as $\theta = 1^\circ \pm 1$ depending on the reference sample edge (black lines, fig. 4.10 c), which is in agreement with the accurate Moiré pattern deduction.

By the above described methods, twist angles were determined for a number of 30 TBG samples. Results are summarized in a histogram of occurrence in θ , distinguishing between folded structures involving zero, one and two tears respectively (fig. 4.11): Apparently, zero-rip structures exclusively favor configurations at low interlayer twist; one-rip structures are evenly distributed with a minor inclination towards small rotational mismatch; two-rip structures are preferentially found at large θ with scattered occurrence in the low and intermediate angular range.

Regarded as a whole, the here determined angular distribution interestingly resembles the ones found in CVD-grown TBG [24, 140] as shown in fig. 4.1.

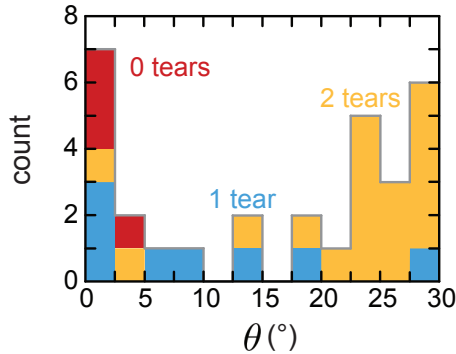


Figure 4.11 a: Histogram of occurrence in rotational mismatch. Contributions from folds created at zero tears and grown at one or two rips respectively are color coded according to the legend in the picture.

It follows separate consideration according to the folded geometry:

Accumulation in interlayer twist at small angles, as found for the flipped-over structures created in the exfoliation process, is also reported for TBG and folded graphene fewlayers prepared by random mechanical stimulation via ultrasound in liquid suspension[142]. The distribution is explained by achievement of energetically favorable *AB*-stacking in folding around an armchair or zigzag axis respectively; apparently other configurations are likely to detach under continuous excitation. As the mechanical stimulus during exfoliation will also be unselective with respect to the cleaved graphite’s crystallographic orientation as well as distinction between already folded and flat fragments, the drawing of a parallel seems to be justified: Mechanical exfoliation randomly folds and unfolds flakes on the tape; strongly bound small-angle TBG configurations stay adhered together and may be found among the exfoliation yield.

Structures prepared via AFM-induced growth require special consideration:

A notable preference of twist angles above $\sim 20^\circ$ stands out in the case of two-rip structures (yellow, fig. 4.11).

Note that the underlying reason is unlikely to be found in selectively directed mechanical stimulus as application of cuts via AFM nanoindentation, which is the predominant initiator behind two-rip folds (see fig. 4.3 b), was conducted in an arbitrary fashion with respect to lattice orientation. Furthermore, directions of an applied cut and growth of initiated TBG areas are not strictly correlated as evident e.g. from fig. 4.2 c.

Instead, the proposed mechanism of growth[17] (fig. 4.7 and discussion) may be influenced by anisotropic factors: Expansion of TBG areas under certain rotational mismatch may thus be energetically favored, while growth at other particular θ would be terminated at an early stage, placing correspondingly small folded structures under the radar of observation.

The distinguishing factor may in fact be found in interlayer commensuration: As mentioned in sec. 4.1, two-rip structures examined in ref.[17] have been demonstrated to exhibit incommensurate stacking configuration, which was argued to enable dissipation-less sliding growth in the first place. Here examined two-rip structures resemble the ones from ref.[17] in preparatory origin as well as geometric shape; assumption of a further common trait in the lack of commensurability thus seems justified. It is therefore tempting to speculate, that the accumulation of two-rip structures in large twist angles is favored by the low density of commensurate structures around 21.787° and 27.796° (fig. 2.9, $(n, r) = (1, 1)$ and $(n, r) = (3, 2)$). At smaller interlayer twist, commensurate structures are more dense; small deviations in growth direction (as e.g. observed in fig. 4.5) are here of potential to shift the TBG into commensurate lock, thereby disabling superlubric sliding for further growth.

The observed accumulation in large rotational mismatch is therefore likely related to the available parameter space devoid of commensurate configuration, enabling free extension of the according incommensurate two-rip structures.

One-rip structures in contrast, appear scattered across the entire angular range, with a slight preference towards the smallest rotational mismatch (blue, [fig. 4.11](#)).

In the previous section [4.1](#), folds evolving at the creation of one rip were proposed to grow under rotation due to different energetic situations at the native sample edge and the newly created torn edge ([fig. 4.6](#)). Therefore, the fold is bound to pass through commensurate twist angles during rotating expansion; in such a case, friction can be expected to suddenly increase, which will lock the one-rip fold into a commensurate configuration. Assumption of a small commensurate period λ_C and thus higher spatial density of atomic overlap can herein be expected most effective.

As it turns out, all of the examined one-rip structures may in fact be assigned to a commensurate angle of low wavelength λ_C : [Figure 4.12](#) shows commensurate structures in a parameter space window of twist angle θ and wavelength λ_C ; only the lowest two generations of commensuration (i.e. the one on the Moiré curve at $r = 1$, and the $\sqrt{3}$ -times larger one at $r = 3$) are required to find matches (yellow dots) for the angles of rotational mismatch as extracted for the examined one-rip structures (red dots). Note that at lower twist angle as shaded by the green area in [fig. 4.12](#), commensurate configurations grow increasingly dense in θ which leads to inevitable match at the smallest possible wavelength defined by the Moiré equation (gray line). To reduce the range in λ_C for a better resolution at small values, according low-angle structures are therefore omitted from the assignment.

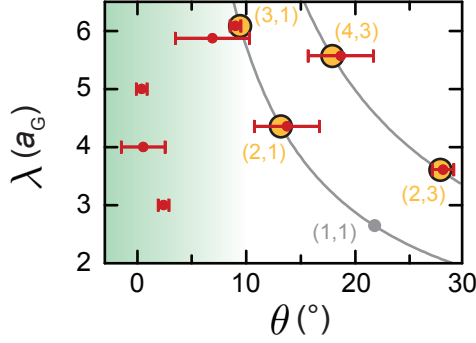


Figure 4.12 Assignment of twist angles in one-rip structures to commensurate configurations: Gray and yellow dots indicate wavelength λ_C vs. rotational mismatch θ for the entirety of commensurate structures (identified via index pairs (n, r)) within the depicted parameter window; matches to measured angles (red dots) are marked in yellow. In the shaded green range, availability of matches in the first period of r (lower gray line) is inevitable due to the increasing density of commensurate structures in low θ ; accordingly redundant illustration of angular assignment is therefore desisted from.

Assignability of twist angles found in folds grown at one rip to commensurate structures from the first generations (index $r = 1$, $r = 3$; compare [eq. 2.9a](#)), may thus be seen as validation for the above proposed mechanism of growth termination through locking into commensurate configuration.

Though being limited by the resolution in twist angles, the above findings promote the model developed in [sec. 4.1](#):

The assumption of sliding as well as termination of growth at incommensurate interlayer arrangement is sustained for two-rip structures which are mainly found at large interlayer twist, where density in commensurate structures is low.

All of the observed one-rip folds in contrast can be assigned to small-angle commensurate stacking configurations based on their interlayer twist. This strengthens the proposed scenario of growth under rotation (fig.4.6) and termination of sliding expansion in commensurate lock.

Mechanically stimulated flip-over as mechanism behind zero-rip structures from exfoliation is found to stabilize at small interlayer twist only. This is ascribed to there found most stable stacking configurations which are least likely to be ripped apart by further random mechanical stimulus.

4.2.2 Interlayer Distance

The variation in stacking configuration between TBG of different interlayer twist θ can be expected to impact interlayer distance Δh :

At small θ , Δh is modulated in various degrees of corrugation as theoretically predicted and confirmed in experimental study[56, 58]; furthermore, unison out-of-plane distortions in both top and bottom layer over as much as 1.8 Å have been found in recent simulations[63] (see sec. 2.1.4).

At larger rotational mismatch of $\theta \gtrsim 10^\circ$, corrugation amplitudes become significantly smaller due to the declining Moiré wavelength[53, 56, 58]. Resulting planar equilibrium is comparatively little explored: There are reports on measured TBG interlayer distances from 3.4 Å to 4.1 Å[1, 97] corresponding to an elevation of up to ~ 0.7 Å with respect to $\Delta h_{AB}=3.35$ Å known from Bernal-stacking. Moreover, ref.[17] measures a fold grown in a graphene trilayer at ~ 1.5 nm above the underlying sample plane, which corresponds to as much as 4.5 Å in addition to its thickness of $3 \times \Delta h_{AB} = 1.05$ nm in AB-stacking. The above findings are not evaluated or put into systematic context (e.g. with interlayer twist) however.

Similarly, theoretical predictions for the planar Δh are scarce, where calculations for interlayer interaction energy E_{int} appear contradictory: A virtually θ -independent E_{int} was found, based on Lennard-Jones interaction between lattice atoms[55]. Density functional theory calculations predict a monotonous decrease of E_{int} over θ on the order of ~ 1 meV/atom[22, 53]. While none of the former references find more than ~ 0.3 Å in variation of Δh , a larger span of up to 1 Å is found via sophisticated quantum chemistry methods under consideration of complex p -orbital interaction [54].

In light of this ambivalence, systematical investigation of Δh is called for; according experimental data are presented in the following.

Here, AFM topography of TBG and surrounding MLG is recorded, taking special care to minimize crosstalk artifacts (sec. 3.3.3). Data are leveled via a polynomial plane fit to substrate or MLG, thereby accounting for a possible tilt in the mounted sample and potential bow in the scanner (sec. 3.3.1).

A histogram of occurrence in relative height is then built over the topography data as shown in fig. 4.13. Contributions of substrate, MLG and TBG are identified in Gaussian distributions, the sum of which is fit to the histogram. Interlayer distance Δh is calculated as the difference between maxima in TBG- and MLG-distribution; the error is estimated from the sum of corresponding fitting uncertainties which exceeds crosstalk-related inaccuracies in the majority of cases.

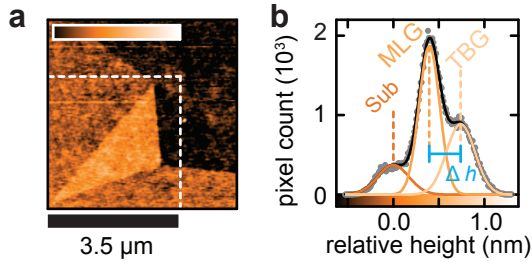


Figure 4.13 a: AFM topography of TBG (bright orange triangle) folded out of monolayer graphene (dark orange) on a SiO_2 -substrate (dark brown) The white square marks the area of evaluation for **b**. Colorscale spans 2 nm in height. **b:** Gray dots: Histogram of pixel frequency in dependence on relative height within the white square in **a**. Black line is the sum of three Gaussian distributions fit to the data. Colored lines are three summands according to the legend in the picture. Interlayer distance is indicated in blue.

Results are plotted in fig. 4.14 as Δh vs. interlayer twist angle θ .

The blue line marks Δh_{AB} as measured from a terrace in single crystal (SC) bilayer graphene and apparently defines the lower border of Δh in TBG. This is in accordance with expectation, as AB -stacking constitutes the energetic optimum of interlayer configurations[22, 53–55].

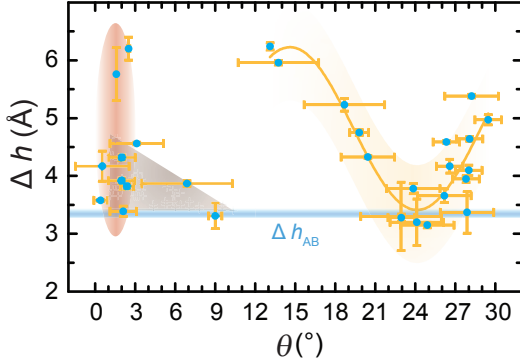


Figure 4.14 Interlayer distance $\Delta h_{(AB)}$ extracted from AFM topography measurements. Blue line indicates Δh_{AB} from a SC -bilayer (experimental uncertainty in width of line); blue dots are data for TBG , plotted in dependence on interlayer twist. Three regimes can be discerned and are marked by red (small θ), brown (intermediate θ) and orange (large θ) backdrops. The orange line is a sinusoidal fit to large-angle data serving as guide to the eyes.

Above the minimum of Δh_{AB} , measured interlayer distance evolves over as much as $\sim 3 \text{ \AA}$, which is discussed in the following for the regimes of small (0° to 3°), intermediate (3° to 10°), and large θ .

At the smallest interlayer twist, Δh appears scattered over a wide range as marked by the red ellipsis in fig. 4.14. Here, a subset of data may in fact be AB -stacked within the corresponding ranges of uncertainty, which would account for the lowest of measured Δh .

The emergence of large and intermediate measured values may be understood taking into account the finite sharpness of AFM-tips. Between a scanning probe with tip radius of curvature r_{tip} and Moiré pattern corrugation of wavelength λ_M , three scenarios may be envisioned:

- At $r_{\text{tip}} \ll \lambda_M$, the scanning probe accurately traces the corrugated topography. Lateral resolution of the employed setup is limited by thermal fluctuation and drift however, which will lead to effective averaging over minima and maxima on a scale of 10 nm.
- At $r_{\text{tip}} \gg \lambda_M$, the AFM-tip does not penetrate corrugation valleys; measurements in close contact will largely reflect corrugation maxima which is interpreted as large planar Δh .
- At $r_{\text{tip}} \approx \lambda_M$, the tip will partly follow corrugation as depicted in fig. 4.15. Between thusly underestimated minima and corrugation maxima, thermal averaging applies like in point one.

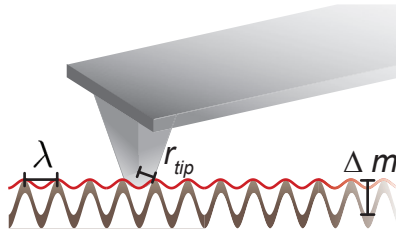


Figure 4.15 Schematic of an AFM scanning probe with tip radius of curvature r_{tip} tracing a corrugated surface (brown) of wavelength λ . Red line indicates effective height as sensed by a tip of $r_{\text{tip}} \approx \lambda$. Note that the vertical dimension is exaggerated for clarity.

In the here investigated cases, r_{tip} lies at $r_{\text{tip}} \lesssim 10 \text{ nm}$, which is close to the Moiré wavelength in the center of the discussed small-angle range ($\lambda_{\text{M}} = 10 \text{ nm}$ at 1.4°). At a given corrugation amplitude Δm , measured height may therefore take on values between $\sim \frac{1}{2}\Delta m$ and Δm above a minimal interlayer distance, depending on the interplay between tip sharpness and the exact λ_{M} , which explains the observed scattering between 0° and 3° .

At larger angles, the second of above listed scenarios will apply for all TBG structures, as $\lambda_{\text{M}} \ll r_{\text{tip}}$; expected planar heights are $\Delta h_{\text{AB}} + \Delta m$. The brown triangle in fig. 4.14 marks the range of corrugation amplitudes found via STM in refs.[56, 58] (summarized in fig. 2.15). Added to the minimal line of Δh_{AB} , good congruence to here measured interlayer distance is found.

In summary for the corrugation-dominated regime at twist angles below $\sim 10^\circ$, measured Δh are explained by the interplay between AFM-tip and Moiré wavelength λ_{M} . Assuming that corrugation minima take on Bernal-stacked interlayer distance (justified due to close approximation of AB -stacking in corresponding areas as illustrated in fig. 2.14), good congruence to corrugation data from STM-studies is found.

At large rotational mismatch, interlayer distance displays oscillating behavior with a pronounced dip around 24° , where $\Delta h \approx \Delta h_{\text{AB}}$ (fig. 4.14). Maximal values of $\sim 6 \text{ \AA}$ and $\sim 5 \text{ \AA}$ are assumed around 15° and 30° respectively.

The observed range in Δh is within limits of reported examples [1, 17, 97] as summarized in the beginning of this section. Due to the lack of consentaneous theoretical prediction for planar interlayer interaction however, the mechanism behind the presented experimental findings on θ -dependence can only be speculated on:

As evident from [fig. 2.9](#), the angular range around 21.787° (to a lesser degree also 27.796°) clearly takes a prominent place in the parameter space of interlayer configuration, as it exhibits an exceptionally low density of commensurate structures. In [sec. 4.2.1](#), this was associated with preferred occurrence of two-rip folds at large rotational mismatch.

Secondly, focusing on commensuration rather than a lack thereof, experimental relevance of the commensurate structure at $\theta=21.787^\circ$, close to the observed minimum in Δh , was recently demonstrated in transport through rotatable inter-graphitic junctions: A sharp dip in angle-dependent resistance is explained via superior atomic overlap in the corresponding $(r, n) = (1, 1)$ -structure[[30](#), [49](#)].

In light of the above considerations it is therefore tempting to relate the discussed evolution of Δh in large θ to the commensurate parameter space.

As all of the structures contributing to the observed dip in Δh are two-rip structures ([fig. 4.11](#)) and thus most likely incommensurate, the second of the above points loses in relevance; it is therefore probably the lack of commensuration between $\theta=21.787^\circ$ and $\theta=27.796^\circ$, which defines the mechanism behind low interlayer distances in the respective angular range.

One might speculate about the role of repulsive interaction between p_z -orbitals for different degrees of atomic overlap, as considered in [ref.\[54\]](#). A more thorough understanding of the underlying mechanisms should encourage further theoretical effort though.

In summary, a pronounced twist-angle dependence is found in [TBG](#) interlayer distance as measured via [AFM](#). Minimal values around Δh_{AB} and evolution over $\sim 3 \text{ \AA}$ are observed and connected to well studied Moiré pattern corrugation at small angles $\theta \lesssim 10^\circ$. At large rotational mismatch, oscillating Δh with a global minimum at $\theta \approx 24^\circ$ are linked to the commensurate parameter space of [TBG](#).

4.2.3 Folded Edge

The bended edge connecting top and bottom layer is an exclusive feature in TBG produced by folding; a number of associated phenomena make it a topic worth studying:

In a magnetic field perpendicular to the folded planes, the edge is e.g. predicted to give rise to snake states[151].

In a magnetic field parallel to the edge, gathering of a phase around the flux enclosed by the fold might lead to Aharonov–Bohm-like interference phenomena as observed for carbon nanotubes[152].

The first part of the following segment investigates the folded edge’s lateral extension, which has been discussed as criterion for termination of growth in two-rip TBG structures in sec. 4.1.

Furthermore, folding of graphene gives rise to a vertical bulge due to a finite bending stiffness, lending the edge a shape reminiscent of carbon nanotubes[34]; further reaching parallels in the bending radius will be revealed in the second half of the following segment.

Lateral Extension

In the first section 4.1 of this chapter, thermally activated growth has been introduced as mechanism behind the expansion of folds in graphene. In TBG grown at two tears, a successive narrowing of the folded edge is herein caused by associated strain; the growth process stops, when the energetic gain from interlayer interaction (proportional to length ℓ of the folded edge) no longer exceeds the tearing energy for extension along the two rips. This hypothesis was confirmed by a constant termination width ℓ in folds grown at equal interlayer twist[17]. For this work, a wide range of different termination widths are found. Determination of rotational mismatch and interlayer distance in the previous segments of this section now allows for a correlation of ℓ to these central TBG parameters.

In structures grown at two tears, both folded length ℓ and interlayer distance Δh should be related to interlayer interaction energy and would accordingly show correlation between each other. Respective energetic dependencies derive as follows:

The criterion for growth termination is estimated via

$$\ell \delta E dx = 2 \delta R dx, \quad (4.2)$$

with dx as incremental length in the direction of TBG growth, δE as interlayer interaction energy per unit area and δR as tearing energy per unit length, where the factor of 2 accounts for the number of rips to be torn. TBG expansion becomes energetically unfavorable when the left-hand side of eq. 4.2 is smaller than the right-hand side.

The interaction energy per atom E_{atom} follows as

$$E_{\text{atom}}(\ell) = \frac{\sqrt{3} \delta R a_{\text{G}}^2}{2} \ell^{-1} \quad (4.3)$$

from solving for δE and multiplication with graphene's unit cell area $A = \frac{\sqrt{3}}{2} a_{\text{G}}^2$, divided by two (accounting for the bi-atomic basis).

The relation between Δh and interaction energy on the other hand may be described via the Lennard-Jones (LJ) potential. Ref.[55] uses the expression

$$E_{\text{atom}}(d) = 4\epsilon \left(\left(\frac{\sigma}{d} \right)^{12} - \left(\frac{\sigma}{d} \right)^6 \right) \quad (4.4)$$

for the potential between pairs of carbon atoms with separation d . Modeling the interaction energy in a Bernal-stacked graphene bilayer via integration over atomic sites in both layers, parameters are found to lie around $\epsilon \approx 2.5$ meV and $\sigma \approx 3.37$ Å [55].

In the following, the carbon-carbon potential from eq. 4.4 is taken as qualitative measure for interaction between two sheets of graphene.

In further simplification, the term with power law of 12 is assumed negligible for the examined range of interlayer distance where $\Delta h \gtrsim \sigma$, which leaves

$$E_{\text{atom}}(\Delta h) \approx 4\epsilon \left(\left(\frac{\sigma}{\Delta h} \right)^6 \right), \quad (4.5)$$

where the conventional minus sign is omitted. Equating eq. 4.3 with eq. 4.5 and solving for ℓ finds

$$\ell \approx \frac{\sqrt{3}\delta R a_G^2}{8\epsilon\sigma^6} \Delta h^6. \quad (4.6)$$

Figure 4.16 plots Δh vs. ℓ as found in here examined two-rip structures. A largely monotonous trend, straight in the frame of the chosen logarithmic scaling, complies to the above assumption of a power-law dependence.

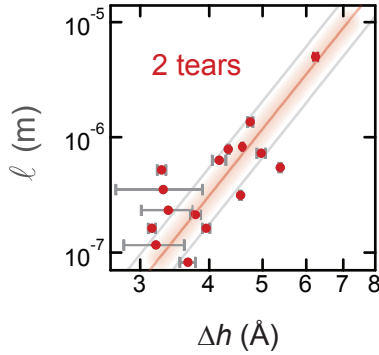


Figure 4.16 Length of the folded edge ℓ vs. interlayer distance Δh for two-rip structures. The straight line is a fit of eq. 4.6 to the data.

The red line in [fig. 4.16](#) is a fit of [eq. 4.6](#) to the evolution of data, displaying a reasonable agreement between estimated and experimentally found correlation; the prefactor to $\Delta\hbar^6$ is fit as $\sim 7.5 \times 10^{49} \text{ m}^{-5}$.

Under the assumption of $\delta R = 2 \text{ eV \AA}^{-1}$ [[141](#)] and with $\epsilon \approx 2.5 \text{ meV}$ and $\sigma \approx 3.37 \text{ \AA}$ [[55](#)], [eq. 4.6](#) yields a prefactor value of $\sim 7 \times 10^{49} \text{ m}^{-5}$. The surprisingly good match to the fitting result should not be overestimated though, as the above described model is certainly oversimplified and merely designed as a rough estimation of the expected correlation between ℓ and $\Delta\hbar$.

Note that the observed scattering of data might be connected to different magnitudes of δR in dependence on the direction of tearing:

From geometrical consideration of the honeycomb lattice it becomes evident, that tearing in the direction of a lattice vector \mathbf{a} along the zigzag-edge requires rupture of one carbon-carbon bond per lattice constant a_G , where a straight rip along the armchair direction requires rupture of one bond per nearest-neighbor distance b_G ([fig. 4.9](#)). With the energy of a C-C σ -bond at 4.3 eV , this corresponds to $\sim 2.8 \text{ nJ m}^{-1}$ for the zigzag- and $\sim 4.9 \text{ nJ m}^{-1}$ for the armchair-direction (the above assumed value of $\sim 3.2 \text{ nJ m}^{-1}$ or 2 eV \AA^{-1} from ref. [[141](#)] considers a mixed edge).

The gray lines beneath the centered red one in [fig. 4.16](#) accordingly illustrate evolution of [eq. 4.6](#) under variation of the fit prefactor to $\Delta\hbar^6$ by $\frac{4.9}{2.8}$ (upper line) and $\frac{2.8}{4.9}$ (lower line), providing an estimation of the maximally expected range of scattering from δR . While the above defined range does not account for the entirety of fluctuation, the underlying reasoning provides an explanation for the general observation of deviation beyond the range of measurement uncertainty in $\Delta\hbar$ (gray bars around data points, [fig. 4.16](#)).

One might further speculate that relatively large ℓ in small Δh are related to the onset of repulsive interaction as described by the neglected term from eq. 4.4 with power of 12; a hook-like dip around $\Delta h \approx 3.5 \text{ \AA}$ would herein reflect the minimum in the LJ potential. Given the limited accuracy of data and employed model though, this remains mere speculation for the nonce.

Qualitatively, the clear correlation between ℓ and Δh with general evolution after a power law supports the validity of the proposed growth mechanism, where the length of the folded edge ℓ dictates termination of TBG expansion in dependence on the density of interlayer interaction energy δE (eq. 4.2), which is related to Δh via vdW-interaction.

Note that the above applies to two-rip structures only; fold-growth at one tear has been shown to likely terminate in commensurate lock rather than in consequence of a narrowing edge (sec. 4.1, sec. 4.2.1). One-rip structures are therefore not necessarily expected to exhibit systematic relation between ℓ and δE (and in turn Δh).

Figure 4.17 plots Δh vs. ℓ as found in here examined one-rip structures; no apparent correlation is in evidence, which further stresses the distinction between TBG grown under the creation of one and two tears respectively.

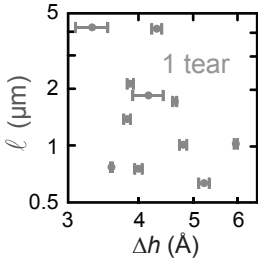


Figure 4.17 Length of the folded edge ℓ vs. interlayer distance Δh for one-rip structures. Data appear scattered and contra-indicative of correlation between folded length and interlayer distance.

From the largely monotonous dependency between folded length ℓ and interlayer distance Δh in two-rip structures, correlation between ℓ and twist angle θ inductively follows from the one between Δh and the latter as observed in [sec. 4.2.2](#).

Indeed, the plot in [fig. 4.18 a](#) suggests an oscillating behavior of the folded length over interlayer twist, similar to the one of interlayer distance as depicted in [fig. 4.14](#). Due to the preferred arrangement of two-rip structures in large angles and the limited available data below, the behavior for $\theta \lesssim 20^\circ$ as interpolated by the sinusoidal fit is merely a suggestion, under the additional assumption of maximal δE (and thus minimal ℓ , see [eq. 4.2](#)) at the smallest interlayer twist [[142](#)].

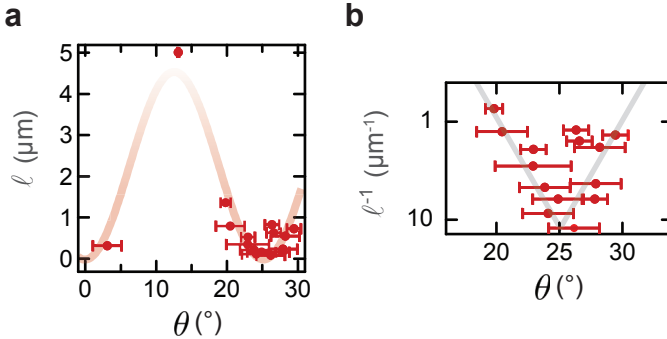


Figure 4.18 a: Length of the folded edge ℓ vs. interlayer twist angle θ for two-rip structures. The transparent sinusoidal curve served as guide to the eye, suggesting a similar correlation to the one between Δh and θ from [fig. 4.14](#). **b:** Inverse length of the folded edge (small to large from top to bottom) in large θ ; straight gray lines provide guides to the eye.

Figure 4.18 b shows a close-up of the densely populated large-angle range; the vertical axis scales the inverse of the folded length, which is proportional to interlayer interaction energy δE in the frame of eq. 4.2 (note that orientation of the axis is switched for qualitative comparability to panel a).

This alternative depiction highlights a clearly defined dip around 25° , suggesting a corresponding minimum in interaction energy. As argued towards the end of sec. 4.2.2, this behavior is likely connected to incommensurate stacking of the examined two-rip structures and particular configurations of overlap between π -orbitals at the atomic positions in the individual layers.

Thusly confirmed correlation between rotational mismatch θ and length of the folded edge ℓ in two-rip structures ties together the oscillating evolution of Δh in θ as observed in fig. 4.14 and the above established dependency between ℓ and Δh via interlayer interaction energy density δE (fig. 4.16).

This demonstrates the consistency of the above established correlations and further cements the validity of the proposed growth mechanism[17] for folded graphene along two tears (fig. 4.7).

In summary the findings from ref.[17] are extended by investigating the central parameter of termination width ℓ over the whole range of rotational mismatch θ and a wide span of interlayer distance Δh ; based on a vdW-interaction model, Δh is quantifiably correlated to ℓ as indicator of interlayer interaction energy density δE .

Moreover, the here identified class of TBG grown at one tear is further distinguished from the two-rip structures introduced in ref.[17]; ℓ is clearly not related to interaction energy δE (fig. 4.17). Instead, the proposed scenario of TBG expansion under rotation (fig. 4.6) and termination in commensurate lock (fig. 4.12) is further substantiated as alternative mechanism of growth for one-rip structures.

Vertical Extension

The cross-sectional shape of the folded edge, in the plane normal to the bending axis, is influenced by the interplay of vdw-adhesion between layers and bending energy in the fold. A critical adhered length of $x_0 = 2.5 \text{ nm}$ [153] is theoretically found to stabilize a folded graphene monolayer in a racket shape with a bended portion around 5 nm [153, 154]. Similarly, ref.[151] calculates a bending radius of $r \approx 7 \text{ \AA}$ for the cylindrical part of the edge. In general, bending rigidity and resulting edge shapes are found to be largely isotropic.

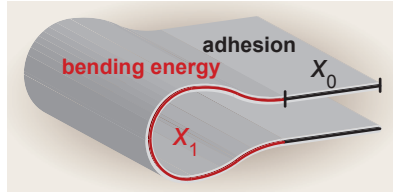


Figure 4.19 Schematic of a folded graphene sheet with adhered (x_0 , black) and bended length (x_1 , red). The folded shape is symmetric in top and bottom layer in the absence of a substrate.

In contrast to the symmetric scenario depicted in fig. 4.19, the bended shape will be affected by the bottom layer's flat conformation to a substrate in the here examined cases. As suggested in fig. 4.20 a the protrusion of the folded edge will show as a bump in topography which may be quantified as elevation Δb over the TBG plane (in turn defined by interlayer distance Δh). The corresponding bending radius r , may be estimated as

$$r = \frac{\Delta h + \Delta b}{2}. \quad (4.7)$$

Figure 4.20 b shows AFM topography across a particularly pronounced bump which protrudes about 8 \AA over the TBG plane to the right; the corresponding cross-section is plotted in orange to the top of fig. 4.20 c. Note that other folds exhibit significantly smaller bump heights: examples of intermediate (beige line) and low Δb (i.e. virtually non-existent, brown line) are shown in comparison.

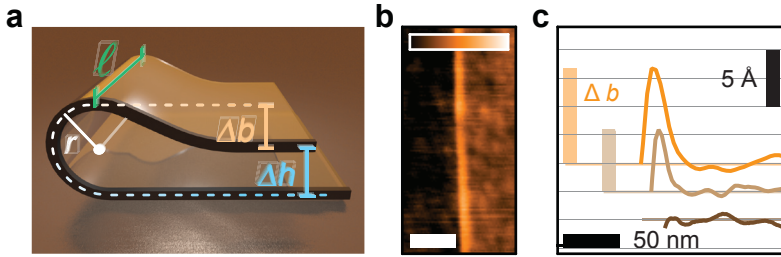


Figure 4.20 a: 3D schematic of a folded graphene sheet. Indicated are characteristic magnitudes of interlayer distance (blue), folded length (green) and the bend-related quantities of vertical extension over the TBG plane (yellow) and bending radius (white). **b:** AFM topography over the folded edge (bright orange) between substrate (dark brown, left) and TBG (dark orange, right). Scalebar indicates 100 nm, colorscale spans 3 nm. **c:** Orange line: cross-section of topography in **b**; the example shows the largest of measured bump heights. Beige and brown lines: cross-sections from similar topography at intermediate (beige) and small Δb (brown).

Bending radii corresponding to the maximal and minimal Δb depicted in fig. 4.20 c are calculated via the according Δh and eq. 4.7 as 2.3 \AA and 6.3 \AA . Where the larger value is close to the above mentioned theoretical prediction of $r \approx 7 \text{ \AA}$, the smaller significantly deviates from calculated equilibrium.

The observed spread in bending radius between values matching theoretical prediction and clearly decreased r poses an interesting problem; systematic investigation in a number of folds is presented in the following:

Note that accurate capture of the folded edge requires high resolution. Buckling of the AFM-cantilever at the sharp topographic feature of Δb furthermore leads to significant crosstalk (sec. 3.3.3); minimization requires time-consuming slow scans. Edge measurements were therefore confined to a subset of the earlier presented TBC; to maximize comparability, only structures of two-rip geometry were chosen for examination.

Figure 4.21 shows a plot of the accordingly determined vertical edge parameter r vs. lateral length of the edge ℓ , interestingly revealing a clear correlation: Large bending radii close to theoretical prediction are found in long folded edges, where a largely monotonous decrease in r is observed towards short ℓ . Note that, although r depends on Δh as well as Δb (eq. 4.7), the observed trend is dominated by the latter as plotted in the appendix fig. A.1, which is due to the larger span of variation (~ 1 nm in Δb vs. ~ 3 Å in Δh).

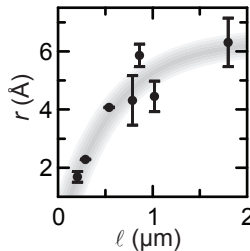


Figure 4.21 Bending radius r vs. length of the folded edge ℓ . An exponential fit serves as guide to the eye.

Apparently, the third dimension parallel to the folding axis affects the cross-sectional shape of the bended edge, substantially lowering the bending radius for small folded lengths. Note that in theoretical prediction, the problem is treated as purely two-dimensional, as the considered factors of interlayer adhesion and bending energy both scale proportionally in the direction of the folding axis. The energy associated with the torn edges of a fold as grown in the model from ref.[17] however (see eq.4.2) is constant and thus of increasing potential import at decreasing folded length:

As all of the examined TBG are two-rip structures, the energy associated with the furthering of tears can be assumed constant for a given increment of growth perpendicular to the folded edge and lies at roughly $2 \times 2 \text{ eV \AA}^{-1}$ [141]. As found in ref.[153], shortening of the bended portion of a fold x_1 (fig.4.19, marked in red) from the optimized length of 5 nm to ~ 2.5 nm (and correspondingly halving the bending radius) leads to an increase in bending energy of $\sim 2.5 \text{ eV}$ for every nanometer of folded length ℓ . Torn at two rips from the sample, this difference in x_1 corresponds to $\sim 100 \text{ eV}$. Corresponding reduction of the tearing path at the cost of a lowered bending radius therefore yields a gain in energy for folded lengths up to 40 nm.

The above estimation demonstrates the comparability of energy scales in bending and tearing at small ℓ . The proposed influence of the torn edges of a folded area on the bending radius is therefore conceivable. The apparent saturation of r between 6 Å and 7 Å at high ℓ (see exponential guide to the eye in fig.4.21) is furthermore in accordance with theoretical prediction in the same range, as energetic contribution from tearing will loose proportional impact at large integration length over bending energy.

Interestingly, the observed behavior can be linked to calculations on carbon nanotubes[155, 156], which find increasing stability for larger tube lengths, which would render a short bended area more prone to deformation or even rupture upon shifting in the bulk.

Furthermore a tendency to larger tube diameters for bigger systems is predicted due to energetic struggle between strain of curvature and number of edge atoms[155], similar to the above considerations. As a folded edge may be seen as half a carbon nanotube, the presented findings are qualitatively in line with the discussed predictions[155, 156].

In summary of the established findings on vertical extension of the folded edge, bending radius r in folds grown along two tears is demonstrated to depend on the folded length ℓ . At large ℓ , accordance with theoretical prediction based on interlayer adhesion and bending rigidity is found at $r \approx 7 \text{ \AA}$. Decreasing r down to $\sim 1.7 \text{ \AA}$ at smaller folded lengths are attributed to increasing impact of tearing energy in comparison to the bending energy integrated over ℓ . Parallels to the predicted struggle between strain of curvature and number of edge atoms in carbon nanotubes are pointed out, thereby linking two important subjects in chemistry and physics.

Comparative investigation of bending radii in folds grown at one rip as well as flipped over structures with no tear would constitute an interesting extension of the presented study; a weakened ℓ -dependence can herein be expected for one-rip structures where, following the model developed in the above section, r should be virtually unaffected by the folded length in TBG prepared by mechanical flip-over.

4.2.4 Friction on TBG

As final topic in the structural investigation of TBG, the frictional behavior under lateral AFM-measurements is presented in the following. As a background, AFM-measured friction has been found to systematically decrease with the number of layers from monolayer graphene over single-crystal (SC) fewlayers to bulk graphite[128–130]. Interestingly, the effect is believed to be rooted in out-of-plane elasticity and puckering of the probed material before the AFM-tip rather than in surface roughness[129, 157]; successive layers in Bernal-stacking will lend the probed top layer increasing rigidity.

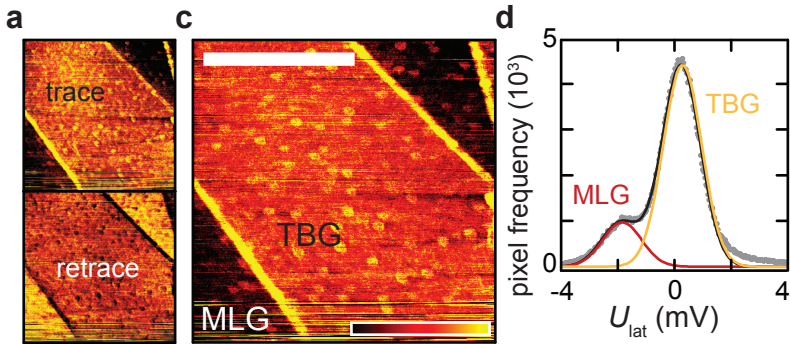


Figure 4.22 a: Torsional signal from trace (top panel) and retrace scan (bottom panel) of TBG (diagonal strip in the middle) folded from a monolayer (top right and bottom left). Notice the sign inversion of features (colorscale from **b**, spanning from -2 mV to 2 mV). **b:** Difference between trace and retrace signals in **a**, divided by two. Scalebar indicates 500 nm. **c:** Histogram for number of pixels per increment of lateral photodetector signal U_{lat} . The sum of two Gaussian distributions is fit to the data. Slight mismatch at large U_{lat} is due to contributions from the TBG edges (**b**, bright yellow).

Figure 4.22 shows an example for the acquisition of frictional information from **TBG**. Trace and retrace scans are recorded to account for possible anisotropies in sensitivity of the scanning probe. Due to the sign inversion in the torsional response at opposite scanning orientation, the average of subpanels in fig. 4.22 a is build via subtraction and division by two and is depicted in panel b. Analog to the extraction of interlayer distance information in sec. 4.2.2, the corresponding histogram is fit by a double-Gaussian distribution to determine the difference in frictional response on **TBG** and **MLG**.

To ensure comparability, all measurements were performed at constant scanning speed of $2\mu\text{m s}^{-1}$ (note the velocity-dependence in nanoscale friction[128]) and similar normal forces. Furthermore, **TBG** data presented in the following stem from folds in two neighboring graphene flakes on the same substrate wafer, ensuring comparable influence through the latter; as in the study of Δb , here examined structures are moreover of two-rip geometry only.

Figure 4.23 a shows data for **TBG** and an *AB*-stacked **SC**-bilayer, determined as demonstrated in fig. 4.22. Notably, all measured **TBG** surfaces provoke larger frictional interaction than the monolayer they are folded onto; the Bernal-bilayer behaves as expected from the above literature review and causes lower frictional response.

To enable more effective comparison to **SC**-fewlayer data[129, 130], the here measured *AB*-bilayer value is scaled to the average difference between unity (monolayer value in fig. 4.23 b) and the four reported *AB*-bilayer values (fig. 4.23 b, blue bars at 2_{AB}); **TBG** friction is scaled proportionally and data are offset by one.

Results are shown as red bars in fig. 4.23 b and illustrate substantial deviation from **SC**-behavior in in the examined **TBG**: The decreasing trend in friction over layer number is broken; addition of one layer in twisted stacking may furthermore increase measured friction on a scale comparable to its decrease over many layers from monolayer to bulk graphite.

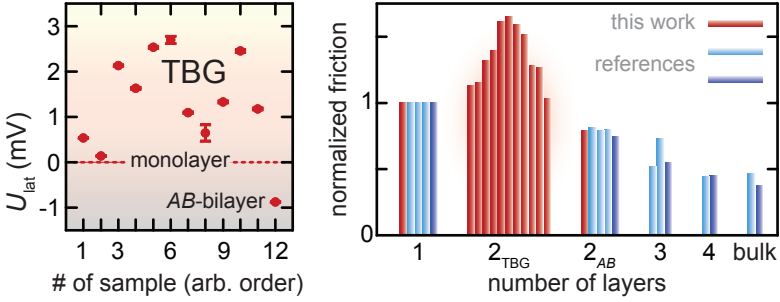


Figure 4.23 a: As a proportional measure for friction: difference to the monolayer value in U_{lat} as extracted via the steps summarized in fig. 4.22. Frictional AFM-response on TBG exceeds the one on monolayers which is in turn larger than on the measured SC-bilayer. **b:** Red bars: Data from a, normalized and offset by 1 as described in main text. Blue bars are data from ref.[129] (light) and ref.[130] (dark).

Different explanations for the observed behavior may be thought of, considering the proposed dynamic puckering[129, 157] of a probed sheet as main source for frictional interaction:

In principal, additional out-of-plane elasticity may locally be caused by Moiré pattern corrugation which will furthermore provide increased surface area and thus heightened frictional interaction. However, there is no discernible difference in frictional response between low- and high-angle TBG, which renders the hypothesis unlikely.

An alternative scenario focuses on interlayer interaction: Local detachment of the twisted top layer and dynamic deformation in response to a scraping AFM tip will effectively increase frictional response and is conceivably exclusive to TBG due to weaker interlayer binding with respect to Bernal-configuration.

Furthermore, the TBG as a whole is likely to be more ductile in response to the scanning probe than its Bernal-stacked counterpart for a combination of two factors: Firstly, bending rigidity was found to strongly depend on interlayer shear interaction[145]. Secondly, all of the frictionally probed TBG are two-rip structures and likely in incommensurate stacking[17] which is associated with superlubricity[18]. Therefore, top and bottom layer will shear freely, increasing the bilayer's out-of-plane ductility with respect to AB -stacking and increase frictional interaction.

A combination of locally detaching layers and superlubric interaction in TBG conceivably gives rise to even higher ductility than in a monolayer on SiO_2 .

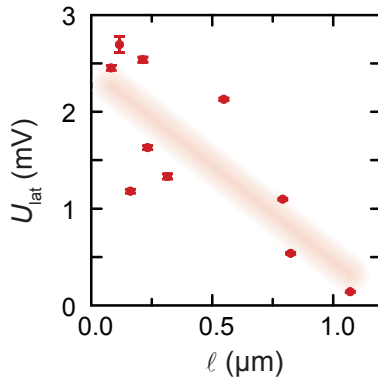


Figure 4.24 U_{lat} from [fig. 4.23 a](#), plotted vs. length of the folded edge. A decreasing trend is suggested by a linear fit serving as guide to the eye.

The correlation presented in [fig. 4.24](#) provides means to assess the above hypothesis: Friction is found to decrease towards longer folded edges.

On one hand, this is counter-intuitive: In folds grown along two tears, a short edge indicates high interlayer interaction energy[17] (eq. 4.2), placing corresponding TBG closer to the optimized binding in Bernal-stacked bilayers which constitute a low-friction material.

On the other hand, the folded edge is likely to stabilize relative interlayer position and render the TBG more rigid, which applies in the proposed model: At short ℓ , layers shear freely and allow for heightened ductility in the TBG top layer and bulk, which causes rising frictional interaction potential. At long ℓ , layers are effectively fixated along one edge; top and bottom layer are held rigid which stifles the dynamic response to a scraping AFM-probe.

In summary, TBG probed via lateral force microscopy provoke heightened frictional response in comparison to monolayers and SC-fewlayers. The effect is linked to superlubric shearing between top and bottom layer of the examined two-rip structures, which increases out-of-plane elasticity in response to an AFM-tip.

TBG friction systematically decreases with length of the folded edge; long edges are proposed to impede interlayer sliding and lower the elastic response of the folded area, thereby lowering measured friction.

The presented findings once more demonstrate the importance of the bended edge in folded TBG, showing its impact in phenomena which are intuitively assumed to be rooted in the bulk. An extension of the presented study to one- and zero-rip structures would constitute an interesting direction of further research: commensurate stacking as presumably prevalent configuration in one-rip structures can herein be expected to cause substantially different frictional interaction profiles.

4.3 Summary

In summary of this chapter, [sec. 4.1](#) identifies three basic geometries in [TBG](#) from folded monolayers, which are linked to distinct mechanisms behind their creation:

Flip-over of a whole flake area without tearing of graphene is found as byproduct of mechanical exfoliation. Ripples and wrinkles in smaller areas of correspondingly created [TBG](#) are indicative of local strain and suggest folding in response to external stimulus. As demonstrated in [sec. 4.2](#), according structures exclusively stabilize at small interlayer twist; less stable folding configurations are likely to be reversed in the repetitive, random exfoliation process.

Induced via [AFM](#)-scanning at elevated spring loads or selectively invasive nanoindentation, folds preferentially tear out of graphene at one or two rips respectively. In both geometries, a dynamic growth behavior at speeds $> 10 \text{ nm s}^{-1}$ is observed. These findings are attributed to a thermally activated process as proposed in [ref.\[17\]](#) (see also [fig. 4.7](#)).

For structures grown at two tears, [ref.\[17\]](#) identifies the criterion for termination of growth as lying in the interplay between tearing energy and gain from interlayer adhesion integrated over the length of the folded edge ℓ . Here, the study is substantially extended via correlation of ℓ to a number of central [TBG](#) parameters: A power-law dependence on interlayer distance Δh is observed and described in a [vdW](#)-based model. Furthermore, the bending radius at the folded interconnection between layers is found to decrease towards shorter bended edges; in analogy to the growth termination criterion, struggle between constant tearing energy and the bending energy, scaling with folded length, is proposed as underlying mechanism.

For one-rip structures, strong indicators of growth under rotation are found. Free sliding at incommensurate interlayer configuration and termination of growth in commensurate lock, due to the associated rise in friction, are suggested in view of the corresponding angular distribution.

For all folded geometries, a strong twist-angle dependence is found in AFM-measured interlayer distance: Evolution over $\sim 3 \text{ \AA}$ above minimal values around Δh_{AB} of Bernal-stacking are observed. Increasing apparent height at small twist angles towards 0° is attributed to Moiré pattern corrugation in accordance with theoretical prediction and prior STM studies. Between 20° and 30° of rotational mismatch, a pronounced minimum is connected to special features in commensurate parameter space in the corresponding angular range.

Finally, the frictional behavior on the TBG surface is measured via AFM. Heightened interaction with respect to monolayer graphene breaks the decreasing trend over layer number as found in SC fewlayer graphene. The observations are linked to superlubric interlayer interaction at incommensurate stacking configurations. Furthermore, the length of the folded edge is once more found to be of decisive import for TBG behavior: A longer edge is found to stabilize the bulk against deformation in response to the scanning probe, thereby lowering frictional interaction.

5 Magnetotransport in Twisted Bilayer Graphene

The present chapter finally takes focus on the experimental study of electronic structure in **TBG**. Magnetotransport signatures in a number of small-angle samples are evaluated, finding evidence for two distinct phenomena:

The electronic merging of the individual layers' Dirac cones in dependence on energy and magnetic field is presented in [sec. 5.1](#). Probing at small Fermi energies reveals decoupled monolayer dispersions in top and bottom layer; significant electron-hole asymmetries as well as highly detuned energetic offsets between layers are examined. Transition to a Berry phase of 2π at constant Fermi velocity reveals a novel coupled bilayer system at high energy and magnetic field.

In [sec. 5.2](#), satellite Landau fans in longitudinal resistance are found to originate in high charge carrier concentrations for a number of small-angle **TBG** samples. The findings are discussed in the scenario of electronic backfolding into the superlattice mini-Brillouin zone, connected with the filling of the lowest mini-band; furthermore, the alternative coupling scenario between Dirac cones of equal helicity from ref. [10] ([sec. 2.2.2](#)) is considered as possible explanation for the additional signatures of Dirac singularities in the transport measurements.

5.1 Berry Phase Transition in a Twisted Graphene Bilayer

The present section investigates the magnetotransport behavior of a small-angle TBG sample created as byproduct of mechanical exfoliation. Parts of the following discussions are published in ref.[45].

An overview on sample parameters like rotational mismatch, interlayer distance and electrical contact scheme is presented in the first subsection.

Transport properties are then analyzed, starting at low Fermi energies: Contributions from two monolayers are identified and analyzed in terms of corresponding charge carrier concentrations and Fermi velocity. A model for screening of backgate influence accounts for layer asymmetries; the role of electron-hole asymmetries is discussed.

Quantization of a single coupled system is found at high Fermi energy. A transition in Berry phase to the Bernal-stacked value of 2π is observed at the persistence of a linear dispersion, which is in accordance with theory[19, 20] and constitutes a significant extension to previous experimental findings[92]. A magnetic-field dependence in transition is discussed with respect to the above-mentioned layer asymmetries.

Conflicting theoretical predictions and alternative experimental findings in TBG of similar interlayer twist are finally discussed with respect to superlattice corrugation and substrate-dependence.

5.1.1 Sample Properties

The flake was selected via optical microscopy and etched as well as contacted after the description in chap. 3. Figure 5.1 a,b shows optical pictures before and after processing; in panel b, the etched sample structure is colored in brown of different shades according to the local graphene configuration.

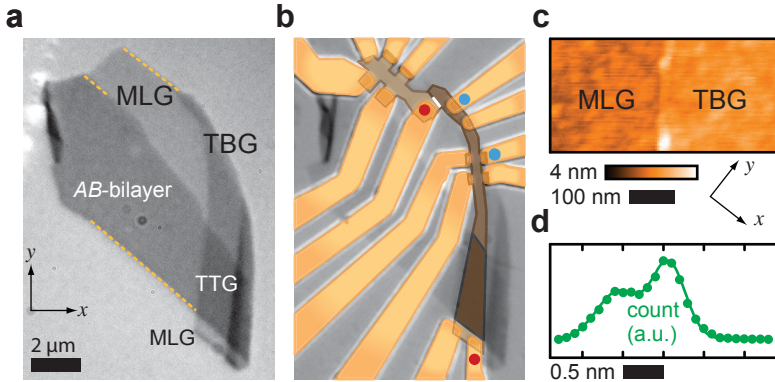


Figure 5.1 a: Optical picture of the unprocessed flake: a large *SC*-bilayer area is found to the bottom left, the fold originates from the monolayer area to the top right and covers monolayer and *AB*-bilayer alike, thereby creating *TBG* and "twisted trilayer" graphene (*TTG*). The edge to the right is curved and, to the bottom, scrolled into a bulb by multiple subsequent folds. Yellow lines indicate possible armchair- or zigzag directions. **b:** Same area as in **a** after processing. For clarity, the etched graphene sample is colored in brown. The darker shade of gray in the plasma-etched bilayer region is due to scattered residues as confirmed in *AFM*-probing and can be assumed electrically passive. Red dots mark the contacts used for sourcing of current in the here examined measurements of voltage drop between contacts marked by blue dots. The white line between upper red and blue dots indicates position of *MLG-TBG*-step measured in **c**. **c:** *AFM*-topography over the step between monolayer graphene and *TBG*. The coordinate system to the bottom provides orientation with respect to the optical pictures (compare bottom left in **a**). **d:** Histogram of pixel count per increment of relative height in **c**. The sum of two Gaussian distributions is fit to the data.

All transport data presented in the following are recorded as voltage drop between the contacts marked in blue at a current sourced through contacts marked in red (fig. 5.1 b). Panel c depicts AFM-topography recorded over the step between monolayer and folded region. The double-Gaussian fit to the corresponding histogram in panel d reveals an interlayer distance of $6.2 \text{ \AA} \pm 0.2 \text{ \AA}$.

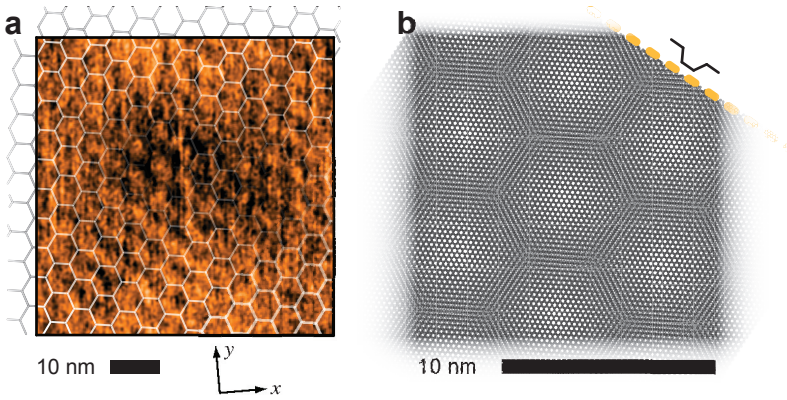


Figure 5.2 a: *AFM* resolution in lateral force mode of the Moiré superstructure in the area of the topography scan shown in fig. 5.1 c; the coordinate system to the bottom provides means of comparative orientation. Parameters are similar to the ones described in the context of fig. 4.10. An overlain honeycomb pattern clarifies the resolved structure of $\lambda_M \approx 5.7 \text{ nm}$ corresponding to a twist angle of $\theta \approx 2.5^\circ$. **b:** Schematic of a *TBG* structure of 2.5° rotational mismatch; the armchair direction of the bottom layer is aligned to the prevalent edge direction found in fig. 5.1 a., closely reproducing the orientation of the resolved superstructure in a.

Due to the lack of straight definition in the folded edge on a longer scale, estimation of rotational mismatch via sample geometry proves difficult in the present case. However, the TBG exhibits a long-wavelength Moiré superstructure which has been resolved via friction force microscopy at the parameters introduced in [sec. 4.2.1](#) and is depicted in [fig. 5.2 a](#). A honeycomb frame is manually fit to the pattern and confirms a trigonal lattice of wavelength $\lambda_M = 5.7 \text{ nm} \pm 0.2 \text{ nm}$. Uncertainty stems from slight anisotropy in the scanned features' dimension; this may be due to mild strain between lattices[158] but could also be explained via thermal drift in the measurement setup. Via [eq. 2.5](#), the twist angle follows as $\theta = 2.5^\circ \pm 0.1^\circ$ which puts the examined TBG structure in a range of potentially highly complex low-energy dispersion.

Note that under the assumption, that the marked edges in [fig. 5.1 a](#) are indicating symmetry directions of the lattice, the resolved superstructure's orientation is accurately reproduced in an according schematic ([fig. 5.2](#)) and even allows for identification of the corresponding edges as armchair-like.

5.1.2 Low Fermi Energy

The following pages focus on magnetotransport signatures in the above presented sample. The present subsection begins with measurements at low Fermi energy, recorded over a span of 30 V in back-gate voltage U_{BG} , which corresponds to a range of $\sim 2 \times 10^{16} \text{ m}^{-2}$ in charge carrier concentration n (see [sec. 3.4](#) for conversion).

All here presented measurements have been recorded at a temperature of 1.5 K, unless stated otherwise. At a DC source current of 500 nA, voltage drop is detected in four-probe configuration as indicated in [fig. 5.1 b](#). Conversion to resistance follows via Ohm's law.

Figure 5.3 shows according data. As evident from panel a, resistance is largely symmetric in magnetic field (see also fig. A.2) which indicates homogeneity and absence of pn-junctions in the probed sample area[125]. In backgate bias however, the data show clear deviations from the symmetric Landau fan picture as would be expected for longitudinal magnetoresistance in gated mono- or bilayer graphene (sec.2.3.2): Features of quantization exhibit a curved slope in the map over U_{BG} and B . In combination with the differential resistance in panel b moreover, converse evolution of Landau levels becomes evident as suggested by the dotted lines in both panels.

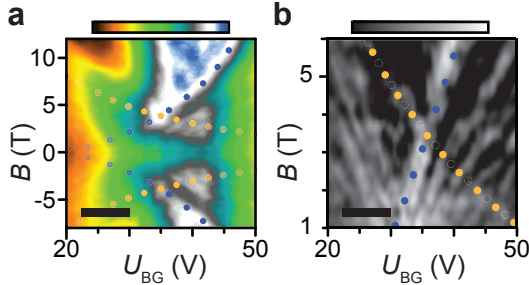


Figure 5.3 a: Resistance in dependence on backgate voltage U_{BG} and magnetic field B . Colored lines indicate two directions of feature evolution in the resistance map. The black scalebar indicates a span of $5 \times 10^{15} \text{ m}^{-2}$ in n , as induced via the backgate; colorscale to the top goes from $10 \text{ k}\Omega$ to $45 \text{ k}\Omega$. **b:** Derivative dR/dB of **a**; colored lines and black scalebar indicate the same. Colorscale goes from $-0.5 \text{ k}\Omega\text{T}^{-1}$ to $4.5 \text{ k}\Omega\text{T}^{-1}$.

The latter observation is indicative of two CNPs in the system; this is either rooted in decoupled dispersions, offset in energy (sec.2.3.1), or the filling of superlattice mini-bands (sec.2.2.3).

The observed curving of LL evolution however indicates dynamic screening of charge in the corresponding systems, which strengthens the assumption of decoupled layers over the backfolding scenario.

Figure 5.4 provides a more quantitative evaluation of the data. Assuming superposition of resistance contributions from decoupled top and bottom layer, a cross-section of data from fig. 5.3 is plotted vs. inverse magnetic field and fit by the following equation:

$$R = \sum_{j=0}^2 R_j B^{(j)} + \sum_{i=1}^2 A_i \cos\left(\frac{2\pi}{\Delta B_i^{-1}} B^{-1} + \pi + \beta\right) \exp\left(-d_i B^{-1}\right). \quad (5.1)$$

The polynomial in B accounts for a background resistance[159]. The summands in i describe SdH-oscillations according to eq. 2.35; the Berry phase is constrained to $\beta = \pi$, accounting for monolayer-like low-energy dispersions (sec. 2.2.2).

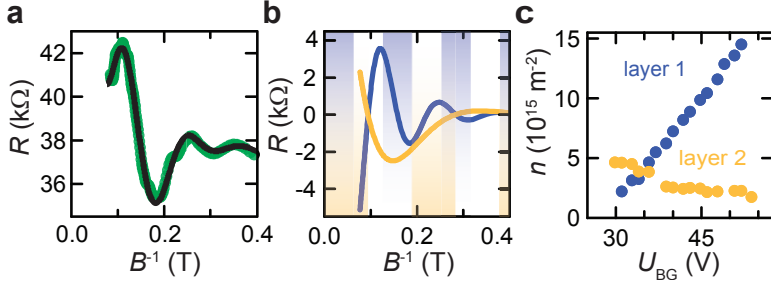


Figure 5.4 a: Green dots: Resistance vs. inverse magnetic field for a backgate voltage of $U_{\text{BG}}=41.8$ V. Black line: Fit according to eq. 5.1. **b:** Two cosine contributions from the sum over i in eq. 5.1. Transparent bars mark increments of $\Delta\nu = 2$ in both oscillations according to color code. **c:** Charge carrier concentrations in dependence on U_{BG} , derived from oscillation frequencies via eq. 2.36.

A good fit of eq. 5.1 to the TBG resistance data confirms the validity of the hypothesis of two decoupled monolayers conducting in parallel (subtracted positive polynomial background resistance of a span comparable to the oscillation amplitudes is depicted in the appendix fig. A.3).

The individual layers' carrier densities are extracted from the frequency of SdH-oscillations in B^{-1} under the assumption of fourfold degeneracy (eq. 2.36) and depicted in fig. 5.4 c. The different slopes and origins in U_{BG} reflect the initial observations on LL-evolution in fig. 5.3. In the examined range, the backgate efficiently induces electrons into layer 1, where the hole-charge in layer 2 shows much lower response to U_{BG} ; the individual layer's CNPs are lying to opposite ends of the examined energetic range.

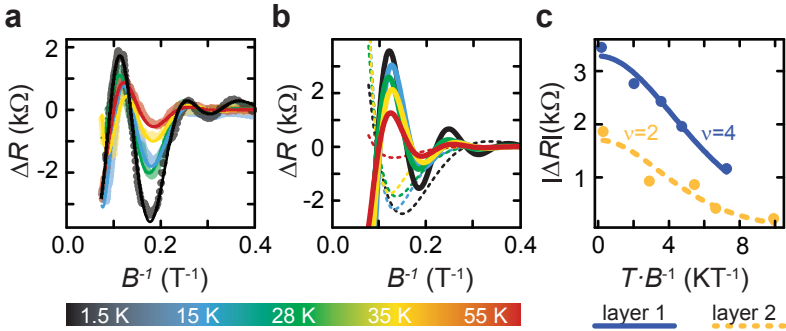


Figure 5.5 a: Resistance oscillation and fit from fig. 5.4 a (after removal of background resistances) in dependence on temperature according to the legend in the bottom. **b:** Extracted SdH-contributions from both layers to oscillations in a. **c:** Fits of eq. 2.38 to temperature-dependent resistance values from b at filling factor $\nu=4$ (layer 1, blue) and $\nu=2$ (layer 2, yellow).

To extract further information about the underlying dispersions, temperature-dependent transport behavior is investigated: As illustrated in [fig. 5.5](#), oscillation amplitudes decline towards higher temperatures in both layers as qualitatively expected; quantitative behavior holds information about effective charge carrier mass. The resistances' temperature dependence at filling factors $\nu = 4$ (maximum, layer 1) and $\nu = 2$ (minimum, layer 2) respectively is extracted from [fig. 5.5 b](#), plotted vs. the composite variable of inverse magnetic field times temperature and fit by [eq. 2.38](#) as depicted in [fig. 5.5 c](#).

Effective masses m^* from the above described fitting procedures are determined for a range of U_{BG} and depicted in the appendix [fig. A.4](#). Corresponding Fermi velocities v_{F} are depicted in [fig. 5.6](#) and follow from m^* via [eq. 2.39](#) and the charge carrier density n .

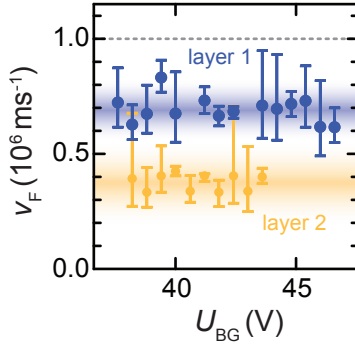


Figure 5.6 Fermi velocities for layers 1 (blue) and 2 (yellow); error bars stem from fitting uncertainty in the parameter m^* (see [fig. 5.5 c](#) and [eq. 2.38](#)). Both layers exhibit clearly reduced \tilde{v}_{F} (compare theoretical native value at dashed gray line) centering around $0.69 \times 10^6 \text{ m s}^{-1}$ and $0.38 \times 10^6 \text{ m s}^{-1}$ respectively.

Evidently, both layers display reduced Fermi velocities with $\sim 69\%$ and $\sim 38\%$ of the monolayer value $v_F = 1 \times 10^6 \text{ m s}^{-1}$ respectively. Such a reduction is theoretically expected: with the commonly found hopping energy of $t^\theta = 0.1 \text{ eV}$, eq. 2.22 yields $\sim 62\%$ of v_F for the examined sample's twist angle of 2.5° : This is close to the situation in layer 1; lower \tilde{v}_F in layer 2 and corresponding asymmetry between layers may have two different causes:

Firstly, the Fermi velocity v_F in MLG has been shown to significantly depend on the used substrate[160]; layer asymmetry may thus be given through the different environment of top and bottom layer: the former is lying on top of the latter which thus effectively acts as graphene substrate, where the latter in turn senses the graphene top layer and is under the added influence of the underlying SiO_2 -substrate.

In praxis, screening of electron-electron interaction by impurities will significantly lessen the theoretically expected severity of the effect though[160, 161]. As discussed in ref.[78] moreover, slowdown of carrier velocity due to electron-phonon interactions in contact to a substrate is strongly suppressed in the presence of electronic coupling in multilayer systems.

A more likely explanation is therefore found in electron-hole asymmetry: $\tilde{v}_{F_e} > \tilde{v}_{F_h}$ has been observed in STM[78] and transport studies[80] on TBG; as the above carrier velocities correspond to electrons in layer 1 and holes in layer 2 (see figs. 5.4 c and 5.8 b), the findings are in qualitative accord with the named references.

To combine thus far acquired data into a comprehensive picture of the examined TBG system, the screening model from sec. 2.3.1 shall be applied to the here examined sample. As the extracted charge carrier concentrations (fig. 5.4 c) suggest significant energetic offset between layers, an additional feature is implemented as motivated and described by means of fig. 5.7 in the following:

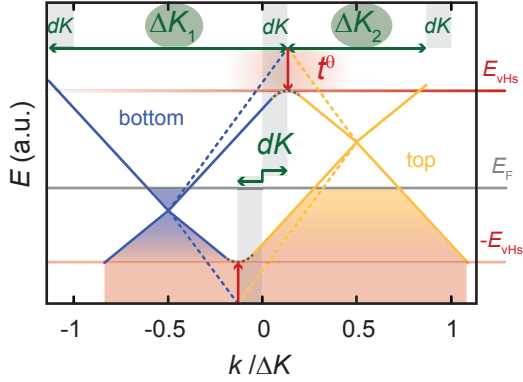


Figure 5.7 Schematic of the low-energy TBG dispersion under interlayer bias. Reciprocal-space axis is scaled by the magnitude of rotational displacement ΔK between Dirac points of bottom (blue) and top layer (yellow). Dashed lines indicate dispersions in the absence, solid lines in the presence of interlayer coupling t^θ (red arrow). Position of crossing bands is shifted away from midpoint between Dirac points ($k = 0$) by an amount of dK (gray bars). Effective reciprocal distances $\Delta K_{1,2}$ for the estimation of layer-specific \tilde{v}_F are indicated as green arrows to the top of the figure.

The separation between a given Dirac point and crossing of dispersions in the absence of coupling scales proportionally in energy and momentum via the slope of bands i.e. native Fermi velocity. A finite interlayer hopping lowers the bands by a constant energetic amount of t^θ though, which should lead to a disproportionately larger effect in Fermi velocity renormalization when the Dirac point is closer to the crossing (as applies to the conduction band of the top and valence band of the bottom layer in the example of fig. 5.7).

The quantitative behavior of the described effect may be estimated via the definition of rescaled effective magnitudes of displacement $\Delta K_{1,2}$: Due to the energetic offset, crossing between individual layers' Dirac cones in k -space is shifted away from midpoint between rotationally displaced K -points by an amount of dK , as illustrated in [fig. 5.7](#). Measured from a given Dirac point, crossing of dispersions takes place at $\Delta K/2 \pm dK$; an effective magnitude of displacement is therefore given by

$$\Delta K_{1,2} = \Delta K \pm 2dK,$$

as indicated by green arrows to the top of [fig. 5.7](#). According values are fed into the equation for reduction in Fermi velocity ([eq. 2.22](#)) which is thereby rendered specific to the individual layer as well as carrier polarity. Corresponding dynamic adjustment of \tilde{v}_F is implemented in the screening model from [sec. 2.3.1](#), which may now be fit to the extracted data sets of top and bottom layers' Fermi velocity and carrier concentration.

A fixed parameter is herein given by rotational mismatch which is known as 2.5° from Moiré pattern resolution. Furthermore, and based on the above discussion on asymmetry in Fermi velocity, the native value v_F is assumed layer-symmetric and fixed at $1 \times 10^6 \text{ m s}^{-1}$ which is typical for graphene on SiO_2 [\[161\]](#).

Interlayer distance is held flexible, as the measured value of $\Delta h = 6.2 \text{ \AA}$ is likely reflecting a corrugated morphology (see [sec. 2.1.4](#) and [sec. 4.2.2](#)) and effective Δh_{eff} in interlayer capacitance can accordingly be expected to deviate. Further fitting parameters are $t_{\text{e,h}}^\theta$ which account for electron-hole asymmetric reduction in Fermi velocity; the parameter of doping charge δn sensitively determines the offset between individual layers' CNPs in backgate voltage. Finally, ΔU adjusts the overall offset of features in U_{BG} .

Figure 5.8 shows calculations via the screening model as fit to data from fig. 5.6 (black bars in panel a) and fig. 5.4c (dots in panel b) with the optimized set of parameters listed in tab. 5.1.

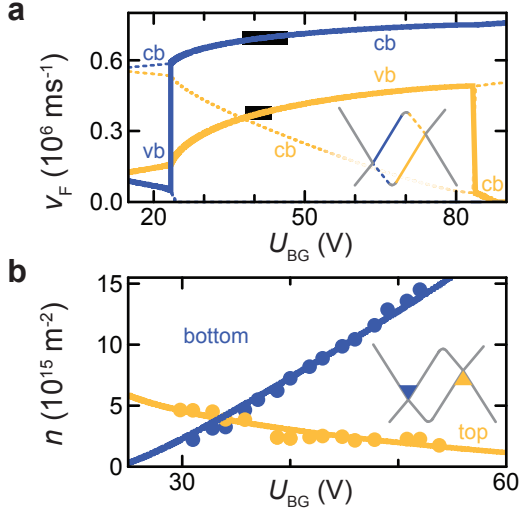


Figure 5.8 Fits of the extended screening model to TBG data; fixed parameters are $\theta=2.5^\circ$ and $v_{\text{F}}=1 \times 10^6 \text{ ms}^{-1}$, fit parameters are listed in tab. 5.1. **a:** Fits to Fermi velocities: bold black line segments indicate average velocities in bottom (higher) and top (lower) layer from fig. 5.6. Solid lines are fit evolutions of \tilde{v}_{F} in the carrier polarity hosting Fermi energy (notice the switch between conduction band [cb] and valence band [vb] at the bottom layer's $U_{\text{CNP}} \approx 25 \text{ V}$ and the top layer's $U_{\text{CNP}} \approx 85 \text{ V}$); dashed lines model the opposite carrier polarity. **b:** Lines: fits to the charge carrier densities extracted from frequency of SdH-oscillations (dots) in bottom (blue) and top layer (yellow).

Fermi velocities as well as offset in gate voltage and curved evolution of carrier densities are nicely reproduced with the parameters listed in [tab. 5.1](#).

t_e^θ (eV)	t_h^θ (eV)	δn (m ⁻²)	U_Δ (V)	Δh (Å)
0.108	0.154	-7.3×10^{15}	10.5	10

Table 5.1: Fitting parameters in the extended screening model as applied in [fig. 5.8](#).

Note that the number of digits in $t_{e,h}^\theta$ reflects correspondingly high sensitivity in calculated \tilde{v}_F at an inflexible v_F . Variation of the native Fermi velocity by $\pm 0.05 \times 10^6$ m s⁻¹ around the fixed value of $v_{F=1} = 1 \times 10^6$ m s⁻¹ is found to be compensated by $\sim \pm 0.01$ eV in both polarities' hopping parameter t^θ , thus establishing a realistic assessment of accuracy.

The value of $t_e^\theta \approx 0.11$ eV compares well to the most typically found magnitudes of interlayer hopping. Its counterpart of $t_h^\theta \approx 0.15$ eV on the valence-band side lies at the upper border of a recently reported range of hopping energies[44]; the origin of different t^θ is likely to be found in the morphology of sample and substrate (see also ref.[44]).

A relatively small offset voltage of $U_\Delta \approx 10$ V suggests largely symmetric doping around $\delta n \approx -7 \times 10^{15}$ m⁻² in each layer (note that dispersion is layer-symmetric at $U_{BG} = U_\Delta$; compare [sec. 2.3.1](#)).

On one hand this may simply be due to processing chemicals. In this case however, the doping concentration would be quite high in comparison to similarly produced [TBG](#). Furthermore, the top layer can generally be expected to suffer disproportionately more from exposure to [PMMA](#) and processing solvents, where the covered bottom layer is mostly protected; this is in discord with the discussed indication for layer-symmetric doping.

Alternatively, an intrinsic offset in Fermi energy has been connected to electron-hole asymmetry in TBG[8]. From eq. 2.15 and with $\tilde{v}_F \approx 0.1 \times 10^6 \text{ ms}^{-1}$ at $U_{\text{BG}} \approx 10 \text{ V}$ (as extrapolated in the screening model), the corresponding shift in Fermi level is estimated as $\sim 0.01 \text{ eV}$ which lies well within the range of prediction for turbostratic graphite[162].

Interestingly, the effective interlayer distance of $\Delta h_{\text{eff}} \approx 10 \text{ \AA}$ is much larger than the measured one at 6.2 \AA . Calculations for the effective capacitance of a corrugated double-layer system are complicated; the exact shape of interlayer distance modulations is unknown. A possible range of effective Δh_{eff} is therefore determined from consideration of extreme cases:

- The least possible layer separation is generally defined by the Bernal-stacked value of $\Delta h_{\text{AB}} = 3.35 \text{ \AA}$ and potentially given at corrugation minima.
- As argued in sec. 2.1.4, corrugation may symmetrically take shape in top and bottom layer alike; in this scenario, maximal interlayer distance is given by $2 \cdot 6.2 \text{ \AA} - \Delta h_{\text{AB}} = 9.05 \text{ \AA}$ (see illustration in fig. 5.9).

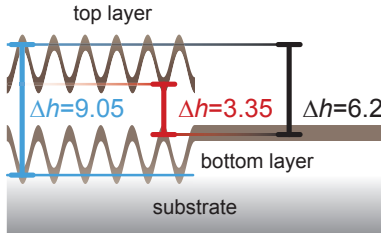


Figure 5.9 Symmetrically corrugated TBG. Minimal interlayer distance (red) is found between corrugation dips, measured Δh is indicated in black, maximal layer separation between corrugation peaks is indicated in blue.

The correspondingly established morphological maximum around 9 \AA is only slightly below the above found $\Delta h_{\text{eff}} \approx 10 \text{ \AA}$ from fits to the electrical measurements. Note that an even larger discrepancy between $\Delta h_{\text{eff}} \approx 1.5 \text{ nm}$ and $\Delta h_{\text{AFM}} \approx 6 \text{ \AA}$ was found in ref.[15] for another TBG on a SiO_2 substrate, although the accuracy of the according AFM topography measurements may have been limited.

For a TBG device encapsulated in hBN on the other hand, interlayer capacitance indicated significantly lower effective heights[97], which fits the suggested dampening effect of the corresponding substrate environment on lattice corrugation, as discussed towards the end of sec. 2.1.4.

With this, the low-energy range between $\sim U_{\text{BG}} = 20 \text{ V}$ and $\sim U_{\text{BG}} = 50 \text{ V}$ has been characterized:

Two superposed SdH-oscillations are identified as contributions from top and bottom layer.

Evolution of carrier densities and reduction of Fermi velocities are fit by a screening model accounting for dynamic, layer-asymmetric reduction in Fermi velocity and induction of charge via the backgate.

Fitting results suggest pronounced electron-hole asymmetry in the interlayer hopping parameter t^θ and a nearly layer-symmetric offset around -0.01 eV in Fermi energy for the unbiased dispersion.

As further fitting parameter, a large effective layer separation of $\Delta h_{\text{eff}} \approx 10 \text{ \AA}$ is found and connected to lattice corrugation in the examined scenario of TBG on a substrate of SiO_2 .

On a practical note, the sum of n_b and n_t from fig. 5.8 provides a new way of scaling the energetic dimension in terms of total charge carrier density n_{tot} , which is used alternatively to backgate voltage U_{BG} in the following.

5.1.3 High Fermi Energy

Transport signatures at higher absolute Fermi energy appear qualitatively different from the above examined low-energy range.

Figure 5.10 shows according measurements in the regime of electron conduction: In the derivative dR/dB , straight Landau fan features are clearly resolved in showing a disruption at intermediate magnetic fields around $B = 6.5$ T (panel a). As indicated by colored arrows, oscillation minima from low magnetic fields can approximately be extrapolated to oscillation maxima in high fields and vice versa; this suggests a corresponding phase shift of π .

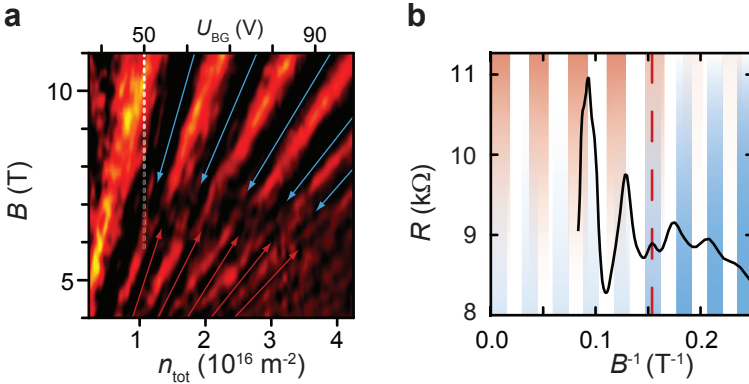


Figure 5.10 a: Differential resistance in dependence on magnetic field B and U_{BG} as well as n_{tot} . A discontinuity in the high-energy Landau fan is marked by colored arrows (note that the low-energy LL left of the dashed white line evolves without disruption). **b:** Resistance vs. inverse magnetic field at $n_{\text{tot}} = 2.97 \times 10^{16}$ m $^{-2}$. Colored bars of half a wavelength in B^{-1} approximate high-field (red, small B^{-1}) and low-field (blue, large B^{-1}) oscillations respectively.

In [fig. 5.10 b](#), resistance is displayed vs. inverse magnetic field at a fixed carrier concentration: Here too, two different regimes of quantization can be discerned. The frequency and phase of SdH-oscillations are approximated for low- and high-field data by accordingly colored bars, finding the following distinctions:

Firstly, the wavelengths in B^{-1} are slightly different between oscillations at high magnetic fields (red) and low fields (blue), indicating an offset in involved carrier density.

Secondly, the phase shift of π , suggested in [fig. 5.10 a](#), is confirmed: notice how at low B^{-1} , a given maximum is described by the transition from a red bar to a void (left to right), where at high B^{-1} (traced by blue bars), the order is reversed.

The above described points shall be investigated more closely in the following, starting with SdH-frequencies and corresponding n :

[Figure 5.11 a](#) shows a further example of an oscillation; the wavelengths indicated by colored bars correspond to frequency peaks revealed in a corresponding fast Fourier transform (FFT), as shown in panel b. To enable an efficient overview, data have been rescaled in B^{-1} and subjected to Fourier transformation over a wider range in n_{tot} ; lower panels of [fig. 5.11](#) show the derivative in the direction of B_{F} (i.e. frequency in B^{-1}):

A double-peak structure like the one in panel b is observed at high positive as well as negative Fermi energies, as indicated by dashed lines in [fig. 5.11 c,d](#). Evolution of frequency appears linear; both regimes share an equal slope. Closer examination identifies larger frequency in the low- B^{-1} than in the high- B^{-1} regime for negative n_{tot} (see also example in [fig. 5.11 b](#)) and smaller frequency in low B^{-1} for positive n_{tot} (see also example in [fig. 5.10 b](#)).

Frequencies proportionally relate to charge carrier concentration via [eq. 2.36](#). Thusly calculated n (corresponding to linear approximations, dashed lines in [fig. 5.11 c,d](#)) scale with a proportionality factor close to unity with respect to n_{tot} (assuming fourfold degeneracy).

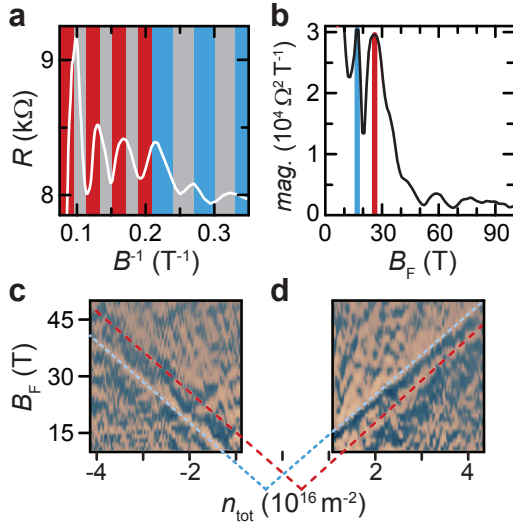


Figure 5.11 **a:** Resistance vs. inverse magnetic field at $n_{tot} = -2 \times 10^{16} m^{-2}$. Periods in B^{-1} correspond to frequency peaks in **b**, according to color-code. **b:** FFT of **a**: a double-peak is indicated by colored lines. **c:** Derivative d/dB_F of the FFT over resistance vs. inverse magnetic field for a range of carrier densities in the regime of hole-conduction; frequency peaks from **b** can be identified over the whole parameter range (dashed lines, color-coded in accordance with **a,b**). **d:** Same as in **c** but for positive n_{tot} .

From the above observations, SdH-oscillations in the examined high-energy range are attributable to a coupled system, as the entirety of backgate-induced charge is involved in according quantization. With respect to n_{tot} , extrapolated charge neutrality is slightly offset into the negative (low magnetic field oscillations) and positive (high magnetic field oscillations) respectively.

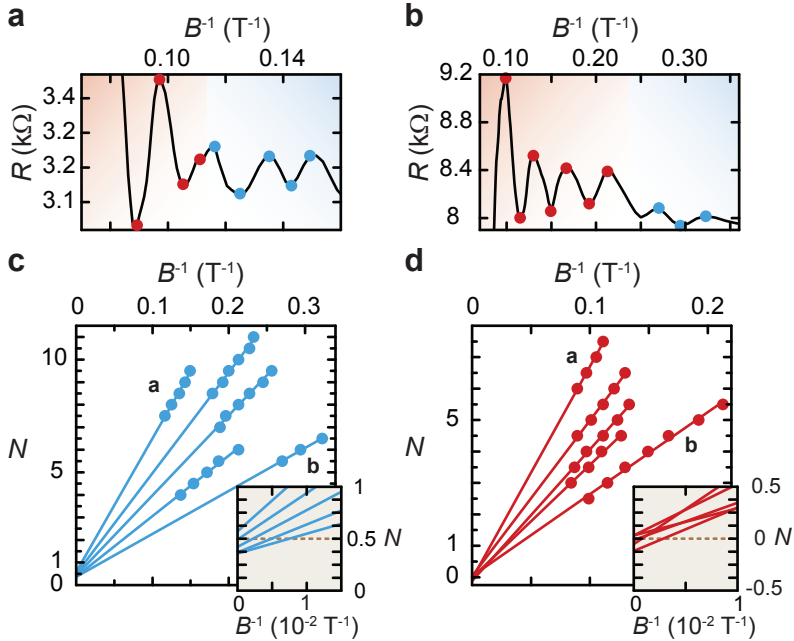


Figure 5.12 a,b: Resistance vs. inverse magnetic field at $n_{\text{tot}} = -6 \times 10^{16} \text{ m}^{-2}$ and $n_{\text{tot}} = -2 \times 10^{16} \text{ m}^{-2}$ respectively. Red and blue backdrops indicate different ranges of quantization, colored dots mark extrema in *SdH*-oscillations (numbered as integer for minima and half-integer for maxima). **c:** Number of extremum N in *SdH*-oscillations vs. inverse magnetic field for the range of quantization in large B^{-1} (blue backdrop in **a,b** as well as three further not depicted examples). Lines are linear fits to data; inset shows a magnified region of intercept with the N -axis. **d:** Same as **c** but for the range of quantization in small B^{-1} (red backdrop in **a,b** as well as three further not depicted examples).

Next, quantitative information about the Berry phase in the two observed regions is acquired as presented in [fig. 5.12](#).

In a proceeding similar to the ones described in refs.[6, 7, 99], extrema in oscillations are numbered by integers (minima) and half-integers (maxima) from small to high B^{-1} ; this is done separately for both regimes of quantization as suggested by colored dots in the examples shown in [fig. 5.12](#) a,b.

Panels c and d show the according number N over position in inverse magnetic field at the two depicted (panels a,b) and three further carrier concentrations. Extrapolation to $B^{-1} = 0 \text{ T}^{-1}$ is performed via linear fits to N .

For high B^{-1} (blue), the inset shows intercepts close to $N(0 \text{ T}^{-1}) = 0.5$, which indicates a Berry phase of π .

At low B^{-1} (red), the intercepts center around $N(0 \text{ T}^{-1}) = 0$, indicating a Berry phase of 2π (or multiple integers).[6, 7, 99]

In intermediary summary, figure 5.13 provides an overview of thus far established TBG signatures: Two superposed SdH-oscillations with Berry phase of π indicate effectively decoupled monolayers at low energy (middle range, yellow). At high absolute Fermi energies, oscillations indicate a coupled system; the Berry phase changes from π (blue area) to $i \times 2\pi$ (red area) at intermediate magnetic fields (where i is an integer including zero).

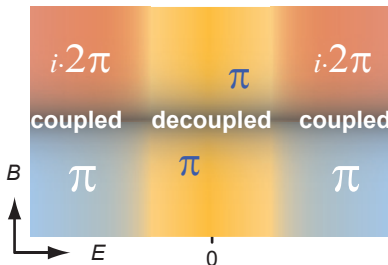


Figure 5.13 Schematic overview of distinct regimes: At low energy, two decoupled monolayers are quantized at $\beta = \pi$. At high energies, a coupled TBG-system is quantized at magnetic-field-dependent Berry phase.

The observed transition in Berry phase in conjunction with layer coupling constitutes a highly interesting TBG signature. A Berry phase of $\beta = i \times 2\pi$ corresponds to an even topological winding number which is in turn indicative of an even number of Dirac points, enclosed by a given cyclotron orbit in reciprocal space[98, 99]. In TBG, there are three possible scenarios for this:

1. The first one is discussed in sec. 2.3.2 and illustrated in fig. 2.39 b: a winding number of zero is found for a hole-like band above the vHs[50, 90]; corresponding LL originate in high n and evolve in opposite direction to the ones around the original Dirac points. As here observed high-energy LL originate in the vicinity of top and bottom layers' original Dirac cones, the above backfolding scenario can be discarded for the present consideration.
2. A study on TBG with high gated layer asymmetry found supposed oscillations with intercepts $N(0 \text{ T}^{-1})$ around zero and 0.5 respectively[91] (in an analysis similar to the one presented in fig. 5.12). The observations are attributed to the filling of a second subband; here, the winding number corresponding to $N(0 \text{ T}^{-1}) = 0$ is two, as cyclotron orbits enclose both layers' Dirac points. In contrast to the above described mBz-scenario[50, 90], the band with 2π -quantization is not connected with a change in carrier type, which is in accordance with the behavior found in the present work. In disagreement however, no sign of a parallel subband is found; furthermore, the degrees of layer asymmetry are not comparable.
3. As discussed in sec. 2.3.2 and illustrated in fig. 2.39 a, refs.[19, 20] predict a transition in Berry phase from $\beta = \pi$ to $\beta = 2\pi$ upon crossing the vHs. Carrier type and associated direction of LL-evolution stay undisrupted at the transition point which fits the here observed behavior.

5.1 Berry Phase Transition in a Twisted Graphene Bilayer

The most likely explanation for the here observed phenomena therefore lies in scenario 3. which will be briefly recapitulated in the following. Figure 5.14 b shows the schematic of a TBG dispersion as introduced in sec. 2.2.2:

Below the vHs, cyclotron orbits enclose one Dirac point each, which corresponds to a Berry phase of π . In the absence of inter-layer bias or asymmetric doping, top and bottom layers' LL-energies are degenerate. Accordingly, ref.[19] finds an eightfold degenerate MLG-sequence (twofold spin, valley and layer) at energies $E < E_{vHs}$ (fig. 5.14 a).

Above the vHs, a single cyclotron orbit encloses both Dirac points due to the change in the dispersion's topology. This corresponds to a Berry phase of 2π and thus the LL-sequence of a Bernal-stacked bilayer, as evident from the indicated filling factors in fig. 5.14 a.

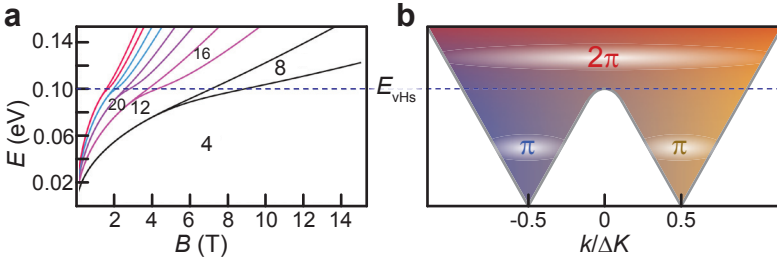


Figure 5.14 a: From ref.[19]: LL-evolution in dependence on energy and magnetic field for a TBG of around $\theta = 2^\circ$. Dashed line marks the position of vHs-energy; numbers in the panel indicate filling factors. **b:** Schematic of TBG dispersion: Dirac cones of individual layers (blue, yellow) are displaced in momentum by ΔK ; the dispersion merges at the vHs. White stripes signify Landau levels corresponding to cyclotron orbits encircling one ($E < E_{vHs}$) and two Dirac points respectively ($E > E_{vHs}$).

In connection to the above model, AB-bilayer-like quantization has previously been found in a TBG sample grown from SiC[92]; however no evidence for MLG-like quantization (and for the lack of this, no phase transition) could be resolved.

Although the described model does not account for the here found energetic offset and corresponding asymmetries between layers (sec. 5.1.2), it captures the main observation of a transition between two decoupled Dirac cones at low and one coupled system with a Berry phase of 2π at high energies.

Interestingly, ref.[20] finds a unitless value

$$\mathbf{b} = \sqrt{\frac{\hbar}{8eB}|\Delta K|}, \quad (5.2)$$

which determines between massless- or massive-like energetic sequence E_{LL} of LL: For $\mathbf{b} > 1$, E_{LL} resembles the spectrum of massless carriers like in MLG; at $\mathbf{b} < 1$, E_{LL} starts to scale equidistantly as associated with a constant carrier mass.

The critical magnetic field up to which massless behavior is retained, accordingly lies around 45 T, which is well above the here examined range for the studied twist of $\theta=2.5^\circ$ (determining ΔK).

To test this prediction, Fermi velocities are extracted from temperature dependence of SdH-oscillations in the coupled range as depicted in fig. 5.15 a (using eq. 2.38 like in the low-energy range). Oscillations with Berry phase of π at low magnetic fields prove too shallow for extraction of reliable data. However, 2π -data in high magnetic fields reveal constant Fermi velocity close to the one of native graphene as depicted in fig. 5.15 b.

This establishes further congruence with theoretical prediction for the assumed scenario[19, 20]. Furthermore, the coalescence of massless signature and $\beta = 2\pi$ constitutes a novel experimental observation and reveals yet another variation in graphene-based systems.

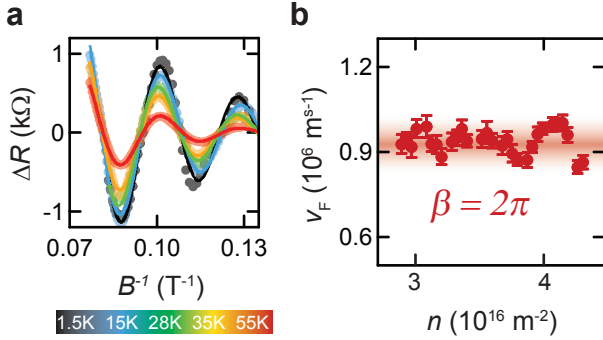


Figure 5.15 a: Temperature-dependent damping of SdH-oscillations at $n_{\text{tot}} = 3.68 \times 10^{16} \text{ m}^{-2}$ and $\beta = 2\pi$ (color-coded according to legend in the bottom). A background resistance has been removed (analog to the proceedings is the low-energy range); lines are fits of eq.2.35 to data. **b:** Fermi velocities as calculated from effective masses m^* extracted from temperature-dependent fits like in **a** and corresponding charge carrier densities; v_F appear constant around $0.94 \times 10^6 \text{ m s}^{-1}$.

Not captured in the above discussed model[19, 20] is the persistence of $\beta = \pi$ at low magnetic fields in the coupled range.

Firstly, this could simply be ascribed to a region of transition between decoupled $\beta = \pi$ and coupled $\beta = 2\pi$ -regimes (fig. 5.13, yellow and red respectively), as described in the following:

In the symmetric scenario from refs.[19, 20], the transition in LL-degeneracy (splitting lines, fig.5.14 a) is where the change in topology comes into effect. Though splitting of different LL takes place over a narrow energetic range, closely centered around the vHs, there is still some spread as evident from fig. 5.14 a: notice e.g. that filling factor $\nu=8$ reaches around 0.02 eV below E_{vHs} .

Ref.[20] finds a dependence on \mathfrak{b} again (eq. 5.2): critical fields are 9.5 T, 5.1 T and 3.5 T for the first three nonzero LL at $\theta=2.5^\circ$, which is comparable to the range between 6 T and 7 T observed in fig. 5.10 a.

A further energetic spread of the transition in topology could potentially be accounted for by the gated layer asymmetries in the here examined case.

Moreover however, two interesting cohesions are found in the collective picture of extracted charge carrier densities, which may further the understanding of coupling between energetically offset Dirac cones:

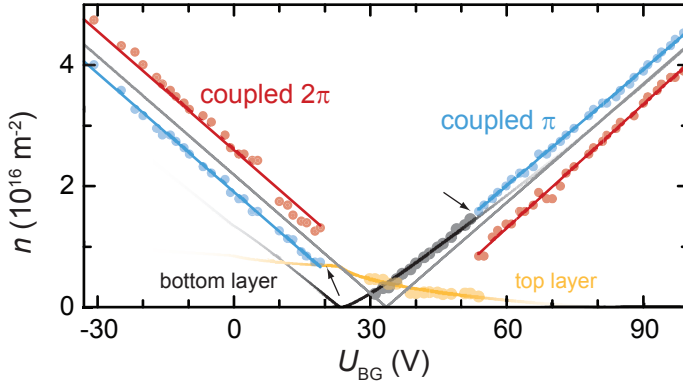


Figure 5.16 Charge carrier densities vs. backgate voltage. **Black, yellow:** bottom and top layer data from fig. 5.8; fit curves are extrapolated according to the screening model. **Gray:** n_{tot} as calculated from n_{b} , n_{t} . **Red, blue:** extracted in the coupled regime from SdH-oscillations at $\beta = 2\pi$ (red) and $\beta = \pi$ (blue); lines are linear fits to the data.

Figure 5.16 shows n_b and n_t as well as n_π and $n_{2\pi}$, as extracted from frequency of SdH-oscillations.

Notice how $n_b \approx n_\pi$ at the decoupled-coupled transition around $U_{BG} = 50$ V; $n_t \approx n_\pi$ is found on the opposite side around $U_{BG} = 20$ V, where n_t could not reliably be extracted but is extrapolated via the screening model.

Notice further that $n_\pi - n_{2\pi} \approx 6 \times 10^{15} \text{ m}^{-2}$ which is about the number of states in a fourfold degenerate Landau level at a magnetic field of $B_{\text{trans}} = 6.5$ T which, in turn, is where the transition in Berry phase is observed (fig. 5.10 a).

In a possible interpretation of the above observations, the coupled system with Berry phase of π takes over in the dominant layer's Dirac cone (bottom layer on electron, top layer on hole side), where Fermi energy is close to the Dirac point in the other layer. Exclusion of this other layer may be linked to the vicinity between Dirac point and crossing of individual MLG bands (fig. 5.7), which can be expected to affect the dispersion most severely as discussed in sec. 5.1.2: In estimation of accordingly reduced Fermi velocities; the proposed screening model finds near-zero \tilde{v}_F in the excluded layer around the transition energy (fig. 5.8 a: conduction band of the top layer [dashed yellow line] at $U_{BG} \sim 50$ V, and valence band of the bottom layer [solid blue line] at $U_{BG} \sim 20$ V).

One may further speculate that the respective layer excluded in n_π comes back into play in the following way: Note that

$$n_b \approx n_t \approx \frac{n_\pi - n_{2\pi}}{2}$$

at the decoupled-coupled transition. According to the above consideration, this approximately corresponds to a twofold degenerate Landau level at the magnetic field B_{trans} of Berry phase transition.

Note that the zeroth LL in MLG extends with twofold degeneracy into electron and hole branch of the dispersion each. For $B > B_{\text{trans}}$, Fermi energy will therefore jump to the Dirac point of the respective low- n layer, as depicted in fig. 5.17.

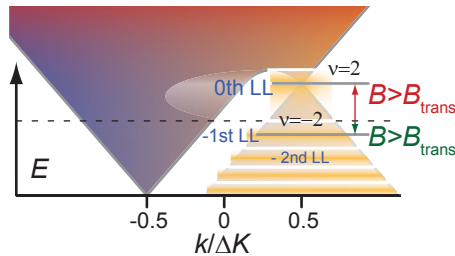


Figure 5.17 Schematic of a layer-asymmetric TBG dispersion. LLs in the top layer’s hole branch (right) are indicated in shaded yellow. Depending on magnetic field, the Fermi energy E_F (gray lines) is pinned in the zeroth LL at the Dirac point or in the minus first LL, where the dashed black line marks E_F in the absence of Landau quantization.

The described transition of Fermi energy into a zero mode conceivably plays a decisive role in the observed magnetic-field dependence of the Berry phase transition, as involvement of both layers’ Dirac points is crucial to the observation of $\beta = 2\pi$. Moreover, associated energetic jumps may explain the offset in carrier densities between the coupled Berry-phase-of- π and -2π systems (figs. 5.11 and 5.16).

While the above considerations are merely speculative, they point out a number of interesting coherencies and suggest mechanisms behind the persistence of high-energy $\beta = \pi$ -quantization and Berry phase transition at absolute Fermi energies which are slightly below the expected vHs.

In summary, Landau quantization of a coupled TBG system with constant Fermi velocity and Berry phase of 2π is observed in high Fermi energies, according with theoretical prediction.

Not theoretically described as yet, carrier densities in the coupled range appear offset with respect to n_{tot} from the low-energy range; moreover, signatures of a coupled TBG system at Berry phase of π persist in high energies and low magnetic fields.

Corresponding phenomena are discussed on the basis of the energetic layer asymmetries established in [sec. 5.1.2](#). As mechanism behind the transition between π and 2π in Berry phase, magnetic-field-dependent pinning of Fermi energy into the zeroth LL of the respective layer with lower carrier concentration is proposed.

The above findings highlight the fascinating physics to be witnessed in small-angle TBG. The energetic range of interlayer coupling, enriched by asymmetrical gating, exhibits a number of interesting peculiarities, which should encourage further theoretical treatment of the matter.

Note that the model from refs.[[19](#), [20](#)], underlying the above interpretation of transport phenomena in the examined TBG of $\theta=2.5^\circ$, neglects backfolding into the superlattice mBz. While this principal has also been found to apply in TBG of similar rotational mismatch from SiC[[92](#)] and CVD[[91](#)], signatures of the contrasting backfolding scheme were recently found in a further device of comparable twist angle[[90](#)] which, unlike the others, was embedded between layers of hBN. As discussed in [sec. 2.1.4](#), such encapsulation should greatly restrict out-of-plane lattice corrugation.

The described correlation of distinctions in real-space and electronic structure may thus be taken to emphasize the important role of sample morphology on electronic properties in TBG as introduced in [sec. 2.1.4](#) and discussed in [sec. 2.2.3](#).

5.2 Satellite Landau Fans in Twisted Graphene Bilayers

In the following section, two qualitatively similar transport signatures in small-angle TBG samples are presented: Satellite Landau fans with origin in higher carrier density away from the main charge neutrality are observed in longitudinal magnetoresistance. Parts of the presented data are published in ref.[12].

In the first sample A, a pronounced satellite fan is found at positive energy. Degeneracy and position in carrier density are analyzed, additional features evaluated. Observations are discussed with respect to the coupling models introduced in sec. 2.2.2 and sec. 2.2.3.

Satellite features in the second presented sample B are most pronounced at negative energies. Details are investigated, differences to the first presented signatures in sample A are discussed; it follows an evaluation in terms of possible underlying coupling scenarios.

5.2.1 Sample A

The here examined TBG sample was again created via folding, as byproduct of mechanical exfoliation.

Figure 5.18 provides information about sample geometry and scheme of electrical contacts: As suggested in the bottom panel, the area marked in brown forms a connected plane which has been flipped over onto the gray area as well as the substrate to the left (assumption of this scenario is rooted in AFM measurements where different sharpness of covered [by the top layer] and uncovered edges is observed). A TBG area is thus created between MLG portions of top and bottom layer each, which are electrically contacted as indicated in the top panel.

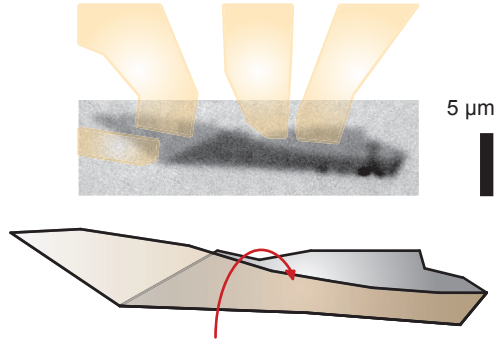


Figure 5.18 *Top: Optical picture of the TBG sample; position of later defined electrical contacts is marked by transparent bars. Bottom: Schematic of sample geometry; the area marked in brown marks the top layer which has been folded over onto the bottom, protruding onto the substrate to the left.*

A twist angle of 1.6° is extracted from an AFM-resolved Moiré period of 9 nm as demonstrated in [fig. 4.10](#) of [sec. 4.2](#). Note that this potentially places the sample in a range beyond the applicability of the commonly employed continuum model ([sec. 2.2.2](#)).

The interlayer distance lies at $5.8 \text{ \AA} \pm 0.5$ as extracted from AFM topography measurements; the value is likely influenced by superstructure corrugation, as discussed on [fig. 4.15](#) and in [sec. 5.1.2](#).

Electrical measurements were carried out across the TBG area in four-probe configuration at a current of $200 \text{ nA} + 100 \text{ nA}$ with DC (first) and AC contributions (second, frequency of 18.33 Hz). Measuring temperature was kept at 1.5° .

Figure [5.19](#) shows a map of resistance in dependence on backgate voltage and magnetic field:

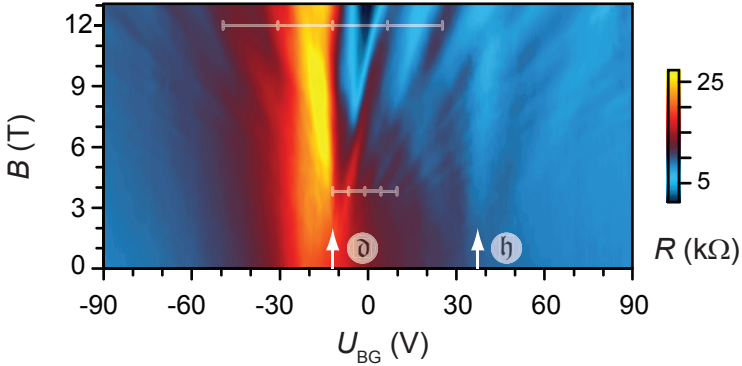


Figure 5.19 Resistance vs. backgate voltage and magnetic field. Origin of two Landau fans is indicated by white arrows. Transparent scales in the middle of the panel trace equidistant maxima in SdH-oscillations of the dominant Landau fan \mathfrak{d} .

The measurement reveals evolution of Landau levels in SdH resistance modulations; clearly resolved are two Landau fans with origin in different carrier concentration.

As evident from [fig. 5.20](#), charge neutrality in the electric field effect at zero magnetic field is located at the origin of the more prominent set of SdH-features which will therefore be referred to as dominant Landau fan \mathfrak{d} in the following. Where evolution of conductance is undisrupted and linear on the hole-side, a dip is observed around the origin of the SdH-features around higher positive energy which are from hereon out referred to as higher Landau fan \mathfrak{h} .

Resistance maxima in Landau fan \mathfrak{d} appear equidistant in backgate voltage at a fixed magnetic field (transparent white bars, [fig. 5.19](#)), which indicates quantization of a coupled TBG system as opposed to the screening scenario in the last-analyzed measurements ([sec. 5.1](#)).

From the spacing ΔU_{BG} in gate voltage, a capacitive coupling of $C^* = 6.6 \times 10^{14} \text{ V}^{-1} \text{ m}^{-2} \pm 0.3$ is determined via eq. 2.33a under assumption of fourfold degeneracy. The value agrees well with expectation from the thickness of the SiO_2 -dielectric (sec. 3.4); all of the backgate-induced charge carriers can therefore be assumed to occupy the quantized states in the dominant Landau fan over the examined energetic range. The measuring parameter of backgate voltage may accordingly be translated to a charge carrier concentration with $n=0$ around the minimum of the field effect conductance, as applied to depictions on the following pages.

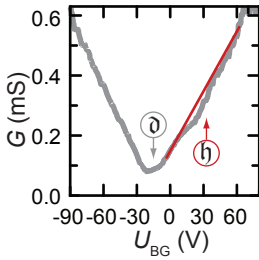


Figure 5.20 Conductance vs. backgate voltage at $B = 0 \text{ T}$. Main charge neutrality lies around $U_{\text{CNP}} = -14 \text{ V}$; a dip in conductance below linear evolution (red line) is observed around $U_{\text{BG}} = 30 \text{ V}$ as indicated by the red arrow.

The higher Landau fan shall be investigated more closely in the following. From fig. 5.19, it becomes already evident that the frequency of corresponding SdH-oscillations is smaller than in the dominant fan (spacing in U_{BG} at constant B is larger).

Figure 5.21 shows a plot of resistance for $n \geq 0 \text{ m}^{-2}$ vs. inverse magnetic field, where LLs emerge equidistantly. As indicated by white dots, the main fan d intersects the higher one h at every one of the drawn equi- B^{-1} lines (transparent white); the higher fan however crosses the same LL out of the dominant fan at only every second interval (indicated by yellow dots).

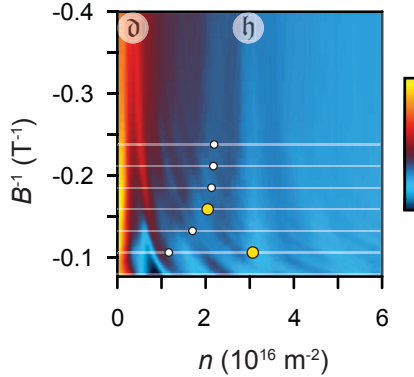


Figure 5.21 Resistance vs. inverse magnetic field and charge carrier concentration in the regime of electron conduction (in the frame of the dominant Landau fan with origin at $n = 0 \text{ m}^{-2}$). Equidistant transparent white lines trace intersections of *LLs* between lower (\mathfrak{d}) and higher Landau fan (\mathfrak{h}). Level of the dominant fan cross the first nonzero one from the higher fan at every line as indicated by white dots. A given level from Landau fan \mathfrak{d} however is crossed at every second interval only, as marked by yellow dots. Colorscale spans $25 \text{ k}\Omega$.

The above relations indicate doubled degeneracy in the higher with respect to the dominant Landau fan. As the latter is fourfold degenerate in accordance with the expected carrier densities, the dispersion quantized in Landau fan \mathfrak{h} is therefore revealed to be of eightfold degeneracy.

Before the isolated signatures are evaluated and put into theoretical context, a further detail is presented in [fig. 5.22](#). Panel a shows differential resistance dR/dB , where the higher Landau fan is resolved as a cross-like feature in the middle of the plot.

Interestingly, a further less pronounced feature of similar shape is found at roughly double the charge carrier concentration.

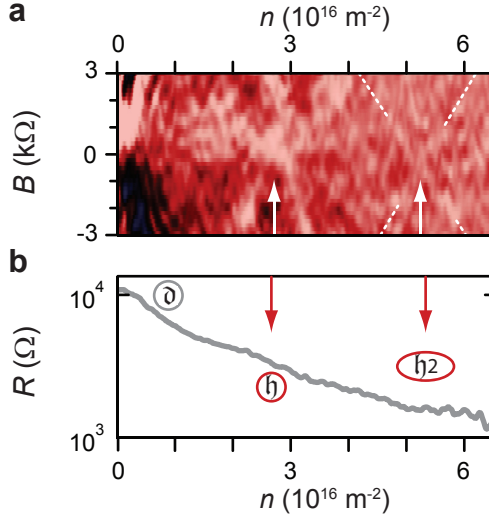


Figure 5.22 a: Derivative dR/dB vs. magnetic field and carrier density. Features of the higher Landau fan are indicated by the left white arrow. At roughly doubled carrier concentration, further cross-like features around the right arrow may be discerned as suggested by dashed white lines. **b:** Field effect resistance at $B = 0$ T in logarithmic display vs. charge carrier density. Elevated features corresponding to the fans from **a** are pointed out by red arrows.

The resistance at zero magnetic field (fig. 5.22 b) correspondingly reveals a further disturbance at higher carrier concentrations (beside the features from Landau fan h already established in fig. 5.20), as marked by the identifier h_2 .

The findings from [fig. 5.22](#) suggest a third Landau fan in the measurements; in light of its weak pronunciation, a more detailed examination is not possible however.

In summary, a dominant Landau fan with **MLG**-like sequence and degeneracy is found to originate near zero backgate voltage. Straight evolution of corresponding **LLs** indicates quantization of a single, coupled system. The field effect at zero magnetic field is roughly symmetric around the fan's origin.

A further, less pronounced Landau fan is found around $n \sim 3 \times 10^{16} \text{ m}^{-2}$ in the reference frame of the fourfold degenerate Landau levels of the dominant fan. This higher Landau fan exhibits the signature of an eightfold degenerate graphene monolayer; its origin in $B = 0 \text{ T}$ is accompanied by a modulation of the field effect resistance around the main **CNP**.

Around $n \sim 5.5 \times 10^{16} \text{ m}^{-2}$, features of a third, least pronounced Landau fan are found, again accompanied by slight modulation of the zero-tesla field effect.

In principal, the here observed scenario is reminiscent of the backfolding schemes introduced in [sec. 2.2.3](#). Here, satellite Landau fans arise at the edge of the lowest subband, where the superlattice **mBz** is filled ([fig. 2.39](#)).

With the here found superlattice wavelength of $\lambda \approx 9 \text{ nm}$, [eq. 2.24](#) finds $n \approx 5.7 \times 10^{16} \text{ m}^{-2}$ for the correspondingly expected number of states, which is roughly double of the span between here observed fans. This renders the explanation via backfolding at the **mBz** boundary somewhat incongruent.

An alternative scenario to witness multiple Landau fans in, is given in Mele's uncompensated class of interlayer coupling[10], as introduced in [sec. 2.2.2](#) and illustrated in [fig. 2.29](#). Here, secondary Dirac singularities form at midpoint between rotationally displaced K -points.

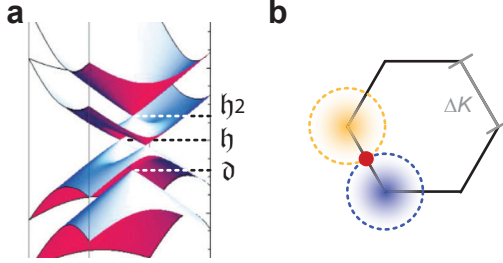


Figure 5.23 a: From ref.[10]: *TBG* band structure in the uncompensated coupling model. Dashed lines to the right have been inserted to indicate the suggested relation to here performed measurements, where numbers signify the origin of dominant (\mathfrak{d}), higher (\mathfrak{h}), and second higher (\mathfrak{h}_2) Landau fan. **b:** Schematic of the *mBz*; secondary Dirac singularities (red dot) arise, where the individual layers' Dirac cones (blue and yellow circles) meet. Span of rotational displacement ΔK is indicated in gray.

The dispersion depicted in [fig. 5.23 a](#) exhibits all of the here identified features, which are

- three instances of local charge neutrality,
- each with *MLG*-like dispersion around Dirac singularities
- and a twofold layer degeneracy in the energetically centered Dirac cones.

The number of states in a circle of radius $\Delta K/2$ is given by

$$\frac{\pi(\Delta K/2)^2}{4\pi^2} \approx 4.5 \times 10^{15} \text{ m}^{-2}, \quad (5.3)$$

where the denominator stems from the two-dimensional k-space volume of a single state and $\Delta K \approx 4.75 \times 10^8 \text{ m}^{-1}$ as calculated for $\theta = 1.6^\circ$ via [eq. 2.21](#).

The two layers' dispersions are thus approximated to meet at $3.6 \times 10^{16} \text{ m}^{-2}$ which derives from [eq. 5.3](#) via multiplication by 4×2 , accounting for graphene's fourfold degeneracy and the filling of both layers' Dirac cones.

The good match of the calculated value to the intervals of $\sim 3 \times 10^{16} \text{ m}^{-2}$ found between origins of Landau fans in the here examined sample makes a strong additional case for the scenario suggested in [fig. 5.23](#).

Two peculiarities in the suggested electronic scenario require special consideration and might be explained via the geometry of the examined sample:

Firstly, the layer degeneracy in Landau fan \mathfrak{h} is not lifted in spite of the asymmetric influence of the backgate, contrasting the observations from the first segment [5.1](#) of this chapter.

Ref. [\[10\]](#) does not treat the case of interlayer bias; one may speculate that the corresponding behavior in the uncompensated class of interlayer coupling is different to the one found in the commonly applied model [\[8\]](#) ([sec. 2.2.2](#)).

Alternatively, the persistence of energetic layer-symmetry is rooted in the comparatively large bare [MLG](#) areas surrounding the [TBG](#) ([fig. 5.18](#)): portions of both bottom and top layer respectively are not screened and under full influence of the backgate to either side of the bilayer area; corresponding lateral enclosure between equally gated top and bottom layer may be assumed to enforce a level Fermi energy in the vertical [TBG](#) arrangement as well.

Secondly, the three Landau fans appear very differently pronounced, which might in principal be ascribed to disorder broadening in the coupled dispersion. In the suggested scenario however, the dominant transport signature \mathfrak{d} is based on the secondary Dirac singularity at negative energies ([fig. 5.23 a](#)), where signatures of the

supposed primary cones (\hbar , [fig. 5.23 a](#)) appear much weaker and the secondary Dirac singularity at positive energies (\hbar_2 , [fig. 5.23 a](#)) is barely pronounced.

It is again tempting to ascribe this to sample geometry and configuration of electrical contacts, as addressed in the above first point: The unscreened, fully gated portions of top as well as bottom layer to either end of the **TBG** area may be speculated to adjust Fermi energies in such a way that states in the single Dirac cone on the valence side of the coupled dispersion are favored in the measured transport from one monolayer portion through the bilayer into the other constituting **MLG** area ([fig. 5.18](#)).

In summary, the alternative coupling model from ref.[\[10\]](#) provides a likely frame for the magnetotransport signatures observed in a twisted bilayer of $\theta=1.6^\circ$.

While the model applied in [sec. 5.1](#) reaches the limits of applicability at this very small interlayer twist, further reason behind qualitatively different signatures observed in the previous [sec. 5.1](#) and the present [sec. 5.2.1](#) may be found in the real-space superlattice: Comparison between [fig. 4.10 a](#) (p. 152) and [fig. 5.2 a](#) (p. 188) reveals different overall appearance, most notably the superior long-range order in the former. Associated distinctions in particular superlattice formation and shape may influence the relation between different coupling terms[\[10\]](#) and thus change electronic situation.

The observation of qualitatively distinct transport signatures in analogly prepared **TBG** with only 1° of difference in rotational mismatch highlights the complexity of the twisted graphene bilayer system. A further instance of satellite Landau fans in longitudinal magnetoresistance is presented in the following and hints towards yet another electronic scenario in small-angle **TBG**.

5.2.2 Sample B

The second sample which shall be investigated in the present section on satellite Landau fans in **TBG** magnetoresistance, is depicted in [fig. 5.24](#): A folded area of $\sim 2\ \mu\text{m} \times 6\ \mu\text{m}$ has been folded over during mechanical exfoliation. Straight sample edges in both bottom (panel b, blue) and top layer (yellow) relate via $\phi \bmod 30^\circ \approx 1.5^\circ$ and $\phi \bmod 30^\circ \approx 0.5^\circ$ to the folded edge, where ϕ indicates the angular difference between native and folded edges respectively; interlayer twist follows as $\theta \approx 2^\circ \pm 1^\circ$ from [eq. 4.1](#).

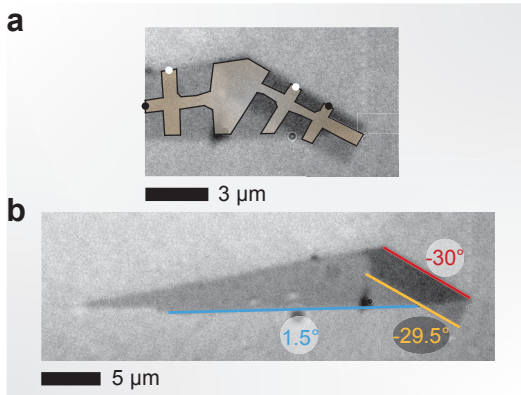


Figure 5.24 a: Optical picture around the **TBG** portion in a folded **MLG** flake; geometry of a subsequently etched sample structure is marked by the brown overlay. Black dots mark position of later defined source, white dots of measuring contacts. **b:** Optical picture of the entire flake; straight edges are traced by colored lines, according angles are indicated in a cartesian frame of reference.

The sample is etched into a defined geometry as indicated by the transparent brown area in [fig. 5.24 a](#).

Electrical measurements are performed at a constant source current with amplitude of 100 nA and AC frequency of 13.3 Hz, which is driven through the TBG area as marked by the black dots in fig. 5.24 a; voltage drop is measured in four-probe configuration (white dots). The measuring temperature is adjusted to 1.5 K.

Sample resistance is determined in dependence on backgate voltage (sweep) and perpendicular magnetic field (step); the derivative dR/dB is depicted in fig. 5.25 a:

Clearly resolved is a main Landau fan with origin close to $U_{BG}=0$ V. At negative gate voltages, additional features are observable in converging towards zero magnetic field; the according fan-like structures have a slightly frayed appearance and are less clearly pronounced than the ones in sec. 5.2.1.

Panel b shows the fast Fourier transform (FFT) of resistance in inverse magnetic field: A major peak is evolving linearly in frequency B_f and gate voltage U_{BG} (mirror symmetric between negative and positive) as traced by the dashed white line for positive U_{BG} . The feature is attributable to SdH-oscillations in the main Landau fan from panel a, where the peak position in B_f is given by the inverse of corresponding wavelength ΔB^{-1} for a given charge carrier concentration n . With eq. 2.36, capacitive coupling in the involved n to U_{BG} is determined via

$$C^* = \frac{4}{\Phi_0} \frac{dB_f}{dU_{BG}}$$

as $C^* \approx 6.4 \times 10^{14} \text{ V}^{-1} \text{ m}^{-2}$, under assumption of fourfold degeneracy. Close similarity to the value of $6.53 \times 10^{14} \text{ V}^{-1} \text{ m}^{-2}$ (reflecting the nominal parameters of the used substrate, see sec. 3.4) indicates absence of screening.

The examined main Landau fan can thus be assumed to arise in quantization of a coupled TBG system; alternatively, as one source and measuring lead each contact the bottom layer only (see fig. 5.24 a),

reflection of the corresponding quantized MLG density of states in the observed main Landau fan cannot be ruled out.).

The FFT in fig. 5.25 b further resolves frequency features associated with the satellite structures observed in panel a: Though not yielding further quantitative information, e.g. on degeneracy, the symmetry of evolution in multiple clusters of frequency peaks suggests more than one center of satellite features in magnetoresistance, as pointed towards by white arrows.

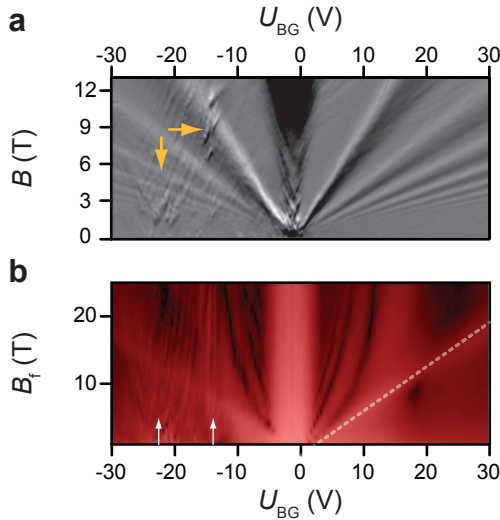


Figure 5.25 a: Derivative dR/dB in dependence on backgate voltage U_{BG} and magnetic field B . Apparent satellite features of Landau quantization are indicated by yellow arrows. **b:** FFT of resistance in inverse magnetic field vs. backgate voltage and frequency in B^{-1} . Linear evolution of the main peak in the regime of electron conduction is traced by a white dashed line.

The regime of electron conduction (in the frame of the main Landau fan) shows no apparent traces of satellite fans or other additional features in the above depictions. A closer look is taken in [fig. 5.26](#):

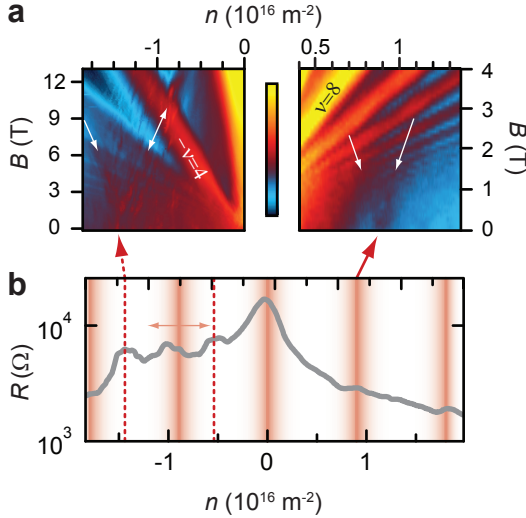


Figure 5.26 a: Close-ups of resistance vs. magnetic field and charge carrier concentration n in the frame of reference of the main Landau fan; according filling factors are indicated for orientation. Satellite Landau fan features are indicated by white arrows. Colorscale spans $90 \text{ k}\Omega$ and $5.5 \text{ k}\Omega$ for left and right panel respectively. **b:** Field effect resistance at $B = 0 \text{ T}$ on a logarithmic scale vs. carrier density n . Marked are equidistantly positioned peaks.

Panel b shows the field effect resistance at zero magnetic field. Like in the measurements presented in [sec. 5.2.1](#), the dominant CNP lies at the origin of the main Landau fan.

The satellite features in negative n , already observed in [fig. 5.25](#), show in three roughly equidistant elevations in resistance, modulating the flank of the field effect.

Furthermore, two lesser peaks are revealed in the regime of electron conduction; the one at smaller n is complemented by a fanning-out evolution in magnetic field as resolved in the close-up on the corresponding parameter space in the right panel of [fig. 5.26 a](#).

Viewed in conjunction, systematic placement of resistance peaks in carrier concentration with constant intervals around $1 \times 10^{16} \text{ m}^{-2}$ becomes apparent, as stressed by the red bars in [fig. 5.26 b](#).

Features on the hole-side may herein be interpreted as split into one primary and two further satellite peaks as suggested by the red arrow; note that the interval of $\sim 5 \times 10^{15} \text{ m}^{-2}$ between locally split features is roughly half the global one.

In summary of the observed transport signatures, satellite peaks in resistance are found to modulate a dominant field effect at $B = 0 \text{ T}$; features arise in regimes of both hole and electron conduction, positions in carrier concentration are systematically related by a characteristic interval of $\sim 1 \times 10^{16} \text{ m}^{-2}$.

At negative carrier concentration, the observed resistance peaks define origins of magnetic-field-dependent evolution in structures reminiscent of Landau-fans; according features appear sharp and pronounced but frayed, limiting the degree of deducible quantitative information about the underlying sequence of Landau quantization.

At positive carrier concentration, satellite features in finite magnetic fields are less pronounced but still clearly evident in the position around lower carrier density at $n \approx 1 \times 10^{16} \text{ m}^{-2}$.

On one hand, the above observations are similar to the ones found in sample A as presented in [sec. 5.2.1](#): Resistance is dominated by a field effect, modulated by **SdH**-oscillations in a fourfold degenerate **MLG** sequence. The according main **CNP** lies close to $U_{\text{BG}}=0$ V. Satellite peaks in various degrees of lesser pronunciation are evident in resistance at zero magnetic field, indicating lessened density of states in equidistantly placed intervals; originating from here, more or less pronounced satellite Landau fans are found to modulate the magnetoresistance.

A couple of major distinctions however point towards a different underlying electronic scenario in the present sample B:

Firstly, satellite features are found to both energetic sides of the dominant **CNP**, which is in contrast to the additional structures in positive U_{BG} only, as found in the previous segment [sec. 5.2.1](#). Where the overall context suggested the fourfold degenerate dominant Landau fan to reflect a secondary Dirac singularity in the according sample A (see discussion towards the end of [sec. 5.2.1](#)), the qualitatively symmetric configuration of satellite features around the main **CNP** suggests the dominant Landau fan to be a primary signature in the here discussed sample B.

Secondly, though a quantitative analysis of the observed satellite fans in sample B proves challenging due to their frayed appearance, a heightened degeneracy like in the center Landau fan of sample A is unlikely: The slope of the most pronounced **LLs** in magnetic field and charge carrier concentration, as pointed out by white arrows in [fig. 5.26 a](#), is comparable to the one of the first nonzero level in the main fan (left panel, [fig. 5.26 a](#): $\nu=-4$) and clearly steeper than the one of the second nonzero level (right panel, [fig. 5.26 a](#): $\nu=8$). Correspondingly assumable presence of satellite **LLs** at a filling factor below $\nu=8$ rules out a layer-degenerate **MLG** spectrum, rather hinting towards the common fourfold sequence instead.

In light of the above considerations, the backfolding scenario from figure 2.31[88], 2.32[93] or 2.33[90] provides the most likely frame for the here observed satellite CNP and LL features (in contrast to the coupling between Dirac cones in the uncompensated class[10] explaining transport signatures in sample A).

According to eq.2.24, filling of subbands in intervals of $1 \times 10^{16} \text{ m}^{-2}$ corresponds to a superstructure unit cell area of $A = 400 \text{ nm}^2$ and a wavelength of $\lambda \approx 21 \text{ nm}$. Assuming the Moiré relation, eq.2.5 finds an interlayer twist of $\theta \approx 0.7^\circ$. Though this angle, as calculated from electronic features, lies 0.3° below the geometrically estimated range of $2^\circ \pm 1^\circ$, an error bar slightly larger than 1° (as deduced from upper and lower bounds according to different edge measurements) is quite conceivable. The scenario of secondary and tertiary features at the edge of subsequently folded subbands thus constitutes a possible explanation for the observed transport phenomena within sensible limits of angular accuracy.

Having established backfolding at the superlattice mBz as a likely general scenario, two important details shall be addressed in the closing:

Electron-hole asymmetry, as here observed in the pronunciation and quantitative play-out of satellite features, is quite common in the related material system of graphene on hBN (see fig. 2.31 for principals of the scenario): Ref.[99], for example, accordingly finds strong, even qualitative differences between secondary signatures in the regimes of electron and hole conduction. Partly, the phenomenon is rooted in second-order potential from different atomic species in the hBN sublattices[163], which is not transferable to TBG. Furthermore though, next-nearest neighbor interlayer hopping has been shown to induce a periodic modulation between sublattices, which induces significant asymmetry between satellite features in conduction and valence band[11].

The here observed, more complicated split structures in negative carrier densities are thus a conceivable intricacy in the **TBG** spectrum and may again be substantially influenced by corrugation and distortion, determining vicinity and magnitude of hopping between lattice sites in top and bottom layer graphene.

Secondly, fourfold degeneracy as evident from the central, primary Landau fan, deviates from expectation according to theoretical prediction[41, 93] (fig. 2.32, fig. 2.33): With two Dirac cones in the **mBz**, low-energy transport signatures should either display eightfold degeneracy (as in the center Landau fan of sample A, sec. 5.2.1) or two fourfold sequences split by screening (see first segment 5.1 of this chapter). The observed signature is therefore more reminiscent of graphene on **hBN**[11, 88], where a single Dirac cone is reflected at the **mBz** boundaries (fig. 2.31).

Given the geometry and contact scheme of the examined sample (fig. 5.24 a), where half of the source and measuring contacts apply to the bottom layer only, the following scenario is suggested: The measured signatures are dominated by the quantized states in the bottom layer dispersion which is folded back in the long-range superlattice potential imposed by the twisted top layer. Largely screened from backgate influence (significant effective interlayer distance has been suggested in sec. 5.1.2) and contacted only by half of the source and measuring probes, the latter does not significantly contribute to the observed transport.

As shown in the appendix figs. A.5/A.6, a very similar spectrum to the here discussed one has been observed in a further instance, where (this time in two-probe configuration) source and measuring contacts were again applied to the **TBG** on one and the bare **MLG** bottom layer on the other side. The near identical features (energetically scaled via θ) at equivalently asymmetric sample geometry and contact scheme fortify the above construct of reasoning.

In summary of the discussed signatures from samples B and C in the present subsection 5.2.2, systematic satellite features in longitudinal magnetoresistance, modulating a dominant MLG signature at angle-dependent charge carrier concentrations, are ascribed to the bottom layer in according small-angle TBG, where the top layer imposes a long-range periodic potential modulation; effective isolation of a single layer's signature is achieved by the asymmetric setup of electrical contacts in conjunction with bare MLG portions in the TBG bottom layer.

Intricate split features in the regime of hole conduction likely arise due to next-nearest neighbor interlayer interaction, which can be expected to sensitively depend on atomic positions in a lattice-relaxed TBG.

Complementing the findings on direct coupling between rotationally displaced Dirac cones from sec. 5.2.1, the here observed phenomena reflect an alternative electronic context of secondary Dirac singularities in TBG, in analogy to the related material system of closely aligned MLG-hBN heterostructures.

5.3 Summary

In the present chapter 5, magnetotransport experiments on three small-angle TBG samples were presented, revealing two qualitatively different signatures, rooted in three distinct electronic scenarios:

Firstly, the findings presented in sec. 5.1 reflect a commonly found scenario: At low energy, the individual layers' monolayer dispersions are effectively decoupled but exhibit reduced Fermi velocity, scaling with interlayer twist and hopping amplitude t^θ ; pronounced electron-hole asymmetry is here found in the latter, confirming elsewhere reported trends. Low induction of charge into the top layer via the applied backgate voltage furthermore reveals an exceptionally large effective interlayer distance in the corresponding capacitive model, which is ascribed to out-of-plane lattice corrugation. At high energy, the signature of a coupled dispersion at Berry phase of 2π is detected in conjunction with constant Fermi velocity, confirming theoretical prediction. Persistence of a Berry phase of π in low magnetic fields is discussed with respect to pronounced gated layer asymmetries. The mechanism of phase transition is linked to a possible jump of Fermi energy between Landau levels around a critical magnetic field.

Secondly, an alternative coupling model predicts the generation of secondary Dirac singularities at the crossing of rotationally displaced MLG dispersions. Section 5.2.1 presents the according transport signature featuring multiple Landau fans of different degeneracy.

Thirdly, secondary Dirac singularities may arise in backfolding at the superlattice mBz boundaries. The signatures presented in sec. 5.2.2 suggest transport through a TBG bottom layer, modulated by the long-range superlattice potential imposed by a partly covering top layer. According satellite Landau fan features exhibit electron-hole asymmetry and split structures on the valence side; the observed electronic situation bears general resemblance to the related case of closely aligned graphene on hBN.

6 Conclusions

The previous chapters of the dissertation at hand covered two major topics: the real-space morphology of twisted bilayer graphene (TBG), as investigated via AFM and the electronic TBG structure, as probed in magnetotransport.

Subject of study are TBG samples created via folding of monolayer graphene (MLG) from mechanical exfoliation. In small numbers, flipped-over flakes are found among the exfoliation yield; further folding events are induced via AFM-tip.

The former, byproducts of exfoliation, are found to exhibit varying degrees of rippling and wrinkling; correspondingly indicated strain in the TBG configuration suggests a mechanically forced folding process, reflecting the motions of the exfoliating tape. Thusly created structures exclusively exhibit small interlayer twist; this is explained by here found energetically favorable stacking configuration and the random, repetitive nature of mechanical stimulus in the exfoliation process, where any less stable stacking configuration is detached in a subsequent peeling cycle.

Where samples from exfoliation are predominantly folded as a whole without any rupture of the lattice, AFM-induced folds are found to tear from MLG along one or two paths respectively. According one-rip structures are predominantly induced during scanning motion at elevated spring load in the AFM probe. Two-rip structures are in most cases spreading from sites of nanoindentation, i.e. scratches applied to the graphene plane.

Interestingly, a time-dependent, progressive expansion of AFM-induced folds at speeds $> 10 \text{ nm s}^{-1}$ could be observed, is however limited in resolution by the finite capture time of a frame in AFM imaging.

A similar behavior was recently reported for folded structures resembling the here found two-rip structures[17]. Interaction energy between two graphene sheets, superior to the one between graphene and a substrate of SiO_2 , was proposed to progressively stabilize an initially small folded configuration over larger and larger areas, driven by thermal fluctuation. Expansion of the according TBG takes place under rupture of carbon-carbon bonds along two paths, which is energetically compensated by the gain in interlayer interaction. This applies as long as the width of the progressing structure is large enough; as it narrows due to strain from bending at the folded edge, TBG expansion is terminated at a characteristic width indicative of interlayer interaction energy.

The model was supported by the observation of different termination widths ℓ over varying thickness (i.e. number of layers) in folded graphene[17]. In the work at hand, studies are extended to the whole range of rotational mismatch, finding correlation between ℓ and the magnitudes of interlayer distance Δh as well as radius of the folded edge, as determined for a larger number of AFM-induced TBG areas:

The width of growth termination is estimated to stand in reciprocal relation to interaction energy density, relation between interlayer distance and binding energy is described via vdW-interaction following an inverse power law; comparison of both suggests a power-law dependence between Δh and ℓ , which is in fact found to be satisfied in here measured data.

The radius of the folded edge is furthermore observed to decrease below theoretical expectation for short folded widths, which can be related to the balance between bending and tearing energy in the above model of dynamic growth.

In principal the folded width is thus shown to be a reliable indicator of **TBG** energetics, which should be quantifiable upon refinement of the here applied elementary model.

In contrast, folded widths in one-rip structures show no such correlations. Here, a different mechanism of growth termination is proposed: As according **TBG** form asymmetrically, along the pre-existing native sample edge to one side and along a torn path to the other, correspondingly asymmetric speeds of expansion may be inferred, effectively equating to growth under rotation (the scenario is in agreement with inferences from an according **AFM** capture frame). On its rotated path, the one-rip structure is now bound to pass commensurate interlayer stacking configuration where friction will instantly increase and lock the **TBG** into permanent position. The model is supported by the good match between measured rotational mismatch and theoretically expected commensurate twist angles.

The findings on dynamic growth of **TBG** from folds initiated via **AFM** tip substantiate the model introduced in ref.[17], furthermore extending the range of relatable **TBG** parameters by interlayer distance and bending radius of the folded edge. In addition, a distinct class of folded geometry is identified in **TBG** expanding at one tear, which are shown to be governed by different growth dynamics.

Throughout all of the examined **TBG**, a dependence in interlayer distance on rotational mismatch is detected: In accordance with theoretical expectation, Δh_{AB} from Bernal-stacking defines the lower border of observed values, while evolution over a span of $\sim 3 \text{ \AA}$ exceeds the predicted spread. Scattering in **AFM**-measured Δh at small angles is explained via the interplay between out-of-plane superlattice corrugation and the scanning-probe tip. A pronounced minimum around 25° of rotational mismatch is connected to a there found lack of commensurate interlayer configurations.

AFM-measured friction on the surface of TBG is found to exceed the one from monolayer graphene, breaking the decreasing trend over layer number as known from fewlayers in Bernal-stacking. This is ascribed to enhanced pliancy in a TBG stack under the AFM probe due to superlubric interlayer interaction at incommensurate stacking configuration. Interestingly, the bended edge is herein found to have a stabilizing effect, which is reflected in lower measured friction at larger length of folded interlayer connection.

In addition to the above summarized real-space characterization, magnetotransport experiments were conducted on a number of samples to gather information about TBG electronic structure; the focus is herein laid on small interlayer twist where especially rich electronic spectra are predicted.

A most commonly applied and experimentally verified interlayer coupling model describes merging of rotationally displaced Dirac cones from top and bottom layer in low-energy van-Hove singularities (vHs). For the high-energy dispersion above the merging point, theoretical expectations become controversial: In a scheme of rigorous backfolding into the superlattice mini-Brillouin zone (mBz), a hole-like band with Berry phase of zero is predicted[50]. Alternatively, the merged band structure is found to continue as electron-like past the formal mBz boundary; here, the topology of a Bernal-stacked bilayer with Berry phase of 2π is expected[19, 20].

The latter scenario is found to apply for a TBG sample with 2.5° of rotational mismatch: At small Fermi energy, the (uncontroversial) signature of two superposed monolayer dispersions is found in longitudinal magnetoresistance. Corresponding charge carrier concentrations are strongly asymmetric between top and bottom layer; Fermi velocities, rescaled in accordance with theoretical prediction, indicate a pronounced electron-hole asymmetry in the interlayer hopping

parameter t^θ . A commonly applied model, describing the screening of backgate influence in the TBG top layer is extended to account for the observed reduction of Fermi velocity at high degree of energetic layer asymmetry. Fits to the data indicate a large effective layer separation (corresponding to a small interlayer capacitance), which is in accordance with former reports on TBG lying on top of a SiO₂-substrate. A device encapsulated between layers of hBN in contrast, has interestingly been reported to display an unexpectedly large capacitance instead which is indicative of a low effective interlayer distance. The degree in out-of-plane corrugation allowed in a given substrate environment is discussed as likely reason behind the identified discrepancies.

Transport signatures in larger Fermi energies reveal the transition (at unchanged carrier polarities) from two effectively decoupled systems to a coupled one; in high magnetic fields, the latter exhibits a Berry phase of 2π and constant Fermi velocity in accordance with theoretical prediction. A persisting Berry phase of π in low magnetic fields is discussed with respect to the above established layer-asymmetries and according strongly reduced Fermi velocities. The mechanism of change in Berry phase is linked to a possible jump of Fermi energy between Landau levels around a critical magnetic field of transition.

The contrasting high-energy scenario of rigorous backfolding has recently been demonstrated in a TBG sample of similar interlayer twist (2°), which was encapsulated between layers of hBN. It is again tempting to relate the observed distinctions in electronic structure to the degree of lattice relaxation allowed in a given sample environment. The flat lattices of the embedded sample are likely to be accurately captured by the tight-binding model from ref.[50], where the continuum approach from ref.[19, 20] might be more suitable for the freely corrugated case of the here examined TBG on SiO₂.

Qualitatively different transport signatures are found in a number of further **TBG** samples with smaller interlayer twist; additional Landau fans in longitudinal resistance indicate the presence of secondary Dirac singularities in the **TBG** spectrum. These may arise in two different electronic scenarios:

For a particular relation in three interlayer hopping terms between different lattice sites, the rotationally displaced Dirac cones from top and bottom layer do not merge in a **vHs** as in the above described, most commonly applicable model, but generate secondary Dirac singularities, due to the effective pseudospin structures of the crossing **MLG** bands[10] .

Here, a folded structure with 1.6° of rotational mismatch is found to exhibit three differently pronounced Landau fans in longitudinal resistance. Spacing between respective origins in charge carrier concentration as well as eightfold degeneracy in one of the fans are in general accordance with this latter, alternative coupling model.

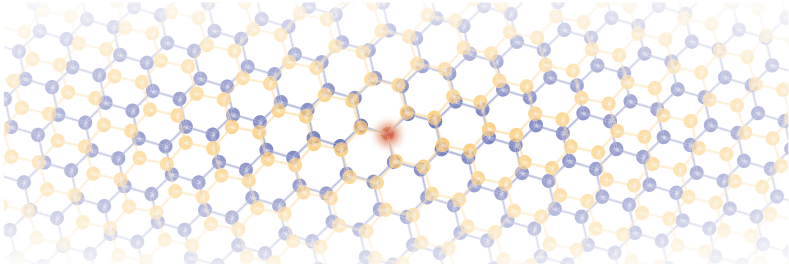
Play-out of different merging scenarios is discussed with respect to distinctions in superlattice formation as resolved via **AFM**; the particular manner of lattice relaxation can herein be expected to sensitively affect inter-atomic configuration and thus hopping terms between **TBG** layers.

The satellite features resolved in the last presented **TBG** samples are likely rooted in another electronic scenario:

Periodic recurrence of peaks, modulating a dominant central field-effect resistance, suggests backfolding of the dispersion at the boundaries of a superlattice **mBz**. As the corresponding central Landau fan exhibits a fourfold **MLG** sequence, signatures are reminiscent of the related material system of graphene on **hBN**[11].

Special to the discussed samples, the **TBG** top layer does only partly cover the bottom and is in contact to just half of the electrical leads, which motivates consideration of the following scenario:

Transport signatures are dominated by the bottom layer, modulated by the superlattice potential imposed via varying lattice registry in interplay with the twisted top layer; the latter itself does not significantly take part in electronic transport, as it is largely screened from backgate influence.



Viewed in conjunction, the here presented experimental studies on **TBG** indicate high sensitivity on interlayer stacking configuration in morphology as well as electronic structure.

At large rotational mismatch, interlayer commensurability is found to play an important role for **TBG** interaction.

In small twist angles, it is lattice relaxation in response to long-wavelength periodicities in interlayer registry, which determines potentially decisive details in interlayer coupling.

An important factor for the particular manner and freedom of interlayer configuration is furthermore identified in the sample's substrate environment.

The above observations highlight the complexity and riches of the **TBG** system, explaining the seemingly controversial outcomes from different models of theoretical prediction. Thorough consideration of negligible vs. crucial details in the formulation of the initial **TBG** model should therefore be encouraged in future theoretical efforts.

Appendix

Supplementary Material for: [sec. 4.2](#)

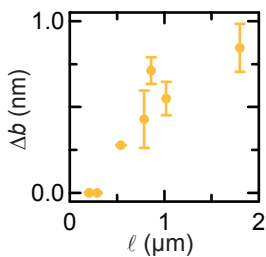


Figure A.1 Bump height Δb vs. folded length ℓ . Dots mark the average between data from trace and retrace scan, error bars indicate the spread between the two. The presented values in Δb represent the primary data behind the bending radius r as depicted in [fig. 4.21](#).

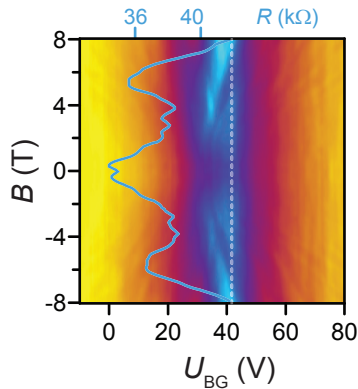
Supplementary Material for: **sec. 5.1**

Figure A .2 Longitudinal resistance in dependence on backgate voltage U_{BG} and magnetic field B of both polarities; colorscale goes from 2 $k\Omega$ to 43.7 $k\Omega$ (bottom to top). The overlain blue graph plots a cross-section at $U_{BG}=41.6$ V on a resistance axis scaled by blue numerals to the top. As referred to on p. 190, the depiction illustrates the symmetry of quantized features in magnetic field. A small linearly slanted background may be ascribed to contributions from the classical Hall effect.

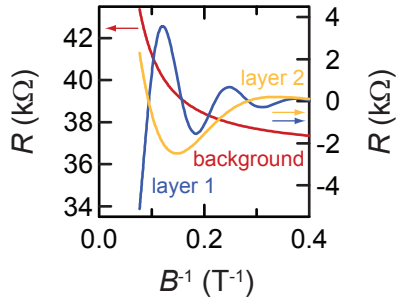


Figure A.3 Contributions to the fit in *fig. 5.4 a*, including the polynomial (second order in B) accounting for background resistance (red). Oscillations (yellow, blue) describe *SdH*-oscillations in decoupled top and bottom layer.

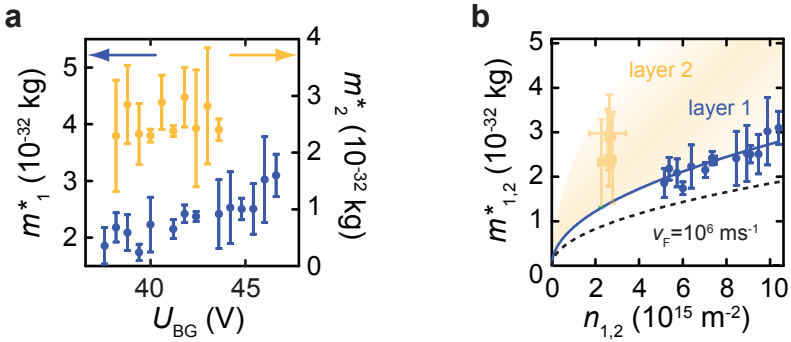


Figure A.4 **a:** Effective masses extracted from temperature dependence in the two decoupled layers' SdH-oscillations (see fig. 5.5) for various backgate voltages U_{BG} . **b:** Data from **a** plotted vs. charge carrier concentrations n extracted from the frequency of a given oscillation via eq. 2.36. Black line indicates evolution of m^* over n at graphene's native Fermi velocity; blue line is a fit of the interrelations in eq. 2.39 to data of layer 1; yellow area indicates range of uncertainty for fit to data from layer 2.

Supplementary Material for: **sec. 5.2**

As referred to on p.232, the structure of sample C as presented in fig. A.5 exhibits principal traits similar to the ones of sample B from sec. 5.2.2 (see fig. 5.24): Electrical probes contact the folded TBG on one and the bare MLG bottom layer to the other side.

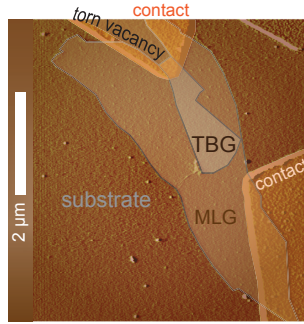


Figure A.5 *AFM deflection signal from a scan of sample C; different elementary portions are colored and labeled for clarity. The TBG area to the top has been folded out of the indicated vacancy during exfoliation. Contacts are applied in two-probe configuration with one lead on the fold of the bilayer and one on the bare MLG bottom layer.*

Magnetotransport signatures as presented in fig. A.6 are qualitatively equivalent to the ones of sample B (compare figs. 5.25/5.26), where main satellite features appear in about three times larger intervals of $n \approx 2.9 \times 10^{16} \text{ m}^{-2}$ (see bottom of panel c).

In the scenario of backfolding at the mBz boundaries, eq. 2.24 finds a superstructure unit cell area of $A \approx 140 \text{ nm}^2$ and a wavelength of $\lambda \approx 13 \text{ nm}$. Assuming the Moiré relation, interlayer twist follows as $\theta \approx 1.1^\circ$ from eq. 2.5.

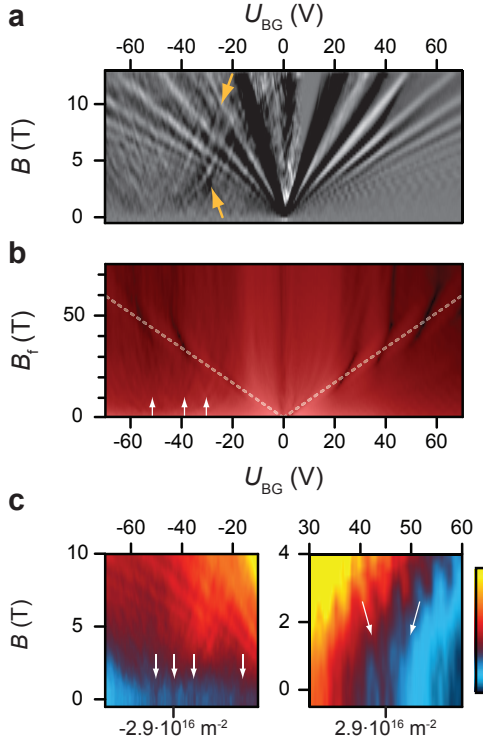


Figure A.6 Sample C **a:** Derivative dR/dB ; satellite features are pointed to by yellow arrows. **b:** FFT of R in B^{-1} ; straight slopes in the primary feature (dashed white lines) suggest an unscreened, fourfold degenerate *MLG* dispersion; additional features are indicated by white arrows. **c:** Close-ups of resistance for hole (left) and electron conduction (right) reveal satellites originating at $B=0$ T around $|n| \approx 2.9 \times 10^{16} \text{ m}^{-2}$. Colorscale spans 11 k Ω and 600 Ω for left and right panel respectively.

Bibliography

- ¹A. K. Geim; K. S. Novoselov,
The rise of graphene,
[NATURE MATERIALS](#) **6**, 183–191 (2007).
- ²J. C. Meyer; A. K. Geim; M. I. Katsnelson; K. S. Novoselov; T. J. Booth; S. Roth,
The structure of suspended graphene sheets,
[NATURE](#) **446**, 60–63 (2007).
- ³H. P. Boehm; A. Clauss; G. O. Fischer; U. Hofmann,
Das Adsorptionsverhalten sehr dünner Kohlenstoff-Folien,
[ZEITSCHRIFT FÜR ANORGANISCHE UND ALLGEMEINE CHEMIE](#) **316**, 119–127 (1962).
- ⁴H. P. Boehm; R. Setton; E. Stumpp,
Nomenclature and terminology of graphite intercalation compounds (IUPAC recommendations 1994),
[PURE AND APPLIED CHEMISTRY](#) **66**, 1893–1901 (1994).
- ⁵K. S. Novoselov; A. K. Geim; S. V. Morozov; D. Jiang; Y. Zhang; S. V. Dubonos; I. V. Grigorieva; A. A. Firsov,
Electric field effect in atomically thin carbon films,
[SCIENCE](#) **306**, 666–669 (2004).
- ⁶K. S. Novoselov; A. K. Geim; S. V. Morozov; D. Jiang; M. I. Katsnelson; I. V. Grigorieva; S. V. Dubonos; A. A. Firsov,
Two-dimensional gas of massless Dirac fermions in graphene,
[NATURE](#) **438**, 197–200 (2005).

- ⁷Y. Zhang; Y.-W. Tan; H. L. Stormer; P. Kim,
Experimental observation of the quantum Hall effect and Berry's phase in graphene,
[NATURE](#) **438**, 201–204 (2005).
- ⁸J. M. B. Lopes dos Santos; N. M. R. Peres; A. H. Castro Neto,
Graphene bilayer with a twist: electronic structure,
[PHYSICAL REVIEW LETTERS](#) **99**, 256802 (2007).
- ⁹G. Li; A. Luican; J. M. B. Lopes dos Santos; A. H. Castro Neto;
A. Reina; J. Kong; E. Y. Andrei,
*Observation of van Hove singularities
in twisted graphene layers*,
[NATURE PHYSICS](#) **6**, 109–113 (2010).
- ¹⁰E. J. Mele,
*Band symmetries and singularities
in twisted multilayer graphene*,
[PHYSICAL REVIEW B](#) **84**, 235439 (2011).
- ¹¹M. Yankowitz; J. Xue; D. Cormode; J. D. Sanchez-Yamagishi;
K. Watanabe; T. Taniguchi; P. Jarillo-Herrero; P. Jacquod; B. J.
LeRoy,
*Emergence of superlattice Dirac points in graphene on hexagonal
boron nitride*,
[NATURE PHYSICS](#) **8**, 382–386 (2012).
- ¹²H. Schmidt; J. C. Rode; D. Smirnov; R. J. Haug,
Superlattice structures in twisted bilayers of folded graphene,
[NATURE COMMUNICATIONS](#) **5**, 5742 (2014).
- ¹³H. Min; R. Bistritzer; J.-J. Su; A. H. MacDonald,
Room-temperature superfluidity in graphene bilayers,
[PHYSICAL REVIEW B](#) **78**, 121401(R) (2008).

-
- ¹⁴S. Kim; E. Tutuc,
Coulomb drag and magnetotransport in graphene double layers,
[SOLID STATE COMMUNICATIONS 152, 1283–1288 \(2012\)](#).
- ¹⁵H. Schmidt; T. Lüdtke; P. Barthold; E. McCann; V. I. Fal'ko;
R. J. Haug,
Tunable graphene system with two decoupled monolayers,
[APPLIED PHYSICS LETTERS 93, 172108 \(2008\)](#).
- ¹⁶A. K. Geim; I. V. Grigorieva,
Van der Waals heterostructures,
[NATURE 499, 419–425 \(2013\)](#).
- ¹⁷J. Annett; G. L. W. Cross,
*Self-assembly of graphene ribbons by spontaneous self-tearing
and peeling from a substrate*,
[NATURE 535, 271–275 \(2016\)](#).
- ¹⁸M. Dienwiebel; G. S. Verhoeven; N. Pradeep; J. W. M. Frenken;
J. A. Heimberg; H. W. Zandbergen,
Superlubricity of graphite,
[PHYSICAL REVIEW LETTERS 92, 126101 \(2004\)](#).
- ¹⁹R. de Gail; M. O. Goerbig; F. Guinea; G. Montambaux; A. H.
Castro Neto,
Topologically protected zero modes in twisted bilayer graphene,
[PHYSICAL REVIEW B 84, 045436 \(2011\)](#).
- ²⁰M.-Y. Choi; Y.-H. Hyun; Y. Kim,
*Angle dependence of the Landau level spectrum in twisted bilayer
graphene*,
[PHYSICAL REVIEW B 84, 195437 \(2011\)](#).

- ²¹K. S. Novoselov; D. Jiang; F. Schedin; T. J. Booth; V. V. Khotkevich; S. V. Morozov; A. K. Geim,
Two-dimensional atomic crystals,
[PROCEEDINGS OF THE NATIONAL ACADEMY OF SCIENCES OF THE UNITED STATES OF AMERICA](#) **102**, 10451–10453 (2005).
- ²²J. M. Campanera; G Savini; I. Suarez-Martinez; M. I. Heggie,
Density functional calculations on the intricacies of Moiré patterns on graphite,
[PHYSICAL REVIEW B](#) **75**, 235449 (2007).
- ²³J. M. B. Lopes dos Santos; N. M. R. Peres; A. H. Castro Neto,
Continuum model of the twisted graphene bilayer,
[PHYSICAL REVIEW B](#) **86**, 155449 (2012).
- ²⁴C.-C. Lu; Y.-C. Lin; Z. Liu; C.-H. Yeh; K. Suenaga; P.-W. Chiu,
Twisting bilayer graphene superlattices,
[ACS NANO](#) **7**, 2587–2594 (2013).
- ²⁵M. M. van Wijk; A Schuring; M. I. Katsnelson; A Fasolino,
Relaxation of Moiré patterns for slightly misaligned identical lattices: graphene on graphite,
[2D MATERIALS](#) **2**, 034010 (2015).
- ²⁶H. Beyer; M. Müller; Th. Schimmel,
Monolayers of graphite rotated by a defined angle: hexagonal superstructures by STM,
[APPLIED PHYSICS A: MATERIALS SCIENCE & PROCESSING](#) **68**, 163–166 (1999).
- ²⁷M. L. Kronberg; F. H. Wilson,
Secondary recrystallization in copper,
[TRANSACTIONS OF THE AIME](#) **185**, 501–514 (1949).
- ²⁸S. Ranganathan,
On the geometry of coincidence-site lattices,
[ACTA CRYSTALLOGRAPHICA](#) **21**, 197–199 (1966).

- ²⁹E. J. Mele,
*Commensuration and interlayer coherence
in twisted bilayer graphene*,
[PHYSICAL REVIEW B **81**, 161405\(R\) \(2010\)](#).
- ³⁰E. Koren; I. Leven; E. Lörtscher; A. Knoll; O. Hod; U. Duerig,
*Coherent commensurate electronic states at the interface between
misoriented graphene layers*,
[NATURE NANOTECHNOLOGY **11**, 752–757 \(2016\)](#).
- ³¹J. Jung; A. M. DaSilva; A. H. MacDonald; S. Adam,
Origin of band gaps in graphene on hexagonal boron nitride,
[NATURE COMMUNICATIONS **6**, 6308 \(2015\)](#).
- ³²Wikipedia,
Diamond cubic — Wikipedia, The Free Encyclopedia, [Online;
accessed 25-August-2016], 2016.
- ³³H. W. Kroto; J. R. Heath; S. C. O'Brien; R. F. Curl; R. E. Smalley,
C 60: Buckminsterfullerene,
[NATURE **318**, 162–163 \(1985\)](#).
- ³⁴S. Iijima,
Helical microtubules of graphitic carbon,
[NATURE **354**, 56–58 \(1991\)](#).
- ³⁵J. Bischoe; B. E. Warren,
An X-ray study of carbon black,
[JOURNAL OF APPLIED PHYSICS **13**, 364–371 \(1942\)](#).
- ³⁶G. Oster; M. Wasserman; C. Zwerling,
Theoretical interpretation of Moiré patterns,
[JOURNAL OF THE OPTICAL SOCIETY OF AMERICA **54**, 169–175 \(1964\)](#).

- ³⁷K. Creath; J. C. Wyant,
Moiré and fringe projection techniques, (Wiley, New York, 1992),
pp. 653–685.
- ³⁸Wikipedia,
Moiré pattern — *Wikipedia, The Free Encyclopedia*, [Online; ac-
cessed 25-August-2016], 2016.
- ³⁹A. T. N'Diaye; J. Coraux; T. N. Plasa; C. Busse; T. Michely,
Structure of epitaxial graphene on Ir (111),
NEW JOURNAL OF PHYSICS **10**, 043033 (2008).
- ⁴⁰S. Tang; H. Wang; Y. Zhang; A. Li; H. Xie; X. Liu; L. Liu; T. Li;
F. Huang; X. Xie, et al.,
*Precisely aligned graphene grown on hexagonal boron nitride by
catalyst free chemical vapor deposition*,
SCIENTIFIC REPORTS **3**, 2666 (2013).
- ⁴¹P. Moon; M. Koshino,
Optical absorption in twisted bilayer graphene,
PHYSICAL REVIEW B **87**, 205404 (2013).
- ⁴²Wikipedia,
List of trigonometric identities — *Wikipedia, The Free Encyclo-
pedia*, [Online; accessed 24-August-2016], 2016.
- ⁴³Wikipedia,
Beat (acoustics) — *Wikipedia, The Free Encyclopedia*, [Online;
accessed 24-August-2016], 2016.
- ⁴⁴L.-J. Yin; J.-B. Qiao; W.-X. Wang; W.-J. Zuo; W. Yan; R. Xu;
R.-F. Dou; J.-C. Nie; L. He,
*Landau quantization and Fermi velocity renormalization in twisted
graphene bilayers*,
PHYSICAL REVIEW B **92**, 201408(R) (2015).

-
- ⁴⁵J. C. Rode; D. Smirnov; H. Schmidt; R. J. Haug,
Berry phase transition in twisted bilayer graphene,
[2D MATERIALS](#) **3**, 035005 (2016).
- ⁴⁶R. Bistritzer; A. H. MacDonald,
Moiré butterflies in twisted bilayer graphene,
[PHYSICAL REVIEW B](#) **84**, 035440 (2011).
- ⁴⁷S. Shallcross; S. Sharma; O. Pankratov,
Emergent momentum scale, localization, and van Hove singularities in the graphene twist bilayer,
[PHYSICAL REVIEW B](#) **87**, 245403 (2013).
- ⁴⁸M. Koshino; P. Moon,
Electronic properties of incommensurate atomic layers,
[JOURNAL OF THE PHYSICAL SOCIETY OF JAPAN](#) **84**, 121001 (2015).
- ⁴⁹T. Chari; R. Ribeiro-Palau; C. R. Dean; K. L. Shepard,
Resistivity of rotated graphite-graphene contacts,
[NANO LETTERS](#) **16**, 4477–4482 (2016).
- ⁵⁰P. Moon; M. Koshino,
Energy spectrum and quantum Hall effect in twisted bilayer graphene,
[PHYSICAL REVIEW B](#) **85**, 195458 (2012).
- ⁵¹H. B. Ribeiro; K. Sato; G. S. N. Eliel; E. A. T. de Souza; C.-C. Lu; P.-W. Chiu; R. Saito; M. A. Pimenta,
Origin of van Hove singularities in twisted bilayer graphene,
[CARBON](#) **90**, 138–145 (2015).
- ⁵²S. Shallcross; S. Sharma; E. Kandelaki; O. A. Pankratov,
Electronic structure of turbostratic graphene,
[PHYSICAL REVIEW B](#) **81**, 165105 (2010).

- ⁵³K. Uchida; S. Furuya; J.-I. Iwata; A. Oshiyama,
Atomic corrugation and electron localization due to Moiré patterns in twisted bilayer graphenes,
[PHYSICAL REVIEW B **90**, 155451 \(2014\).](#)
- ⁵⁴J. Berashevich; T. Chakraborty,
Interlayer repulsion and decoupling effects in stacked turbostratic graphene flakes,
[PHYSICAL REVIEW B **84**, 033403 \(2011\).](#)
- ⁵⁵Y. Shibuta; J. A. Elliott,
Interaction between two graphene sheets with a turbostratic orientational relationship,
[CHEMICAL PHYSICS LETTERS **512**, 146–150 \(2011\).](#)
- ⁵⁶I. Brihuega; P. Mallet; H. González-Herrero; G. Trambly de Laisardière; M. M. Ugeda; L. Magaud; J. M. Gómez-Rodríguez; F. Ynduráin; J.-Y. Veuillen,
Unraveling the intrinsic and robust nature of van Hove singularities in twisted bilayer graphene by scanning tunneling microscopy and theoretical analysis,
[PHYSICAL REVIEW LETTERS **109**, 196802 \(2012\).](#)
- ⁵⁷W.-T. Pong; C. Durkan,
A review and outlook for an anomaly of scanning tunnelling microscopy (STM): superlattices on graphite,
[JOURNAL OF PHYSICS D: APPLIED PHYSICS **38**, R329 \(2005\).](#)
- ⁵⁸M. Neek-Amal; P. Xu; D. Qi; P. M. Thibado; L. O. Nyakiti; V. D. Wheeler; R. L. Myers-Ward; C. R. Eddy Jr.; D. K. Gaskill; F. M. Peeters,
Membrane amplitude and triaxial stress in twisted bilayer graphene deciphered using first-principles directed elasticity theory and scanning tunneling microscopy,
[PHYSICAL REVIEW B **90**, 064101 \(2014\).](#)

- ⁵⁹C. R. Dean; A. F. Young; I. Meric; C. Lee; L. Wang; S. Sorgenfrei; K. Watanabe; T. Taniguchi; P. Kim; K. L. Shepard, et al., *Boron nitride substrates for high-quality graphene electronics*, [NATURE NANOTECHNOLOGY](#) **5**, 722–726 (2010).
- ⁶⁰J. Xue; J. Sanchez-Yamagishi; D. Bulmash; P. Jacquod; A. Deshpande; K. Watanabe; T. Taniguchi; P. Jarillo-Herrero; B. J. LeRoy, *Scanning tunnelling microscopy and spectroscopy of ultra-flat graphene on hexagonal boron nitride*, [NATURE MATERIALS](#) **10**, 282–285 (2011).
- ⁶¹C. R. Woods; L. Britnell; A. Eckmann; R. S. Ma; J. C. Lu; H. M. Guo; X. Lin; G. L. Yu; Y. Cao; R. V. Gorbachev, et al., *Commensurate-incommensurate transition in graphene on hexagonal boron nitride*, [NATURE PHYSICS](#) **10**, 451–456 (2014).
- ⁶²M. M. van Wijk; A. Schuring; M. I. Katsnelson; A. Fasolino, *Moiré patterns as a probe of interplanar interactions for graphene on h-BN*, [PHYSICAL REVIEW LETTERS](#) **113**, 135504 (2014).
- ⁶³S. Dai; Y. Xiang; D. J. Srolovitz, *Twisted bilayer graphene: Moiré with a twist*, [NANO LETTERS](#) **16**, 5923–5927 (2016).
- ⁶⁴J. S. Bunch; A. M. Van Der Zande; S. S. Verbridge; I. W. Frank; D. M. Tanenbaum; J. M. Parpia; H. G. Craighead; P. L. McEuen, *Electromechanical resonators from graphene sheets*, [SCIENCE](#) **315**, 490–493 (2007).
- ⁶⁵K. I. Bolotin; K. J. Sikes; Z. Jiang; M. Klima; G. Fudenberg; J. Hone; P. Kim; H. L. Stormer, *Ultrahigh electron mobility in suspended graphene*, [SOLID STATE COMMUNICATIONS](#) **146**, 351–355 (2008).

- ⁶⁶A. V. Kretinin; Y. Cao; J. S. Tu; G. L. Yu; R. Jalil; K. S. Novoselov; S. J. Haigh; A. Gholinia; A. Mishchenko; M. Lozada, et al.,
Electronic properties of graphene encapsulated with different two-dimensional atomic crystals,
[NANO LETTERS 14](#), 3270–3276 (2014).
- ⁶⁷A. S. Mayorov; R. V. Gorbachev; S. V. Morozov; L. Britnell; R. Jalil; L. A. Ponomarenko; P. Blake; K. S. Novoselov; K. Watanabe; T. Taniguchi, et al.,
Micrometer-scale ballistic transport in encapsulated graphene at room temperature,
[NANO LETTERS 11](#), 2396–2399 (2011).
- ⁶⁸V. Geringer; M. Liebmann; T. Echtermeyer; S. Runte; M. Schmidt; R. Rückamp; M. C. Lemme; M. Morgenstern,
Intrinsic and extrinsic corrugation of monolayer graphene deposited on SiO₂,
[PHYSICAL REVIEW LETTERS 102](#), 076102 (2009).
- ⁶⁹N. N. T. Nam; M. Koshino,
Spontaneous strain on twisted bilayer graphene and its effect on the electronic structure,
[International Conference on the Physics of Semiconductors](#) (2016).
- ⁷⁰M. Binnewies; M. Jäckel; H. Willner; G. Rayner-Canham,
Allgemeine und anorganische Chemie, (Elsevier, 2004).
- ⁷¹P. R. Wallace,
The band theory of graphite,
[PHYSICAL REVIEW 71](#), 622 (1947).
- ⁷²D. S. L. Abergel; V. Apalkov; J. Berashevich; K. Ziegler; T. Chakraborty,
Properties of graphene: a theoretical perspective,
[ADVANCES IN PHYSICS 59](#), 261–482 (2010).

- ⁷³M. I. Katsnelson; K. S. Novoselov; A. K. Geim,
Chiral tunnelling and the Klein paradox in graphene,
[NATURE PHYSICS 2, 620–625 \(2006\)](#).
- ⁷⁴E. McCann; V. I. Fal'ko,
Landau-level degeneracy and quantum Hall effect in a graphite bilayer,
[PHYSICAL REVIEW LETTERS 96, 086805 \(2006\)](#).
- ⁷⁵C.-H. Park; N. Marzari,
Berry phase and pseudospin winding number in bilayer graphene,
[PHYSICAL REVIEW B 84, 205440 \(2011\)](#).
- ⁷⁶K. Zou; X. Hong; J. Zhu,
Effective mass of electrons and holes in bilayer graphene: electron-hole asymmetry and electron-electron interaction,
[PHYSICAL REVIEW B 84, 085408 \(2011\)](#).
- ⁷⁷K. S. Novoselov; E. McCann; S. V. Morozov; V. I. Fal'ko; M. I. Katsnelson; U. Zeitler; D. Jiang; F. Schedin; A. K. Geim,
Unconventional quantum Hall effect and Berry's phase of 2π in bilayer graphene,
[NATURE PHYSICS 2, 177–180 \(2006\)](#).
- ⁷⁸A. Luican; G. Li; A. Reina; J. Kong; R. R. Nair; K. S. Novoselov; A. K. Geim; E. Y. Andrei,
Single-layer behavior and its breakdown in twisted graphene layers,
[PHYSICAL REVIEW LETTERS 106, 126802 \(2011\)](#).
- ⁷⁹W. Yan; M. Liu; R.-F. Dou; L. Meng; L. Feng; Z.-D. Chu; Y. Zhang; Z. Liu; J.-C. Nie; L. He,
Angle-dependent van Hove singularities in a slightly twisted graphene bilayer,
[PHYSICAL REVIEW LETTERS 109, 126801 \(2012\)](#).

- ⁸⁰H. Schmidt; T. Lüdtkke; P. Barthold; R. J. Haug,
*Mobilities and scattering times
in decoupled graphene monolayers*,
[PHYSICAL REVIEW B **81**, 121403 \(2010\)](#).
- ⁸¹R. Bistritzer; A. H. MacDonald,
Moiré bands in twisted double-layer graphene,
[PROCEEDINGS OF THE NATIONAL ACADEMY OF SCIENCES **108**,
12233–12237 \(2011\)](#).
- ⁸²M. S. Dresselhaus; G. Dresselhaus,
Intercalation compounds of graphite,
[ADVANCES IN PHYSICS **30**, 139–326 \(1981\)](#).
- ⁸³A. Pal; E. J. Mele,
Nodal surfaces in photoemission from twisted bilayer graphene,
[PHYSICAL REVIEW B **87**, 205444 \(2013\)](#).
- ⁸⁴J. Hass; F. Varchon; J.-E. Millán-Otoya; M. Sprinkle; N. Sharma;
W. A. de Heer; C. Berger; P. N. First; L. Magaud; E. H. Conrad,
*Why multilayer graphene on 4H-SiC(0001) behaves like a single
sheet of graphene*,
[PHYSICAL REVIEW LETTERS **100**, 125504 \(2008\)](#).
- ⁸⁵J. Hicks; M. Sprinkle; K. Shepperd; F. Wang; A. Tejada; A. Taleb-
Ibrahimi; F. Bertran; P. Le Fèvre; W. A. De Heer; C. Berger, et
al.,
*Symmetry breaking in commensurate graphene rotational stack-
ing: comparison of theory and experiment*,
[PHYSICAL REVIEW B **83**, 205403 \(2011\)](#).
- ⁸⁶C. R. Dean; L. Wang; P. Maher; C. Forsythe; F. Ghahari; Y. Gao;
J. Katoch; M. Ishigami; P. Moon; M. Koshino, et al.,
*Hofstadter’s butterfly and the fractal quantum Hall effect
in Moiré superlattices*,
[NATURE **497**, 598–602 \(2013\)](#).

- ⁸⁷B. Hunt; J. D. Sanchez-Yamagishi; A. F. Young; M. Yankowitz; B. J. LeRoy; K. Watanabe; T. Taniguchi; P. Moon; M. Koshino; P. Jarillo-Herrero, et al.,
Massive Dirac fermions and Hofstadter butterfly in a van der Waals heterostructure,
[SCIENCE](#) **340**, 1427–1430 (2013).
- ⁸⁸L. A. Ponomarenko; R. V. Gorbachev; G. L. Yu; D. C. Elias; R. Jalil; A. A. Patel; A. Mishchenko; A. S. Mayorov; C. R. Woods; J. R. Wallbank, et al.,
Cloning of Dirac fermions in graphene superlattices,
[NATURE](#) **497**, 594–597 (2013).
- ⁸⁹C.-H. Park; L. Yang; Y.-W. Son; M. L. Cohen; S. G. Louie,
New generation of massless Dirac fermions in graphene under external periodic potentials,
[PHYSICAL REVIEW LETTERS](#) **101**, 126804 (2008).
- ⁹⁰Y. Kim; P. Herlinger; P. Moon; M. Koshino; T. Taniguchi; K. Watanabe; J. H. Smet,
Charge inversion and topological phase transition at a twist angle induced van Hove singularity of bilayer graphene,
[NANO LETTERS](#) **16**, 5053–5059 (2016).
- ⁹¹S. J. Hong; J. A. Rodríguez-Manzo; K. H. Kim; M. Park; S. J. Baek; D. I. Kholin; M. Lee; E. S. Choi; D. H. Jeong; D. A. Bonnell, et al.,
Magnetoresistance (MR) of twisted bilayer graphene on electron transparent substrate,
[SYNTHETIC METALS](#) **216**, 65–71 (2016).
- ⁹²D. S. Lee; C. Riedl; T. Beringer; A. H. Castro Neto; K. von Klitzing; U. Starke; J. H. Smet,
Quantum Hall effect in twisted bilayer graphene,
[PHYSICAL REVIEW LETTERS](#) **107**, 216602 (2011).

- ⁹³Z.-D. Chu; W.-Y. He; L. He,
Coexistence of van Hove singularities and superlattice Dirac points in a slightly twisted graphene bilayer,
[PHYSICAL REVIEW B 87, 155419 \(2013\)](#).
- ⁹⁴J. Martin; N. Akerman; G. Ulbricht; T. Lohmann; J. H. Smet; K. von Klitzing; A. Yacoby,
Observation of electron-hole puddles in graphene using a scanning single-electron transistor,
[NATURE PHYSICS 4, 144–148 \(2008\)](#).
- ⁹⁵Y.-W. Tan; Y. Zhang; K. Bolotin; Y. Zhao; S. Adam; E. H. Hwang; S. Das Sarma; H. L. Stormer; P. Kim,
Measurement of scattering rate and minimum conductivity in graphene,
[PHYSICAL REVIEW LETTERS 99, 246803 \(2007\)](#).
- ⁹⁶E. H. Hwang; S. Adam; S. Das Sarma,
Carrier transport in two-dimensional graphene layers,
[PHYSICAL REVIEW LETTERS 98, 186806 \(2007\)](#).
- ⁹⁷J. D. Sanchez-Yamagishi; T. Taychatanapat; K. Watanabe; T. Taniguchi; A. Yacoby; P. Jarillo-Herrero,
Quantum Hall effect, screening, and layer-polarized insulating states in twisted bilayer graphene,
[PHYSICAL REVIEW LETTERS 108, 076601 \(2012\)](#).
- ⁹⁸R. de Gail; M. O. Goerbig; G. Montambaux,
Magnetic spectrum of trigonally warped bilayer graphene: semiclassical analysis, zero modes, and topological winding numbers,
[PHYSICAL REVIEW B 86, 045407 \(2012\)](#).
- ⁹⁹P. Wang; B. Cheng; O. Martynov; T. Miao; L. Jing; T. Taniguchi; K. Watanabe; V. Aji; C. N. Lau; M. Bockrath,
Topological winding number change and broken inversion symmetry in a Hofstadter’s butterfly,
[NANO LETTERS 15, 6395–6399 \(2015\)](#).

-
- ¹⁰⁰D. R. Hofstadter,
Energy levels and wave functions of Bloch electrons in rational and irrational magnetic fields,
[PHYSICAL REVIEW B **14**, 2239 \(1976\)](#).
- ¹⁰¹Z. F. Wang; F. Liu; M. Y. Chou,
Fractal Landau-level spectra in twisted bilayer graphene,
[NANO LETTERS **12**, 3833–3838 \(2012\)](#).
- ¹⁰²R. J. Haug,
Edge-state transport and its experimental consequences in high magnetic fields,
[SEMICONDUCTOR SCIENCE AND TECHNOLOGY **8**, 131 \(1993\)](#).
- ¹⁰³B. Cheng; Y. Wu; P. Wang; C. Pan; T. Taniguchi; K. Watanabe; M. Bockrath,
Gate-tunable Landau level filling and spectroscopy in coupled massive and massless electron systems,
[PHYSICAL REVIEW LETTERS **117**, 026601 \(2016\)](#).
- ¹⁰⁴A. J. van Bommel; J. E. Crombeen; A. Van Tooren,
LEED and Auger electron observations of the SiC (0001) surface,
[SURFACE SCIENCE **48**, 463–472 \(1975\)](#).
- ¹⁰⁵Y. Gamo; A. Nagashima; M. Wakabayashi; M. Terai; C. Oshima,
Atomic structure of monolayer graphite formed on Ni (111),
[SURFACE SCIENCE **374**, 61–64 \(1997\)](#).
- ¹⁰⁶D. R. Cooper; B. D’Anjou; N. Ghattamaneni; B. Harack; M. Hilke; A. Horth; N. Majlis; M. Massicotte; L. Vandsburger; E. Whiteway, et al.,
Experimental review of graphene,
[ISRN CONDENSED MATTER PHYSICS **2012**, 501686 \(2012\)](#).

- ¹⁰⁷D. J. Henry; G. Yiapanis; E. Evans; I. Yarovsky,
Adhesion between graphite and modified polyester surfaces: a theoretical study,
[THE JOURNAL OF PHYSICAL CHEMISTRY B](#) **109**, 17224–17231 (2005).
- ¹⁰⁸P. Barthold,
Strukturierungsverfahren und elektrische Transporteigenschaften von Graphen, PhD thesis (Leibniz Universität Hannover, 2011).
- ¹⁰⁹O. Leenaerts; B. Partoens; F. M. Peeters,
Water on graphene: hydrophobicity and dipole moment using density functional theory,
[PHYSICAL REVIEW B](#) **79**, 235440 (2009).
- ¹¹⁰Y. J. Shin; Y. Wang; H. Huang; G. Kalon; A. T. S. Wee; Z. Shen; C. S. Bhatia; H. Yang,
Surface-energy engineering of graphene,
[LANGMUIR](#) **26**, 3798–3802 (2010).
- ¹¹¹B. Brechtken,
Herstellung und Untersuchung von 2D-Kristallen auf unterschiedlichen Substraten, MA thesis (Leibniz Universität Hannover, 2016).
- ¹¹²R. R. Nair; P. Blake; A. N. Grigorenko; K. S. Novoselov; T. J. Booth; T. Stauber; N. M. R. Peres; A. K. Geim,
Fine structure constant defines visual transparency of graphene,
[SCIENCE](#) **320**, 1308–1308 (2008).
- ¹¹³P. Blake; E. W. Hill; A. H. Castro Neto; K. S. Novoselov; D. Jiang; R. Yang; T. J. Booth; A. K. Geim,
Making graphene visible,
[APPLIED PHYSICS LETTERS](#) **91**, 063124 (2007).

- ¹¹⁴R. W. Havener; H. Zhuang; L. Brown; R. G. Hennig; J. Park,
Angle-resolved Raman imaging of interlayer rotations and interactions in twisted bilayer graphene,
[NANO LETTERS 12](#), 3162–3167 (2012).
- ¹¹⁵H. Schmidt,
Zweidimensionale Kohlenstoffkristalle: Elektrischer Transport in Einzel- und Doppellagen-Graphen, PhD thesis (Leibniz Universität Hannover, 2012).
- ¹¹⁶J. Moser; A. Barreiro; A. Bachtold,
Current-induced cleaning of graphene,
[APPLIED PHYSICS LETTERS 91](#), 163513 (2007).
- ¹¹⁷L. Gammelgaard; J. M. Caridad; A. Cagliani; D. M. A. Mackenzie; D. H. Petersen; T. J. Booth; P. Bøggild,
Graphene transport properties upon exposure to PMMA processing and heat treatments,
[2D MATERIALS 1](#), 035005 (2014).
- ¹¹⁸N. Lindvall; A. Kalabukhov; A. Yurgens,
Cleaning graphene using atomic force microscope,
[JOURNAL OF APPLIED PHYSICS 111](#), 064904 (2012).
- ¹¹⁹A. M. Goossens; V. E. Calado; A. Barreiro; K. Watanabe; T. Taniguchi; L. M. K. Vandersypen,
Mechanical cleaning of graphene,
[APPLIED PHYSICS LETTERS 100](#), 073110 (2012).
- ¹²⁰G. Binnig; C. F. Quate; C. Gerber,
Atomic force microscope,
[PHYSICAL REVIEW LETTERS 56](#), 930 (1986).
- ¹²¹G. Binnig; H. Rohrer; C. Gerber; E. Weibel,
Surface studies by scanning tunneling microscopy,
[PHYSICAL REVIEW LETTERS 49](#), 57 (1982).

- ¹²²X. Xiao; L. Qian,
Investigation of humidity-dependent capillary force,
[LANGMUIR](#) **16**, 8153–8158 (2000).
- ¹²³F. J. Giessibl,
Forces and frequency shifts in atomic-resolution dynamic-force microscopy,
[PHYSICAL REVIEW B](#) **56**, 16010 (1997).
- ¹²⁴H. Jung; D.-G. Gweon,
Creep characteristics of piezoelectric actuators,
[REVIEW OF SCIENTIFIC INSTRUMENTS](#) **71**, 1896–1900 (2000).
- ¹²⁵H. Schmidt; J. C. Rode; C. Belke; D. Smirnov; R. J. Haug,
Mixing of edge states at a bipolar graphene junction,
[PHYSICAL REVIEW B](#) **88**, 075418 (2013).
- ¹²⁶B. Vasić; M. Kratzer; A. Matković; A. Nevošad; U. Ralević; D. Jovanović; C. Ganser; C. Teichert; R. Gajić,
Atomic force microscopy based manipulation of graphene using dynamic plowing lithography,
[NANOTECHNOLOGY](#) **24**, 015303 (2012).
- ¹²⁷P. Nemes-Incze; Z. Osváth; K. Kamarás; L. P. Biró,
Anomalies in thickness measurements of graphene and few layer graphite crystals by tapping mode atomic force microscopy,
[CARBON](#) **46**, 1435–1442 (2008).
- ¹²⁸H. Lee; N. Lee; Y. Seo; J. Eom; S. Lee,
Comparison of frictional forces on graphene and graphite,
[NANOTECHNOLOGY](#) **20**, 325701 (2009).
- ¹²⁹C. Lee; Q. Li; W. Kalb; X.-Z. Liu; H. Berger; R. W. Carpick; J. Hone,
Frictional characteristics of atomically thin sheets,
[SCIENCE](#) **328**, 76–80 (2010).

-
- ¹³⁰C. Lee; X. Wei; Q. Li; R. Carpick; J. W. Kysar; J. Hone,
Elastic and frictional properties of graphene,
[PHYSICA STATUS SOLIDI \(B\) 246, 2562–2567 \(2009\)](#).
- ¹³¹C. J. Shearer; A. D. Slattery; A. J. Stapleton; J. G. Shapter; C. T. Gibson,
Accurate thickness measurement of graphene,
[NANOTECHNOLOGY 27, 125704 \(2016\)](#).
- ¹³²R. J. Warmack; X.-Y. Zheng; T. Thundat; D. P. Allison,
Friction effects in the deflection of atomic force microscope cantilevers,
[REVIEW OF SCIENTIFIC INSTRUMENTS 65, 394–399 \(1994\)](#).
- ¹³³J. Stiernstedt; M. W. Rutland; P. Attard,
A novel technique for the in situ calibration and measurement of friction with the atomic force microscope,
[REVIEW OF SCIENTIFIC INSTRUMENTS 76, 083710 \(2005\)](#).
- ¹³⁴C. D. Onal; B. Sümer; M. Sitti,
Cross-talk compensation in atomic force microscopy,
[REVIEW OF SCIENTIFIC INSTRUMENTS 79, 103706 \(2008\)](#).
- ¹³⁵Á Hoffmann; T Jungk; E Soergel,
Cross-talk correction in atomic force microscopy,
[REVIEW OF SCIENTIFIC INSTRUMENTS 78, 016101 \(2007\)](#).
- ¹³⁶G. Schitter; A. Stemmer,
Identification and open-loop tracking control of a piezoelectric tube scanner for high-speed scanning-probe microscopy,
[IEEE TRANSACTIONS ON CONTROL SYSTEMS TECHNOLOGY 12, 449–454 \(2004\)](#).

- ¹³⁷L. Wang; I. Meric; P. Y. Huang; Q. Gao; Y. Gao; H. Tran; T. Taniguchi; L. M. Watanabe K .and Campos; D. A. Muller, et al.,
One-dimensional electrical contact to a two-dimensional material,
[SCIENCE](#) **342**, 614–617 (2013).
- ¹³⁸K. Kim; M. Yankowitz; B. Fallahazad; S. Kang; H. C. P. Movva; S. Huang; S. Larentis; C. M. Corbet; T. Taniguchi; K. Watanabe, et al.,
Van der Waals heterostructures with high accuracy rotational alignment,
[NANO LETTERS](#) **16**, 1989–1995 (2016).
- ¹³⁹K. Lee; S. Kim; M. S. Points; T. E. Beechem; T. Ohta; E. Tutuc,
Magnetotransport properties of quasi-free-standing epitaxial graphene bilayer on SiC: evidence for Bernal stacking,
[NANO LETTERS](#) **11**, 3624–3628 (2011).
- ¹⁴⁰J. Yin; H. Wang; H. Peng; Z. Tan; L. Liao; L. Lin; X. Sun; A. L. Koh; Y. Chen; H. Peng, et al.,
Selectively enhanced photocurrent generation in twisted bilayer graphene with van Hove singularity,
[NATURE COMMUNICATIONS](#) **7**, 10699 (2016).
- ¹⁴¹D. Sen; K. S. Novoselov; P. M. Reis; M. J. Buehler,
Tearing graphene sheets from adhesive substrates produces tapered nanoribbons,
[SMALL](#) **6**, 1108–1116 (2010).
- ¹⁴²J. Zhang; J. Xiao; X. Meng; C. Monroe; Y. Huang; J.-M. Zuo,
Free folding of suspended graphene sheets by random mechanical stimulation,
[PHYSICAL REVIEW LETTERS](#) **104**, 166805 (2010).

-
- ¹⁴³Z. Ni; Y. Wang; T. Yu; Y. You; Z. Shen,
Reduction of Fermi velocity in folded graphene observed by resonance Raman spectroscopy,
[PHYSICAL REVIEW B 77, 235403 \(2008\)](#).
- ¹⁴⁴V. Carozo; C. M. Almeida; E. H. M. Ferreira; L. G. Cançado;
C. A. Achete; A. Jorio,
Raman signature of graphene superlattices,
[NANO LETTERS 11, 4527–4534 \(2011\)](#).
- ¹⁴⁵X. Chen; C. Yi; C. Ke,
Bending stiffness and interlayer shear modulus of few-layer graphene,
[APPLIED PHYSICS LETTERS 106, 101907 \(2015\)](#).
- ¹⁴⁶C. M. Almeida; P. M. Bede; B. Fragneaud; C. A. Achete,
Engineering graphene superlattices with crystallographic orientation control using atomic force microscope, in *Materials challenges and testing for manufacturing, mobility, biomedical applications and climate* (Springer, 2014), pp. 3–11.
- ¹⁴⁷W. Bao; F. Miao; Z. Chen; H. Zhang; W. Jang; C. Dames; C. N. Lau,
Controlled ripple texturing of suspended graphene and ultrathin graphite membranes,
[NATURE NANOTECHNOLOGY 4, 562–566 \(2009\)](#).
- ¹⁴⁸K. Kim; S. Coh; L. Z. Tan; W. Regan; J. M. Yuk; E. Chatterjee;
M. F. Crommie; M. L. Cohen; S. G. Louie; A. Zettl,
Raman spectroscopy study of rotated double-layer graphene: misorientation-angle dependence of electronic structure,
[PHYSICAL REVIEW LETTERS 108, 246103 \(2012\)](#).
- ¹⁴⁹R. Podila; R. Rao; R. Tsuchikawa; M. Ishigami; A. M. Rao,
Raman spectroscopy of folded and scrolled graphene,
[ACS NANO 6, 5784–5790 \(2012\)](#).

- ¹⁵⁰S. Neubeck; Y. M. You; Z. H. Ni; P. Blake; Z. X. Shen; A. K. Geim; K. S. Novoselov,
Direct determination of the crystallographic orientation of graphene edges by atomic resolution imaging,
[APPLIED PHYSICS LETTERS](#) **97**, 053110 (2010).
- ¹⁵¹D. Rainis; F. Taddei; M. Polini; G. León; F. Guinea; V. I. Fal'ko,
Gauge fields and interferometry in folded graphene,
[PHYSICAL REVIEW B](#) **83**, 165403 (2011).
- ¹⁵²A. Bachtold; C. Strunk; J.-P. Salvetat; J.-M. Bonard; L. Forró; T. Nussbaumer; C. Schönenberger,
Aharonov–Bohm oscillations in carbon nanotubes,
[NATURE](#) **397**, 673–675 (1999).
- ¹⁵³X. Meng; M. Li; Z. Kang; X. Zhang; J. Xiao,
Mechanics of self-folding of single-layer graphene,
[JOURNAL OF PHYSICS D: APPLIED PHYSICS](#) **46**, 055308 (2013).
- ¹⁵⁴S. Cranford; D. Sen; M. J. Buehler,
Meso-origami: folding multilayer graphene sheets,
[APPLIED PHYSICS LETTERS](#) **95**, 123121 (2009).
- ¹⁵⁵S. B. Sinnott; R. Andrews; D. Qian; A. M. Rao; Z. Mao; E. C. Dickey; F. Derbyshire,
Model of carbon nanotube growth through chemical vapor deposition,
[CHEMICAL PHYSICS LETTERS](#) **315**, 25–30 (1999).
- ¹⁵⁶A. Rochefort; D. R. Salahub; P. Avouris,
Effects of finite length on the electronic structure of carbon nanotubes,
[THE JOURNAL OF PHYSICAL CHEMISTRY B](#) **103**, 641–646 (1999).

-
- ¹⁵⁷J. S. Choi; J.-S. Kim; I.-S. Byun; D. H. Lee; M. J. Lee; B. H. Park; C. Lee; D. Yoon; H. Cheong; K. H. Lee, et al.,
Friction anisotropy-driven domain imaging on exfoliated monolayer graphene,
[SCIENCE](#) **333**, 607–610 (2011).
- ¹⁵⁸A. Summerfield; A. Davies; T. S. Cheng; V. V. Korolkov; Y. Cho; C. J. Mellor; C. T. Foxon; A. N. Khlobystov; K. Watanabe; T. Taniguchi, et al.,
Strain-engineered graphene grown on hexagonal boron nitride by molecular beam epitaxy,
[SCIENTIFIC REPORTS](#) **6**, 22440 (2016).
- ¹⁵⁹Y.-B. Zhou; B.-H. Han; Z.-M. Liao; H.-C. Wu; D.-P. Yu,
From positive to negative magnetoresistance in graphene with increasing disorder,
[APPLIED PHYSICS LETTERS](#) **98**, 222502 (2011).
- ¹⁶⁰C. Hwang; D. A. Siegel; S.-K. Mo; W. Regan; A. Ismach; Y. Zhang; A. Zettl; A. Lanzara,
Fermi velocity engineering in graphene by substrate modification,
[SCIENTIFIC REPORTS](#) **2**, 590 (2012).
- ¹⁶¹K. R. Knox; S. Wang; A. Morgante; D. Cvetko; A. Locatelli; T. O. Menten; M. A. Niño; P. Kim; R. M. Osgood Jr.,
Spectromicroscopy of single and multilayer graphene supported by a weakly interacting substrate,
[PHYSICAL REVIEW B](#) **78**, 201408 (2008).
- ¹⁶²J.-C. Charlier; J.-P. Michenaud; Ph. Lambin,
Tight-binding density of electronic states of pregraphitic carbon,
[PHYSICAL REVIEW B](#) **46**, 4540 (1992).

- ¹⁶³J. R. Wallbank; A. A. Patel; M. Mucha-Kruczyński; A. K. Geim;
V. I. Fal'ko,
*Generic miniband structure of graphene
on a hexagonal substrate,*
[PHYSICAL REVIEW B **87**, 245408 \(2013\).](#)

Curriculum Vitae

Johannes Christopher Rode,
born November 26th, 1986 in Lüneburg

2016 Research assistant at the Institute for Solid State Physics of the Leibniz University of Hanover (LUH)

2013-2016 Scholarship holder within the Hannover School for Nanotechnology

since 2014 Preparation of the Dissertation at the Institute for Solid State Physics with Prof. Dr. Rolf Haug

January 2014 MSc degree in physics at the LUH

December 2010 BSc degree in physics at the LUH

2007-2013 Study of physics at the LUH

2006-2007 Civil service at Johann und Erika Loewe-Stiftung in Lüneburg

June 2006 Abitur at the Herderschule in Lüneburg

1999-2006 Education at the Gymnasium Herderschule in Lüneburg

1997-1999 Education at the Orientierungsstufe Kreideberg in Lüneburg

1993-1997 Education at the Hermann Löns Grundschule in Lüneburg

List of Publications

Listed are authored and co-authored scientific publications within the timeframe of working as a Phd-student:

- D. Smirnov; J. C. Rode; R. J. Haug,
Suppression of decoherence in a graphene monolayer ring,
[APPLIED PHYSICS LETTERS 105, 082112 \(2014\)](#).
- H. Schmidt; J. C. Rode; D. Smirnov; R. J. Haug,
(shared first-authorship)
Superlattice structures in twisted bilayers of folded graphene,
[NATURE COMMUNICATIONS 5, 5742 \(2014\)](#).
- J. C. Rode; D. Smirnov; H. Schmidt; R. J. Haug,
Berry phase transition in twisted bilayer graphene,
[2D MATERIALS 3, 035005 \(2016\)](#).
- J. C. Rode; C. Belke; H. Schmidt; R. J. Haug,
Interlayer Configurations in Twisted Bilayers of Folded Graphene,
[ARXIV:1608.08133 \[COND-MAT.MTRL-SCI\] \(2016\)](#).

Listed are co-authored scientific publications prior to working as a Phd-student:

- H. Schmidt; J. C. Rode; C. Belke; D. Smirnov; R. J. Haug,
Mixing of edge states at a bipolar graphene junction,
[PHYS. REV. B 88, 075418 \(2013\)](#).
- H. Schmidt; D. Smirnov; J. C. Rode; R. J. Haug,
Multi-terminal magnetotransport measurements over a tunable graphene p-n junction created by AFM-nanomachining,
[AIP CONF. PROC. 1566, 175 \(2013\)](#).

Contributions to Scientific Conferences

Listed are selected contributions to scientific conferences:

- Poster at the
GRAPHENE WEEK,
2014 in Gothenburg, Sweden.
- [Talk](#) at the
WORKSHOP OF THE NTH
SCHOOL FOR CONTACTS IN NANOSYSTEMS,
2014 in Clausthal-Zellerfeld, Germany.
- [Talk](#) at the
79. JAHRESTAGUNG DER DPG UND
DPG-FRÜHJAHRSTAGUNG,
2015 in Berlin, Germany.
- Talk at the
3RD WORKSHOP OF THE DFG SCHWERPUNKTPROGRAMM 1459
"GRAPHENE",
2015 in Beetz-Sommerfeld, Germany.
- [Talk](#) at the
21ST INTERNATIONAL CONFERENCE ON ELECTRONIC
PROPERTIES OF TWO-DIMENSIONAL SYSTEMS,
2015 in Sendai, Japan.

- [Talk](#) at the
80. JAHRESTAGUNG DER DPG UND
DPG-FRÜHJAHRSTAGUNG
2016 in Regensburg, Germany.
- [Talk](#) at the
22ND INTERNATIONAL CONFERENCE ON HIGH MAGNETIC
FIELDS IN SEMICONDUCTOR PHYSICS
2016 in Sapporo, Japan.
- [Poster](#) at the
33RD INTERNATIONAL CONFERENCE ON THE PHYSICS OF
SEMICONDUCTORS,
2016 in Beijing, China.
- [Talk](#) at the
33RD INTERNATIONAL CONFERENCE ON THE PHYSICS OF
SEMICONDUCTORS,
2016 in Beijing, China.

Credits

Credits to Dr. Henrik Schmidt for preparation and electrical characterization of samples A and C as analyzed in [sec. 5.2.1](#) and in the appendix [figs. A.5/A.6](#) respectively; furthermore for the technical realization of [figure 4.20 a](#). Thanks moreover for advise and fruitful discussion with respect to many of the here presented subjects.

Credits to Dr. Dmitri Smirnov for preparation and electrical characterization of sample B as analyzed in [sec. 5.2.2](#) and many thanks for his mentoring in my early stages.

Danksagung

Credit, where credit is due! Aber den Rest machen wir mal auf Deutsch zwecks persönlicher Note:

Zunächst gilt mein Dank Prof. Dr. Rolf Haug, für die Betreuung meiner Arbeit über die letzten Jahre. Ich habe eine Menge gelernt -z.B. in Sachen akzentuierter, zielgruppengerechter Präsentation- und fühlte mich fast immer an den richtigen "Hebel" gesetzt.

Im konkreten Rahmen des Verfassens dieser Arbeit weiß ich zudem den guten erteilten Rat sowie gewährten Freiraum sehr zu schätzen.

Einen herzlichen Dank an Prof. Dr. Patrik Recher für die abermalige Übernahme eines Graphen-Korreferats in unserer Gruppe. Hoffentlich war etwas Interessantes auch für den Theoretiker dabei.

Prof. Dr. Peter Behrens sei für das interdisziplinäre Korreferat sowie chemischen Rat und sein Interesse an meiner Arbeit gedankt; und des Weiteren auch ganz herzlich für die Zweitbetreuerschaft im Rahmen der Hannover School for Nanotechnology.

Spezifisch auf besagtes Promotionsprogramm der Hannover School for Nanotechnology bezogen möchte ich zudem Dr. Fritz Schulze Wischeler für sein offenes Ohr, sein persönliches Engagement und die erstklassige Organisation danken.

Und dann wären da noch die Mitarbeiter; Nanos und Femtos:

Gemeinsame Doktorandenschaft mag oftmals mehr sein als bloßes Kollegentum. In meinem Fall kann ich jedoch sagen: Analog zum Doktorvater Haug (und Großvater von Klitzing ;-)) hätte ich mir keine besseren Doktorgeschwister wünschen können. Ob bei der Arbeit, after-hours oder gar im fernen Osten- ihr habt den curvigen(!) Weg durch die letzten Jahre zu einer angenehmen und spannenden Reise gemacht.

Ganz wichtig: Mama und Papa- Danke für Alles.

Desweiteren sei meinem sozialen Umfeld im Allgemeinen- allen voran den BNB- für Rücksichtnahme und Verständnis in Bezug auf jene beinahe kompromisslose Turbi-Schaffensphase gedankt, welche sich nun zu guter Letzt in diesem hübschen Buch manifestiert.